Mixed Pixel Retrieval of Soil Moisture from L-band Passive Microwave Observations

YE Nan

Submitted in fulfilment of the requirements for the degree of

Doctor of Philosophy

January 2014

Department of Civil Engineering

Monash University

ADDENDUM

Page 2-50 Line 8: Add "However in practice the SMOS and SMAP antenna gain patterns are not corrected, and the contribution of side-lobe is not removed, which will induce a slight difference when applying the results of this thesis to space-borne sensors".

Page 3-6 Line 14: Change "~1K" to "1K error when combined with 1.3K error in the root-mean-square sense may not impact the retrieval performance significantly".

Page 5-5 Line 3: Add "which is the maximum of ground surface height measurements".

Page 6-6 Line 2: Add "A key assumption of this step is that the microwave behaviour of the studied cities represents that of urban areas world-wide".

Page 7-20 Line 30: Add "It should be noted that SMAP radar observations are expected to provide a capability identify water pixels and detect pixel water fraction with a tolerance level of 5% error when 10% of a 36km pixel is occupied by water bodies. This capacity potentially limits the impact of water on SMAP brightness temperature within 2.5 K, based on analysis using a 5% water fraction uncertainty".

Table of contents

List of symbols

Symbol	*Units*	*Definition*
α	-	Attenuation coefficient
α_t		Spectral surface albedo
α_v	-	Offset of Eqn.(2.43)
β_v	-	Coefficient of Eqn.(2.43
γ	-	Transmissivity of the vegetation layer
γ_D	[m]	Penetration depth
θ	[°]	Incidence angle
θ_{obs}	[°]	Observed incidence angle
θ_{ref}	[°]	Reference angle
ω	-	Single scattering albedo
ω_f	[Hz]	Angular frequency
ε'	-	Real part of dielectric constant
ε''	-	Imaginary part of dielectric constant
ε_0'	[F/m]	Permittivity of free space ($\sim 8.9\times10^{-12}$)
ε_r	-	Relative dielectric constant of the material
ρ_s	[kg/m^3]	Dry soil density
ρ_w	[kg/m^3]	Density of water
σ	[S/m]	Electrical conductivity
σ_{hh}	[dB]	Backscatter in HH polarisation
σ_{norm}	[dB]	Normalised backscatter
σ_{obs}	[dB]	Observed backscatter
σ_{pp}^{int}	[dB]	Backscatter from the interaction between the vegetation and soil surface
σ_{pp}^{S}	[dB]	Soil surface backscatter
σ_{pp}^{T}	[dB]	Total co-polarised backscatter

Symbol	*Units*	*Definition*
σ_{pp}^{vol}	[dB]	Backscatter from the vegetation volume
σ_r	[dB]	Surface Root-Mean-Squared height
σ_{ref}	[dB]	Backscatter observation at the reference angle
σ_T	[S/m]	Electrical conductivity at temperature of T °C
σ_{t1}	[dB]	Backscatter coefficients at $t1$
σ_{t2}	[dB]	Backscatter coefficients at $t2$
σ_{vv}	[dB]	Backscatter in VV polarisation
λ	[m]	Wave length
λ_t	[W/(m·K)]	Soil thermal conductivity
τ	-	opacity
τ_C	-	vegetation layer opacity
τ_{NAD}	-	Optical depth at nadir
Γ_p	-	Reflectivity in polarisation of p
Γ_p^*	-	Smooth surface reflectivity in polarisation of p
a_i	-	Spatial weight of land surface components in sensors' field-of-view
a_t	-	Empirical parameter of Eqn.(2.22
a_b	-	Empirical parameter of Eqn.(2.28)
a_w	[m]	semi-major radius of the PLMR elliptic field-of-view in x direction
A	[m^2]	Area of overlap of the two plates
$A_{a,b}$	-	$m \times n$ coefficient matrix in Eqn.(4.7)
ATI	[J/(m^2·K·$s^{1/2}$)]	Apparent thermal inertia
b	-	Empirical parameter of Eqn.(2.42)
b_b	-	Empirical parameter of Eqn.(2.28)
b_t	-	Empirical parameter of Eqn.(2.22)
b_w	[m]	semi-minor radius of the PLMR elliptic field-of-view in x direction

Symbol	*Units*	*Definition*
b_{w0}	-	Semi-empirical parameters in Eqn.(2.37)
C	[F]	Capacitance
C_t	-	Empirical attenuation coefficient
c	[m/s]	Velocity of an electromagnetic wave in free space (3×10^8)
c_t	[J/(kg·K)]	Soil heat capacity
d	[m]	Separation between the plates
e	-	Emissivity of soil layer
e_p	-	Emissivity in polarisation of p
f	[Hz]	Frequency
f_i		Cover fraction
$f_{Landsat}$	-	Landsat derived binary water fraction
f_{PLMR}	-	Water fraction of each PLMR brightness temperature pixel
f_R	-	Rock cover fraction
f_U	-	Urban cover fraction
f_{water}	-	Water cover fraction
H_R	-	Surface roughness parameter
I	-	Transfer index
j	-	Imaginary unit which is equal to $\sqrt{-1}$
K	[m^{-1}]	geometric constant of TDR probe
L	[m]	TDR probe length
M_s	[kg]	Mass of solid constituent
M_t	[kg]	Mass of soil-water mixture
M_w	[kg]	Mass of water constituent
n	-	Number of layers
N_{Rp}	-	Surface roughness parameter in polarisation of p
P	-	Soil porosity

Symbol	*Units*	*Definition*
p	-	Polarisation
Q	[C]	Amount of charge
Q_R	-	Polarisation mixing parameter
R	-	Correlation coefficient
$R_{0.86}$	-	Apparent reflectance observed at 0.86 μm
$R_{0.66}$	-	Apparent reflectance observed at 0.66 μm
$R_{1.24}$	-	Apparent reflectance observed at 1.24 μm
$R_{1.64}$	-	Apparent reflectance observed at 1.64 μm
$R_{2.13}$	-	Apparent reflectance observed at 2.13 μm
R_{green}	-	Reflectance at green band
R_{NIR}	-	Reflectance at near infrared band
R_{SWIR}	-	Reflectance at shortwave infrared band
S	-	Microwave brightness temperature and backscatter observations
SM_{fc}	[m^3/m^3]	Field capacity
SM_g	[kg/kg]	Gravimetric soil moisture
SM_{sat}	[m^3/m^3]	Saturation soil moisture or water holding capacity
SM_v	[m^3/m^3]	Volumetric soil moisture
$SM_{v,i}$	[m^3/m^3]	Volumetric soil moisture of layer i
SM_{wilt}	[m^3/m^3]	wilting point
T	[K]	Physical temperature of the material
T_{eff}	[K]	Effective soil temperature
T_{deep}	[K]	Deep soil temperature
T_{surf}	[K]	Surface soil temperature
T_s	[K]	Physical temperature of soil layer
T_v	[K]	Physical temperature of vegetation layer
t	[s]	Round-trip time of the wave

Symbol	*Units*	*Definition*
TB_p	[K]	Brightness temperature in polarisation of p
TB_{err}	[K]	Brightness temperature error
$TB_{grd,p}$	[K]	Ground brightness temperature in the sensor's field-of-view
TB_{norm}	[K]	Normalised brightness temperature
$TB_{obs,p}$	[K]	Sensor's apparent brightness temperature observation
TB_{ref}	[K]	Brightness temperature observation at the reference angle
TB_B	[K]	Brightness temperature of bulk medium
TB_R	[K]	Brightness temperature of rock component
TB_S	[K]	Brightness temperature of soil component
TB_{SMOS}	[K]	SMOS brightness temperature observations
TI	[J/(m^2·K·s$^{1/2}$)]	Thermal inertia
V	[V]	Voltage
V_0	[V]	Signal amplitude from the TDR instrument
V_∞	[V]	Signal amplitude at the infinite time, about 10 times larger than the propagation time
V_a	[m^3]	Volumes of air constituent
V_B	[V]	Signal amplitude after partial reflections from the beginning of TDR probe
V_E	[V]	Signal amplitude after partial reflections from the end of TDR probe
V_g	[m^3]	Volume of gaps between soil particles
V_s	[m^3]	Volume of soil solid phase
V_t	[m^3]	Total volume of soil
V_w	[m^3]	Volumes of water constituent
W	-	elliptical weight
w_0	[m^3/m^3]	Semi-empirical parameters in Eqn.(2.37)
x	[ms]	Period of reflected waves

Symbol	*Units*	*Definition*
x_a	[ms]	Specific output periods for air
x_s	[ms]	Specific output periods for soil
x_w	[ms]	Specific output periods for water
x_{water}	[m]	Location of Landsat-derived water fraction pixel in x direction
y_{water}	[m]	Location of Landsat-derived water fraction pixel in y direction
Z	[Ω]	characteristic impedance of TDR cable
z	[m]	Soil depth
z_i	[m]	Thickness of layer i

List of abbreviations

AACES	Australian Airborne Cal/val Experiments for SMOS
ALOS	Advance Land Observing Satellite
AMMA	African Monsoon Multidisciplinary Analysis
AMSR-E	The Advanced Microwave Scanning Radiometer for EOS
AMSR2	The Advanced Microwave Scanning Radiometer 2
ARVI	Atmospherically Resistant Vegetation Index
ASAR	Advanced Synthetic Aperture Radar
ASCAT	Advanced Scatterometer
ASD	Analytica Spectra Devices.
ATBD	Algorithm Theoretical Basis Document
AVHRR	Advanced Very High Resolution Radiometer
CAROLS	Cooperative Airborne Radiometer for Ocean and Land Studies
CDF	Cumulative Distribution Function
CDTI	Centro para el Desarrollo Tecnologico Industrial
CMEM	Community Microwave Emission Modelling
CNES	Centre National d'Etudes Spatiales
CSIRO	Commonwealth Scientific and Industrial Research Organisation
DGG	Discrete Global Grid
DMSP-OLS	Defence Meteorological Satellite Program-Operational Line Scanner
EASE	Equal-Area Scalable Earth
ECOCLIMAP	Ecosystem classification and land surface parameters database
ENVISAT	ENVIronmental SATellite

ERS-1/2	The 1st/2nd European Remote Sensing Satellite
ESA	European Space Agency
ESTAR	Electronically Scanned Thinned Array Radiometers
FDR	Frequency Domain Reflectometry
FOV	Field-Of-View
GLC2000	Global Land Cover 2000
GlobCover	Global land Cover
GIS	Geographic Information System
GISA	Global Impervious Surface Area
GPS	Global Positioning System
GRUMP	Global Rural-Urban Mapping Project
H	Horizontal polarisation
HDAS	Hydraprobe Data Acquisition System
HUT-2D	L-band airborne radiometer using 2-Dimensional aperture synthesis developed by Helsinki University of Technology
HYDE	History Database of the Global Environment
IEM	Integral Equation Model
IFOV	Instantaneous Field Of View
IFR	Instrument Flight Rules
IGBP/DIS	International Geosphere-Biosphere Programme Data and Information System
INRA	Institut National de Recherches Agronomiques
ISEA	Icosahedral Snyder Equal Area
L1	Level 1
L2	Level 2
L-MEB	L-band Microwave Emission of the Biosphere model
LAI	Leaf Area Index
LITES	DMSP-OLS nighttime lights
LPRM	Land Parameter Retrieval Model

LST	Land Surface Temperature
LUNSW	Land Use New South Wales
JERS	Japanese Earth Resources Satellite
MERIS	Medium Resolution Imaging Spectrometer
MIRAS	Microwave Imaging Radiometer using Aperture Synthesis
MNDWI	Modified Normalised Difference Water Index
MODIS	MODerate resolution Imaging Spectroradiometer
NAFE	National Airborne Field Experiment
NASA	National Aeronautics and Space Administration
NBMI	Normalised Backscatter Moisture Index
NCRS-SCAN	Natural Resources Conservation Service – Soil Climate Analysis Network
NDVI	Normalised Difference Vegetation Index
NDWI	Normalised Difference Water Index
NEDT	Noise Equivalent Differential Temperature
NIR	Near InfraRed
NMDI	Normalised Multiband Drought Index
NSW	New South Wales
OXTS	Oxford Technical Solutions
OzNet	Australian monitoring network for soil moisture and micrometeorology
PALSAR	Phased-Array L-Band Synthetic Aperture Radar
PBMR	PushBroom Microwave Radiometer
PLIS	Polarimetric L-band Imaging Synthetic aperture radar
PLMR	Polarimetric L-band Multi-beam Radiometer
RADARSAT-1/2	The 1st/2nd RADARSAT satellite
REMEDHUS	Red de MEDición de la HUmedad del Suelo
RFI	Radio Frequency Interference
RMSE	Root-Mean-Squared Error

SAR	Synthetic Aperture Radar
SAZE	SMOS Arid Zone Experiment in Australia
SGP97	Southern Great Plains 1997
SkyLab	A space station launched and operated by NASA
SMAP	Soil Moisture Active and Passive
SMAPEx	SMAP Experiments
SMEX02	Soil Moisture Experiment 2002
SMOS	Soil Moisture and Ocean Salinity
SMOSMANIA	Soil Moisture Observing System-Meteorological Automatic Network Integrated Application
SMOSREX	Surface Monitoring Of the Soil Reservoir EXperiment
SPOT	Systeme Probatoire d'Observation de la Terre
STARSS	Salinity Temperature and Roughness Remote Scanner
SVAT	Soil-Vegetation-Atmosphere Transfer scheme
SWIR	ShortWave InfraRed
TDR	Time Domain Reflectometry
TerraSAR	TerraSAR satellite
TM	Thematic Mapper
TRMM-TMI	Tropical Rainfall Mission Microwave Imager
TVDI	Temperature-Vegetation Dryness Index
TVX	Temperature-Vegetation Contextual
USGS	U.S. Geological Survey
V	Vertical polaristion
VFR	Visual Flight Rules
VIS	VISable band
VIT	Vegetation Index/Temperature
VMAP	Vector MAP
VWC	Vegetation Water Content
WindSat	Space-borne multi-frequency polarimetric microwave radiometer

Abstract

Soil moisture plays a key role in the water, energy, and carbon exchanges at the interface between the atmosphere and earth surface. Its spatial and temporal distributions at regional and global scales are required by many disciplines, including hydrology, meteorology, and agriculture. During the last three decades, passive microwave remote sensing has been widely acknowledged as the most promising technique to measure the spatial distribution of near surface (top few centimetre) soil moisture, due to its direct relationship to the soil dielectric constant, its ability to penetrate clouds, and its reduced sensitivity to vegetation canopy and surface roughness. Therefore, the first two space missions dedicated to soil moisture, the Europe Space Agency (ESA)'s Soil Moisture and Ocean Salinity (SMOS) mission and the National Aeronautics and Space Administration (NASA)'s Soil Moisture Active Passive (SMAP) mission, are based on L-band (~1.4 GHz) passive microwave observations every two to three days. Using radiative transfer models, brightness temperature observations are used to estimate water content of the top approximately five centimetres soil with a target accuracy of ~0.04 m^3/m^3.

Based on the current level of antenna technology, the best spatial resolution that can be achieved at L-band by both the SMOS and SMAP radiometer approaches is approximately 40 km. At such a coarse scale, non-soil targets such as surface rock, urban areas, and standing water are present within many SMOS and SMAP pixels across the world, potentially confounding the radiometric observations, and in turn degrading the soil moisture retrieval if not accounted for their contribution. Consequently, the objective of thesis is to determine the impact of land surface heterogeneity conditions on L-band passive microwave satellite footprints using airborne passive microwave brightness temperature observations collected during five Australian airborne field campaigns conduced within the past eight years.

Using the Polarimetric L-band Multi-beam Radiometer (PLMR) mounted on a scientific aircraft, brightness temperature of the SMOS and SMAP sized study

areas were measured at viewing angles of 7°, 21.5°, and 38.5°. Due to the strong angular dependency of brightness temperature, the multi-angular PLMR observations need to be normalised to a reference angle. The angle 38.5° was chosen to closely replicate the fixed incidence angle of SMAP. In this thesis the Cumulative Distribution Function (CDF) based method is developed for incidence angle normalisation by matching the CDF of observations for each non-reference angle. Subsequently, the effects of surface rock, urban areas, and standing water were explored using the incidence-angle-normalised airborne brightness temperature observations and coincident ground sampling data. The brightness temperature difference between that of the mixed pixel and its soil only equivalent was defined as the non-soil targets induced brightness temperature contribution that will potentially lead to a soil moisture retrieval error if not accounted for. It was found that about 13% of SMOS and SMAP pixels on the world's land mass may be adversely affected by surface rock, urban areas, or standing water. However, such pixels are not uniformly distributed or coincident, meaning that such factors may be particularly important in some parts of the world.

Declaration

This thesis contains no material which has been accepted for the award of any other degree or diploma in any university or other institution and affirms that to the best of my knowledge, the thesis contains no material previously published or written by another person, except where due reference is made in the text of thesis.

YE Nan

January 2014

Acknowledgements

There are a number of people without whom this thesis might not been written and to whom I would greatly appreciate.

First of all I would like to express my greatest and sincerest gratitude to my main supervisor Professor Jeffrey Walker for his patience, motivation, enthusiasm, and encouragement throughout my study. His systematic guidance helped me understand how to think, speak, and write in a scientific way, and his passion for research showed me how to be a scientist. I would also like to thank my two co-supervisors, Dr. Dongryeol Ryu from the Univeristy of Melbourne and Professor Robert Gurney from Reading University, for their constructive advices to my research, and insightful comments on my papers.

A special thank goes to Dr Christoph Rüdiger and Dr Rocco Panciera for their guidance, discussion, and hard questions, which helped me have a clearer and deeper understanding of my research. Also, a great thank goes to my colleagues Sandy Peischl and Ranmalee Bandara, for working side by side with me, answering my questions at any time, and providing indispensable supports in GIS, language, field works, and lab experiments. More importantly, they together with other members in the group made this journey more colourful.

I want to thank all participants in the SAZE and AACES campaigns: M. Allahmoradi, C. Betgen, S. Bircher, T. Che, J. Costelloe, A. French, C. Gruhier, X. Han, S. Hayes, J. Johanson, C. Jolly, E. Kim, O. Klimczak, J. Lai, D. Leroux, X. Li, M. Lukowski, V. Matic, A. Mialon, R. Pipunic, U. Port, P. Richardson, R. Schrooten, S. Slowinska, G. Tomlinson, M. Vreugdenhill, J. Wen, A. Woijciga and R. Young, for their helps with the in-situ and airborne data collection, and also making a lot of fun during the campaigns.

Last but not the least, I would like to thank my parents Enliang YE and Ling ZHAO, for giving birth to me at the first place and continuously supporting my dreams even very far from home. Thanks to my wife Danyang JIN for marrying me and encouraging me, and thanks to my parents-in-law: Shangjin

JIN and Xiaohua Xu, for supporting me and taking caring my wife when I was away.

List of figures

List of tables

1 Introduction

This thesis demonstrates the effects of surface rock, urban area, and standing water on brightness temperature observations, and consequently the potential impact on soil moisture retrieval accuracy at the ~40km scale of L-band (~1.4 GHz) space-borne radiometers, if not accounted for in retrieval algorithms. Particular reference is made to the Europe Space Agency's (ESA) Soil Moisture and Ocean Salinity (SMOS) satellite launched in November 2009, and the National Aeronautics and Space Administration's (NASA) Soil Moisture Active and Passive (SMAP) satellite scheduled for launch in 2014. In both these space-borne missions, the derived soil moisture products are expected to have a target accuracy of 0.04 m^3/m^3. However, at the coarse scales of the SMOS and SMAP missions, non-soil targets such as surface rock, urban area, and standing water are present in the field-of-view of many pixels. Their contribution to the overall passive microwave response and subsequent impact on soil moisture retrieval has not been well considered to date, potentially introducing considerable error in the retrieved soil moisture from current state-of-art algorithms.

To demonstrate the potential effect of land surface heterogeneity on soil moisture retrieval accuracy, the cover fraction of non-soil targets was compared with induced brightness temperature contributions and soil moisture status of corresponding pixels, using airborne brightness temperature and *in-situ* sampling data collected from Australian field experiments. A cover fraction threshold was thus determined for the SMOS and SMAP target accuracy. The SMOS and SMAP pixels expected to have a soil moisture error in excess of the 0.04 m^3/m^3 target were subsequently identified from land surface cover maps. This chapter describes the motivation of this research, the context in which it has been studied, and the outline of this thesis.

1.1 Motivation

Soil moisture is a key variable in the water, energy, and carbon exchanges between the atmosphere and the ground surface (Betts et al., 1996, Entekhabi et al., 1996). Moreover, the distribution of soil moisture at regional and global scales are required to improve climate prediction and weather forecasting skill, which will benefit climate-sensitive socio-economic activities, including water management (Entekhabi et al., 1999, Krajewski et al., 2006, Wagner et al., 2007), flood forecasting (Koster et al., 2010), numerical weather prediction (Albergel et al., 2010, Entekhabi, 1995), and agricultural modelling (Bolten et al., 2010, De Wit and Van Diepen, 2007, Koster et al., 2004, Koster et al., 2009, Weaver and Avissar, 2001).

A straightforward means to measure temporal variation of soil moisture is time series soil moisture profile monitoring using point-based networks. However, it is difficult to install and maintain monitoring stations over regional or global scales. Consequently, in the last three decades many researchers have demonstrated the use of remote sensing techniques to directly measure spatial distribution of near-surface soil moisture. These techniques, including visible, thermal infrared, active and passive microwave, are based on the relationship between water content of soil and electromagnetic radiation emitted or reflected from the measured land surface (Schmugge et al., 1980, Engman, 1991).

The possibility of using optical (visible/infrared) observations to measure soil moisture has been proved in some controlled experiments (Idso et al., 1975, Price, 1977, Adegoke and Carleton, 2002, Wang et al., 2007b), and this technique can achieve a high spatial resolution (< 1 km) and revisit frequency (<1 day). However, their applicability is limited by daytime solar illumination, cloud-free weather condition, and bare soil surfaces or shortly vegetated surfaces since cloud and vegetation coverage are opaque at visible and infrared ranges. Under bare soil conditions, visible/infrared signal is also highly related to soil types, and only soil wetness index rather than soil water content is directly retrievable.

Space borne radars (i.e. JERS, PALSAR) are able to measure soil moisture with a high spatial resolution (< 100 m). However, they normally suffer from a narrow beam width that cannot satisfy the temporal (~3 days) and spatial (global) coverage requirements of hydrology applications. In addition, radar measurements are more sensitive to soil surface roughness and vegetation scattering than radiometers, resulting in a high uncertainty of the soil moisture retrievals from radar observations (Dubois et al., 1995, Shi et al., 1997).

The microwave radiometers operating at C-band (i.e. AMSR-E, AMSR2, Wind-Sat), or X-band (i.e. TRMM-TMI) are also sensitive to soil moisture, but the microwave emission from the soil layer is significantly affected by attenuation from the vegetation canopy and scattering by the atmosphere (Jackson et al., 2002, Wigneron et al., 1995). Moreover, the soil layer thickness observed is reduced to ~1 cm (Njoku et al., 2003). Consequently, microwave radiometers at high frequency need to account for the contribution of atmosphere, are only sensitive to a very shallow layer of soil, and are limited to areas with vegetation water content < 1.5 kg/m^2 (Njoku and Li, 1999).

To date, the passive microwave remote sensing approach at L-band is considered the most promising due to its ability to penetrate cloud, direct relationship with soil moisture through the soil dielectric constant, and a reduced sensitivity to land surface roughness and vegetation cover (Shutko and Reutov, 1982, Schmugge et al., 1986, Jackson and Schmugge, 1989, Njoku et al., 2002). The first space borne passive microwave observations at L-band were collected by the short duration SkyLab mission in the 1970s, providing the earliest demonstration of soil moisture retrieval from passive L-band observations on orbit (Jackson et al., 2004b). However, the first satellite dedicated to soil moisture was not launched until November 2009, which carries a 2D interferometric radiometer to measure microwave emission from the earth surface at L-band (1.413 GHz). The development of the Soil Moisture and Ocean Salinity (SMOS) mission was led by the ESA with the aim to map global soil moisture every 2 to 3 days and a target accuracy of 0.04 m^3/m^3. Moreover, the second satellite dedicated to soil moisture, the Soil Moisture Active and Passive (SMAP) mission under development by NASA, is

scheduled for launch in October 2014. This mission will combine L-band radiometer (1.41 GHz) and radar (1.26 GHz) instruments in order to achieve the same target soil moisture retrieval accuracy as SMOS, but with an enhanced spatial resolution. However, based on current antenna technology, the spatial resolution of both space borne radiometers is limited to 40 to 50 km. Thus, microwave observations at such a coarse scale are easily affected by the land surface heterogeneity within the sensors' field-of-view.

The contribution of non-soil targets, such as surface rock, urban area, and standing water, that are present in many radiometer sized pixels across the world, has not been well considered in current state-of-art soil moisture retrieval models. Consequently, this thesis aims to develop a better understanding of the effect that land surface heterogeneity conditions may have on soil moisture derived from L-band passive microwave satellite footprints. In particular, this research will focus on three specific land surface features that have not been well studied: i) surface rock; ii) urban areas; and iii) standing water.

1.2 Importance of soil moisture estimation

Soil moisture plays a significant role in land-atmosphere interactions, since it controls the rainfall partitioning into infiltration and runoff (Aubert et al., 2003), influences the evapotranspiration and vegetation photosynthetic rate (Olioso et al., 1999), and impacts soil micro-organism activities (Schnürer et al., 1986). Its temporal and spatial distributions are required to improve the understanding of the Earth's water, energy, and carbon cycles. Soil moisture information would therefore have numerous benefits in the fields of weather and climate, extreme events, agriculture, human health and defence. The main benefits in these application areas include:

- Weather forecasting and climate monitoring

  The prediction accuracy of weather and climate forecasting is dependent dominantly on modelling the water, energy, and carbon exchange at the land surface (Engman, 1992, Betts et al., 1994, Koster et al., 2003, Conil et

al., 2007), and thus the initialisation of key variables in such models (Beljaars et al., 1996). Many studies show that accurate soil moisture measurements should improve the quality of atmospheric predictions, and thus extend the lead-time of reliable forecasts, including short-term weather prediction (Drusch, 2007), long-term terrestrial water cycle trends (Jung et al., 2010), climate variability (Seneviratne et al., 2010), and the global carbon cycle (Falloon et al., 2011).

- Extreme events (flood, drought, and landslides) forecasting

  The prediction of flood and drought depends not only on precipitation, but also on soil moisture state, which controls the partitioning the precipitation to runoff and infiltration. Additionally, the soil moisture in mountainous areas is one of the most important factors of landslides. Therefore, availability of global soil moisture from satellite missions such as SMOS and SMAP should enhance modelling of surface runoff and infiltration (Bindlish et al., 2009, Crow et al., 2005), benefit solute transport and erosion analyses and management (Castillo et al., 2003, Jackson and O'Neill, 1987), and improve the understanding of stream flow generation mechanisms (Berg and Mulroy, 2006) and drought processes (Cai et al., 2009). Due to this enhanced process knowledge, the prediction skill of flood (Norbiato et al., 2008), drought (Dai et al., 2004), and landslides (Pelletier et al., 1997) will be improved (Jackson et al., 1987, Sridhar et al., 2008).

- Agricultural applications

  The long-term soil moisture prediction can assist farmers to select the best time to plant, depth to plant, and most suitable crop to plant. Moreover, for irrigated crops water efficiency gains may be achieved by better determination of when to water and how much (Jackson et al., 1987, Saha, 1995, Bastiaanssen et al., 2000, Chung et al., 2003, Engman, 1991).

- Human health

  Soil moisture information has also been shown to impact disease vector abundance (Githeko et al., 2000, Shaman and Day, 2005). Additionally, better weather and flood forecasting enhanced by accurate soil moisture information could improve the predictions of virus spreading rates and heat stress, and disaster preparation and response(Entekhabi et al., 2010).

- Defence

  Soil moisture affects terrain trafficability assessment, which is significant to land autonomous deployments. It is also important to the initialization of aviation weather forecast models which could enhance the predications of density altitude, fog formation, and dust emission (Laurent et al., 2008).

1.3 The mixed pixel problem

Any objects with a temperature above absolute zero Kelvin (K) radiates electromagnetic energy proportional to its emissivity (Ulaby et al., 1981). In turn, the emissivity is a function of the dielectric constant, which varies significantly according to soil moisture, since there is a large difference between the dielectric constant of dry soil and that of water (Ulaby et al., 1981, 1982). At L-band, with a wavelength ~21cm, the emissivity of the soil layer is determined by the dielectric constant of the top ~5cm layer of soil (Jackson and Schmugge, 1989).

For soil with a physical temperature of 300 K, the variation of near surface moisture from ~0 m^3/m^3 for very dry soil to ~0.6 m^3/m^3 for saturated soil corresponds to a brightness temperature observation ranging from ~270 K to ~180 K, respectively. This brightness temperature difference of up to ~90 K is considerable, with typical radiometers having a radiometric sensitivity of ~1 K. Consequently, the sensitivity of brightness temperature observations to soil moisture makes the passive microwave technique suitable to measure soil moisture.

Over a natural soil surface, brightness temperature observations are also influenced by other factors: soil roughness (Choudhury et al., 1979, Tsang and Newton, 1982, Mo and Schmugge, 1987), attenuation and self-emission effects of vegetation layer (Jackson et al., 1982, Ulaby et al., 1983, Pampaloni and Paloscia, 1986, Jackson and Schmugge, 1991), and land surface heterogeneity (Tsang et al., 1975, Wilheit, 1978, Kerr and Njoku, 1990). However, at L-band, the coarse resolution achieved for space-borne radiometers means that there is significant land surface heterogeneity within the radiometer pixels of SMOS and SMAP for many parts of the world. Consequently, typical SMOS and SMAP radiometer pixels are always characterised as a mixture of land surface conditions, such as grass, crops, standing water, forest, rock, and urban. Since each of these surface types has different dielectric properties, geometric shape, roughness, etc., they have unique microwave responses that may impact considerably on the pixel-average microwave emission, and therefore the soil moisture retrieval accuracy if not appropriately accounted for. Therefore, the objective of this thesis is to improve our understanding of the effect that land surface heterogeneity conditions may have on L-band passive microwave satellite footprints, and thus the potential error in soil moisture retrieval from space-borne observation. In particular, this thesis will focus on three specific land surface features that have not been well studied: i) surface rock; ii) urban areas; and iii) standing water.

1.4 Outline of approach

This study involves two parts: (A) incidence angle normalisation of airborne brightness temperature observations; and (B) identification of the impacts of surface rock, urban areas, and standing water respectively on brightness temperature observations and retrieved soil moisture accuracy.

To investigate the impacts of studied non-soil targets, the SMOS/SMAP brightness temperature over soil mixed with surface rock, urban areas, and standing water is simulated by upscaling airborne brightness temperature observations. Due to the strong dependency of brightness temperature on incidence angle, multi-angular airborne brightness temperature observations

need to be normalised to a fixed reference angle before the upscaling process is applied. Since the two currently used normalisation methods, the ratio-based and histogram-based methods, are linear, the geo-referenced image of normalised brightness temperature data has a stripe pattern along flight direction over heterogeneous land surfaces. The brightness temperature error induced by this stripe pattern could be considerable compared with the brightness temperature impacts of surface rock, urban areas, and standing water. To deal with the stripe problem, a non-linear normalisation method is developed based on the Cumulative Distribution Function (CDF) matching technique. This supports the upscaling process done in the subsequent steps of this thesis.

Surface Rock: According to Kerr et al. (2010a), rock is assumed to behave like very dry bare soil with a fixed dielectric constant of $5.7 - j\times0.074$. To verify this assumption, the impacts of rock on brightness temperature observations and retrieved soil moisture are simulated using a radio transfer model, and subsequently compared with airborne brightness temperature observations and ground soil moisture sampling data collected over a study area covered with rocks. A rock cover fraction threshold is then obtained for the SMOS and SMAP target accuracy of 0.04 m^3/m^3. Finally, this threshold is used to identify the SMOS pixels with rock induced error exceeding the 0.04 m^3/m^3 target accuracy globally. This result could help to understand the distribution of rock induced uncertainty in soil moisture retrieval, and be used to either flag or mask the area significantly affected by the presence of rock.

Urban Areas: Although a major concern about urban areas is Radio Frequency Interference (RFI), a large effort has been made to switch off RFI sources globally. However, when all RFI has been removed, urban areas might still induce soil moisture retrieval error, if its presence is not considered in the retrieval model. The impact of urban areas on soil moisture retrieval accuracy has only been assessed in a synthetic study to date (Loew, 2008), assuming urban areas behave like forest. Consequently, the impacts of urban areas are investigated using airborne brightness temperature observations and soil moisture measurements collected from a monitoring station network. First, a

regional high resolution land cover classification map is used to calculate the urban cover fraction of each airborne brightness temperature pixel. Then the relationship between brightness temperature observation and urban cover fraction is established, and urban fraction thresholds obtained for the radiometric error budgets of SMOS and SMAP. Taking these thresholds as benchmarks for the 0.04 m^3/m^3 target accuracy, the SMOS and SMAP pixels with potential urban induced soil moisture retrieval error in excess of 0.04 m^3/m^3 are identified. The result can be used to mask and flag areas with urban induced uncertainty in soil moisture retrieval.

Standing Water: Since water has a very high dielectric constant compared with that of soil, microwave radiation is sensitive to the content of water in the near surface soil layer. However, this also means that any standing water within sensors' field-of-view also has a strong microwave response, and might induce a considerable soil moisture retrieval error if its contribution to the brightness temperature is not carefully accounted for in retrieval models. Thus, brightness temperature and corresponding pixel water cover fraction are compared at different scales using multi-resolution and multi-temporal airborne brightness temperature observations collected over a partly flooded study area. In addition, the impacts of standing water on brightness temperature are investigated under various land surface conditions. A water cover fraction threshold is obtained for the 0.04 m^3/m^3 target accuracy and used to identify the SMOS and SMAP pixels affected by standing water. Using a MODIS water fraction product over Australia for the years between 2001 to 2010, the dynamics of water fraction is obtained and compared with the defined threshold for standing water induced soil moisture error, if only the static water fraction map was used in retrieval. The result shows the significance of the dynamics of water fraction, and the temporal and spatial distribution of water induced soil moisture error. Again, the result can be used to mask and flag areas with important standing water induced brightness temperature contributions.

1.5 Organization of thesis

This thesis explores the impacts of surface rock, urban area, and standing water on L-band (~1.4 GHz) passive microwave observations and soil moisture retrieval accuracy at the ~40km scale of space-borne radiometers, if not accounted for in retrieval algorithms, using airborne brightness temperature observations. This chapter has described the motivation, background, and methodology of this research. The remainder of this thesis is organized as follows

Chapter 2 critically reviews the techniques used to measure soil moisture, the foundation of microwave radiometry, the theoretical and experimental background of passive microwave soil moisture remote sensing.

Chapter 3 presents the details of experiments and datasets used in this study, while Chapter 4 describes a new method for incidence angle normalisation. This is important to upscale airborne brightness temperature observations to the scale of SMOS and SMAP with an adequate accuracy. The method was validated using airborne multi-angle observations over various land surface conditions.

Chapter 5 explores the effect of surface rock on soil moisture retrieval accuracy using both model simulated and real data, while Chapter 6 analyses the brightness temperature difference between urban areas and the surrounding natural soil surface, and Chapter 7 presents the standing water impact on brightness temperature. The SMOS and SMAP pixels with potential soil moisture retrieval errors in excess of the 0.04 m^3/m^3 target error are identified in each of the respective chapters. However, Chapter 8 summarises the main conclusions of this work, and provides the recommendations for future work.

2 Literature review

This chapter presents an overview of the soil moisture estimation techniques, and discusses their applicability to measure global soil moisture at an adequate spatial resolution and sampling frequency (temporal resolution), with a focus on the effect of land surface heterogeneity on soil moisture retrieval at the coarse scale of a space-borne radiometer at L-band. The chapter starts with the definition of soil moisture and introduction of *in-situ* methods for soil moisture measurements, followed by a discussion of soil moisture variability in time and space, before introducing remote sensing techniques, which are more suitable to capture the spatial distribution of soil moisture globally. Subsequently, the first two space missions dedicated for soil moisture, using the L-band passive microwave remote sensing technique, are introduced. Last, the problem of land surface heterogeneity on passive microwave observations and soil moisture retrievals are discussed, and the method of demonstrating affected pixels are presented.

2.1 Soil moisture definition

Due to the porosity of soil, the total volume of soil (V_t) consists of a solid phase (V_s) with gaps between soil particles (V_g), meaning

$$V_t = V_s + V_g . \tag{2.1}$$

The gaps are filled with air and/or water, and therefore

$$V_g = V_a + V_w , \tag{2.2}$$

where V_a and V_w are the volumes of air and water constituents respectively. Soil moisture (or water content of soil) is defined as the ratio of water to the total soil media using one of two systems

1. Volumetric soil moisture

$$SM_v = \frac{V_w}{V_t} \tag{2.3}$$

2. Gravimetric soil moisture

$$SM_g = \frac{M_w}{M_t} = \frac{M_w}{M_w + M_s}, \tag{2.4}$$

where M_w, M_s, and M_t indicate the masses of water constituent, solid constituent, and entire soil-water mixture respectively. Soil moisture prediction models, in-situ sensors and remote sensing all traditionally express soil moisture on a volumetric basis.

The water content in the top 10 cm or so of soil is defined as the surface soil moisture, while that available to plants is defined as the root zone soil moisture, which is normally considered to be in the top 100 to 200 cm of soil (Arnold, 1999). When the soil pores are filled with water, the soil is at saturation, being the maximum moisture content. This is defined as the saturation soil moisture or water holding capacity (SM_{sat}). Under natural conditions, water in saturated soil cannot be held against gravitational drainage, and a part of it will infiltrate to deeper layer. After gravitational drainage has occurred, the water content retained under soil suction is defined as the field capacity (SM_{fc}). In contrast, when soil moisture is at the wilting point (SM_{wilt}), the point at which the plants begin to wilt and die, water is held by the soil particles so strongly that it cannot be accessed by plants (Hillel, 1998). The actual maximum volume of water available to plants is the field capacity minus the permanent wilting point. The field capacity and the wilting point are dependent on soil and vegetation properties such as soil texture and vegetation type (Sperry et al., 2002, Hupet et al., 2005).

2.2 In-situ soil moisture measurement

There are many methods to measure *in-situ* soil moisture at the point-based scale, such as thermo-gravimetric, tensiometer, neutron scattering, gamma attenuation, and electromagnetic techniques. The principals, advantages, and limitations of these methods are presented below.

2.2.1 Thermo-gravimetric method

The thermo-gravimetric method is the standard method to determine soil moisture, and used to calibrate all other soil moisture sampling methods. By weighing the destructive soil sample before and after drying in a temperature controlled oven at 105 °C until the weight of sample becomes consistent with time, the mass difference corresponds to the water loss of the soil sample (M_w), allowing the gravimetric soil moisture to be easily calculated through Eqn. 2.4. The volumetric soil moisture is calculated using Eqn. (2.3 by introducing the dry soil density (ρ_s) and the density of water (ρ_w) such that

$$SM_v = \frac{M_w \cdot \rho_s}{M_s \cdot \rho_w}. \tag{2.5}$$

Due to its direct approach, the thermo-gravimetric method is a reliable method to measure *in-situ* soil moisture. Nevertheless, the accuracy of soil moisture measurements is affected by the presence of organic matters and mass loss of the soil sample during sampling, packaging, transferring, oven-drying, and the repeated weighing processes. In addition, the field sampling (especially deep soil) and laboratory processing is difficult and time consuming, and the destructive sampling process make it impossible to repeatedly monitor soil moisture at exactly the same location.

2.2.2 Tensiometric method

By measuring the capillary tension (the energy with which water is sucked by the soil) in moist soil using tensiometers, soil moisture can be determined based on the relationship between soil water tension and soil water content. The tensiometer is a combination of a porous ceramic cup fully-filled with

water or other solutes and a manometer or pressure sensor connected by a liquid-filled tube (Schmugge et al., 1980).

The benefits of using this system are its ease to design and construct with a relative low cost, and ability to monitor both soil moisture tension and water table elevation (negative reading) over a long time period. Nevertheless, this method provides a soil moisture tension measurement which needs to be translated to soil moisture based on knowledge of the moisture characteristics for the soil. Moreover, the tensiometer system can be easily broken during the installation, and the soil moisture tension measurements are limited to 800 cm, meaning that this method will fail under very dry soil conditions (Schmugge et al., 1980, Wilson, 1971).

2.2.3 Nuclear methods

Neutron scattering method

The neutron scattering technique is a method to measure the content of hydrogen in a material, and can be used to estimate soil moisture indirectly (Gardner and Kirkham, 1952). When using a radioactive source to emit neutrons with high energy into the soil, the neutrons are slowed down by elastic collisions with nuclei of atoms and become thermalised. The average energy loss of the neutrons is dependent mainly on the weight of atoms that are collided with. The lower the atomic weight, the larger the resulting energy loss is derived. Consequently, hydrogen, having the lowest atomic weight, can slow down neutrons much more rapidly than any other element present in the soil, thus linking to soil moisture content in the liquid, solid, or vapour state. The number of slow neutrons returning to the detector per unit time is counted, and the soil moisture content is estimated from a pre-determined calibration curve of counts versus volumetric moisture content (Schmugge et al., 1980, Wilson, 1971).

Calibration of the neutron scattering probes is dependent on the strength of the radioactive source, the nature of the detector, the geometry of the source, the detector in the probe (McCauley and Stone, 1972), the materials used to

construct the probe, the size and composition of the access tube, and the physical and chemical properties of the soil (Wilson, 1971). Consequently, for an accurate moisture content measurement, the laboratory calibration should be conducted for each soil type with homogeneous texture, structure, density, and moisture content (Belcher, 1952, Douglass, 1966, Schmugge et al., 1980, Van Bavel et al., 1961). Nevertheless, field calibration of the neutron probe is extremely difficult (Grimaldi et al., 1994, Grismer et al., 1995, Lawless et al., 1963). Additionally, the drifting potential of all electrical equipment has to be considered, and periodic recalibration is required (Schmugge et al., 1980).

The advantages of this system are that volumetric average of soil moisture contents can be estimated, measurements are insensitive to temperature, it can accommodate automatic reading, and temporal variation of soil moisture can be monitored at exactly the same site. Besides the complicated calibration, the disadvantages are a poor depth resolution, limited sampling depth (near the soil surface), and the health risks from exposure to radioactive sources (Schmugge et al., 1980).

Gamma attenuation method

When a gamma ray penetrates a media, the energy is attenuated (scattered and absorbed) by the media, and the attenuation ratio is assumed to be related to the density of the media in the path of the gamma ray. Using the gamma attenuation technique (Gurr, 1962, Ferguson and Gardner, 1962, Davidson et al., Reginato and Van Bavel, 1964), the bulk density of a 1 to 2 cm soil layer is measured and subsequently used to estimate the soil moisture content. Since the dry density of soil (ρ_s in Eqn. 2.5) remains relatively constant, the density of moist soil varies with water content alone. Therefore, soil moisture content can be estimated from gamma ray measurement of bulk soil density (Schmugge et al., 1980).

The advantages of this technique are that: i) it is a non-destructive method; and ii) measurements can be made over very small vertical or horizontal distances. Its disadvantages are that: i) field instrumentation is costly and difficult to use;

and ii) special caution is required to avoid possible health hazards from the radioactive source (Schmugge et al., 1980).

2.2.4 Electromagnetic methods

The electromagnetic methods for soil moisture measurements are based on the large difference between the dielectric constant of soil particles and that of water. The dielectric constant (also known as electric permittivity, magnetic permeability, or specific inductive capacity) is a complex value denoted as $\varepsilon' + j \cdot \varepsilon''$, where the real part ε' is a measure of the polarisability of the materials constituents including water. Normally ε' is expressed as a ratio to that of free space ($\varepsilon_0' \approx 8.854 \times 10^{-12}$ [F/m]) as the relative dielectric constant (for a vacuum, $\varepsilon_r' = 1$). The imaginary part of the dielectric constant ε'' represents the energy absorption by ionic conduction and dielectric loss. The term j is the imaginary unit which is equal to $\sqrt{-1}$.

The relative dielectric constant of soil-water mixture is a composite of its constituents weighted by their volumetric fractions (Jackson et al., 1996). Since liquid water has a dielectric constant of approximately 80 at 20 °C, which is much larger than that of dry soil which is about 2 to 5 (Engman and Chauhan, 1995, Jackson et al., 1981), a wide range of soil dielectric constant is obtained as the volumetric soil moisture content varies from dry soil (dielectric constant of ~3) to saturated soil (dielectric constant of ~40). By measuring the bulk dielectric constant of soil, the volumetric soil moisture can be estimated using a number of electromagnetic techniques. The theoretical background, advantages, and limitations of these methods for soil moisture measurement are briefly presented in the following.

2.2.4.1 Capacitance Probes

By measuring the capacitance of two parallel plate probes inserted in the soil, the dielectric constant of soil between the probes can be determined through

$$C = \varepsilon' \cdot \varepsilon_0' \cdot \frac{A}{d}, \qquad (2.6)$$

where A is the area of overlap of the two plates, and d is the separation between the plates. The capacitance C, defined as $C = Q/V$, is the amount of charge (Q) needed to increase the voltage (V) between two probes for 1 [volt] (Nadler and Lapid, 1996). Subsequently, the soil moisture can be estimated from soil dielectric constant measurements using a pre-calibrated function for specific soil types. Parallel plate probes have been widely used in laboratory determination of moisture content for porous materials, but their use in the field is less convenient because of the problem with plate insertion and soil disturbance. Nadler and Lapid (1996) converted split capacitance probes to cylindrical electrodes that can be buried in the soil or installed at different depths in the soil.

The advantages of capacitance probes are that: i) they are able to continuously measure *in-situ* soil moisture and record the measurement using a data logger; ii) it is relatively easy to translate capacitance measurements to volumetric soil moisture; iii) it is extremely sensitive to small changes in soil moisture content, particularly at dry soil moisture contents; iv) it has a high depth resolution; and v) it is a relatively cheap instrument for soil moisture measurements. The disadvantages are that: i) its soil moisture measurements have a relatively small effective zone; ii) it can be influenced by the adjacent region; and iii) it is

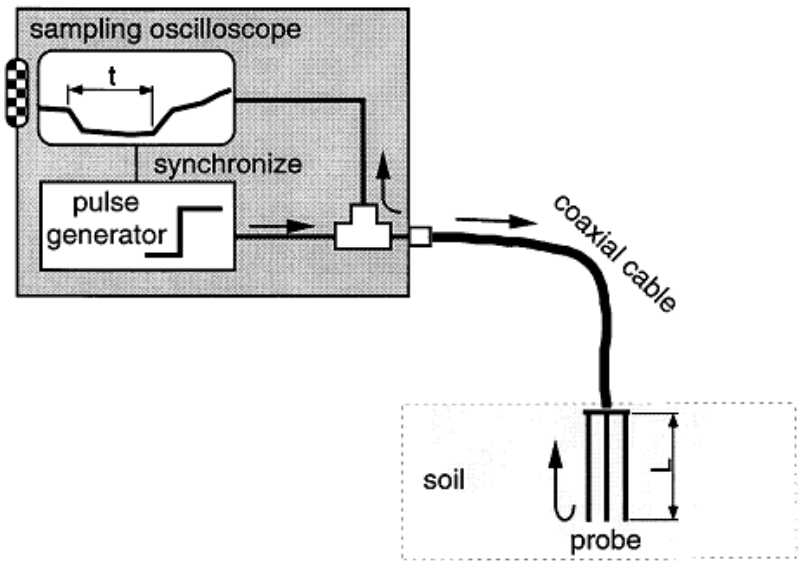

Figure 2.1: Schematic of TDR to measure water content and bulk electrical conductivity of soil. Arrows indicate directions of electromagnetic waves. L and t represent the TDR probe length and propagation time displayed on the detector, respectively. (adapted from Noborio, 2001).

significantly affected by air gaps surrounding the probes.

2.2.4.2 Time Domain Reflectometry Probes

The Time Domain Reflectometry (TDR) approach was developed by Davis and Chudobiak (1975) based on the procedure introduced by Fellner-Feldegg (1969). It can be used to determine both water content and electrical conductivity of soil by measuring i) the propagation time of electromagnetic waves through the TDR probe immersed in the soil and ii) the signal amplitude difference between incidence and reflected electromagnetic waves. The TDR consists of a pulse generator, a probe (usually a rod made of stainless steel or brass) embedded in the soil, a detector which is a sampling oscilloscope, and coaxial cables connecting them (as shown in Figure 2.1). The electromagnetic wave can be generated and sent to the TDR probe through the coaxial cable. A part of the incident wave is reflected at the beginning of the TDR probe because of the impedance difference between the cable and the probe. The remainder propagates through the probe and is reflected back at the end of the probe. The waveforms of reflections are captured and recorded by the detector using the sampling oscilloscope.

The speed of the signal in the TDR probe decreases proportional to the increase of dielectric constant of the surrounding soil. According to Fellner-Feldegg (1969), the real part of the apparent soil dielectric constant (ε') can be determined through

$$\varepsilon' = \left(\frac{ct}{2L} \right)^2, \tag{2.7}$$

where c is the velocity of an electromagnetic wave in free space (3×10^8 m/s), and L is the TDR probe length [m]. The parameter t is the round-trip time of the wave, from the beginning to the end of the probe, which can be obtained by measuring the time difference between reflections at the beginning and the end of the TDR probe.

The electrical conductivity (σ) [S/m] can be also determined from the reflection coefficient using the TDR waveform (Fellner-Feldegg, 1969), and

thus to estimate the imaginary part of the dielectric constant. Dalton et al. (1984) described the relationship of electrical conductivity to signal amplitudes of TDR reflections as

$$\sigma = \frac{\sqrt{\varepsilon'}}{120\pi \cdot L \cdot \ln(V_B/(V_E - V_B))}, \tag{2.8}$$

where V_B and V_E are the signal amplitude after partial reflections from the beginning and end of the probe. However, the reflections are indistinguishable when the waveform is distorted due to loss of higher frequencies. Alternatively, Nadler et al. (1991) proposed to use the signal amplitude from the TDR instrument (V_0) and that at the infinite time (V_∞; e.g., about 10 times larger than the propagation time t) as

$$\sigma = \frac{K}{Z} \cdot \frac{2V_0 - V_\infty}{V_\infty}, \tag{2.9}$$

where K is the geometric constant of a probe [m^{-1}] and Z is the characteristic impedance of a cable [Ω]. The geometric constant K is experimentally determined by immersing the probe in solutions with the known electrical conductivity σ_T at temperature of T °C (Dalton et al., 1990), or determined by

$$K = \left(\frac{\varepsilon_0' \cdot c}{L} \right) \cdot Z, \tag{2.10}$$

where ε_0' is the permittivity of free space (~8.9×10^{-12} F/m) (Baker et al., 1993). The imaginary part of soil dielectric constant is subsequently determined as

$$\varepsilon'' = \frac{\sigma}{\omega_f}, \tag{2.11}$$

where ω is the angular frequency. For an electromagnetic wave at frequency f, the angular frequency ω_f is equal to $2\pi \cdot f$.

For homogeneous soil, the volumetric soil moisture (SM_v) is often determined from the dielectric constant measurements (ε') using an empirically determined calibration curve such as that by Topp et al. (1980)

$$SM_v = -5.3\times10^{-2} + 2.92\times10^{-2}\cdot\varepsilon' - 5.5\times10^{-4}\cdot\varepsilon'^2 + 4.3\times10^{-6}\cdot\varepsilon'^3. \quad (2.12)$$

It has been found that the real part of soil dielectric constant ε' was not strongly sensitive to temperature (10 – 36 °C), soil texture (clay to sandy loam), bulk density of soil (1.14 – 1.44 g/cm^3, for non-swelling soils) and soluble salt content (moistened with salt-free water, 0.01 $CaSO_4$, or 2000 ppm NaCl solution). In comparing between the Topp et al. (1980) empirical curve and the theoretical relationship between soil dielectric constant and volumetric soil moisture based on dielectric mixing models, a good agreement was found over peat to crushed limestone (Jacobsen and Schjoenning, 1995). Consequently, the Topp et al. (1980) model was suggested as the first choice, with a soil moisture accuracy of $\pm$ 0.02 – 0.03 m^3/m^3.

In order to improve the accuracy of this calibration curve, Malicki et al. (1996) introduced the soil bulk density (ρ_s) into Eqn. (2.12 as

$$SM_v = \frac{\sqrt{\varepsilon'} - 0.819 - 0.168\cdot\varepsilon' + 0.159\cdot\varepsilon'^2}{7.17 + 1.18\cdot\rho_s}. \quad (2.13)$$

According to laboratory tests over wide ranges of soil textures (organic soil to sand), bulk densities (0.13 - 2.67 g/m^3) and organic carbon contents (0 - 487 g/kg), Eqn. (2.13 was shown to reduce the variance of soil moisture estimates to about one-fifth of that derived from Eqn. (2.12. For heterogeneous soil, the TDR measured soil moisture has a good agreement with the weighted average of water content $\overline{SM_v}$ for a horizontally layered soil (Nadler et al., 1991). The $\overline{SM_v}$ is expressed as

$$\overline{SM_v} = \frac{\sum_{i=1}^{n} z_i \cdot SM_{v,i}}{\sum_{i=1}^{n} z_i}, \tag{2.14}$$

where n is the number of layers, z_i is the thickness of layer i, and $SM_{v,i}$ is the volumetric soil moisture of layer i (Topp et al., 1982a, b). However, for vertically heterogeneous soil, the TDR measured soil moisture has a large negative bias (Hokett et al., 1992).

The advantages of the TDR technique are that i) the probe is portable meaning that it can be installed at any depth and accommodate automatic reading, allowing easy monitoring of the soil moisture vertical profile; and ii) there is a general calibration curve that is suitable for most soil texture types. The disadvantages are i) the relatively small effective area of TDR probes; ii) the sensitivity to air gaps contacting to the probes; iii) attenuation of the signal caused by salinity or highly conductive heavy clay soils; and iv) the failure of the general calibration curve for heavy clay soils and at low moisture contents (Schmugge et al., 1980, Noborio, 2001).

2.2.5 Frequency Domain Reflectometry Probes

To avoid the complicated waveform analysis on electromagnetic reflections at the beginning and end of the TDR probe, an inexpensive Frequency Domain Reflectometry (FDR) sensor was developed and tested by Campbell and Anderson (1998). Similar to TDR, an electromagnetic pulse is sent and reflected at the end of the probe embodied in the soil. However, the FDR estimates soil moisture by measuring the frequency of the reflected wave, which varies with water content and has an approximate range of 700 to 1500 Hz (Bilskie, 1997). For soils with an electrical conductivity around 1.0 [dS/m], according to the manufacturer a standard empirical calibration function can be used

$$SM_v = 0.037x + 0.335x^2 - 0.187, \tag{2.15}$$

where x is the period [ms] of reflected waves (Campbell Scientific, 1998). This calibration function does not account for the impact of soil properties and is

not suitable for highly clay soil or soil with organic matter content (Campbell Scientific, 1998). As dielectric mixing models have been successfully used for TDR calibrations in a wide range of soils, Veldkamp and O'Brien (2000) developed a more robust calibration function for the FDR sensor. Following the three-phase mixing models used in TDR calibrations (Dasberg and Hopmans, 1992, Roth et al., 1990, Weitz et al., 1997), the FDR probe output is assumed as the composite result of independent soil, air, and water components of the soil. Therefore, the FDR calibration function is given by Veldkamp and O'Brien (2000) as

$$SM_v = \frac{x^\alpha - (1-P)\cdot x_s{}^\alpha - P\cdot x_a{}^\alpha}{x_w{}^\alpha - x_a{}^\alpha}, \tag{2.16}$$

where α is a geometry parameter, P is soil porosity, and x_s, x_a, and x_w are specific output periods for soil, air, and water. Using undisturbed soil samples, they also compared the FDR measured volumetric soil moisture with gravimetric soil moisture measurements, with an R^2 of 0.99 for the topsoil (0 – 0.5 m depth) and an R^2 of 0.95 for the subsoil (> 0.5 m depth) obtained.

According to more than two years testing on the performance of over 40 FDR probes under harsh environmental conditions, FDR is verified as a reliable, precise, and relatively inexpensive alternative to TDR (Veldkamp and O'Brien, 2000). However, since these sensors often operate at a frequency below that of TDR, they are often criticized for being more susceptible to soil environmental effects (Chen and Or, 2006, Rüdiger et al., 2010).

2.3 Spatial and temporal variability of soil moisture

Soil moisture is highly variable both spatially and temporally (Engman, 1992, Wood et al., 1992). The soil moisture content of natural land surfaces is determined by i) soil texture which controls the infiltration rate and water holding capacity; ii) the topography which impacts the partitioning of precipitation to runoff and infiltration; iii) the vegetation coverage which influences evapotranspiration and deep infiltration, and iv) the precipitation history which determine water inputs to the soil layer (Mohanty and Skaggs,

2001, Crow et al., 2012). Understanding the hydrological and meteorological interactions between the land surface and atmosphere which subsequently determine the temporal and spatial dynamics of soil moisture has been a major interest for decades. An accurate soil moisture estimate over the Earth's surface with an adequate spatial resolution and sampling frequency is required in hydrology, meteorology, and agriculture.

2.3.1 Impact of soil properties

The heterogeneous nature of soil, in terms of texture, organic matter content, porosity, structure, and macro-porosity, affects the distribution pattern of soil moisture. Additionally, the colour of soil impacts the absorption of solar radiation and subsequent evaporation rate of bare or low vegetated soil. The variation of soil particle size distributions within a small area could significantly affect local hydrologic processes and result in an inhomogeneous soil moisture distribution. The hydraulic conductivity of soil has been addressed as an important factor for soil water balance and subsequent soil moisture spatial patterns by many studies (e.g. Moore et al., 1988, Grote et al., 2010). Similarly, the heterogeneity of soil also influences soil water balance processes. When soil evapotranspiration is restricted by percolation through a deep soil layer, an increase of spatially averaged evapotranspiration was found over a heterogeneous soil compared with over a uniform soil (Kim et al., 1997). In a related study, Kim and Stricker (1996) found that the effect of soil spatial heterogeneity on the water budget is stronger for a loamy soil than a sandy soil.

The linkage between soil texture heterogeneity and soil moisture distribution pattern has been studied using data acquired from soil moisture field campaigns. A correlation between the known soil texture data and the soil moisture distribution patterns derived from airborne remotely sensed observations and ground-based soil moisture sampling was found during field campaigns in the south-central United States (Mattikalli et al., 1998, Kim et al., 2002). Similarly, using an *in-situ* monitoring network and ground-based soil moisture sampling data collected over a study area of ~40 km × 40 km during the NAFE'05 field experiment, Panciera (2009) found that soil moisture

variability could be related to spatial patterns of both soil texture and land cover type. In addition, water content of soils with higher sand content exhibited consistently lower soil moisture content than that of soils with lower sand content.

2.3.2 Impact of topography

The spatial distribution of soil moisture is also affected by topographical variations in slope, aspect, curvature, upslope contributing area, and relative elevation. At the small catchment and hill-slope scales, water-routing processes, radiative (aspect) effects, and heterogeneity in vegetation and soil characteristics results in heterogeneous near surface soil moisture distribution. During the First International Satellite Land Surface Climatology Project field experiment, lower standard deviations of soil moisture were found over a flat area at scale of 66 m × 66 m than a sloping or a valley area (Charpentier and Groffman, 1992). The significance of the slope effect on soil moisture variability, soil moisture distribution, and time-stable points for mean soil moisture was found in many studies (e.g. De Rosnay et al., 2009, Mohanty et al., 2000b, Jacobs et al., 2004, Western et al., 1999). Nevertheless, the effect of topography was found to be relative to soil moisture condition and seasonal variations. During soil moisture drying events (mid–moisture range), soil moisture patterns and variability are weakly dependent on terrain but strongly dependent on soil and vegetation properties (Western et al., 1999, Kim and Barros, 2002, Bindlish and Barros, 1999, Chang and Islam, 2003, Ryu and Famiglietti, 2005).

2.3.3 Impact of vegetation

The land cover properties, such as vegetation type, density, and uniformity, control the soil infiltration and evapotranspiration rate, and subsequently play a significant role in the distribution pattern of soil moisture. In addition, the impact of vegetation on spatial variability of soil moisture is more dynamic than that of soil texture and topography (Crow et al., 2012). Hawley et al. (1983) showed a temporal persistence of soil moisture pattern with mixed vegetation,

demonstrated over various vegetation-topography-soil combinations, and suggested that the vegetation coverage may reduce the effect of topography on soil moisture heterogeneity. Similarly, a strong impact of land cover on soil moisture distribution was found during the NAFE'05 field campaign in Australia (Panciera, 2009). Over the approximately 40 km × 40 km NAFE'05 study area, the soil moisture of a grassland dominant (over 0.7 coverage) area was representative of the soil moisture of the entire study area, while some wheat fields and forest areas were consistently wetter or drier than the average soil moisture conditions.

Vinnikov et al. (1996) demonstrated the differences in temporal variations of soil moisture over three catchments in Russia; grassland, growing forest, and old forest. Likewise, Mohanty et al. (2000a) explored the temporal variation of the soil moisture spatial distribution of a wheat-grass-mixed area during the Southern Great Plains 1997 (SGP97) hydrology field campaign. The results showed a dependence of inter-seasonal soil moisture spatial pattern on the vegetation dynamics (growth/decay), land management (tillage), and precipitation events under flat topography and uniform soil texture conditions. The impact of land cover variations on spatial distribution of soil moisture was observed during the Soil Moisture Experiment 2002 (SMEX02) in the Walnut Creek agricultural watershed in Iowa with corn and soybean crops (Jacobs et al., 2004, Cosh et al., 2004, Joshi and Mohanty, 2010).

2.3.4 Impact of meteorological forcing

The temporal and spatial dynamics of soil moisture are also affected by meteorological factors such as solar radiation, wind, and humidity. However, the precipitation was identified as the most important meteorological forcing for soil water content and its distribution (Crow et al., 2012). In the study of Sivapalan et al. (1987), the runoff was dependent on storm characteristics and initial soil moisture conditions, resulting in the spatial and temporal variability of soil moisture. During the SGP97 hydrology campaign, a distinct trend was observed in mean soil moisture for three study areas along a north to south precipitation gradient (Famiglietti et al., 1999). The dependence of soil

moisture storage, drainage, runoff, and evapotranspiration on precipitation was found in the studies of Kim and Stricker (1996) and Salvucci (2001).

2.3.5 Spatial and temporal resolution requirements

Soil moisture has a significant impact on surface evaporative fluxes, runoff potential, and water availability for agriculture and human needs. Thus a global soil moisture observation capability is required to meet the needs of many interrelated disciplines (Entekhabi et al., 1999, Leese et al., 2001). Due to the high variability of soil moisture in space and time, the spatial resolution of the soil moisture observation is expected to be in the range of 1 to 10 km for hydrology applications (Crow et al., 2005, Entekhabi et al., 1999), with a revisit time of less than 3 days needed to capture the impacts of storm sequences combined with the inertia of surface storage (Calvet et al., 1998, Walker and Houser, 2004). However, a lower spatial resolution on the order of 40-50km is satisfactory for weather and climate modelling applications.

Using the traditional soil moisture monitoring network, such as SMOSMANIA (Calvet et al., 2007, Albergel et al., 2008), OzNet (Young et al., 2008), NCRS-SCAN (Schaefer and Paetzold, 2001), AMMA (Redelsperger et al., 2006), REMEDHUS (Martínez-Fernández and Ceballos, 2005), UMSUOL (Brocca et al., 2011), and UDC-SMOS (Loew et al., 2009), the time series of soil moisture at specific points can be measured using soil moisture sensors and stored using

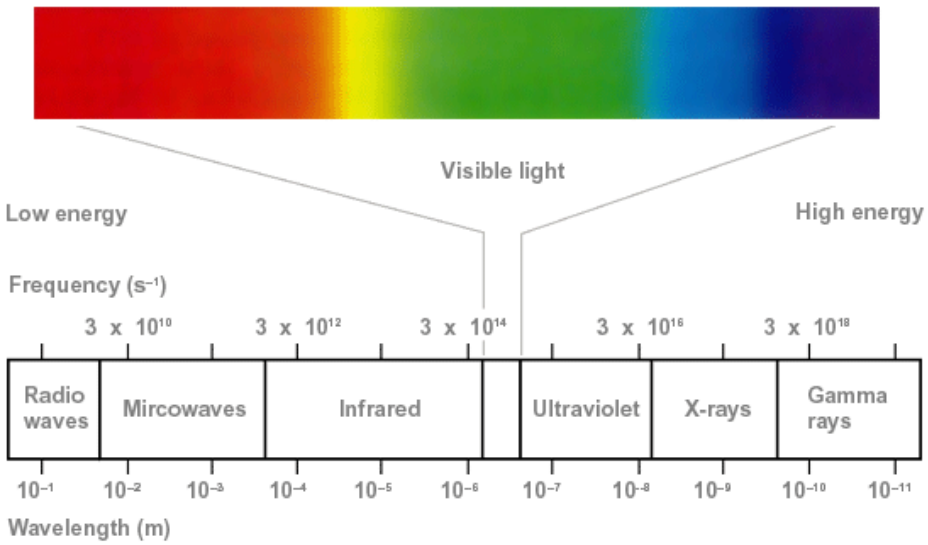

Figure 2.2: Electromagnetic Spectrum.

data logger systems. However, the representativeness of point-based ground soil moisture measurements is limited to 1 km^2 over flat areas with homogeneous soil properties and vegetation conditions. In addition, the integration of point-based measurements to areal average is affected by the spatial variability of soil moisture. Consequently, it is difficult to install and maintain in-situ stations for the purpose of monitoring soil moisture globally.

2.4 Remote sensing of soil moisture

An alternative and cost-effective method for global soil moisture monitoring is remote sensing, a technique which measures the emitted, reflected and/or scattered electromagnetic radiation from the land surfaces. The spatial distribution of soil moisture is subsequently retrieved from the measurement through mathematical models.

During the last three decades, a large number of remote sensing approaches have been developed and tested to measure soil moisture. They differ according to the measured frequency in the electromagnetic spectrum (Figure 2.2) and availability of the radiation source. Compared with point-based soil moisture monitoring techniques, the remote sensing technique has the advantages that i) it measures a spatial average over the sensor's field of view; ii) it can have a global coverage and an adequate revisit time; and iii) it is minimally dependent on complex modelling of land-surface-atmosphere interaction processes. From numerous studies conducted on tower-based, airborne, and space-borne platforms using gamma, optical, thermal infrared, active microwave, and passive microwave sensors, each approach has its own strengths and weaknesses. The following briefly describes the theoretical bases, advantages, and constraints of these approaches.

2.4.1 Optical remote sensing

The sun radiates energy with wavelengths from 0.4 to 2.5 μm, that are subsequently reflected by the earth surface, known as reflectance (Sadeghi et al., 1984). The ratio of reflectance to incoming solar radiation, known as albedo, has been found to be affected by surface soil moisture (Ångström,

1925). The capacity of remote sensing in the solar domain for soil moisture estimation has been investigated in many studies (Dalal and Henry, 1986, Schlesinger et al., 1996, Sommer et al., 1998, Leone and Sommer, 2000).

Several empirical approaches have been developed to describe the relationship between soil surface albedo and soil moisture content (Smith and Bowers, 1972, Jackson et al., 1976, Dalal and Henry, 1986). However, these approaches are highly influenced by many factors, such as mineral composition, organic matter, soil texture, surface roughness, angle of incidence, plant cover and colour (Asner, 1998, Ben-Dor et al., 1999, Engman, 1991, Troch et al., 1997), and therefore are limited to calibrated areas (Wang and Qu, 2009). According to the reflectance studies on four different types of soil with various moisture contents, a physically-based model was developed to link the reflectance of soil to volumetric soil moisture using an exponential function (Asner and Lobell, 2002). Using a similar exponential function, more robust models were proposed by Liu et al. (2002).

In addition, some land surface index based approaches have been developed to suppress the effect of vegetation and enhance the contribution of soil moisture. Such indices were developed by combining the reflectance from visible (0.39 to 0.75 μm), near infrared (0.75 to 1.4 μm), and shortwave infrared (1.4 to 3 μm) wavelengths. The most popular indices is the Normalised Difference Vegetation Index (NDVI) which was used together with land surface temperature data to estimate soil moisture (Carlson et al., 1994, Gillies et al., 1997). The NDVI is defined as

$$\mathrm{NDVI} = \frac{R_{0.86} - R_{0.66}}{R_{0.86} + R_{0.66}}, \tag{2.17}$$

where $R_{0.86}$ and $R_{0.66}$ indicate the apparent reflectance observed at near infrared and red bands, normally centred at 0.86 and 0.66 μm respectively. The two bands used in NDVI are sensitive to vegetation canopies at different depths; the near infrared band can sense approximately eight leaf layers while the red band can only sense the top leaf layer or less (Lillesaeter, 1982). The NDVI has been widely used in numerous studies, such as ecosystem

predication (Turner et al., 2003, Pettorelli et al., 2005), global warming (Kaufmann et al., 2004), and land use change (Volante et al., 2011). By combining the near infrared and red bands reflectance with different complexity, many other vegetation indices were developed but are less popular than the NDVI. Kaufman and Tanre (1992) proposed Atmospherically Resistant Vegetation Index (ARVI) which has self-correction capacity for atmospheric effect by introducing blue band reflectance (0.47 μm).

In order to overcome the difference in penetration depths of near infrared and red bands, and the atmospheric scattering effect on the red band, Gao (1996) developed a Normalised Difference Water Index (NDWI) which replaces the red band reflectance with another near infrared band reflectance, defined as

$$\mathrm{NDWI} = \frac{R_{0.86} - R_{1.24}}{R_{0.86} + R_{1.24}}, \tag{2.18}$$

where $R_{1.24}$ represents NIR reflectance centred at 1.24 μm. The NDWI has been used to monitor the wetness of vegetation canopies over large areas (Jackson et al., 2004a, Chen et al., 2005).

More recently, the Normalised Multiband Drought Index (NMDI) was developed to determine the water content of both soil and vegetation layers using the reflectance at a NIR band and two SWIR bands (Wang and Qu, 2007). The NMDI is defined as

$$\mathrm{NMDI} = \frac{R_{0.86} - (R_{1.64} - R_{2.13})}{R_{0.86} + (R_{1.64} - R_{2.13})}, \tag{2.19}$$

where $R_{1.64}$ and $R_{2.13}$ represent the reflectance of SWIR bands with wavelengths of 1.64 μm and 2.13 μm. Similar to the NDWI, the NMDI uses a NIR band reflectance, which is insensitive to leaf water content changes. However, instead of using a single liquid water absorption band like 1.24 μm wavelength in NDWI, it uses the difference between two liquid water absorption bands (1.64 and 2.13 μm), as the soil and vegetation water sensitive bands.

Under bare or sparsely vegetated soil conditions with Leaf Area Index (LAI) of 0.01, NMDI is a function of soil moisture content, decreasing from 0.85 for very dry soil to 0.15 for wet soil with soil moisture > 0.3 m^3/m^3 (Wang and Qu, 2007). The sensitivity of the NMDI to soil moisture reduces with increasing LAI, and the NMDI alters to be insensitive to soil moisture change when LAI is equal to 2. Subsequently, the NMDI turns to be a complete vegetation water content index under heavily vegetated soil with LAI larger than 2. Under LAI ranging from 2 to 6, a NMDI variation greater than 0.3 is obtained from leaf water content from 0.004 to 0.04 [kg/m^2]. Under moderate vegetation cover conditions, the NMDI is affected by both soil moisture and leaf water content, which decreases with soil moisture and increases with leaf water content. This means that the effects of soil moisture and vegetation water content are not distinguishable using NMDI alone (Wang and Qu, 2007).

Although there is a potential to monitor soil moisture using the optical remote sensing approach, the application is restricted by i) bare soil condition; ii) the requirement for clear sky solar illumination, limiting the observations to day time cloud-free area; and iii) the correction for other factors affecting the soil reflectance.

2.4.2 Thermal infrared remote sensing

Thermal infrared remote sensing measures the thermal emission from the land surface with an electromagnetic wavelength from 3.5 to 14 μm. Due to the correspondence of thermal infrared observations with physical temperature of surface soil, the near surface soil moisture can be estimated based on i) the relationship between soil moisture and soil thermal properties (thermal inertia and thermal conductivity); or ii) the joint relationship among soil, vegetation, and atmosphere.

Thermal inertia method

Due to the daily variation of solar radiation with respect to a specific location on the Earth, the physical temperature of the soil varies with the time of day and with season. The amplitude of the diurnal soil surface temperature relies

highly on the surface soil moisture (Schmugge, 1978, Friedl and Davis, 1994). The soils with higher moisture content are cooler during the day time and warmer at night time (Van de Griend and Engman, 1985).

The thermal inertia (TI) is a physical property that describes the resistance of materials to temperature variations, defined as

$$TI = \sqrt{\lambda_t \cdot c_t}\,, \tag{2.20}$$

where λ_t is the soil thermal conductivity, and c_t is the soil heat capacity (Verstraeten et al., 2006). The soil thermal inertia increases with soil water content, and subsequently reduces the diurnal temperature fluctuation range when the soils are wetter. The apparent thermal inertia (ATI) can be derived from multispectral remote sensing observations through

$$ATI = \frac{1-\alpha_t}{\Delta T}\,, \tag{2.21}$$

where α_t is the spectral surface albedo and ΔT is the diurnal temperature range (Tramutoli et al., 2000, Claps and Laguardia, 2003). Subsequently, the volumetric soil moisture can be estimated through a linear empirical equation

$$SM_v = a_t \cdot ATI + b_t\,, \tag{2.22}$$

where a_t and b_t are empirical parameters. Despite the simplicity and physical basis, its application is limited to bare and low vegetated soil (Xue and Ni, 2006).

Temperature vegetation interaction method

The vegetation water content and land surface temperature (LST) are affected by soil moisture in a complicated way. The relationship between vegetation and atmosphere is described using the vegetation index/temperature (VIT) trapezoid (Moran et al., 1994). According to the studies conducted by (Carlson et al., 1994, Gillies et al., 1997), it was found that a unique relationship among the SM_v, NDVI, and LST, referred to as the "Universal Triangle", can be established over a given land surface. Later, this result was confirmed in good agreement with the Soil-Vegetation-Atmosphere-Transfer (SVAT) model,

which was developed to describe the evapotranspiration processes, rainfall-runoff processes, and soil moisture variations (Gillies and Carlson, 1995). Figure 2.3 is a schematic of the universal triangle. The horizontal and vertical axes represent the scaled soil temperature (T^*) and NDVI (NDVI^*), given as

$$T^* = \frac{T - T_o}{T_s - T_o}, \tag{2.23}$$

$$\mathrm{NDVI}^* = \frac{\mathrm{NDVI} - \mathrm{NDVI}_o}{\mathrm{NDVI}_s - \mathrm{NDVI}_o}, \tag{2.24}$$

where T and NDVI are LST and NDVI observations, and the subscripts o and s indicate minimum and maximum values, respectively. The soil moisture can be regressed using an n^{th} order polynomial function such as

$$SM_v = \sum_{i=0}^{n} \sum_{j=0}^{n} a_{i,j} \cdot \mathrm{NDVI}^i \cdot T^j, \tag{2.25}$$

where $a_{i,j}$ are regression coefficients. This regression equation was simplified to a second order polynomial, and used to estimate daily soil moisture with 1 km resolution by combining *in-situ* soil moisture measurements and MODIS LST and NDVI observations (Wang et al., 2007a).

Based on this triangle technique, numerous approaches have been developed

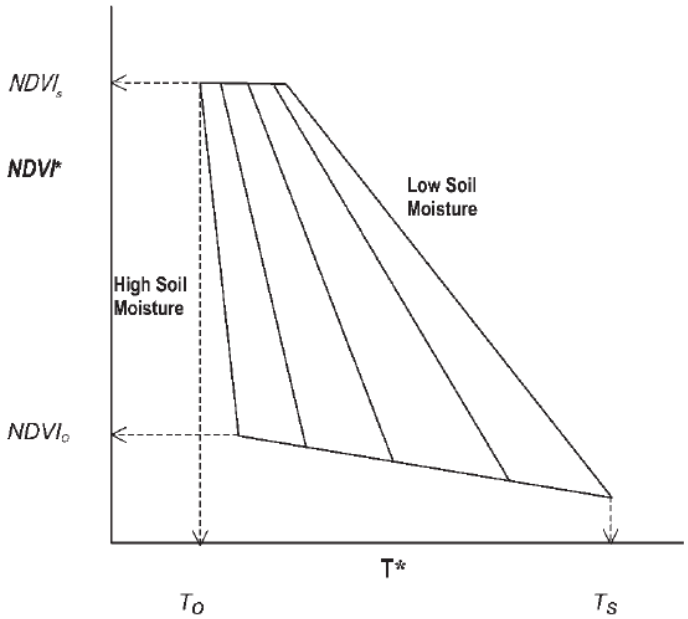

Figure 2.3: Universal triangle relationship between soil moisture, soil temperature, and NDVI (Chauhan et al., 2003).

Table 2.1: Microwave band designations (Lillesand et al., 2004).

Band Designation	*Wavelength (cm)*	*Frequency (GHz)*
K_a	0.75 – 1.10	40.0 – 26.5
K	1.10 – 1.67	26.5 – 18.0
K_u	1.67 – 2.40	18.0 – 12.5
X	2.40 – 3.75	12.5 – 8.0
C	3.75 – 7.50	8.0 – 4.0
S	7.50 – 15.0	4.0 – 2.0
L	15.0 – 30.0	2.0 – 1.0
P	30.0 – 100	1.0 – 0.3

including the Temperature-Vegetation Contextual (TVX) approach (Prihodko and Goward, 1997, Czajkowski et al., 2000), surface temperature-vegetation (*T*/NDVI) space (Lambin and Ehrlich, 1996), Temperature-Vegetation Dryness Index (TVDI; Sandholt et al., 2002), and moisture index (Dupigny-Giroux and Lewis, 1999).

These approaches are powerful and have a clear physical meaning. However, similar to optical remote sensing approaches, they are empirical methods limited to vegetation layer, skin soil and cloud-free conditions (Moran et al., 2004), and dependent on local meteorological conditions, such as wind speed, air temperature, and humidity (Nemani et al., 1993). Therefore, the relationships vary with time and land cover types (Smith and Choudhury, 1991, Czajkowski et al., 2000).

2.4.3 Microwave remote sensing

Microwave remote sensing measures the electromagnetic radiation in the microwave region with an electromagnetic wavelength ranging from 0.5 to 100 cm. This region of the electromagnetic spectrum is subdivided into eight bands as listed in Table 2.1. The intensity of microwave radiation is highly dependent on the dielectric constant of the sensed target. For soil material, the dielectric constant varies with soil water content from approximately 3.5 for very dry soil to approximately 40 for saturated soil (Ulaby et al., 1986), which forms the fundamental basis of microwave remote sensing for soil moisture content. As

shown in Figure 2.4, both the real and imaginary parts of the soil dielectric constant increase with soil water content, with the exact relationship influenced by soil particle distribution (Ulaby et al., 1986).

Based on the provision of electromagnetic radiation sources, microwave remote sensing techniques are divided into two categories: active and passive microwave approaches. Active microwave remote sensing instruments, known as radars, transmit a pulse of microwave radiation and measure the signal scattered back in the direction of the sensor. The coefficient between the power of transmitted and received signal is dependent on the reflectivity of the target which is related to soil moisture content for soil surfaces. In contrast, passive remote sensing instruments, referred to as radiometers, do not transmit any electromagnetic waves but only receive the self-emitted radiation from the land surface at microwave frequencies. The intensity of the microwave emission of soil relies mainly on the soil temperature and soil surface emissivity, which in turn correlates with soil moisture content through the soil dielectric constant.

The following provide a general description of the principals and features of active and passive microwave remote sensing of soil moisture. However, this study will focus on passive microwave remote sensing technique due to its all-weather capability, its less sensitivity to vegetation layer and soil surface roughness, and its direct relationship to soil moisture via soil dielectric constant.

2.4.4 Active microwave remote sensing

Active microwave remote sensing has been widely used to map soil moisture at regional to global scales. The radar system generally consists of a transmitter, receiver, antenna, and processer. An electromagnetic pulse in the microwave frequencies is generated in the transmitter, and transmitted to the target through the radar antenna. Over the land surfaces, a part of the transmitted electromagnetic wave is scattered by the vegetation canopy and/or soil surface, and returned back to the radar system. The backscatter signal is collected by the same antenna and its intensity measured by the receiver. The coefficient between the power of transmitted and backscattered signal is determined in the

processing steps, which can in turn be related to the water content of the sensed soil target.

The most common active microwave mapping configuration is the Synthetic Aperture Radar (SAR) which can provide a spatial resolution in the order of tens of meters over a swath of 50 to 500 km. Currently, active microwave observation from five space-borne SAR systems are available for soil moisture observations: ESA's ERS-1/2 C-band SAR, ESA's ENVISAT (ERS-3) C-band ASAR (Advanced SAR), the Canadian C-band RADARSAR-1/2, the Japanese L-band ALOS (Advance Land Observing Satellite) PALSAR (Phased Array type L-band SAR), and German X-band TerraSAR.

The electromagnetic waves sent and received by radars are normally polarised either horizontally (H) or vertically (V), and therefore there can be up to four

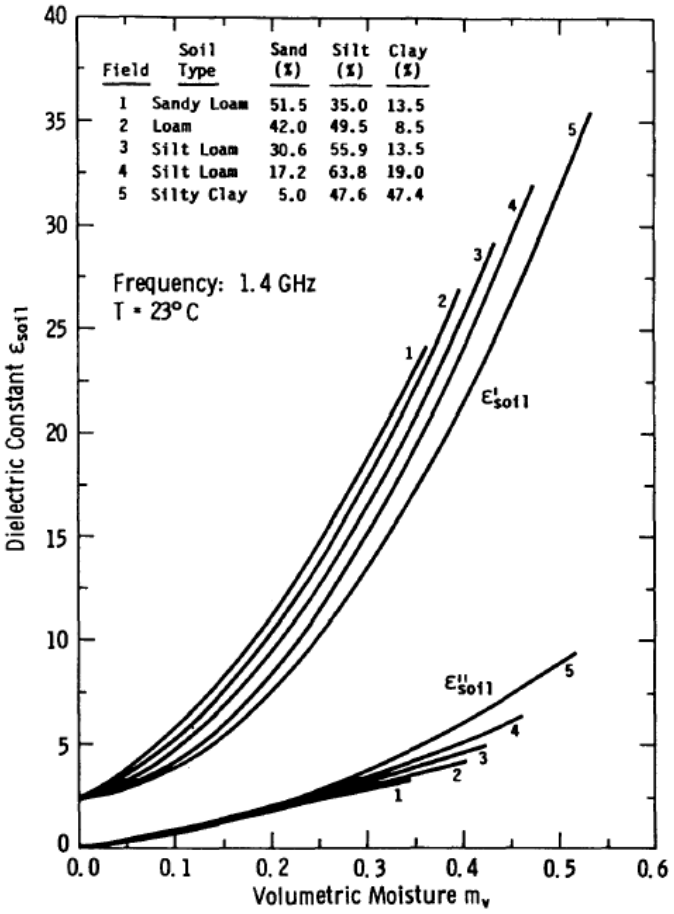

Figure 2.4: Soil dielectric constant as a function of volumetric soil moisture for five soils at 1.4 GHz. Smooth curves were drawn through measured data points (Ulaby et al., 1986).

polarisation combinations: HH, VV, HV and VH, where the first and second letters represent the polarisations of transmitted and received signals respectively. The backscattering coefficient σ_{pp} in decibels [dB] at the polarisation of p is used to describe the intensity of the backscattered radiation (Ulaby et al., 1982). For a given target, the backscattering coefficient is dependent on wave polarisation, frequency, and incidence angle (Ulaby et al., 1982). Under bare soil conditions, the backscattering coefficient obtained using a radar system operating at consistent polarisation, frequency, and incidence angle is affected by the dielectric constant of the soil and surface roughness (Ulaby et al., 1986). Under vegetated soil conditions, the backscattering coefficient is dependent also on the attenuation effect of the vegetation layer, which makes the backscattering response more complicated (Ulaby et al., 1982). In addition, since the soil moisture retrieval is normally based on a flat land surface assumption, the topographic relief causes a variation of local incidence angle and significantly affects the backscattered signal (Van Zyl et al., 1993).

The total co-polarised backscatter σ_{pp}^{T} from the land surface is the sum of three components, given as

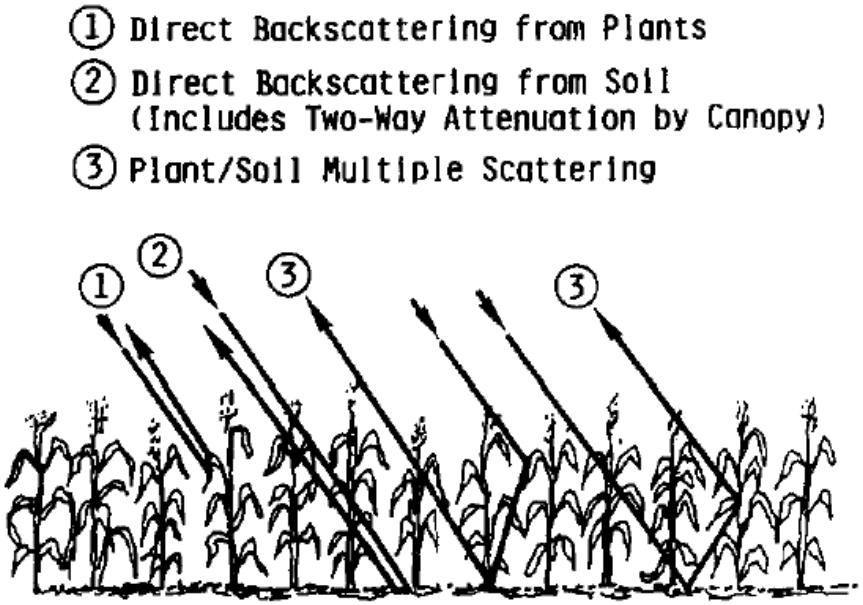

Figure 2.5: Backscattering mechanics of vegetated soil (Ulaby et al., 1996).

$$\sigma_{pp}^{T} = \sigma_{pp}^{vol} + \sigma_{pp}^{S} \cdot \exp(-2 \cdot \tau_{C}) + \sigma_{pp}^{\text{int}}, \quad (2.26)$$

where the first term is the backscatter from the vegetation volume σ_{pp}^{vol}, and the second term is the soil surface backscatter σ_{pp}^{S} attenuated by a vegetation layer with opacity of τ_C during both transmitting toward and reflecting from the soil surface. The third term σ_{pp}^{int} is the interaction between the vegetation and soil surface respectively (Ulaby et al., 1996). For bare or low vegetated soils, the total backscattering coefficients σ_{pp}^{T} is dominated by σ_{pp}^{S} and dependent mainly on the soil moisture and surface roughness. While for highly vegetated soil the σ_{pp}^{T} is determined primarily on the volumetric scattering from the vegetation canopy σ_{pp}^{vol}. Numerous theoretical, empirical, and semi-empirical models have been developed to retrieve the soil electric constant and subsequent soil moisture content from radar backscattering data (Fung et al., 1992, Oh et al., 1992, Dubois et al., 1995, Shi et al., 1995).

Theoretical approaches

Theoretical approaches are normally developed based on the diffraction theory of electromagnetic waves to describe the microwave backscattering from land surfaces with known roughness characteristics. Their applicability is limited to the frequency of electromagnetic waves and the range of surface roughness (Fung et al., 1992, D'urso and Minacapilli, 2006).

Most of the currently used surface scattering models derived from the Small Perturbation Model (SPM; Rice, 1951) and Kirchhoff model (Beckmann and Spizzichino, 1963), which are restricted to slightly rough surface and very rough surface conditions respectively. The Integral Equation Model (IEM) (Fung, 1994, Fung et al., 1992) combines these two theories and is applied to a wider range of roughness conditions than conventional models such as physical optical model and geometric optical mode (Shi et al., 2005, Fung, 1994).

Although the theoretical models can predict the general variation of backscattering coefficient in response to changes in roughness and soil

moisture content (Dubois and Van Zyl, 1994), their complexity and the restrictive requirement for the parameterization of the vegetation and soil surface layer limit their effective applicability for the soil moisture retrieval (Ulaby et al., 1986).

Empirical approaches

Being limited by their validity regions, theoretical backscattering models are not valid for many natural land surface conditions. In addition, theoretical models fail to estimate backscatter in a good agreement with experimental radar backscatter measurements (Walker et al., 2004, Oh et al., 1992). Therefore, many empirical models have been developed from experimental measurements to establish the relationship between soil moisture and backscattering observations (Walker et al., 2004).

The most commonly used empirical method is a linear assumption between soil moisture and radar backscattering polarisation index. For example, Shoshany et al. (2000) proposed an empirical soil moisture retrieval method using the Normalised Backscatter Moisture Index (NBMI) defined as

$$\mathrm{NBMI}=\frac{\sigma_{t1}-\sigma_{t2}}{\sigma_{t1}+\sigma_{t2}}, \tag{2.27}$$

where σ_{t1} and σ_{t2} are the backscatter coefficients at different time steps. Subsequently, the volumetric soil content is calculated through

$$SM_v = a_b \cdot \mathrm{NBMI} + b_b, \tag{2.28}$$

where a_b and b_b are empirical parameters regressed from *in-situ* soil moisture measurements. This approach estimates soil moisture through change detection rather than a direct relationship between microwave backscattering observations and soil moisture content (Engman, 1990, Kite and Pietroniro, 1996). It is based on an assumption that the change of NBMI is caused solely by the variation of soil moisture, and therefore the effects of other factors including soil texture, surface roughness, and vegetation which are relative temporally consistent are minimized (Engman and Chauhan, 1995). Other empirical models have been developed based on the diversity between

horizontally and vertically polarised backscatter observations in order to retrieve both soil moisture and roughness parameters (Wang and Zhang, 2005).

Although empirical methods can result in an accurate soil moisture retrieval with a lower complexity and reduced calculation cost than theoretical methods, their application is restricted by the calibration conditions (Chen et al., 1995, Dubois et al., 1995). To establish a widely applicable empirical relationship for soil moisture retrieval from radar backscattering observations, a large number of experimental measurements are required (Oh et al., 1992), while current empirical models are generally developed from a limited amount of field measurements and therefore valid only under specific land surface conditions (Wang and Qu, 2009).

Semi-empirical approaches

By combining theoretical and empirical approaches, semi-empirical models of backscattering have been developed based on a theoretical foundation with model parameters derived from experimental data.

Oh et al. (1992) developed the first semi-empirical backscattering model, and found that the depolarisation ratio (σ_{hh}/σ_{vv}) is sensitive to soil moisture, and developed a semi-empirical model based on the empirical fitting of scatterometer measurements over bare soil surfaces with different roughness conditions. In the Dubois et al. (1995) method, the co-polarised backscattering coefficients σ_{hh} and σ_{vv} are related to the surface dielectric constant, incidence angle, electromagnetic frequency, and root mean square height of soil surface in a nonlinear way.

Compared with empirical models, semi-empirical backscattering models are not expected to have site-specific problems (Walker et al., 2004). However, the contribution of surface roughness to backscatter observations is normally equal to or greater than that of soil moisture content (Altese et al., 1996, Satalino et al., 2002) and subsequently it is challenging to decouple their effects for active microwave soil moisture remote sensing (Barrett et al., 2009). Although a good agreement between model simulation and backscatter observations has been

found from some studies in vegetated areas (Bindlish and Barros, 2000), these models are generally more suitable for bare soil surface conditions than for vegetated soil conditions (Barrett et al., 2009).

2.4.5 Passive microwave remote sensing

Microwave emission and soil surface emissivity

Due to the thermal motion of atoms, any objects at a physical temperature above absolute zero (~-273 Cº or 0 K) radiate electromagnetic energy. A radiometer is used to measure the intensity of this emission, which increases proportionally with the temperature. To explain the relationship between physical temperature and microwave emission, the black-body concept is used, which was introduced by Planck in his quantum theory in 1901. A black-body is defined as an ideal material that absorbs all incidence radiation and reflects none; it is also a perfect emitter since its temperature would infinitely increase otherwise. Therefore, for a thermodynamic equilibrated black-body, it emits all absorbed energy outward. In addition, the intensity of electromagnetic emission can be quantified using the term brightness temperature, which is defined as the physical temperature of the black-body emitting the same amount of energy. In contrast to a black-body, a white-body is defined as a perfect reflector that reflects all incident energy and therefore emits none. Actually, most natural materials behave between a black-body and white-body (referred to as a gray-body), such that a part of the incident energy is reflected, and the remaining energy absorbed and emitted when thermodynamic equilibrium is reached. Using the emissivity (e) to describe the ability of materials to emit electromagnetic energy, the brightness temperature (TB) of the material is expressed as

$$TB_p = e_p \cdot T, \tag{2.29}$$

where T is the physical temperature of the material in Kelvin [K], and the subscript p indicates the polarisation, either horizontal or vertical. This equation is derived from Plank's black-body radiation law through the Rayleigh-Jeans approximation for microwave frequencies (Njoku and

Entekhabi, 1996, Ulaby et al., 1981). Therefore, the emissivity of a gray-body varies from 0 for a white-body to 1 for a black-body.

For soil, the emissivity varies from ~0.95 for dry soil (with moisture content of 0.05 m^3/m^3) to ~0.6 for wet soil (with moisture content of 0.4 m^3/m^3), depending on electromagnetic wavelength, incidence angle, surface roughness, and soil properties (Jackson and Le Vine, 1996, Njoku and Entekhabi, 1996). Assuming soil at a physical temperature of 300 K, this variation in emissivity corresponds to a brightness temperature variation of 90 K (Njoku and Entekhabi, 1996), which is much larger than the typical radiometric sensitivity of microwave radiometers (approximately 1 K).

Following Kirchoff's reciprocity theorem, the microwave emissivity (e) of the target can be related to its microwave reflectivity through

$$\Gamma_p = 1 - e_p . \tag{2.30}$$

The reflectivity is dependent mainly on the polarisation, electromagnetic wavelength, surface roughness, and dielectric constant of materials. For flat specular surfaces, the reflectivity (Γ_p^*) is determined by the Fresnel equation as

$$\Gamma_H^* = 1 - \left| \frac{\cos\theta - \sqrt{\varepsilon_r - \sin^2\theta}}{\cos\theta + \sqrt{\varepsilon_r - \sin^2\theta}} \right|^2 ; \tag{2.31}$$

$$\Gamma_V^* = 1 - \left| \frac{\varepsilon_r \cdot \cos\theta - \sqrt{\varepsilon_r - \sin^2\theta}}{\varepsilon_r \cdot \cos\theta + \sqrt{\varepsilon_r - \sin^2\theta}} \right|^2 , \tag{2.32}$$

where ε_r is the relative dielectric constant of the material, and θ is the incidence angle of microwave radiation. The subscripts H and V represent horizontal and vertical polarisations respectively.

Accordingly, the intensity of the emission at microwave frequencies that is measured by a radiometer, known as the brightness temperature, can be related to the soils dielectric constant through the reflectivity. For bare soil with a smooth surface, the soil emissivity at a given polarisation and incidence angle can be determined using Eqn. (2.30)-(2.32) for given volumetric soil moisture

content and soil texture properties. However, for more general land surface conditions, the effects of soil temperature profiles, roughness of the soil surface, and vegetation coverage over the soil layer significantly affect the relationship between brightness temperature observations and soil moisture (Choudhury et al., 1979, Jackson and Schmugge, 1991, Njoku and Entekhabi, 1996).

Dielectric permittivity of soil

Microwave emission from the soil surface is related to the soil dielectric constant, which is dependent mainly on soil water content. The dielectric constant is a complex number ($\varepsilon' - j \cdot \varepsilon''$), where $j = \sqrt{-1}$, and the real (ε') and imaginary (ε'') parts determine the propagation speed of the electromagnetic wave though the soil medium and the loss of electromagnetic energy respectively. Normally, it is expressed as a relative value which is the ratio of the dielectric constant of the material to that of free space (as described in Section 2.2.4). Due to the three phases of soil, air, water and soil particles, the soil dielectric constant is a combination of the individual constituents. The soil dielectric value is also affected by other factors including soil texture, temperature, salinity, and electromagnetic wavelength. To relate soil dielectric constant to volumetric soil moisture, many semi-empirical mixing models have been developed with electromagnetic wavelength, soil texture, bulk density, and salinity as inputs (Wang and Schmugge, 1980, Hallikainen et al., 1985, Dobson et al., 1985, Mironov et al., 2004). The Dobson et al. (1985) model was used in this study. While the dielectric constant of moist soil was found to be slightly dependent on temperature, under most natural temperature conditions the effect of temperature on soil dielectric constant can be ignored. However, when soil becomes frozen, its dielectric constant is reduced significantly, since the dielectric constant of water constituent changes from that of liquid water (approximately 80) to that of ice (approximately 3).

In natural land surfaces, soil moisture is not consistent in depth, and passive microwave observations are only affected by the water content in the top soil layer. The effective depth of soil moisture estimated from emitted radiation at

microwave frequencies, known as the penetration depth γ_D, is defined as the depth above which soil contributes 0.63 $(1-1/e)$ of the microwave emission (Ulaby et al., 1981), and can be expressed as a function of electromagnetic wavelength (λ) and complex dielectric constant of soil ($\varepsilon_s^{'} - j \cdot \varepsilon_s^{''}$)

$$\gamma_D = \frac{\lambda \sqrt{\varepsilon_s^{'}}}{2\pi \varepsilon_s^{''}}. \tag{2.33}$$

The penetration depth is very sensitive to the soil moisture conditions for the L-band microwave region with a wavelength of 21 cm, with γ_D varying from approximately 75 cm for dry soil with dielectric constant of $5 - j \cdot 0.1$ to approximately 3.7 cm for wet soil with dielectric constant of $30 - j \cdot 5$. Therefore, the penetration depth is a significant parameter to determine the thickness of the soil surface layer that the variations in moisture content and temperature make a major contribution to the microwave emission. For the purpose of practical application, the effective depth is assumed to be about the top 5 cm (Schmugge and Jackson, 1994, Chanzy et al., 1997).

Impact of vertical soil moisture and temperature profiles

The simple relationship of microwave emission in Eqn. (2.29) is based on an assumption that soil moisture and temperature are constant with depth. At low frequencies in the microwave region, the top several centimetres of soil makes a major impact on the microwave emission (Njoku and Entekhabi, 1996). In natural soil, the vertical distributions of soil moisture content and temperature are determined by many factors, such as solar radiation, precipitation, evapotranspiration, infiltration rate, and vegetation root distribution, which result in a high variability as a function of depth. Therefore the uniform soil moisture and temperature profile assumption is not satisfied to estimate soil brightness temperature and emissivity over most natural land surfaces.

To account for this variability, an effective soil temperature (T_{eff}), being an equivalent temperature in a uniform profile having the same microwave response to the non-uniform temperature profile, can be calculated through radiative transfer theory (Choudhury et al., 1982) as

$$T_{eff} = \int_0^{\infty} T_s(z) \cdot \alpha(z) \cdot \exp\left[-\int_0^{z} \alpha(z')dz' \right] dz , \quad (2.34)$$

where $T_s(z)$ is the soil temperature at depth z, and the attenuation coefficient α is dependent on the real and imaginary parts of complex soil dielectric constant as

$$\alpha(z) = (4\pi / \lambda) \cdot \varepsilon_s''(z) / 2 \cdot (\varepsilon_s'(z))^{1/2} , \quad (2.35)$$

where λ is the electromagnetic wavelength. Using this theoretical method, the effective soil temperature can be calculated from the measured soil temperature and moisture content profile which can be used to estimate the profile of soil dielectric constant using the mixing models. However, the required soil moisture and temperature profile data are only available in instrumented areas and are thus difficult to obtain globally. Therefore, Choudhury et al. (1982) and Wigneron et al. (2001) developed a simple linear parameterisations based on Eqn. (2.34) and experimental data collected at L-band, expressed as

$$T_{eff} = T_{deep} + C_t \cdot (T_{surf} - T_{deep}) , \quad (2.36)$$

where T_{deep} and T_{surf} are the deep soil temperature (approximately at 50 or 100 cm) and surface temperature (approximately corresponding to a depth interval of 0-5 cm). The parameter C_t is an empirical attenuation coefficient to determine the proportion of the contributions from deep and surface soil layers to the effective soil temperature. The surface temperature can be estimated from thermal infra-red observations, or near-surface air temperature derived from meteorological data, while the deep soil temperature can be modelled based on geographic location and season (Choudhury et al., 1982).

The constant values of the C_t parameter were calibrated at several frequency bands, with C_t found to be equal to 0.246 at L-band (Choudhury et al., 1982). In reality, the C_t, similar to penetration depth, is also influenced by soil moisture. For very dry soil, soil layers at depth (deeper than 1 m for dry sand) contribute significantly to the microwave emission from soil, and the C_t is

lower than 0.5. In contrast for very wet soil, the soil emission derives mainly from layers at the soil surface and $C_t \approx 1$.

To take the dependence of C_t on soil moisture into account, Wigneron et al. (2001) proposed a slightly improved formula based on Eqn. (2.36) in which C_t is a function of soil moisture

$$C_t = (SM_{surf} / w_0)^{b_{w0}}, \tag{2.37}$$

where SM_{surf} [m^3/m^3] is the volumetric water content in the top 0-3 cm soil. The w_0 [m^3/m^3] and b_{w0} are semi-empirical parameters depending on the soil properties. The long term suitability of Eqn. (2.37) was tested over several sites at the seasonal to inter-annual temporal scales (De Rosnay et al., 2006). The value of w_0 was found to be close to 0.3 m^3/m^3 over two bare soil sites: INRA Avignon (Wigneron et al., 2001) and SMOSREX (De Rosnay et al., 2006). The value of b_{w0} was close to 0.3 over a corn field at the INRA Avignon site and close to 0.65 over fallow at the SMOSREX site.

Impact of surface roughness

Generally, natural land surfaces are not flat and smooth as the assumption made in Eqn. (2.31) and (2.32). Newton and Rouse Jr (1980) and Wang (1983) found from field measurements that the rougher the soil surface, the higher the soil emissivity and the lower the sensitivity to soil moisture content (see Figure 2.6). It was also found that the effects of surface roughness decreases with the frequency.

In order to take the effect of surface roughness into account, the scattering of the radiation at the soil-air interface was introduced in Eqn. (2.31) and (2.32). A simple semi-empirical model of soil reflectivity for the rough surface was initially developed by Wang and Choudhury (1981) based on two best-fit parameters Q_R and H_R, expressed as

$$\Gamma_p(\theta) = [(1 - Q_R) \cdot \Gamma_p^*(\theta) + Q_R \cdot \Gamma_q^*] \cdot \exp(-H_R \cdot \cos^2(\theta)), \tag{2.38}$$

where the subscripts p and q indicate horizontal and vertical polarisations, or vice versa. The Q_R is a polarisation mixing parameter, and the H_R is a surface height parameter which can be related to the standard deviation of surface heights. Wang et al. (1983) considered in a more detailed study that the $\cos(\theta)$ dependence was much too strong. In addition, H_R increases with surface roughness effects resulting in an increase in soil emissivity at both H and V polarisations, which is in contradiction with theoretical analysis (Mo and Schmugge, 1987, Shi et al., 2002). Consequently, the H_R parameter should be considered as being dependent on incidence angle and polarisation, with a generalised semi-empirical equation of roughness effects proposed as (Wigneron et al., 2007)

$$\Gamma_p(\theta) = [(1 - Q_R(\theta)) \cdot \Gamma_p^*(\theta) + Q_R(\theta) \cdot \Gamma_q^*] \cdot \exp(-H_{Rp}(\theta) \cdot \cos^{N_{Rp}}(\theta)) \quad (2.39)$$

In this generalised formulation, the dependence of Q_R and H_R on reflectivity and polarisation is accounted for and the N_{Rp} exponent is inserted in the

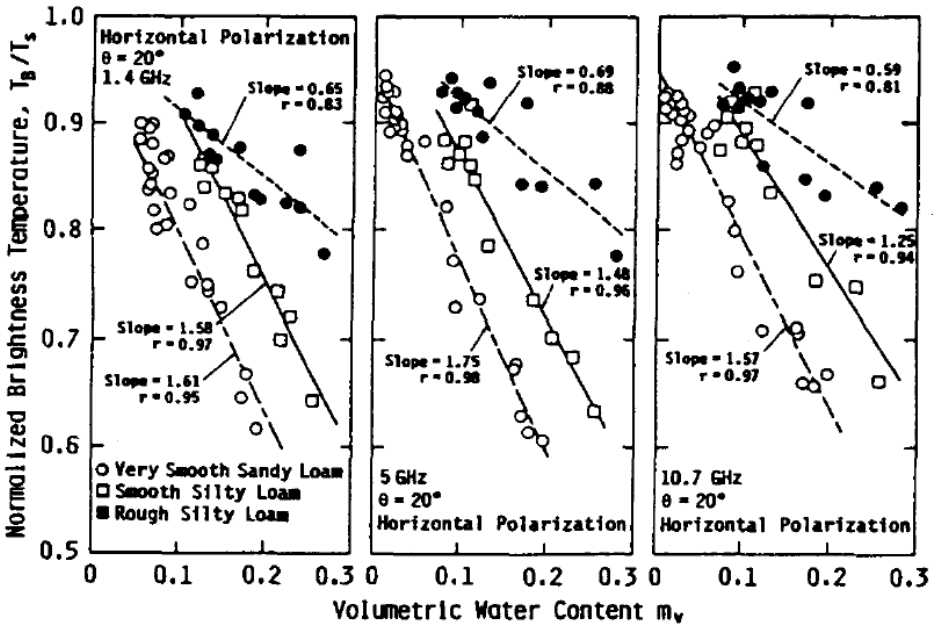

Figure 2.6: Variations in brightness temperature as a function of moisture content; for soils of different roughness at 1.4 GHz, 5 GHz, and 10.7 GHz (Wang et al., 1983).

exponential term.

The Q_R was found to be dependent on the electromagnetic frequency and has very small values at L-band (from 0 to 0.12 for three soil types) (Wang et al., 1983). This is in agreement with most published studies, and is based on a large experimental data set which considered that $Q_R = 0$ (Mo and Schmugge, 1987, Wegmuller and Matzler, 1999, Wigneron et al., 2001).

The dependence of the model roughness parameter $H_{Rp}(\theta)$ on the surface roughness characteristics, such as Standard Deviation (SD) and auto-Correlation Length (LC), is not well known. Two studies (Mo and Schmugge, 1987, Wigneron et al., 2001) found that the best geophysical parameters to model H_R were the slope parameter (m=SD/LC) and the surface soil moisture SM . The dependence of H_R on soil moisture content could be explained by a volume scattering effect that occurs as the soil dries out, with deeper layers of soil contributing to the emission. Wigneron et al. (2007) suggested that the spatial fluctuations of the dielectric constant within the soil volume may be strong during drying events, having an important "dielectric" roughness effect, and therefore H_R could be considered as an effective parameter that accounts for i) "geometric roughness" effects, corresponding to spatial variations of soil surface height, and ii) "dielectric roughness" effects, corresponding to the variation of the dielectric constant at the soil surface. The results obtained by Escorihuela et al. (2007) over the SMOSREX (De Rosnay et al., 2006) bare soil, confirmed the general soil moisture dependence of H_R and found that a linear dependence was preferable to the exponential as given by (Wigneron et al., 2001).

Wang et al. (1983) found that $N_R = 0$ was consistent with measurements at frequencies of 1.4, 5 and 10.7 GHz. This result was also found in studies at L-band (Mo and Schmugge, 1987, Wigneron et al., 2001). Based on long term measurements over a relatively smooth soil during SMOSREX experiment, Escorihuela et al. (2007) found that $N_R \approx 1$ at horizontal polarisation and $N_R \approx -1$ at vertical polarisation.

Impact of vegetation canopy

Over vegetated soil, the microwave emission from the soil is affected by the vegetation canopy layer which attenuates (absorbs and scatters) the soil emission and adds its own contribution to the overall microwave emission. As vegetation density increases, the contribution of the vegetation layer increases and that of the soil layer decreases. When the canopy becomes sufficiently dense, the radiation emitted from the soil layer is masked entirely and the observed microwave emission is from the vegetation alone. The magnitude of the attenuation effect of the canopy depends upon the wavelength and the vegetation water content.

To date, a number of models have been developed to estimate the microwave emission from the soil-vegetation layer (Kirdiashev et al., 1979, Mo et al., 1982, Jackson et al., 1982, Ulaby and Wilson, 1985, Wigneron et al., 1995, Meesters et al., 2005). In these models, the microwave emission from the vegetated soil surface is usually expressed as a zero-order solution of the radiative transfer equations, since it assumes that the scattering phase matrix term can be neglected (Ulaby et al., 1981, 1982, 1986, Mätzler et al., 2006). The $\tau-\omega$ model (Mo et al., 1982) is defined as

$$TB_p = (1-\Gamma_p)\cdot\gamma_p\cdot T_s + (1-\omega_p)\cdot(1-\gamma_p)\cdot T_v + (1-\omega_p)\cdot(1-\gamma_p)\cdot\gamma_p\cdot\Gamma_p\cdot T_v, \quad (2.40)$$

where T_v and T_s are the effective temperature [K] of the vegetation and soil layers. The ω_p and γ_p are the single scattering albedo and transmissivity of the vegetation layers respectively, and Γ_p is the reflectivity of a rough soil surface in p polarisation (either horizontal or vertical). The microwave emission from a vegetated soil surface is considered as the sum of three parts corresponding to the three terms in Eqn. (2.40. The first term represents the upward radiation from the soil layer and attenuated by the overlying vegetation. The second term indicates the upward radiation directly from the vegetation layer. The third term denotes the downward radiation from the vegetation layer, reflected by the soil surface, and attenuated by the vegetation layer again.

The single scattering albedo ω_p indicates the scattering of the microwave emission of soil and is a function of vegetation. At microwave frequencies, the value of ω_p is almost zero, varying between 0.05 and 0.10 (Jackson and Schmugge, 1991, Wigneron et al., 2004, Wigneron et al., 2007). The transmissivity of the vegetation γ_p can be further defined as a function of the vegetation optical depth at nadir (τ_{NAD}), and the incidence angle (θ)

$$\gamma_p = \exp[-\tau_{NAD} \cdot (tt_p \cdot \sin^2(\theta) + \cos^2(\theta)) \cdot \cos^{-1}(\theta)], \quad (2.41)$$

where tt_p is an empirical parameter in relation to vegetation structure and polarisation. The optical depth (τ_{NAD}) is dependent on the vegetation density and frequency, and can be linearly related to the Vegetation Water Content (VWC [kg/m^2]) at L-band using an empirical parameter (b) (Van de Griend and Wigneron, 2004)

$$\tau_{NAD} = b \cdot \mathrm{VWC}. \quad (2.42)$$

Alternatively, the vegetation optical depth could also be linearly related to the log of the Normalised Difference Vegetation Index (NDVI) (Burke et al., 2001) using two empirical factors (α and β)

$$\tau_{NAD} = \alpha_v + \beta_v \cdot (1 - \log(\mathrm{NDVI})). \quad (2.43)$$

There is some experimental evidence indicating possible polarisation and angle dependence of both τ and ω. However, this dependence was found mainly from experimental data collected over non-isotropic vegetation, such as vertical stalks in tall grasses, grains and maize (Kirdiashev et al., 1979, Wigneron et al., 1995, Hornbuckle et al., 2003). The canopy and stem structure of most vegetation covers are randomly oriented, and the effects of any systematic orientation of vegetation would be mostly minimized at satellite scales (Owe et al., 2001, Martinez-Vazquez et al., 2009).

For soil moisture retrieval from space-borne passive microwave observations from soil moisture space-borne mission, the temperature gradients within the soil and vegetation layers can be assumed consistent, since it reaches equilibrium at the 6 am/pm overpass times of satellite missions. Therefore,

Eqn. (2.40) can be simplified assuming equal soil and vegetation temperatures ($T_s = T_v$) (Hornbuckle and England, 2005), expressed as

$$TB_p = [(1-\omega_p)\cdot(1-\gamma_p)\cdot(1+\gamma_p\Gamma_p)+(1-\Gamma_p)\cdot\gamma_p]\cdot T_s . \qquad (2.44)$$

The sensitivity of microwave brightness temperature observation to water content of the soil layer decreases with the increase of the vegetation opacity depth (Jackson and Schmugge, 1991). The brightness temperature variation reduced by the attenuation effect of vegetation canopy is much larger than the noise sensitivity threshold of a microwave radiometer (typically < 1 K). Therefore, passive microwave technique can obtain a large signal-to-noise ratio for accurate soil moisture remote sensing.

2.5 Soil moisture remote sensing missions

Global soil moisture distribution can be derived from many satellites, such as the AMSR-E and ASCAT, but only the dedicated soil moisture missions are discussed here.

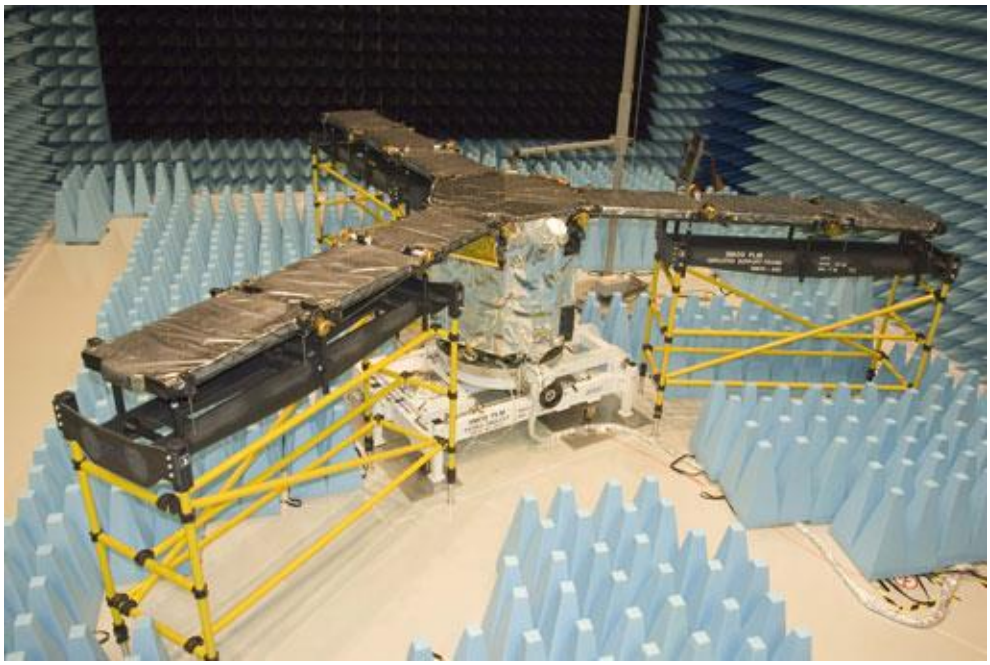

Figure 2.7: SMOS payload undergoing testing in the Maxwell Facility at ESA-ESTEC, The Netherlands (www.esa.int).

2.5.1 Soil Moisture and Ocean Salinity (SMOS) mission

The first space mission dedicated to soil moisture was launched on November 2nd 2009. The Soil Moisture and Ocean Salinity (SMOS) mission, led by the European Space Agency (ESA) in collaboration with the Centre National d'Etudes Spatiales (CNES) in France and the Centro para el Desarrollo Tecnologico Industrial (CDTI) in Spain, aims to measure near surface (top 5 cm) soil moisture and ocean salinity using a 2-D interferometric radiometer operating at L-band (1.413 GHz; Microwave Imaging Radiometer using Aperture Synthesis: MIRAS shown in Figure 2.7) (Kerr et al., 2010b).

SMOS is designed to provide global maps of soil moisture every 2 to 3 days (comparable with the temporal variability of the near surface soil moisture), with a spatial resolution of better than 50 km, and a target accuracy of 0.04 m^3/m^3 volumetric soil moisture (Kerr et al., 2010b). For ocean salinity, maps with an accuracy of better than 0.1 psu (practical salinity units; gram of salt in a litre of water) and 200 km ground resolution are acquired every 30 days. As secondary objectives, SMOS is expected to provide vegetation water content maps with an accuracy of 0.2 kg/m^2 every 6 days, and will contribute to studies of the cryosphere (Kerr et al., 2001). The SMOS mission requirements are summarized in Table 2.2.

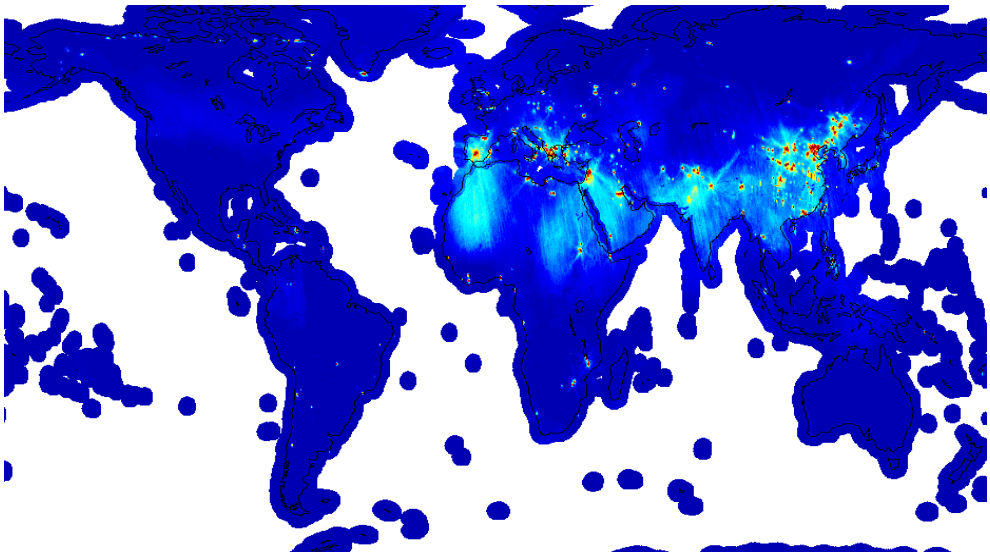

Figure 2.8: Global Radio Frequency Interference (RFI) map. Blue colour shows RFI-free areas, while red colour shows the area significantly affected by RFI (www.esa.int).

Besides its increased penetration depth and reduced sensitivity to vegetation canopy and surface roughness, L-band, compared with other higher frequency bands in the microwave region, is also a protected band for radio-astronomy and remote sensing satellite operations. However, the SMOS observations show a risk for corruption due to Radio Frequency Interference (RFI) in some parts of the world, particularly Europe and Asia (see Figure 2.8). Consequently, the development of an RFI detection and mitigation approach has become a high priority activity during the SMOS commissioning phase.

The only payload of SMOS is the Microwave Imaging Radiometer using Aperture Synthesis (MIRAS), a novel two-dimensional synthetic aperture radiometer with dual-/full-polarimetric imaging capabilities that makes possible brightness temperature observation at different incidence angles within the SMOS field-of-view.

To achieve global coverage and adequate spatial resolution for observing soil moisture at L-band, SMOS has used a synthetic aperture antenna employing an innovative interferometric radiometer concept and synthesizing from 69 separate receivers evenly distributed along three 3.5 m long arms of a Y-shaped antenna array and a central structure. Using the interferometric approach, the

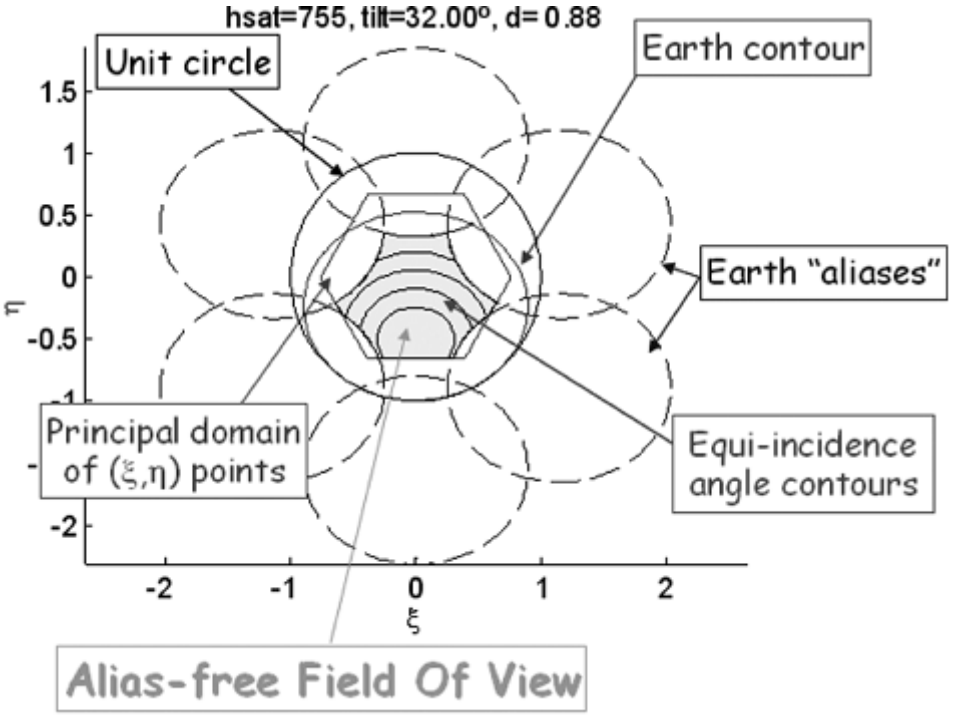

Figure 2.9: SMOS observation geometry (Camps et al., 2005).

Table 2.2: Main requirement for the SMOS Mission objectives of the SMOS (Kerr et al., 2010b).

Variable	Accuracy	Spatial resolution	Temporal sampling
Soil moisture	$0.04 m^3/m^3$	< 50 km	< 3 days
Vegetation water content	$0.2 kg/m^2$	< 50 km	< 5 days
Ocean salinity	0.1 – 0.2 psu	100 - 200 km	10 - 30 days

cross-correlation of the observations are measured from all possible combinations of receiver pairs in order to sample the signal that would be measured by a real aperture antenna.

The MIRAS makes a two-dimensional brightness temperature image every 1.2 seconds over a curved hexagon-shaped Field-Of-View (FOV) with approximately 1000 km swath width. The SMOS FOV in cross-/along-track coordinates (Earth reference frame) is shown in Figure 2.10. As the satellite moves along its orbit, most of pixels are observed in multiple satellite scenes at a range of viewing angles (from 0° to 65°; dashed contours centred at nadir in Figure 2.10). The grid chosen for the delivery of SMOS data is the Resolution 9 of Aperture 4 Hexagon in the Icosahedral Snyder Equal Area (ISEA), which provides a uniform inter-cell distance of approximately 15 km (Sahr et al., 2003).

The MIRAS works in two operation modes: the dual- and full-polarimetric modes (Martín-Neira et al., 2002). In the dual-polarisation mode the MIRAS measures the brightness temperatures in horizontal and vertical polarisations, while in full-polarimetric mode the MIRAS measures the four Stokes parameters. Both internal and external calibrations are performed by injecting stable noise signals into all the receivers several times per orbit and facing towards celestial targets every two weeks (McMullan et al., 2008).

Based on the level of processing on the SMOS observations, the SMOS mission products are categorized into five levels:

Level 0 products consist of unprocessed SMOS data with added Earth Explorer headers, which include satellite data and calibration data from correlators.

Level 1 products are divided into three categories:

i) Level 1a products are calibrated visibilities (cross-correlations) grouped as snap-shots.

ii) Level 1b products are snapshot maps of radiometrically corrected and calibrated brightness temperatures, referenced to the antenna polarisation reference frame.

iii) Level 1c products are swath-based maps of brightness temperatures referenced to a fixed grid on an Earth ellipsoid. Level 1c products are generated separately for land and sea applications.

Level 2 products are soil moisture and ocean salinity swath-based maps derived from the land and ocean parts of Level 1c products respectively. The conversion from Level 1c brightness temperatures to Level 2 products includes a first step to mitigate the impact of Faraday rotation, Sun/Moon/galactic glint, atmospheric attenuation, etc.

Level 3 products are based upon the spatial and temporal aggregation of Level 2 products.

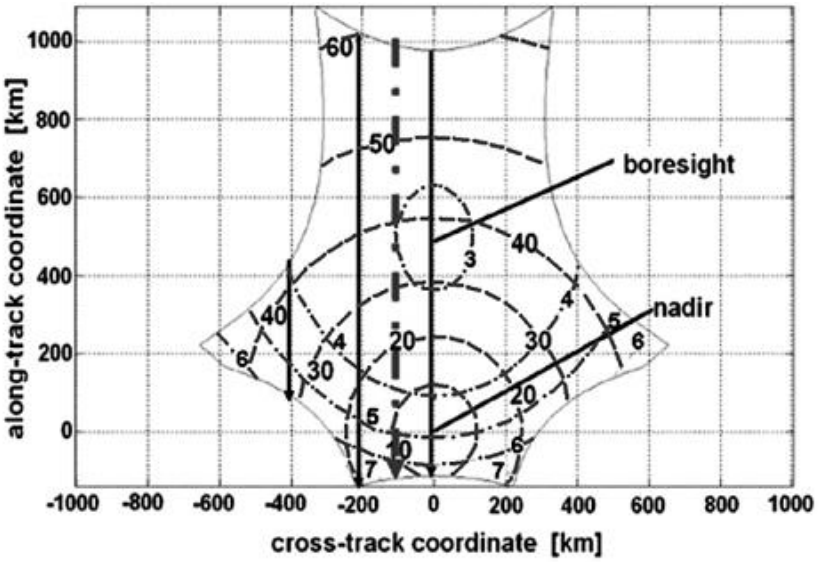

Figure 2.10: Properties of the alias-free FOV mapped from direction cosines coordinates to cross-track and along-track coordinates: incidence angle range from 0 to 60 (dashed contours centred at nadir) and radiometric sensitivity ranges from 3–7 K (dashed–dotted lines centred at boresight) (Camps et al., 2005).

Level 4 products are value-added Level 2/3 products using auxiliary data and/or models from other sources.

2.5.2 Soil Moisture Active and Passive (SMAP) mission

The Soil Moisture Active Passive (SMAP) mission, under development by the National Aeronautics and Space Administration (NASA), is proposed to provide global measurements of the Earth's surface soil moisture and freeze/thaw state (Entekhabi et al., 2010). A fundamental difference between SMOS and SMAP is that it aims to have a spatial resolution of better than 10km for soil moisture. Due to the accuracy and global coverage, the utility of SMAP measurements are being anticipated across many science and application disciplines including hydrology, climate, carbon cycle, as well as the meteorological, environmental and ecological applications communities. Therefore, the SMAP mission was recommended by the National Research Council's (NRC) Decadal Survey after a preliminary study commissioned by NASA, the National Oceanic and Atmospheric Administration (NOAA), and

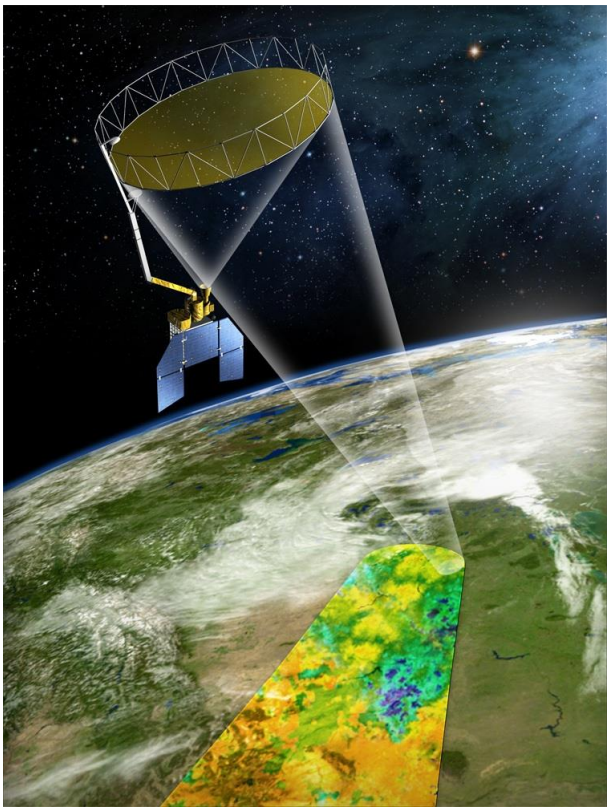

Figure 2.11: An artist rendition of SMAP flying and data swath on Earth (smap.jpl.nasa.gov).

the U.S. Geological Survey (USGS) (National Research Council, 2007). SMAP is scheduled for launch in October 2014.

The payload of SMAP consists of a conically scanning L-band radiometer and radar that share a deployable light-weight mesh antenna with a 6 m diameter. The first three Stokes parameters and backscatter at HH, VV and HV polarisations will be collected at a consistent viewing angle of approximately 40° using a radiometer and a radar system, over a footprint of approximately 40 km and 3 km size respectively. The designed incidence angle is optimal to retrieve soil moisture and vegetation water content simultaneously from the horizontally and vertically polarised brightness temperatures (Entekhabi et al., 2010). However, the space-borne radiometer systems can only provide a resolution in the order of 40 km which is much larger than the spatial resolution of 1 to 10 km required in hydrological modelling. In contrast, space-borne radar systems are able to offer a higher resolution, while they are significantly affected by vegetation coverage and surface roughness that can be used to achieve accurate soil moisture over smooth bare soil. It is expected that by combining SMAP radar and radiometer data, accurate soil moisture with a high spatial resolution can be obtained.

SMAP aims to provide global soil moisture observations with a 3 day revisit time and its main products will be provided in four levels:

Level 1 products are divided into three categories:

i) Level 1a products are raw data of radar backscatter and radiometer brightness temperature in time order.

ii) Level 1B products are calibrated and geolocated instrument measurements of surface radar backscatter cross section and brightness temperatures derived from antenna temperatures in time order.

iii) Level 1C products are calibrated and geolocated instrument measurements of surface radar backscatter cross section and brightness temperatures derived from antenna temperatures on swath/Earth grid.

Level 2 products are on half-orbit retrievals of soil moisture derived from radar, radiometer, and the conjunction of radar and radiometer data on a fixed Earth grid with resolutions of 3 km, 36 km, and 9 km respectively.

Level 3 products are daily global composite Level 3 products are daily composites of Level 2 surface soil moisture and freeze/thaw state data.

Level 4 products are model-derived value-added surface and root zone soil moisture data as well as carbon net ecosystem exchange data.

2.6 The land surface heterogeneity problem

The low spatial resolution of space-borne microwave radiometer sensors and the assumption of a homogeneous land surface are two limiting factors of current soil moisture retrieval algorithms, as space-borne observations suffer from land surface heterogeneity within the sensors' field of view (Njoku and Entekhabi, 1996). Kerr et al. (2003) classified the mixed-pixel problems into three types: 1) the pixel contains similar types of land surface, but with heterogeneous properties (i.e. soil moisture, soil texture, vegetation density, physical temperature, surface roughness); 2) the pixel contains different types of land surface (i.e. water bodies, forested areas, urban area), but with temporally consistent characteristics; and 3) the pixel contains different types of land surface with temporally variable characteristics (i.e. snow partially frozen overnight and partially melted in the daytime).

In the first case, the heterogeneity of land surface properties induces an error in soil moisture retrieval since it nonlinearly affects the relationship between the brightness temperature observation and the average soil moisture of the pixel. Thus, linearly averaged soil moisture cannot be retrieved by using the linear average of parameters of sub-pixel properties (Njoku and Entekhabi, 1996). The impacts of sub-pixel heterogeneity in soil moisture (Drusch et al., 1999), vegetation (Njoku et al., 1996), and soil properties (Galantowicz et al., 2000) on microwave soil moisture retrieval have been assessed. In the second case, the presence of different types of land surfaces complicates the overall microwave radiation from the pixel because of their different microwave

characteristics. Moreover, since most retrieval algorithms were developed with the assumption of a homogeneous land surface, except for the SMOS retrieval algorithm, which considers three different surface types (bare soil, herbaceous and woody vegetation covers), error in soil moisture retrieval above 0.04 m^3/m^3 can be introduced. The mixed pixels in the third case are heterogeneous in space and time, being the most complicated of all three cases. In order to deal with mixed-pixel problems, high spatial and temporal resolution observations are necessary (Kerr et al., 2003).

This thesis aims to the second type of land surface heterogeneity problems, focusing on the effect of surface rock, urban areas, and standing water on brightness temperature observations and soil moisture retrieval accuracy at the scale of ~40 km.

2.7 Proposed approach

The review of existing literature suggests that the land surface heterogeneity at the coarse scale of space-borne radiometers at L-band can adversely affect the soil moisture retrieval accuracy if not carefully accounted for in retrieval models. However, the effect of non-soil targets within a space-borne radiometers' field-of-view on brightness temperature and soil moisture retrieval accuracy has not been well studied using observational data, or taken into account in current soil moisture retrieval models or satellite products. Therefore, this study proposes to address the second type of mixed-pixels problems described in Section 2.6, to determine the non-soil target fractions that can be tolerated and the locations where induced soil moisture error might exceed the SMOS/SMAP 0.04 m^3/m^3 target error budget if their presence is ignored. Specifically, the effects of three types of land cover (surface rock, standing water, and urban areas) are analysed using airborne L-band passive microwave observations and *in-situ* sampling data collected during field experiments in Australia.

The airborne brightness temperature observations collected over surface rock, standing water, and urban areas are used to investigate the effect of urban area on brightness temperature and soil moisture retrieval accuracy. First, land

cover classification datasets were assessed for accuracy in estimating non-soil targets cover fraction of corresponding pixels. Applying a moving window technique, the airborne brightness temperature observations at < 1 km were integrated to lower spatial resolutions to yield a range of cover fractions of non-soil targets. Comparing the brightness temperature against the background brightness temperature non-soil targets induced impact is correlated with their cover fractions, and a cover fraction threshold determined. Finally, this threshold is applied to the global or regional land cover classification dataset to estimate the SMOS and SMAP pixels expected to be adversely affected by non-soil targets world-wide.

2.7.1 General assumptions

Over heterogeneous land surface, the ground brightness temperature in the sensor's field-of-view $TB_{grd,p}$ can be expressed as

$$TB_{grd,p} = \sum_{i=1}^{N} a_i \cdot TB_{i,p}\,, \tag{2.45}$$

where $TB_{i,p}$ is the p (horizontally or vertically) polarised brightness temperature of the i th surface component in N components within the pixel, and a_i is the spatial weight of the components thus $\sum_{i=1}^{N} a_i = 1$ (Njoku and Entekhabi, 1996). In ideal conditions where the antenna pattern is uniform in the main lobe while it is zero in side lobes, or when the antenna pattern effects have been corrected, the sensor's apparent brightness temperature observation $TB_{obs,p}$ is equal to ground brightness temperature $TB_{grd,p}$ (Ulaby et al., 1981), and the weight factor a_i becomes the cover fraction of each land surface component (Njoku and Entekhabi, 1996). Consequently, a general approach to deal with the mixed-pixel problem is to correct the brightness temperature of non-soil components (e.g. surface rock, standing water and urban area) from brightness temperature observations, assuming that the brightness temperature of a heterogeneous pixel $TB_{obs,p}$ is the sum of brightness temperature of all components $TB_{i,p}$ linearly weighted by their cover fractions f_i as

$$TB_{obs,p} = \sum_{i=1}^{N} f_i \cdot TB_{i,p} \ . \tag{2.46}$$

2.7.2 Data simulation

Both model and observation based simulation of brightness temperature data are used in this thesis, with a significant reliance on observational data, especially at the SMOS and SMAP footprint scale. Model simulation is primarily used at the small spatial scale so as to gain a better understanding of the physical process interactions at play. The model equations used in this step are outlined in Figure 2.12. However in practice the SMOS and SMAP antenna gain patterns are not corrected, and the contribution of side-lobe is not removed, which will induce a slight difference when applying the results of this thesis to space-borne sensors.

To investigate the effect of surface rock, urban areas, and standing water on space borne radiometer observations and subsequent soil moisture retrieval accuracy, brightness temperature data at the SMOS and SMAP scale of ~40

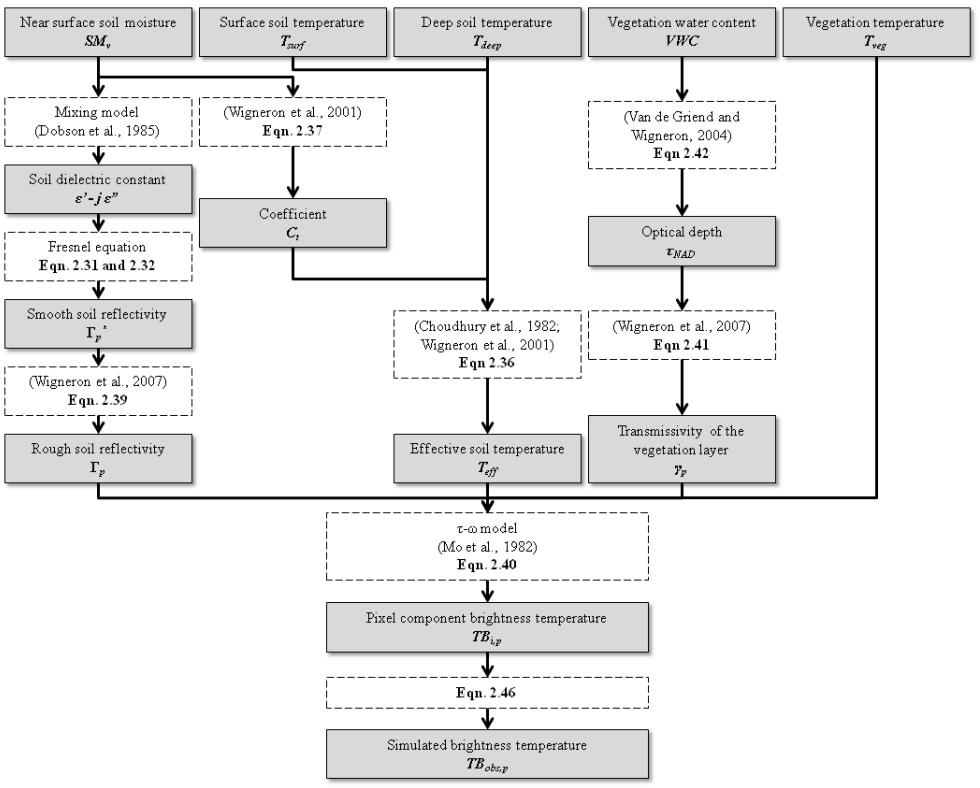

Figure 2.12 Schematic of brightness temperature simulation process.

km are required, so as to have a range of surface rock, urban areas, and standing water cover fractions. In this study, space borne brightness temperature is simulated by upscaling the airborne brightness temperature observations described in Chapter 3. However, the airborne brightness temperature observations collected at multiple incidence angles first need to be normalised to a fixed reference angle, due to the strong dependency of brightness temperature on incidence angle. To simulate SMOS and SMAP brightness temperature with a range of non-soil target cover fractions, a moving window technique is also applied to the geo-referenced map of incidence-angle-normalised airborne brightness temperature observations. As non-soil targets often take only a small fraction of the study areas at ~40 km scale, to simulate SMOS and SMAP brightness temperature with a high non-soil target cover fraction, a zooming window technique is used. The details of upscaling, incidence angle normalisation, and moving/zooming window processes are described below.

Microwave Observation Upscaling

According to Eqn. (2.46), brightness temperature at SMOS and SMAP scale can be simulated by integrating the airborne brightness temperature observations within a SMOS/SMAP footprint. However, in reality there may be a slight difference between the low resolution observation and the spatially averaged value of corresponding high resolution observations, due to uncertainties such as geolocation error, temporal variation of brightness

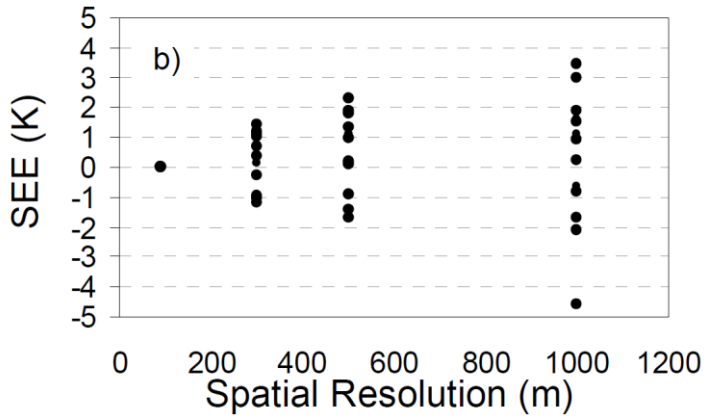

Figure 2.13 The effect of resolution on the Standard Error of Estimate (SEE) (Panciera et al., 2007).

temperature, or antenna gain pattern. Panciera et al. (2007) explored the effect of spatial scale on upscaling by comparing spatially averaged air-borne brightness temperature observations at high resolution (90m) with those at lower resolution (300m, 500m, and 1km). According to comparison results in Figure 2.13 over a grass and crop dominated area (Panciera et al., 2007), the maximum error in TB observations is ~4 K. This implies that airborne brightness temperature observations at 1 km can be upscaled to SMOS and SMAP scale of ~40 km with an uncertainty on the order of few K.

Microwave observations incidence angle normalisation

Many of the air-borne microwave radiometers used to measure the surface soil microwave emission yield a range of across-track viewing angles; e.g. PBMR (Wang et al., 1990), ESTAR (Le Vine et al., 1990), STARSS (Gabarró et al., 2003), PLMR (Panciera et al., 2008), CAROLS (Zribi et al., 2011). Due to the strong sensitivity of microwave signal to incidence angle, such observations need to be normalised to a fixed reference angle for the purpose of visualisation, interpretation, and/or simulation of satellite missions. In this thesis, the airborne multi-angular brightness temperature observations need to be normalised in order to simulate the SMOS/SMAP brightness temperature observations, before integrating to higher resolution observations.

Currently, there are two methods widely used for incidence angle normalisation, referred to here as the ratio-based (Jackson, 2001) and histogram-based (Mladenova et al., 2013) methods. Nevertheless, use of these methods over heterogeneous land surfaces often results in a noticeable stripe pattern when producing geo-referenced maps of angle-normalised microwave observations from multiple swaths. It is shown in this thesis that the striping results (in part) from an assumption of linearity in microwave response across incidence angles, which is particularly limiting over heterogeneous land surfaces. Consequently, a Cumulative Distribution Function (CDF) based method is developed in this thesis to normalise multi-angle microwave observations with only minimal stripping, by avoiding the linearity assumption. This approach is based on the CDF matching which has been routinely applied

to scaling of remotely sensed observations to modelled soil moisture data (Reichle and Koster, 2004), establishing relationships between radar reflectivity and rainfall (Anagnostou et al., 1999, Atlas et al., 1990), and blending of multiple microwave radiometer derived soil moisture products (Liu et al., 2009).

Each of these previous CDF studies has merged two or more data sets by matching their temporal CDFs over the same area based on an assumption of the same temporal variation. In contrast, the CDF-based incidence angle normalisation method developed here is based on matching the spatial CDF of observations measured at each incidence angle. It is assumed that the brightness temperature or backscatter sequence of all observed land surface types is consistent across all incidence angles. Consequently, for a given land surface the cumulative frequency is independent of incidence angle, and can be used to transfer observations at non-reference angles to the reference angle. This CDF-based method is developed and verified in Chapter 4 using microwave radiometer observations collected during three airborne field experiments.

Moving Window and zooming window techniques

According to Eqn. (2.46), airborne brightness temperature observations can be upscaled to the SMOS and SMAP scale by averaging airborne data within a 40-km window, which is the same to calculate cover fractions of non-soil targets. By moving the location of the window, the simulated brightness temperature with a range of cover fractions can be obtained. The range of obtained cover fractions is restricted by the distribution of the given non-soil target at the SMOS and SMAP scale. For targets that are very heterogeneously distributed across the study areas, such as urban areas, the obtained cover fraction varies from zero to a maximum value when the target is fully covered by the window. For the purpose of establishing the relationship between brightness temperature and non-soil target cover fraction over a wide range, the range of the obtained cover fraction is extended using a zooming window method, which increases the minimum value by reducing the size of the window.

Therefore, the moving and zooming window techniques are used in this thesis to simulate SMOS and SMAP brightness temperature observations with a wide range of non-soil targets.

2.7.3 Effect of rock cover fraction

A type of non-soil target that may induce a significant error in retrieved soil moisture if not explicitly accounted for in the retrieval algorithm is surface rock. While a few model simulation studies have been performed to explore the rock cover fraction threshold for the SMOS target soil moisture accuracy of 0.04 m^3/m^3 (Kerr et al., 2010a, Loew, 2008), there has been no assessment of the expected rock impact globally. Current rock fraction thresholds of 0.11 and 0.15-0.20 were obtained from Kerr et al. (2010a) and Loew (2008) respectively, assuming that rock behaves as very dry bare soil with a fixed dielectric constant and roughness, but these results have not been confirmed through field data.

According to the dielectric constant measurements on a range of rock types at a frequency of 400 MHz and 35 GHz, the real part of the dielectric constant of rock ranges from 2.4 to 9.6 (Ulaby et al., 1986). A value of 5.7 - j×0.074 has been suggested in the SMOS Algorithm Theoretical Basis Document (ATBD) as an appropriate value for the dielectric constant of rock (Kerr et al., 2010a). To date only a few experiments (e.g. Jackson et al., 1992, Monerris et al., 2008) have been conducted to explore the impact of surface rock on L-band brightness temperature observations. These have found that i) rock has a very low porosity meaning that it does not absorb any appreciable amount of water; ii) the low dielectric constant of rock reduces the effective dielectric constant of the wet soil surface mixed with rocks; and iii) the presence of rock results in an increase of soil surface roughness. While these studies demonstrate that the joint impact of these three aspects makes microwave emission from the rock covered land surface complex, the findings have not been extrapolated to tolerable land cover fractions or an appreciation of the possible impact globally.

The effect of rock on brightness temperature observation and soil moisture retrieval accuracy is further investigated in Chapter 5, using both synthetic and observational data from a field experiment. These results were then used to

demonstrate the expected impact of rock on brightness temperature observation and soil moisture retrieval accuracy globally, by identifying SMOS and SMAP pixels with rock-induced brightness temperature contribution in excess of the 4 K (the SMOS brightness temperature error budget), implying a possible soil moisture error in excess of the 0.04 m^3/m^3 target for SMOS and SMAP missions (Entekhabi et al., 2010, Kerr et al., 2010b).

2.7.4 Effect of urban cover fraction

At the coarse scale of the SMOS/SMAP missions, urban areas are present within many pixels globally, especially over heavily populated continents like Europe and the United States. While a current concern for urbanised areas is the Radio Frequency Interference (RFI) from man-made emitters, which adversely impacts the quality of passive microwave observations, there are other important factors. Moreover, since SMOS was launched, a great effort has been made to switch off the RFI sources that are present mostly over Europe, China, South Asia and the Middle East (Oliva et al., 2012). Thus, for urban areas where RFI does not exist, and/or after all RFI sources have been removed from the affected areas, the microwave emission contribution from urban areas will continue to exist. This brightness temperature contribution will potentially confound the interpretation of SMOS and SMAP radiometric observations, possibly resulting in soil moisture retrieval accuracy lower than the 0.04 m^3/m^3 target accuracy if not accounted for, since the microwave behaviour of urban areas is significantly different from that of natural targets (Rautiainen et al., 2008). Importantly, the microwave contribution of urban areas to space-borne radiometer observations has not been taken into account in the current soil moisture retrieval models, due to a lack of understanding of their microwave behaviour.

According to Schneider et al. (2010), less than 0.5% of the world's land mass is classified as urban. While this suggests that most of the SMOS and SMAP pixels will have either no or insignificant urban contribution to brightness temperature observations, urbanisation is not homogeneously spread across the globe. Consequently, urban areas are likely to have significant contributions

to brightness temperature observations in SMOS and SMAP pixels with urbanized area fractions that exceed some threshold, resulting in soil moisture retrieval errors exceeding the aforementioned target accuracy of ~0.04 m^3/m^3 for these missions. It is therefore important to know this urban fraction threshold, and thus identify the SMOS and SMAP pixels with a potentially large urban impact on soil moisture retrieval, in order for them to be flagged or a brightness temperature correction applied.

To date the knowledge about how urban area impacts soil moisture retrieval is relatively unknown, and most existing studies are based on simulation results from a limited number of synthetic studies (e.g. Kerr et al., 2010a, Loew, 2008); no studies have been undertaken using real microwave observations. In the SMOS ATBD (Algorithm Theoretical Based Document; Kerr et al., 2010a), the urban area is assumed to behave as very dry bare soil or rock whose dielectric constant is suggested to be 5.7 - j×0.074. Based on model simulations under a range of conditions, a rock cover fraction threshold of 0.11 was derived for the SMOS soil moisture target accuracy of 0.04 m^3/m^3, which was assumed to be applicable to urban areas. Similarly, Loew (2008) derived an urban fraction threshold of 0.15 ~ 0.20 from model simulations conducted over the Upper Danube catchment in southern Germany, assuming that urban behaves like very dry bare soil with a low and fixed dielectric constant and high surface roughness. Consequently, this work examines the previously reported urban fraction thresholds, using real data acquired from Australian field experiments. Subsequently these thresholds are used to identify the SMOS and SMAP pixels where the target soil moisture retrieval error will likely be exceeded as a result of urban induced error.

In Chapter 6, the SMOS and SMAP radiometric error budgets of 4 K (Kerr et al., 2010b) and 1.3 K (Entekhabi et al., 2010) were used as the brightness temperature error budgets to represent the target soil moisture retrieval accuracy of 0.04 m^3/m^3 of the respective mission, to determine the limit on urban induced brightness temperature contribution; the optimistic assumption being that the entire error budget could be attributed to urban effects alone. The urban fraction thresholds obtained using these experimental data were

then used to identify the SMOS and SMAP pixels globally where soil moisture retrieval error will potentially exceed the target accuracy as a result of urban areas, assuming that the Australian cities located in the study areas represent the microwave response to cities world-wide.

2.7.5 Effect of water cover fraction

The brightness temperature of soil is dependent mainly on the physical temperature of the soil layer and its emissivity, which is in turn determined by the soil dielectric constant and surface roughness. Due to the large (real part) dielectric constant difference between soil particles (~2) and water (~80), the microwave brightness temperature observation is highly sensitive to the water content of soil. Consequently, the presence of water bodies within the sensor's field-of-view will result in an overestimation in retrieved soil moisture if not accounted for. The effect of water fraction has been addressed in the SMOS Algorithm Theoretical Basis Document by stating that approximately 0.01 underestimation of standing water fraction in the field-of-view can induce 0.01 m^3/m^3 soil moisture retrieval error under the conditions of wet (water content of 0.4 m^3/m^3) soil and dense (optical depth of 0.6) vegetation (Kerr et al., 2010a). Model simulation (Davenport et al., 2008, Loew, 2008) and observational studies using space-borne data and *in-situ* measurements (Gouweleeuw et al., 2012) have been conducted to investigate the effect of water fraction on brightness temperature and soil moisture retrieval accuracy. The results show that the presence of a small area (<0.05) of standing water could introduce an error in retrieved soil moisture as high as 0.2 m^3/m^3. Nevertheless, this water fraction effect has not been verified using experimental data.

In Chapter 7 airborne L-band passive microwave observations and *in-situ* ground measurements collected over SMOS/SMAP pixel sized areas are used to i) investigate the relationship between water fraction and induced uncertainty in brightness temperature and retrieved soil moisture when ignoring the presence of water bodies in the soil moisture retrieval models, and

ii) determine the extent of SMOS/SMAP pixels in Australia that would be adversely affected as a consequence.

2.8 Chapter summary

The potential of remote sensing for monitoring global soil moisture has been discussed in Chapter 2. The different remote sensing techniques used to measure soil moisture by observing electromagnetic emission or reflection at different parts of the spectrum were presented, including visible, thermal infra-red, active and passive microwave. Their advantages and limitations were compared and their applicability for global soil moisture mapping with adequate accuracy, spatial resolution, and revisit frequency assessed. The L-band passive microwave remote sensing technique was shown to be the most promising method to measure global soil moisture due to its direct relationship to soil moisture through soil permittivity, all weather capability, and less sensitivity to vegetation canopy and surface roughness. However, this technique suffers from being a coarse scale measurement that can be severely affected by land surface heterogeneity.

In current soil moisture retrieval algorithms, the contribution of non-soil targets such as surface rock, urban area, and standing water, to the space-borne passive microwave observations, has not been adequately considered. These non-soil targets are present in many SMOS and SMAP pixels world-wide, and have special microwave behaviour when compared with soil targets. Therefore, their presence may result in an unacceptable error on space-borne passive microwave retrieval of soil moisture if not better understood. As such, this thesis address the question of how much of these target types can be tolerated within a passive microwave pixel, and what pixels are likely to be adversely affected.

3 Datasets

This chapter presents an overview of Australian airborne field experiments, including the airborne and ground instrumentation used. The observation datasets are later used to examine the effect of non-soil targets on passive microwave remote sensing for soil moisture in this research.

3.1 Field experiments used in this thesis

In the last eight years there have been several airborne field experiments conducted in Australia, with an objective of developing the remote sensing of near surface soil moisture, including the National Airborne Field Experiment in 2005 (NAFE'05; Panciera et al., 2008), National Airborne Field Experiment in 2006 (NAFE'06; Merlin et al., 2008), SMOS Arid Zone Experiment in Australia (SAZE; Rüdiger et al., 2013), Australian Airborne Cal/val Experiments for SMOS (AACES-1 to 2; Peischl et al., 2012b), and SMAP Experiments (SMAPEx-1 to 3; Panciera et al., 2012). The data collected from these experiments have been archived, and can be accessed from http://www.nafe.unimelb.edu.au, http://www.moisturemap.monash.edu.au,

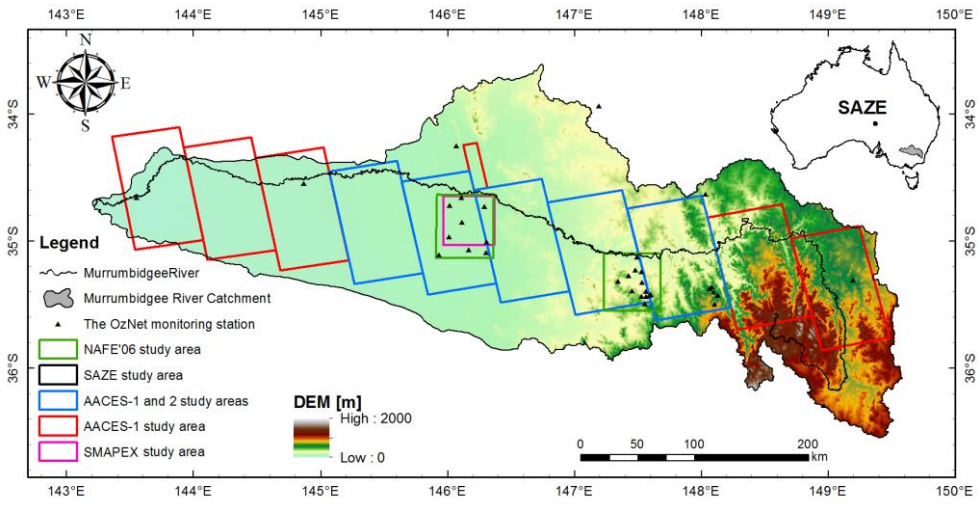

Figure 3.1: Locations of the OzNet monitoring stations, and study areas of NAFE'06, SAZE, AACES-1 and 2, and SMAPEx experiments.

Table 3.1: List of field experiments involved in this research.

Experiment	Date	Location	Land surface	Relevance to this thesis
NAFE'06 (Merlin et al., 2008)	Nov. 2006	Murrumbidgee River catchment	Cropping and grazing land	Urban and water effects
SAZE (Rüdiger et al., 2013)	Aug. 2009	Central Australia	Very dry bare soil	Rock effect and normalisation
AACES-1 (Peischl et al., 2012b)	Jan-Feb. 2010	Murrumbidgee River catchment	Various land surface	Urban effect water effects, and normalisation
AACES-2 (Peischl et al., 2012b)	Sep. 2010	Murrumbidgee River catchment	Various land surface	Urban and water effects
SMAPEx-2 (Panciera et al., 2012)	Dec. 2010	Murrumbidgee River catchment	Cropping and grazing land	Normalisation

and http://www.smapex.monash.edu.au.

In order to understand the land surface heterogeneity impacts within pixels at the scale of SMOS and SMAP radiometers, airborne brightness temperature observations and coincident ground measurements from five of these experiments are used in this thesis. Figure 3.1 provides an overview of their spatial locations/coverage, while Table 3.1 includes a summary of the land surface condition and relevance to this thesis.

Most of these experiments were conducted in the Murrumbidgee River Catchment, southeast of Australia. The ~82,000 km^2 Murrumbidgee River Catchment has an elevation ranging from ~40 m in the western plains to ~2,000 m in the eastern mountainous areas as shown in Figure 3.1. The annual rainfall varies from 300 mm in the west to 1900 mm in the high elevated ranges in the east (Australian Bureau of Rural Science, 2001). Accordingly, the land surface of the Murrumbidgee River Catchment varies from bare soil with sparse vegetation in the west, to irrigated fields mixed with grasslands in the middle, and to forest in the east. Only the SAZE (Rüdiger et al., 2013) field experiment was conducted outside of the Murrumbidgee Catchment, in August 2009 over three 50 km by 50 km study areas in central Australia, aiming to identify vicarious calibration sites for the on-orbit calibration of SMOS using

airborne passive microwave data and in-situ measurements. More detailed and pertinent description is given in the later chapters as required.

During the period of PhD study, the author was fully involved in experiment design, preparation and conduct of the SAZE and AACES. During the AACES-1 and 2, he was entirely responsible for ground sample processing and data management, while also giving necessary support to the preparation of aircraft, calibration of airborne and monitoring station sensors, and ground sampling. He also archived the AACES data including the development of a website www.moisturemap.monash.edu.au/aaces for data distribution.

3.2 Field experiment framework

These experiments have used a set of remote sensing instruments including a L-band radiometer, thermal imager, thermal radiometers and multispectral radiometers mounted on a scientific aircraft. Coincidence with aircraft flights, ground sampling on soil and vegetation properties were undertaken by participants in order to obtain the ground truth and ancillary data used in the

Figure 3.2: Experimental aircraft showing a wingtip installation in the left inset, and the cockpit with cockpit computer display in the right inset (Walker et al., 2009).

soil moisture retrieval algorithm. A brief description for each experiment component is presented below.

3.2.1 Airborne observing system

Airborne instruments were mounted on a small single engine aircraft, including the Polarimetric L-band Multi-beam Radiometer (PLMR), thermal infrared radiometers, and multi-spectral sensors. This facility allows passive microwave radiation, land surface skin temperature, and vegetation index observations to be made simultaneously across large areas.

The aircraft (Figure 3.2) can carry a typical science payload of up to 250 kg (120 kg for maximum range) with cruising speed of 150-270 km/h and range of 9 hours with reserve (5 hours with maximum payload). The aircraft ceiling is 3000 m or up to 6000 m with breathing oxygen equipment, under day/night VFR or IFR conditions. The aircraft can easily accommodate two crew; pilot/scientist plus scientist.

Aircraft instruments are typically installed in an underbelly pod and in the wingtips. Aircraft navigation for science is undertaken using a GPS driven 3-axis autopilot together with a cockpit computer display that shows aircraft position relative to planned flight lines using the OziExplorer software. The aircraft also has an OXTS (OXford Technical Solutions) Inertial plus GPS system (two antennas on the fuselage) for position (geo-referencing) and

Figure 3.3: The RT3003 OXTS Inertial + GPS system. Refer to www.oxts.com for more information.

attitude (pitch, roll and heading) interpretation of the data. When combined with measurements from a base station, the RT3003 (Figure 3.3) can give a positional accuracy of 2 cm, roll and pitch accuracy of 0.03° and heading accuracy of 0.1°. Without a base station the positional accuracy is degraded to about 1.5m (www.oxts.com).

3.2.1.1 Polarimetric L-band Multi-beam Radiometer (PLMR)

The Polarimetric L-band Multi-beam Radiometer (PLMR; Figure 3.4) was developed by ProSensing Inc. (prosensing.com) and owned by a consortium of Australian Universities. It has six receivers at viewing angles of ±7°, ±21.5° and ±38.5° from nadir in either across track (push-broom) or along track (multi-angle) configurations, used to measure both V and H polarisations with a polarisation switch. In the normal push-broom configuration the 3dB beamwidth is 17° along-track and 14° across-track resulting in an overall 90° across-track field of view. The PLMR measures microwave emission at a centre frequency of 1.413 GHz and bandwidth of 24MHz, with specified NEDT (Noise Equivalent Differential Temperature), a radiometric accuracy, better than 1K for an integration time of 0.5s, and 1K repeatability over 4 hours. It weighs 46 kg and is in size of 91.5 cm × 91.5 cm × 17.25 cm. Before and after each flight the PLMR was calibrated using the sky (cold target) and a temperature-recorded blackbody box (warm target). In addition, the calibration

Figure 3.4: View of PLMR with the cover off (Walker et al., 2009).

of the PLMR was confirmed during each flight using brightness temperature observations over a calibration lake having in-situ measurements of water temperature and salinity collected by a floating monitoring station. After pre- and post-flight calibration, the PLMR has an overall accuracy of better than 2 K (Panciera et al., 2008).

The angular difference of brightness temperature observations was corrected by normalising the observations to 38.5° using the Cumulative Distribution Function-based normalisation method proposed in Chapter 4. The method normalises multi-angle observations to a reference angle by matching the cumulative distribution function of each incidence angle to that of the reference angle. This approach assumes that the brightness temperature variations viewed by each incidence angle has the same statistical properties, and has been shown to result in normalisation errors for individual observations as low as 1K error when combined with 1.3K error in the root-mean-square sense may not impact the retrieval performance significantly. Consequently, the normalisation error for scene-averaged brightness temperatures is assumed to be negligible.

The temporal variation of brightness temperatures, due to changes in the physical surface temperatures during the flight, were corrected by multiplying each brightness temperature observation with the ratio between effective soil temperature at the current time and that at a fixed reference time (generally the mid duration of the flight). The effective soil temperature was calculated using the time series of top ~5 cm soil moisture and soil temperature at 2.5-cm and 40-cm depth, collected by monitoring stations within each patch using the method of Choudhury et al. (1982). In this thesis, time series of surface soil temperature observations collected from the OzNet monitoring station network was used for temporal correction of airborne brightness temperature observations. In the NAFE'06 dataset the brightness temperature observations were corrected to 12 noon (local time), while for the AACES-1 and -2 datasets the 6am and 6pm SMOS ascending and descending overpass times were used as the reference time, with data from temporal monitoring stations installed during the campaigns used for the temporal correction. Using this correction

technique, the bias of the brightness temperature observations between the repeated flights reduced to less than 1 K, which is insignificant in comparison with the brightness temperature effects expected from non-natural targets.

The PLMR brightness temperature observations used in this study hereafter are pre-processed including i) incidence angle normalisation; ii) temperature correction; and iii) gridding to regular grids.

3.2.1.2 Thermal infrared instruments

There are six thermal infrared radiometers (Figure 3.5, red box) used together with a thermal imager. The thermal infrared radiometers are the Everest Interscience 3800ZL (see www.everestinterscience.com) used to measure electromagnetic wave at a wavelength between 8.0 and 14.0 μm with 15° FOV and 0 - 5V output corresponding to -40°C to 100°C. These six radiometers are installed at the same incidence angles as PLMR so as to give coincident footprints with the PLMR observations. The nominal relationship between voltage and temperature is given by the manufacturer as V = 1.42857 + (0.03571428*T).

The thermal imager is a FLIR ThermaCam S60 with spectral range 7.5 to 13 μm, accuracy ±2°C or ±2% of reading and thermal sensitivity of 0.08°C. It has an 80° × 60° FOV lens with 1.3 mrad IFOV, resulting in approximately 20m resolution data from a 3000m flying height. The thermal imager looks very

Figure 3.5: Sensor box with 12 multi-spectral radiometers (two upper rows indicated by blue box) and 6 thermal infrared radiometers (bottom row indicated by red box) (Walker et al., 2009).

Table 3.2: Characteristics of multi-spectral radiometers.

Sensor VIS/NIR (SKR 1850A)

Channel	Wavelength	MODIS band
1	620 – 670nm	1
2	841 – 876nm	2
3	459 – 479nm	3
4	545 – 565nm	4

Sensor SWIR (SKR 1870A)

Channel	Wavelength	MODIS band
1	1628 – 1652 nm	6
2	2026 – 2036 nm	-
3	2105 – 2155 nm	7
4	2206 – 2216 nm	-

similar to a digital video camera, with a weight of 2 kg and size of 10 cm × 12 cm × 22 cm, without the 80° FOV lens fitted.

3.2.1.3 Multi-spectral instrument

The multispectral measurements are made using an array of 15° FOV Skye 4-channel sensors (Figure 3.5, blue box), each with 0-5V signal output (www.skyeinstruments.com). When installed, these sensors are configured in a similar way to the Everest thermal infrared radiometers, such that the six downward looking sensors have the same incidence angle and footprints as for the six PLMR beams. However, to correct for incident radiation, an upward looking sensor with cosine diffuser is also installed. Each sensor weighs approximately 400 g and has a size of 8.2 cm × 4.4 cm without the cosine diffuser or field of view collar attached. Two arrays of 4 channel sensors are installed, with the (matched) spectral bands as shown in Table 3.2.

3.2.1.4 Visible imager

A high resolution digital SLR camera, a digital video camera, and a Pika-II

Figure 3.6: Canon EOS-1DS Mark 3 (left), video camera (centre) and Pika II (right).

hyperspectral camera were available to the campaign (Figure 3.6). The digital camera is a Canon EOS-1Ds Mark III that provides 21 Megapixel full frame images. It has a 24 mm (23°) to 105 mm (84°) variable zoom lens. The digital video camera is a JVC GZ-HD5 with 1920 × 1080 (2.1 Megapixel) resolution. Also available is a HD-6600PRO58 wide angle conversion lens to provide full swath coverage of PLMR. The Pika-II is a compact low-cost hyperspectral imaging spectrometer manufactured by Resonon Inc (see www.resonon.com). It acquires data between 400 nm and 900nm at a spectral resolution of 2.1nm. Across track field of view is ~53° using the current Schneider Cinegon 1.8/4.8mm compact lens, with 640 cross-track pixels. It weighs approximately 1 kg and has a size of 10 cm × 16.5 cm × 7 cm. Because of the nil/low light conditions during the campaign flight times, only partial coverage of the study area would have been acquired in some of the campaigns. Consequently, only the digital camera was used and no visible data was acquired from these instruments during the AACES campaigns.

3.2.1.5 Other instruments

A RIEGL LMS-Q560 airborne laser scanner was also available during the campaigns, which incorporates full waveform digitising of the return laser pulses (see www.riegl.co.at), as well as an AisaDUAL 400 to 2500nm (Eagle/Hawke) hyper-spectral scanner (see www.specim.fi). However, because of the particular limitations in terms of maximum sensor flight altitude, sensor field of view, and lighting conditions, it was not practical to use these

Figure 3.7: RIEGL LMS-Q560 airborne laser scanner (left; www.riegl.co.at) and hyper-spectral scanner (right; www.specim.fi).

instruments together with the PLMR in some campaigns. Consequently, they were only used in a limited capacity during the SMAPEx-3 campaign. An L-band SAR was also used during the SMAPEx campaigns. The Polarimetric L-band Imaging Scatterometer (PLIS; as shown in Figure 3.8) is an L-band (1.245 to 1.275 GHz) radar which can measure the surface backscatters at HH, HV, VH, and VV polarisations. The PLIS is composed of two main 2 x 2 patch array antennas inclined at an angle of 30° from the horizontal to either side of the aircraft to obtain push broom imagery over a cross track swath of $\pm 45°$. Both antennas are able to transmit and receive at V and H polarisations. Additional secondary antennas can be deployed for interferometry (there was only one small flight in this configuration during SMAPEx-3). However, except for some limited testing of the angle normalisation algorithm in Chapter 4 using PLIS, these data are not used in this thesis.

3.2.2 Monitoring stations

The OzNet hydrological monitoring network (www.oznet.org.au; Smith et al., 2012) has been operational since 2001 and comprises a total of 62 stations throughout the entire Murrumbidgee River catchment. The network was upgraded in 2003 by adding additional monitoring sites, and in 2006 by including near-surface soil moisture sensors at all stations. In 2009, it was further augmented with two clusters of 12 supplementary stations within a 60

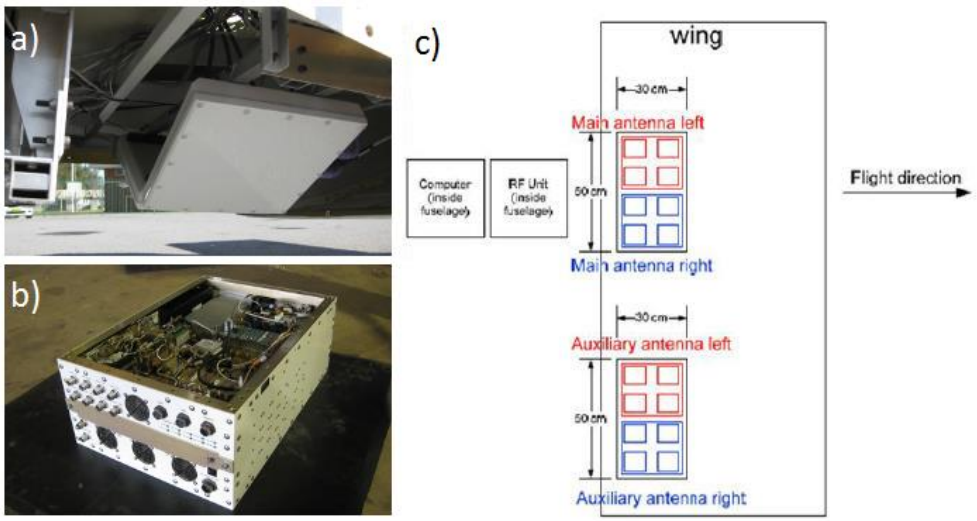

Figure 3.8: View of (a) PLIS antennas, (b) RF unit, and (c) aircraft configuration (www.smapex.monash.edu.au).

km × 60 km area focused on the Yanco region in the western flat plains of the catchment. The network provides area-wide surface soil moisture measurements at 0 - 5 cm (or 0 - 7 cm for the older sites), using CS616 (CS615) water reflectometers, with the majority of stations additionally collecting soil moisture profile data across three depths (0 - 30 cm, 30 - 60 cm, and 60 - 90 cm). Supplementary parameters including i) rainfall using a tipping bucket rain gauge, ii) soil temperature (2.5 cm and 15 cm) and iii) soil suction are also recorded (Figure 3.9). In the AACES, additional monitoring stations were temporally installed in the study areas to collect the temporal variation of rainfall, soil moisture at 0-5 cm (vertically installed) and 25 cm (horizontally installed), soil temperature at depth of 2.5 cm, 5 cm, 15 cm, and 40 cm, soil surface temperature using Thermal InfraRed sensor, and dew presence using Leaf Wetness sensor.

3.2.3 Ground sampling on soil and vegetation properties

The ground observations for the experiments were conducted sparsely across the SMOS and SMAP sized study area or intensively in a smaller focus area within the study area. The locations of the focus areas were selected based on i) the available background information including topography, land use, soil texture and ii) logistics, including the accessibility and travel time from the ground team base. The focus areas were chosen to be fairly homogeneous and represent the locally dominant soil and vegetation type, while capturing the

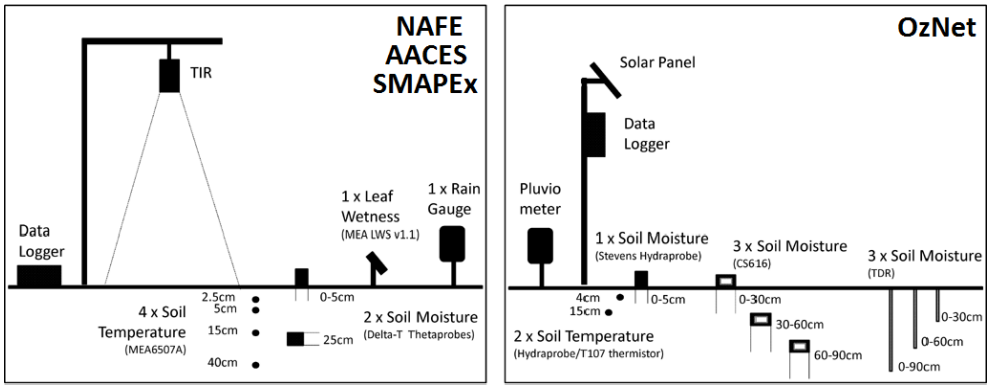

Figure 3.9: Schematic of the temporary monitoring station instrumentation during the NAFE, AACES, and SAMPEx field campaigns (left panel) and the permanent instrumentation at the new OzNet monitoring sites in the Murrumbidgee River catchment (right panel).

naturally existing variability within each study.

The focus areas were mapped with near-surface soil moisture measurements along pre-defined parallel sampling lines. Along each of these transects a minimum of three soil moisture measurements (within a radius of 1 m) of the top 5 cm were made every 50m using the Hydraprobe Data Acquisition System (HDAS; Panciera et al., 2006). By taking replicate measurements at each sampling point the effect of random errors at local scale was sought to be minimized. The HDAS system comprises a Global Positioning System (GPS), a Hydraprobe soil moisture sensor and a Geographic Information System (GIS) that combines the information about location and soil moisture in a visual output (Merlin et al., 2007). The accuracy of the Stevens Water Hydraprobe sensor implemented in the HDAS system has been determined to be ±0.039 m^3/m^3 on the basis of 155 gravimetric soil samples collected across the Murrumbidgee River catchment during NAFE'06, AACES and SMAPEx. The estimated error is consistent with results from an earlier study (Merlin et al., 2008) that used a combined calibration approach with laboratory and field measurements. The gravimetric soil samples from the campaigns have been further analysed for soil texture particle distribution to determine silt, sand and clay content. Ancillary data including vegetation type and height, a visual estimate of rock cover fraction, dew presence and dew characteristics were also recorded for each HDAS sampling location and stored within the system. In the case of visible dew, leaf wetness samples were taken using pre-weighed paper towels to determine the actual amount of dew on the plant leaves (Kabela et al., 2009).

On each focus area, specific vegetation data including biomass and spectral surface samples were collected at multiple locations. In general, all canopy measurements were undertaken within a 1 km^2 area, which corresponded to one PLMR pixel, and for all the major vegetation types present on each focus area. Vegetation Water Content (VWC) information is crucial in the soil moisture retrieval process, and together with the spectral properties of the canopy has been shown to provide relationships for estimating the VWC and other vegetation variables. The actual vegetation data recorded at each focus

farm included i) leaf area index (LAI) using a LI-COR LAI-2000, ii) hyper-spectral properties of the vegetation using a Fieldspec 3 instrument developed by ASD Inc., and iii) destructive biomass samples from a 50 cm × 50 cm area previously observed with the LI-COR and ASD instruments.

To assist with the data analysis, supplementary information including vegetation type and height, row spacing and direction, and photographs of the sky/cloud conditions as well as of the actual sample were taken for each sampling point. To ensure optimal spectral sampling conditions, the ASD vegetation measurements were made between 10:00 a.m. - 02:00 p.m. LST. The LAI data were collected earlier at about 07:00 - 09:30 a.m. to reduce the effect of direct sunlight on the sensor. In addition to the vegetation sampling, the ground teams further recorded at least three surface roughness profiles of 2 m length in North-South and East-West direction across each focus area.

3.3 Summary of chapter

In the last eight years several airborne field experiments were conducted in Australia for the purpose of i) providing ground truth for SMOS brightness temperature calibration and validation; ii) evaluating soil moisture retrieval algorithms at multi-scale, multi-angle, and under heterogeneous land surface conditions; iii) improve the accuracy of estimation on soil temperature, vegetation index, and soil properties using remote sensing data; and iv) testing downscaling approaches and data assimilation techniques. Therefore, different types of remotely sensed data together with point-based ground measurements were collected across a wide range of land surface and weather conditions. The data acquired from these field experiments were used as the basis of this research.

4 Incidence angle normalisation

4.1 Chapter introduction

Due to the strong dependency of brightness temperature on incidence angle, multi-angular airborne brightness temperature observations need to be normalised to a fixed reference angle, for the purpose of visualisation, interpretation, and/or simulation of satellite missions. There are two linear methods currently used for incidence angle normalisation. However, the georeferenced map of normalised data using these methods suffers from a stripe problem, which in turn adversely affects the simulated brightness temperature data. Consequently, this chapter presents a new incidence angle normalisation method which is verified using airborne microwave radiometer and radar observations collected during two Australian field experiments. This Cumulative Distribution Function (CDF) based method normalises the multi-angle observations to a reference angle by matching the CDF of observations for each non-reference angle. The performance of this new method is compared with the two existing normalisation methods using both synthetic and observed microwave radiometer and observed radar data.

4.2 Datasets and study areas

Airborne microwave radiometer and radar observations collected during three Australian field experiments are used to develop and verify the CDF-based method of this chapter. Results are also compared with the two existing normalisation methods, both in terms of visual occurrence of stripping and normalisation accuracy when compared to independent data. These experimental data are from the AACES-1 (the first Australian Airborne Cal/val Experiments for SMOS (Peischl et al., 2012a) in summer 2010), the SAZE (the SMOS Arid Zone Experiments in Australia (Rüdiger et al., 2013) in summer 2008), and the SMAPEx-3 (the third SMAP Experiment (Panciera et al., 2012) in spring 2011). The study locations and flight lines are shown in Figure 4.1.

The L-band microwave radiometer observations were measured across 19 flight days using the Polarimetric L-band (1.413 GHz) Multi-beam Radiometer (PLMR) mounted in push-broom configuration on a scientific aircraft. Both horizontally (H) and vertically (V) polarised brightness temperatures were measured through six across-track beams of the PLMR with viewing angles of ±7°, 21.5°, and 38.5° from nadir, each having a beam width of 17° along-track and 14° across-track. To simulate the brightness temperature observation of SMOS and SMAP, the multi-angular brightness temperature observations need to be normalised to a fixed angle and integrated over the SMOS/ SMAP pixel sized areas. While the three normalisation methods were applied to all sampled patches, only the brightness temperature observations for Patch 09 on 18th February 2010 are shown in this chapter. Results are verified using an independent crossing flight line (see Figure 4.1) from the aircraft transit route back to the airport at the end of the flight.

The SMOS Arid Zone Experiments were conducted over central Australia in November 2008 (SAZE; Rüdiger et al., 2013). The main objective was to provide airborne microwave brightness temperature observations at L-band

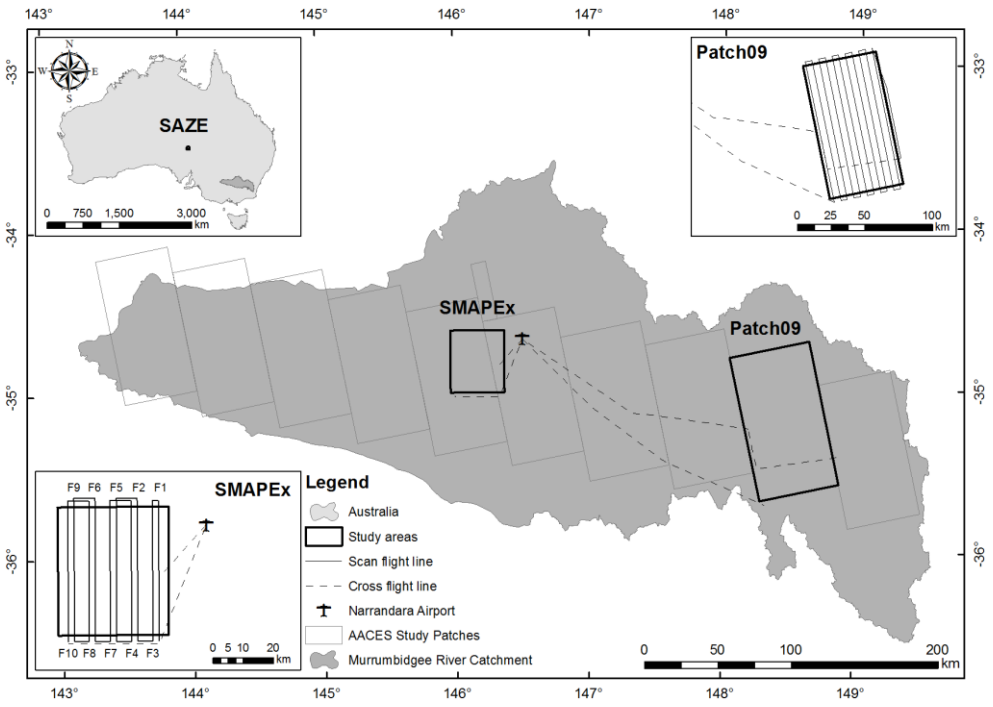

Figure 4.1: Location of study areas, flight lines and transit flights used in this study. Transit flights that cross the study area are used for independent verification.

over SMOS-sized areas which could be used for SMOS on-orbit vicarious calibration (Rüdiger et al., 2013). Totally three 50 km × 50 km areas were sampled using the PLMR with the same configuration as in the AACES. One of the sampled areas, Lake Eyre, was included as a test area in this chapter as shown in Figure 4.1, since the land surface was characterised by extreme variations in brightness temperature, ranging from ~50 to ~300 K. This provided an opportunity for an extreme test of the proposed CDF-based normalisation method.

The CDF-based method was also applied to normalisation of radar observations collected during the SMAPEx-3. The SMAPEx experiments were conducted over a 36 km × 38 km agricultural area in the Murrumbidgee River catchment (Figure 4.1) which is a test-bed of the SMAP (Soil Moisture Active and Passive) mission (Entekhabi et al., 2010), to develop and validate soil moisture retrieval algorithms using a combined L-band radiometer and radar system. The L-band microwave backscatter observations were collected using the Polarimetric L-band (1.26 GHz) Imaging Synthetic aperture radar (PLIS) whose antennas were mounted on the scientific aircraft with a 30° angle from the horizontal, yielding viewing angles ranging from 15° to 45° on both sides of the flight lines. More than 300 across-track backscatter observations in HH, VV, HV, and VH polarisations were measured within ~2 km wide swaths on each side of flight lines, resulting in a spatial resolution of ~7 m. Consequently, backscatter data were obtained over the entire SMAPEx-3 study area from ten consecutive north-south flight lines (F1 to F10) resulting in a total of 20 swaths. Each swath was partially overlapped with adjacent swaths in order to provide a full coverage over the study area. In this chapter, the HH polarised backscatter data collected on 15th September 2011 was used as an example to verify the performance of the CDF-based normalisation method on radar data.

4.3 Approach

The normalisation function typically is an approximation of the corresponding relationship between the observations at an incidence angle and what would be observed at a given reference angle over the same pixels. Two normalisation

methods exist in the literature: the ratio-based (Jackson, 2001) and histogram-based (Mladenova et al., 2013) methods. The ratio-based method was initially used to normalise multi-beam brightness temperature (TB) at observed incidence angle (θ_{obs}) to the reference angle (θ_{ref}), expressed as

$$TB_{norm} = TB_{obs} \cdot \frac{\overline{TB_{ref}}}{\overline{TB_{obs}}}, \tag{4.1}$$

where TB_{obs} and TB_{norm} are the observed brightness temperature observation and its normalised value, while $\overline{TB_{obs}}$ and $\overline{TB_{ref}}$ indicate the mean brightness temperatures of all observations at θ_{obs} and θ_{ref} respectively. The histogram-based normalisation method was developed for the incidence angle normalisation of radar backscatter observations with additional accounting for the standard deviations of backscatter observations. The normalised backscatter σ_{norm} in the histogram-based method is determined by

$$\sigma_{norm} = \overline{\sigma}_{ref} + \hat{\sigma}_{ref} \cdot \frac{\sigma_{obs} - \overline{\sigma_{obs}}}{\hat{\sigma}_i}, \tag{4.2}$$

where σ_{obs} is the backscatter observed at θ_{obs}. $\overline{\sigma}_{org}$ and $\hat{\sigma}_{org}$ indicate the mean and standard deviation of all backscatter observations at θ_{obs} respectively. Similarly, $\overline{\sigma}_{ref}$ and $\hat{\sigma}_{ref}$ indicate the mean and standard deviation of all backscatter observations at θ_{ref}.

Both normalisation methods transfer the original observations to their normalised values through statistic indexes that can be used to scale observations at the observed incidence angle to the equivalent observation expected at the reference incidence angle. Using I and S to represent transfer index and microwave observations (radiometer brightness temperature or radar backscatter) respectively, Eqns. (4.1) and (4.2) can be expressed as

$$\frac{S_{norm}}{\overline{S_{ref}}} = I_{rat,i} = \frac{S_{obs}}{\overline{S_{obs}}}, \tag{4.3}$$

and $$\frac{S_{norm} - \overline{S}_{ref}}{\hat{S}_{ref}} = I_{his,i} = \frac{S_{obs} - \overline{S_{obs}}}{\hat{S}_{obs}}, \qquad (4.4)$$

respectively. The subscripts ***rat*** and ***his*** of I indicate the transfer indexes of the ratio-based and histogram-based normalisation methods. Consequently, the ratio-based method uses the ratio to the mean of all observations at the same incidence angle as the transfer index (I_{rat}), while the histogram-based method uses the difference to the mean observation normalised by the standard deviation of all observations at the same incidence angle (I_{his}).

Both normalisation methods were developed based on an assumption of similar land surface conditions over the fields viewed at different angles, thus the normalised observations at the observed incidence angle are similar to observations at the reference angle. Consequently, the corresponding relationship of original observations between observed incidence angle and the reference angle can be used for incidence angle normalisation. Moreover, both normalisation functions are linear. While this linear assumption may be satisfied over homogeneous land surfaces, since the angular relationship of land surface components over homogeneous land surfaces are the same or parallel to each other that the original observations between incidence angles are linearly corresponded through a similar incidence angle relationship. However, it may not be reasonable over highly heterogeneous land surfaces. Consequently, in the absence of land surface classification information, a noticeable stripe pattern has been observed when using linear normalisation methods over inhomogeneous land surfaces, as shown in Figure 4.4.

This study hypothesises that the normalisation function is nonlinear over a heterogeneous terrain, and the linear normalisation methods are responsible for the stripe pattern in maps of normalised observations (see Figure 4.4 and Figure 4.5). Accordingly, a non-linear normalisation method based on the Cumulative Distribution Function (CDF) was developed. In the CDF-based method, the cumulative probability of a given observation in all observations at the same incidence angle is taken as the transfer index (I_{CDF}) such that

$$f(\theta_{ref}, S_{norm}) = I_{CDF,i} = f(\theta_{obs}, S_{obs}), \quad (4.5)$$

where f indicates the cumulative distribution function of incidence angle and observation value, which can be calculated by sorting the observations for each incidence angle step. As the same as the ratio-based and histogram-based methods, the CDF-based normalisation method also assumes that the similar land surface conditions were observed at different incidence angles.

For instruments with a small number of beams and a big beamwidth, such as the PLMR having three beams with beamwidth of ~15° on each side of the aircraft, the observations of the entire study area are collected at three discrete viewing angles. Over a study area, a big part (about one third) of the area can be observed at each viewing angle, and all land cover types are typically collected from all viewing angles. Consequently, the land surface conditions of the study area viewed at each viewing angle can be assumed representative to the entire study area and also similar between each other. In this case, the similar land surface assumption of the CDF-based normalisation method can be satisfied, and Eqn. (4.5) can be applied to normalise the observations with a reasonable reliability. However, for instruments with a large number of beams of narrow beamwidth, such as the PLIS having over 300 azimuthal bins within the incidence angles range of 15° to 45°, the land surfaces viewed by these very fine beams are generally inhomogeneous between incidence angles, and not all types of land cover responses are captured by each beam. Thus, the land surface heterogeneity of field view between different angles should also be considered during the normalisation. If Eqn. (4.5) was directly applied in this case, the distribution of original observations at all incidence angles over-fits to that at the reference angle. The natural land surface feature is removed and a significant difference can be found over the overlapped area of adjacent normalised images. Therefore, Eqn. (4.5) was updated for sensors with a large beam number, with accounting for retaining the effect of land surface heterogeneity. To do that, a general cumulative probability function for observations and incidence angles is estimated to pre-normalise the main part of angular effect, and then correct the remaining angular effects of all swaths

individually and simultaneously by matching the pre-normalised observations in overlapped parts of adjacent swaths.

For each swath of sensors with a large beam number, a cumulative distribution function $f_i(\theta_{obs}, S_{obs,i})$ can be obtained to describe the cumulative probability of an original observation $S_{obs,i}$ at the incidence angle of θ_{obs}, where the subscript i indicates the swath number. The observations between bins are different from the incidence angle variation and land surface heterogeneity, where the former effect is assumed consistent across swaths and the latter is assumed independently random. By averaging the f_i across swaths, the effect of land surface heterogeneity on the corresponding relationship can be counteracted and eliminated, thus only the angular effect was retained in the mean cumulative distribution function $\overline{f}$ of all swaths. It is known that the angular relationship of microwave observations is a continual and smooth curve. Therefore, the $\overline{f}$ was smoothed in the dimension of incidence angle, and the smoothed function $\overline{f}_{smooth}$ was taken as a pre-normalisation equation, given as

$$\overline{f}_{smooth}(\theta_{ref}, S_{pre-norm}) = \overline{f}_{smooth}(\theta_{obs,}, S_{obs,i}), \tag{4.6}$$

where $S_{pre-norm}$ is the pre-normalised observation of $S_{obs,i}$. However, there is still a slight difference between $\overline{f}_{smooth}$ and the cumulative probability function of the truth normalised observations for a specific swath, which could result in a considerable bias between the pre-normalised observations of two adjacent swathes within their overlapped area. To account for this difference, a polynomial function Δf_i was used based on $\overline{f}_{smooth}$, and shown as

$$\Delta f_i(\theta_{obs,}, S_{obs,i}) = \sum_{a=0}^{m}\sum_{b=0}^{n} A_{a,b} \cdot {S_{obs,i}}^{a} \cdot {\theta_{obs}}^{b}, \tag{4.7}$$

where $A_{a,b}$ is a $m \times n$ coefficient matrix of observation $S_{obs,i}$ and incidence angle θ_{obs} for each individual swath. The values of m and n determine the

freedom of Δf in dimensions of observation and incidence angle. The higher value is used, the better fitting of remaining angular effect can be obtained, and meanwhile the larger normalisation error might be introduced. A default value of 4 is suggested for m and n. The coefficient matrices $A_{a,b}$ of all swaths can be obtained simultaneously using an iterative optimization approach by fitting Δf functions of adjacent swaths to their pre-normalised observations difference over their overlapping areas. Consequently, a upgrade of Eqn. (4.5) is given using $\overline{f}_{smooth}$ and Δf_i with the optimized $A_{a,b}$, shown as

$$\overline{f}_{smooth}(\theta_{ref}, S_{norm}) + \Delta f_i(\theta_{ref,}, S_{norm}) = I_{CDF}$$
$$= \overline{f}_{smooth}(\theta_{obs}, S_{obs,i}) + \Delta f_i(\theta_{obs,}, S_{obs,i}) \quad (4.8)$$

4.4 Verification using synthetic data

This section explores the normalisation function linearity and the theoretical accuracy of all three normalisation methods using synthetic microwave radiometer observations over a land surface. To satisfy the similar land surface assumption of the two linear methods, a 500 × 500 grid was generated to simulate brightness temperature observations over a native grass surface. The soil moisture, vegetation water content, and surface roughness of each pixel were randomly assumed within the pre-defined ranges listed in Table 4.1. It was assumed that odd and even columns of the grid were observed at incidence angles corresponding to the PLMR's outer beams (38.5°) and middle beams (21.5°) respectively, with the intention to normalise the brightness temperature at the non-reference angle of 21.5° (θ_{obs}) to the reference angle of 38.5° (θ_{ref}), using each of the three normalisation methods. The L-MEB (Wigneron et al., 2007, Wigneron et al., 2001) model was used to simulate dual-polarised brightness temperatures of each pixel at the pre-determined incidence angle (S_{ref} for odd columns and S_{obs} for even columns). The parameters required by the model were assigned to values for typical native grass as listed in Table 4.1. For the purpose of this demonstration, the brightness temperature of even columns (observed at θ_{obs}) were also simulated at the

Table 4.1: Land surface parameters used in the L-MEB (after Panciera et al. (2008)) for deriving the synthetic verification data set.

Soil moisture [m^3/m^3]	0 – 0.6	Vegetation structure tt_h [-]	1
Vegetation water content [Kg/m^2]	0 – 2	Vegetation structure tt_v [-]	1
Roughness H_R [-]	0 – 0.6	Vegetation parameter b [-]	0.15
Sand content [%]	67	Scattering albedo ω_h [-]	0
Clay content [%]	15	Scattering albedo ω_v [-]	0.05
Bulk density [g/cm^3]	1.1	Surface soil temperature [K]	300
Roughness N_{Rh} [-]	0	Deep soil temperature [K]	292
Roughness N_{Rv} [-]	0	Vegetation temperature [K]	300

reference angle (θ_{ref}), and subsequently used as the truth, defined as T_i for verifying the normalised observations.

The L-MEB model is the basis for the SMOS Level 2 retrieval algorithm, which retrieves soil moisture and vegetation water content simultaneously from dual-polarised brightness temperature observations by minimizing the differences between observed and simulated brightness temperature using the 'τ-ω model' (Mo et al., 1982). According to the 'τ-ω model', the microwave emission from a vegetated soil surface is defined as the sum of i) the upward radiation from the vegetation layer, ii) the downward radiation from the vegetation layer reflected by the soil surface and attenuated by the vegetation layer, and iii) the upward radiation from the soil layer attenuated by the vegetation layer. Thus

$$TB_p = (1-\omega_p)\cdot(1-\gamma_p)\cdot(1+\gamma_p\Gamma_p)\cdot T_v + (1-\Gamma_p)\cdot\gamma_p\cdot T_s, \qquad (4.9)$$

where T_v and T_s are the effective vegetation and soil temperatures [K]; ω_p and γ_p are the single scattering albedo and transmissivity of the vegetation layer; and Γ_p is the reflectivity of a rough soil surface. The subscript p refers to the polarisation (either horizontal or vertical). The transmissivity of the vegetation

Table 4.2: Bias and Root-Mean-Squared Error (RMSE) of the three normalisation methods when using a synthetic data set of brightness temperatures [K]. The mean (μ) and standard deviation (σ) of TB bias and RMSE for 20 replicates are also given. The best-fit polynomial results provide the theoretical best benchmark.

		Ratio-based method $\mu(\sigma)$	Histogram-based method $\mu(\sigma)$	CDF-based method $\mu(\sigma)$	Best-fit polynomial $\mu(\sigma)$
Horizontal polarisation	Bias	-0.008 (0.151)	-0.008 (0.151)	-0.008 (0.152)	0.000 (0.000)
	RMSE	3.764 (0.023)	2.722 (0.006)	2.643 (0.006)	2.643 (0.004)
Vertical polarisation	Bias	-0.009 (0.113)	-0.009 (0.113)	-0.009 (0.113)	0.000 (0.000)
	RMSE	3.914 (0.012)	1.187 (0.007)	0.941 (0.007)	0.931 (0.002)

layer γ_p is a function of the vegetation optical depth at nadir τ_{NAD}, the vegetation structure parameter tt_p, and the incidence angle θ, given by

$$\gamma_p = \exp[-\tau_{NAD} \cdot (tt_p \cdot \sin^2(\theta) + \cos^2(\theta)) \cdot \cos^{-1}(\theta)], \quad (4.10)$$

where the vegetation optical depth at nadir τ_{NAD} is assumed to be the product of the vegetation water content and parameter b (Jackson and Schmugge, 1991, Van de Griend and Wigneron, 2004). The reflectivity of a rough soil surface Γ_p is dependent on the roughness parameters H_R and N_{R_p} (Wang and Choudhury, 1981, Wigneron et al., 2001) according to

$$\Gamma_p = \Gamma_p^* \cdot \exp[-H_R \cdot \cos^{N_{Rp}}(\theta)], \quad (4.11)$$

as a function of the incidence angle θ and the smooth soil surface reflectivity Γ^*_p, which can be calculated through the Fresnel equations. In this study the Dobson (Dobson et al., 1985) mixing model was used to estimate the relative dielectric constant of the soil, a main input in the Fresnel equations, from information about soil water content, soil texture, and soil bulk density.

The ranges and values of other parameters for natural grass land surfaces required by the L-MEB are listed in Table 4.1. For the pixels in the even columns (observed at θ_{ref}) the simulated brightness temperature observations (S_{ref}) against the truth of normalised observation (T_{obs}) are plotted together

with curves of the three normalisation functions in Figure 4.2. It can be clearly seen that S_{obs} has a nonlinear relationship to T_{obs} for both horizontal and vertical polarisations, confirming that the hypothesis of a non-linear transformation requirement for incidence angle normalisation is correct. To evaluate the accuracy of the three normalisation methods, two fifth order polynomial curves best fit to these relationships were used as the truth of normalisation functions for horizontal and vertical polarisations respectively.

Additionally, due to the integrated effect of soil moisture, vegetation water content, and surface roughness on the angular relationship, the S_{obs} versus T_{obs} plot shows a scattering around the truth curves with a standard deviation of a few K, demonstrating the theoretical uncertainty of normalisation methods. While all three methods fit the main trend of the truth of normalised brightness temperature in Figure 4.2, it can be seen from the difference between S_{obs} and T_{obs} in Figure 4.3 that errors as large as 10 K were observed at the warm and cool ends of the observations. It is this large difference that

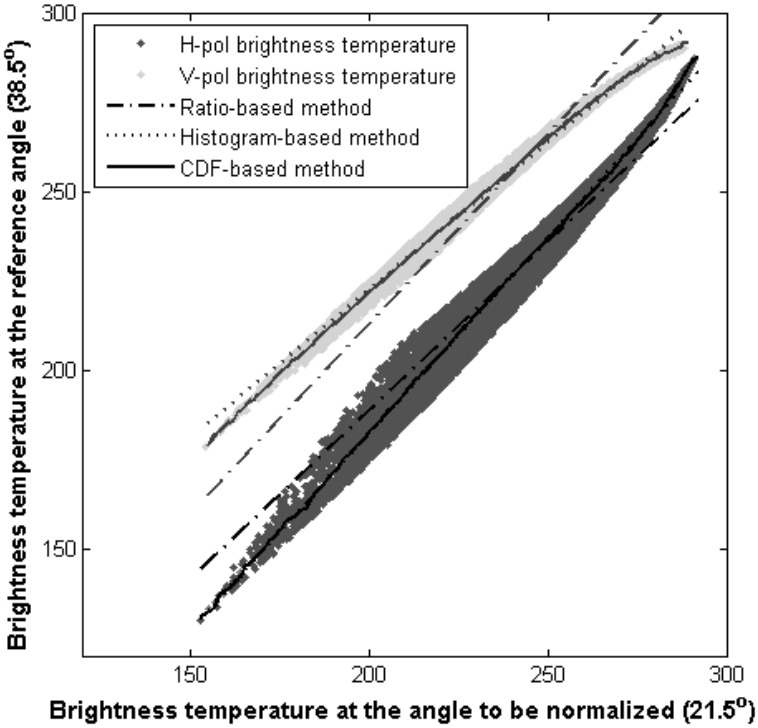

Figure 4.2: Comparison of brightness temperatures normalised from incidence angle of 21.5° to 38.5° against the truth data from the synthetic experiment. Results are for the three normalisation methods tested.

results in the striping pattern in geo-referenced brightness temperature maps. In contrast, the CDF-based method was able to achieve an error of less than 3 K for H polarisation and 1 K for V polarisation across the whole range of brightness temperatures simulated.

To quantify the accuracy of all three normalisation methods, the bias and Root-Mean-Squared Error (RMSE) was calculated for the entire grid by comparing the truth observations (T_{obs}) with the normalised observations (S_{norm}). To minimize any impact from the synthetic experiment design, the analysis was repeated for 20 realisations of soil moisture, vegetation water content, and surface roughness conditions. The mean (μ) and standard deviation (σ) of the bias and RMSE in all 20 realisations were calculated and are listed in **Table 4.2**. The CDF-based method had a mean RMSE of 2.64 K in horizontal polarisation and 0.93 K in vertical polarisation under tested land surface conditions, which closely approximated the theoretical maximum accuracy shown previously. The small bias implies that an insignificant error may be induced when aggregating the whole grid to one pixel.

4.5 Verification using microwave radiometer

The capacity of the CDF-based method to deal with the striping problem was further verified using airborne brightness temperature data collected over Patch 09 during an ~5 hours flight in the AACES-1 experiment. Over each patch during the AACES experiments, about 12 km of the first flight line was

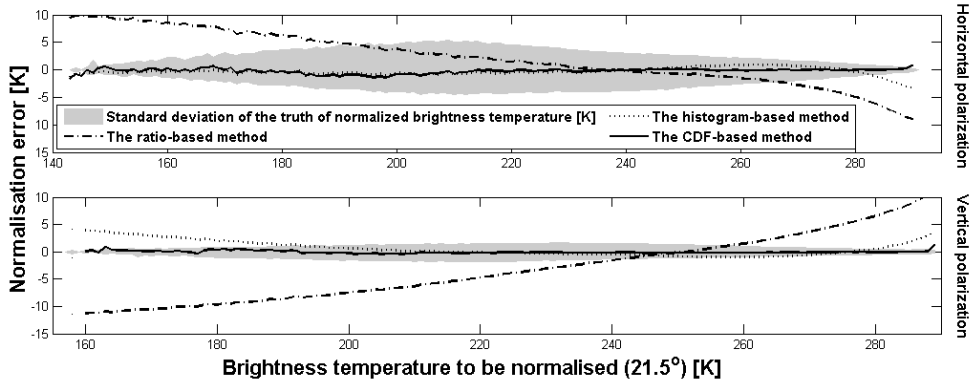

Figure 4.3: Error of the three normalisation methods and standard deviation of the truth of normalised brightness temperature from the synthetic experiment, when normalising from 21.5° to 38.5°.

repeated at the end of the flight in order to assess the temporal variation of brightness temperature observations, which was up to 5 K. This variation was corrected by multiplying the ratio of effective soil temperature at the SMOS nominal overpass time of 6am (local time) to that at the time of each observation. The effective temperature was derived from a time series of top 5 cm soil moisture and physical temperature at 2.5 cm and 40 cm soil depth, which were measured and recorded by temporal monitoring stations installed in each patch during the sampling. After the temporal correction, the brightness temperature difference for the repeat flight line was reduced to ~1 K, implying a negligible temporal impact compared with the SMOS radiometric sensitivity of 4 K (Kerr et al., 2010b).

After temporal correction, brightness temperature observations collected during the mapping flight at incidence angles 7°, 21.5°, and 38.5° ±7.5° were normalised to the reference angle of 38.5° using the three different methods. Due to a small number of viewing angles of the PLMR, the land surface of

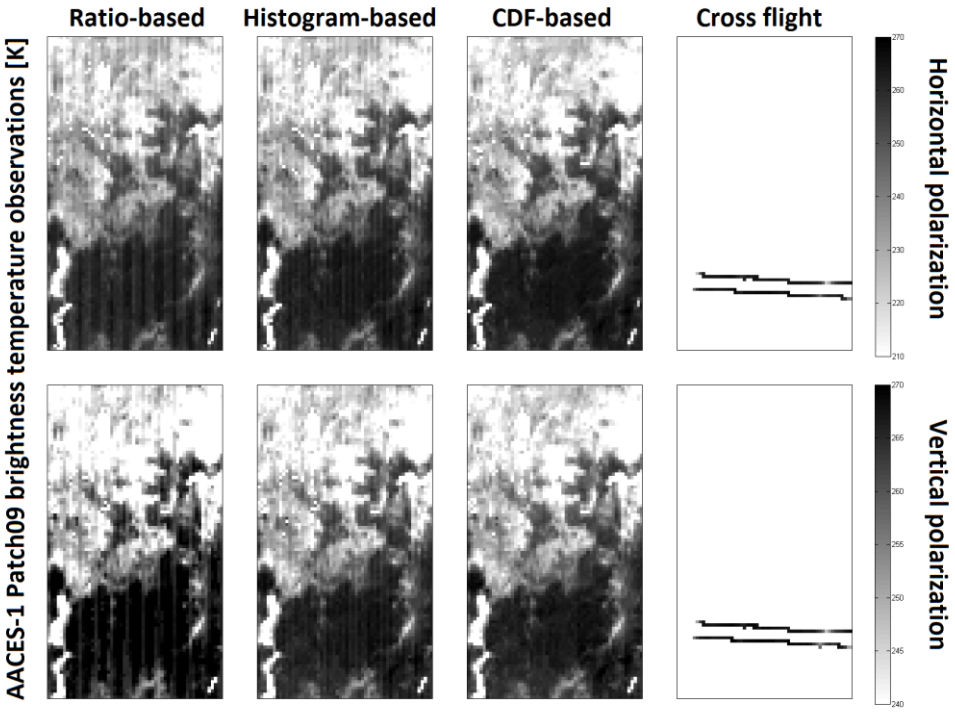

Figure 4.4: The brightness temperature maps [K] of AACES-1 Patch09 at H (top) and V (bottom) polarisation, normalised to the reference angle (38.5°) using the three normalisation methods. Also shown is the directly observed brightness temperature observations from cross flight used for independent verification.

fields viewed by each beam is assumed to be representative of the entire study area, and thus Eqn. (4.5) was used in the CDF-based normalisation method. The normalised brightness temperature observations were then mapped to a 1-km grid using the "drop-in-bucket" technique, as shown in Figure 4.4. Compared with the two linear normalisation methods, it can be clearly seen that the CDF-based method is minimally affected by striping.

To independently verify the angular normalised brightness temperatures, results were compared with the brightness temperature observations measured by the PLMR outer beams (being the 38.5° reference angle) on either side of the flight track during the transit flights that crossed the Patch 9 study area as shown in Figure 4.4. The normalised brightness temperature observations from the mapping flight are compared with the direct observations from the crossing flights over the same pixels in Figure 4.5. Amongst the three methods, the CDF-based approach had the highest accuracy with a RMSE of 4.02 K in horizontal polarisation and 2.68 K in vertical polarisation, under land surface condition of Patch09 during the AACES-1. Similar results were obtained over other study patches during the AACES-1 and AACES-2 that up to 5 K improvement on RMSE was achieved by using the CDF-based method. It can

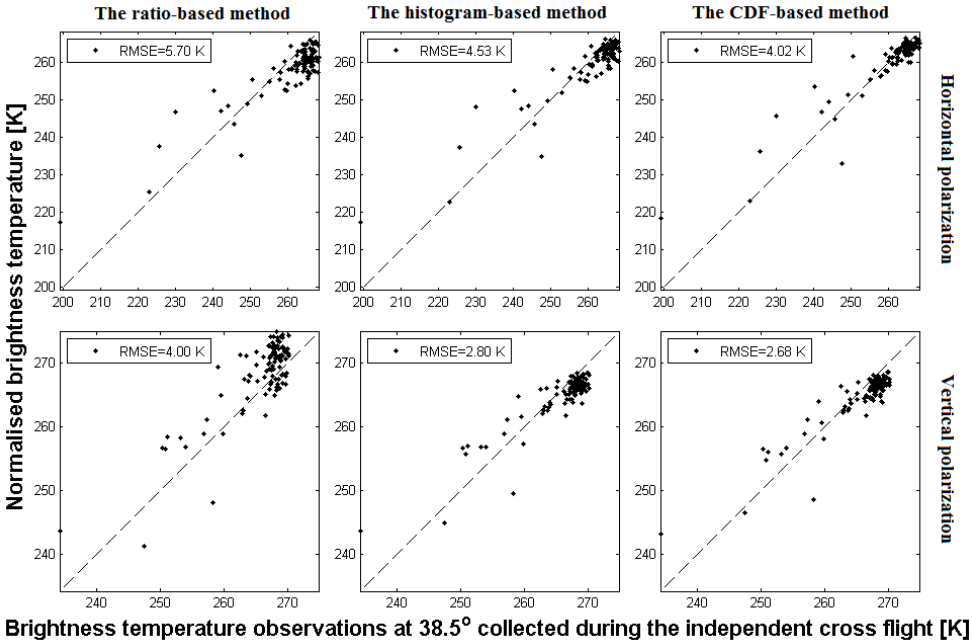

Figure 4.5: Comparison between directly observed cross-flight brightness temperature at 38.5° and normalised scan-flight brightness temperature of Patch 9 in the AACES-1, as shown in Figure 4.4.

be seen that the CDF-based method improvements on the normalisation accuracy are generally higher in V polarisation than in H polarisation due to the increased nonlinearity of angular relationship in V polarisation as shown in Figure 4.2.

The airborne multi-angle brightness temperature observations over the Lake Eyre were also normalised to the reference angle of 38.5° using all three methods individually. Figure 4.6 shows the normalised brightness temperature data and the original observations collected from the reference incidence angle during the cross flight. Due to the land surface over the Lake Eyre being characterised by hyper saline salt pan with super-saturated highly organic material and dry silty material with low salt content, the observed brightness temperature ranged from 50 K to 300 K. It is clear in Figure 4.6 that the brightness temperature observations normalised using linear methods retain a stripe pattern along the north-south flight direction, while the CDF-based method results in a better visual performance. The accuracies of normalisation

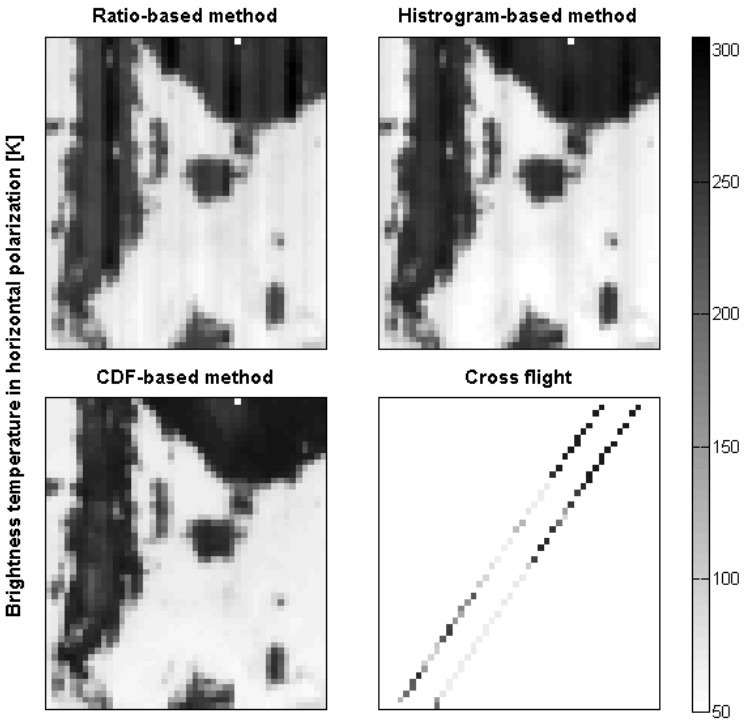

Figure 4.6: The brightness temperature maps [K] of Lake Eyre at H polarisation, normalised to the reference angle (38.5°) using the three normalisation methods, and directly observed brightness temperature observations from cross flight used for independent verification.

methods were quantified by comparing normalised data to the cross flight observations of individual pixels made at the respective incidence angle. Taking the cross flight observations as the truth, the three panels of Figure 4.7 illustrate the true brightness temperature versus the normalised value for each pixel using all three normalisation methods. The Root-Mean-Squared Error (RMSE) of each method was calculated showing that the CDF-based method had an improvement of ~2 K in accuracy, compared with the ratio-based and histogram-based methods, in addition to the more pleasing visual characteristics.

4.6 Verification using microwave radar

In this study, the CDF-based normalisation method (Eqn. (4.8)) was verified using the HH polarised PLIS data collected from twenty ~2 km wide swaths over the entire study area of the SMAPEx-3 experiment. Due to the almost full overlap of the left swaths of F6 and F7, normalised backscatter observations in the left swath of F7 were used as independent data to evaluate the accuracy of normalisation methods applied to F6 and the remaining 18 swaths; these 19 swaths can still make a full coverage over the SMAPEx-3 study area. The backscatter data were normalised to the mid-swath viewing angle of 30° using the three normalisation methods respectively, and the normalisation applied to the entire swath without using land surface classification information.

Figure 4.8 shows the CDF of original observations $S_{obs,i}$ in subset a, the smoothed mean CDF of backscatter observations over all the 19 swaths

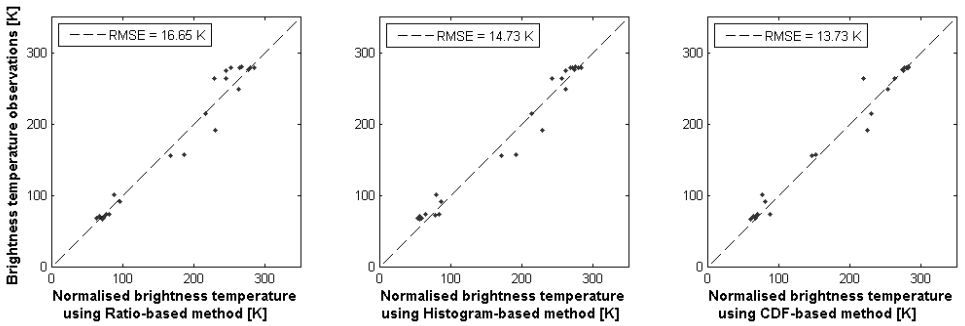

Figure 4.7: Comparison between directly observed cross-flight brightness temperature at 38.5° and normalised scan-flight brightness temperature of Lake Eyre, as shown in Figure 4.6.

($\overline{f}_{smooth}$), the CDF of pre-normalised observations $S_{pre-norm}$, and that of the normalised observations (S_{norm}) over the left swath of F6. It is clear that the CDF of $S_{pre-norm}$ varies with incidence angle and in response to land surface heterogeneity. The rough pattern seen in the CDF of raw observations is the signature of land surface heterogeneity in the given swath. Applying Eqn. (4.5) using $\overline{f}_{smooth}$ (Figure 4.8(b)), the angular impact was corrected whilst maintaining the heterogeneous land surface signature in the CDF of $S_{pre-norm}$ (Figure 4.8(c)). In this study, 4 × 4 coefficient matrices $A_{a,b}$ were used with $S_{pre-norm}$. According to Figure 4.8(c) and (d), the CDF of optimized S_{norm} has a small difference to that of $S_{pre-norm}$, confirming that $\overline{f}_{smooth}$ is the general angular relationship. Thus Eqn. (4.6) can correct the primary angular impact on backscatter observations.

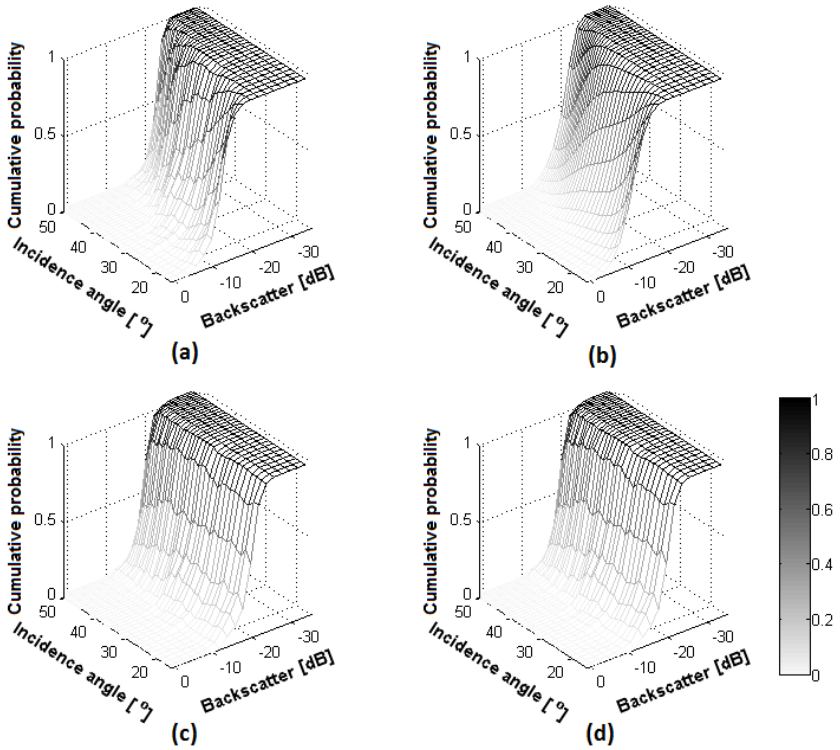

Figure 4.8: (a) The CDF of backscatter observations over the left swath of the 6th flight line (F6) in HH polarisation on 23rd September 2011 during the SMAPEX-3; (b) the smoothed mean CDF of PLIS backscatter for all twenty swaths observed; (c) the pre-normalised CDF of (a) using (b); and (d) the adjusted (c) by comparing with adjacent swaths.

The normalised backscatter observations over the left swaths of F6 and the adjacent left swath of F8 are taken as an example to demonstrate the performance of the CDF-based method on stripe removal in radar data. As shown in Figure 4.9(e), raw backscatter observations in the left swath of F6 and F8 have a mean difference of 7.3 dB within their overlapped area, and more than 90% of overlapped pixels had backscatter differences larger than 4 dB. After applying the CDF-based normalisation method, the mean of

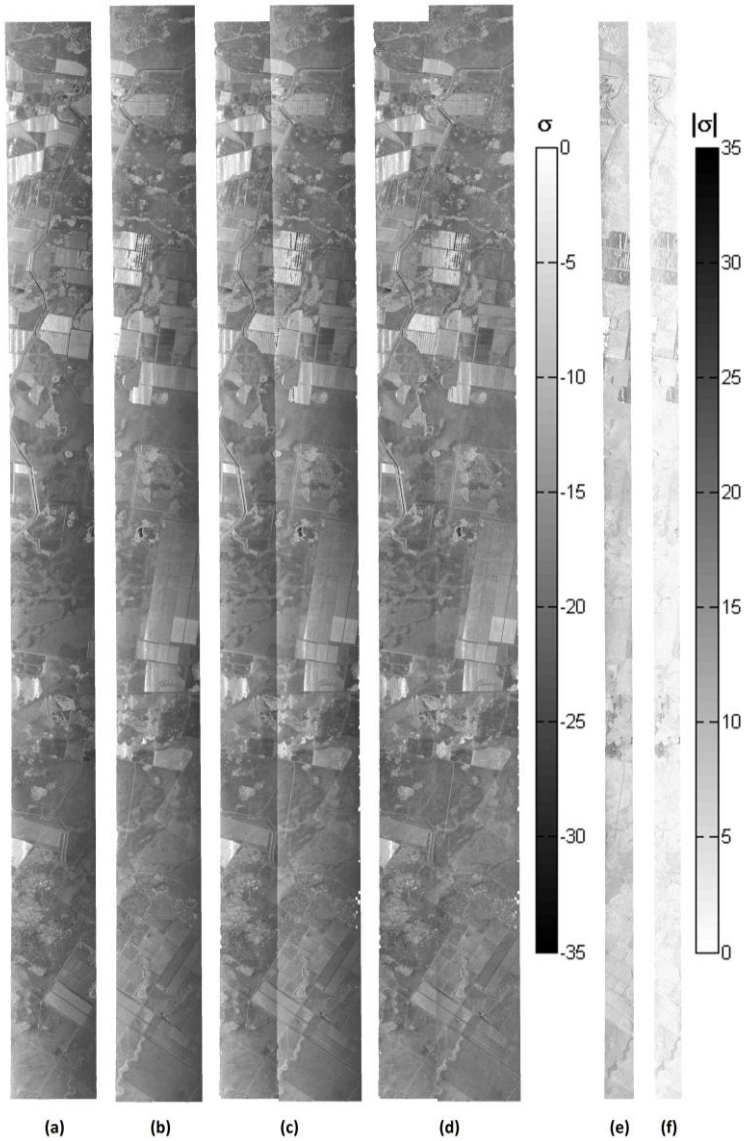

Figure 4.9: PLIS backscatter [dB] at HH polarisation observed on 23rd September 2011 during the SMAPEX-3 over (a) the left swath of the eighth flight line F8 and (b) the left swath of the sixth flight line F6; (c) combined image of (a) and (b) showing incidence angle induced variations; (d) combined image of angle normalised (a) and (b) using the CDF-based method; and absolute difference between the two swaths in their overlapped area (e) before normalisation and (f) after normalisation.

difference reduced to 2.1 dB, with 90% of pixels having differences less than 4 dB, as shown in Figure 4.9(f). However, the backscatter of furrowed areas (very bright areas mostly in the top left of Figure 4.9(b)) has a considerable sensitivity on and an unpredictable relationship to, incidence angle, making it much higher than natural land surfaces at low incidence angles. Consequently, this unusual angular relationship results in ~25 dB difference between the adjacent swaths when using the CDF normalisation method.

To further evaluate the accuracy of the CDF-based method, the backscatter observations collected at the reference angle of 30° in the left swath of F7 were taken as the truth, and compared with backscatter data normalised using the three methods individually, over the overlapped pixels in the left swath of F6, as shown in Figure 4.10. The correlation coefficient (R) and RMSE between the independent reference and normalised observations were calculated for each method. The RMSE of all three methods are 4.44 dB for the ratio-based method, 4.52 dB for the histogram-based method, and 4.26 dB for the CDF-based method with ~0.2 dB lower than the linear methods. However, the accuracies of three methods are different in terms of correlation coefficient. The CDF-based method has the highest R of 0.73, which reduced to 0.53 for the ratio-based and histogram-based methods. Similar conclusions were drawn from normalisation results of the PLIS observations in other polarisation configurations, sampling day, and reference angle between 15° to 45°.

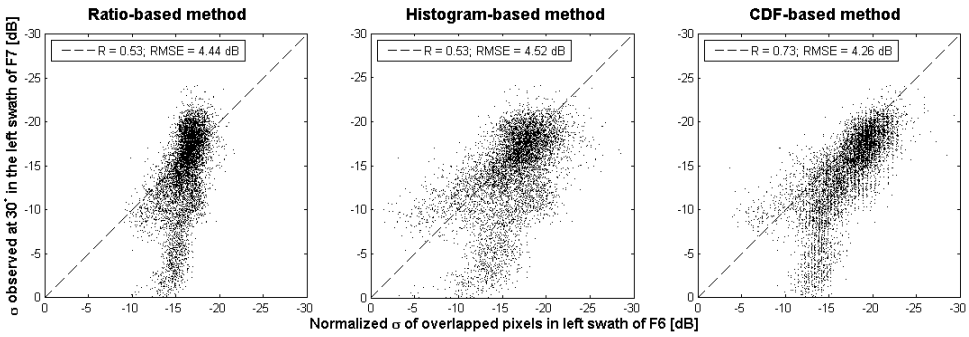

Figure 4.10: Comparison between HH polarised backscatter observed at 30° incidence angle in the left swath of F7 and normalised backscatter of the overlapped pixels in the left swath of F6 using the three normalisation methods respectively.

4.7 Chapter summary

This chapter presented a nonlinear method for incidence angle normalisation of push-broom instruments which was developed to deal with a striping problem observed when using existing normalisation methods over heterogeneous land surfaces. This CDF-based method normalises multi-angle observations by matching the CDF of data viewed at non-reference angles. Its performance was verified using L-band airborne radiometer and radar observations collected during three Australian field experiments. The normalisation accuracy can be improved by up to ~10 K using the CDF-based method, which is considerable when compared with the brightness temperature uncertainties induced by surface rock, urban areas, and standing water, if not accounted for. This new normalisation methodology has been used to produce the data sets that form the basis for analysis in the subsequent chapters.

5 The effect of rock cover fraction

5.1 Chapter introduction

Rock is an impermeable material that absorbs almost no water and thus has a very different microwave response to that of soil. Consequently, this chapter demonstrates the effect of surface rock using both synthetic and observational data collected from the SMOS Arid Zone Experiment outlined in Chapter 3. First, the impacts of surface rock on brightness temperature and soil moisture retrieval error are simulated using a soil moisture retrieval model. Then the simulated results are verified using airborne brightness temperature observations and ground soil moisture measurements during the SAZE. Finally, a rock cover fraction threshold is obtained, and the threshold applied to a global rock cover map to identify the global SMOS and SMAP pixels expected to be adversely affected by rock cover fraction world-wide.

5.2 Data sets and study areas

The airborne passive microwave observations, ground sampling data, and monitoring stations measurements collected during the SMOS Arid Zone Experiment (SAZE; Rüdiger et al., 2013) were used in this study to validate the rock fraction effect determined from model simulation. The field experiment was conducted in August 2009 over three 50 km × 50 km study areas in central Australia, aiming to identify vicarious calibration sites for the on-orbit calibration of SMOS using airborne passive microwave data and *in-situ* measurements. The study area known as Wirrangula Hill is characterized by very sparse vegetation and up to 0.9 fraction of rock pavement known as "gibber", ranging in diameter from 2 cm to 20 cm, as shown in Figure 5.1. Passive microwave observations were collected over the study area using the Polarimetric L-band Multi-beam Radiometer (PLMR) mounted on a scientific aircraft. On the single sampling day over the Wirrangula Hill study area, 12 August 2009, the airborne passive microwave observations were collected at

1000-m resolution over the entire study area and at ~100 m over a 700 m × 3000 m focus area.

Coincident with the flight, top ~5 cm soil moisture was sampled on the ground at a spacing of ~50 m across the focus area using the HDAS (Panciera et al., 2006). The HDAS was developed to make point measurements of water content in the top 5 cm soil using the TDR technique. The soil moisture was measured and stored together with the latitude and longitude of the sampling spot automatically using a handheld computer that forms part of the HDAS system. Ancillary data about the vegetation type, vegetation height, and rock

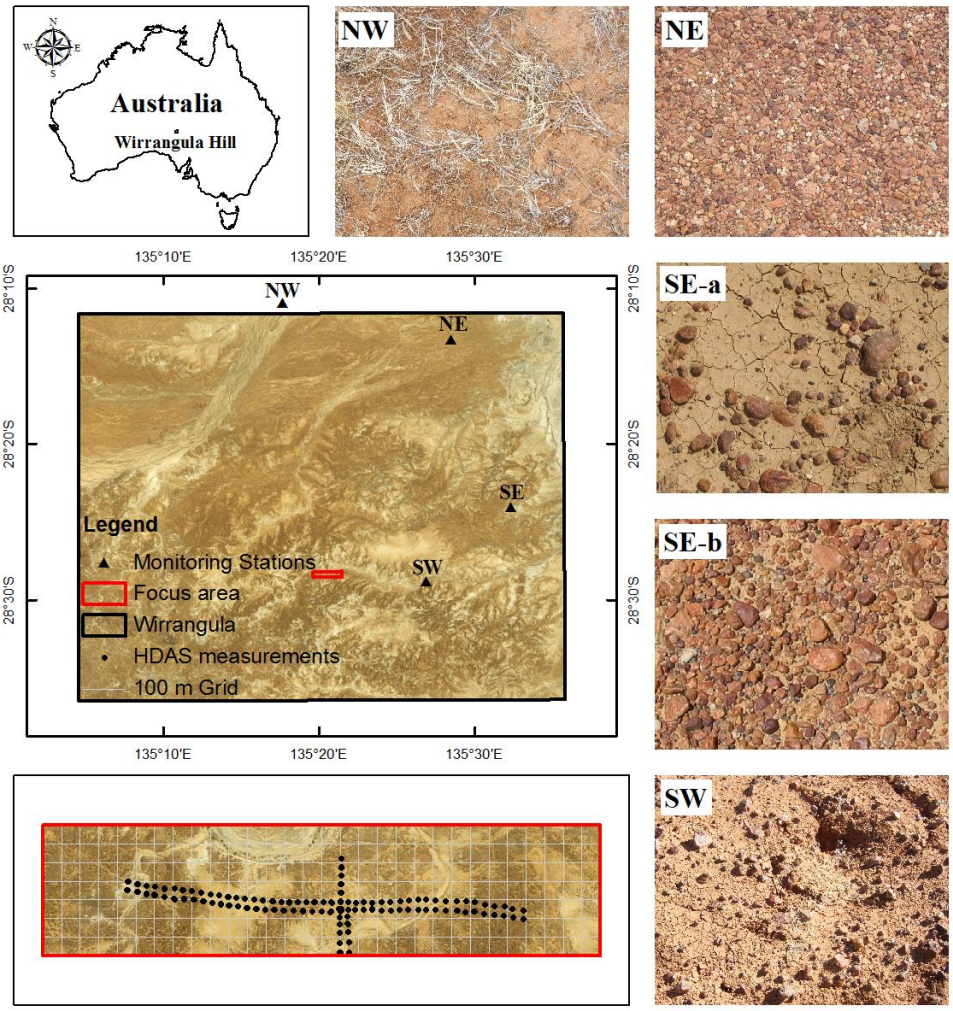

Figure 5.1: Location of the Wirrangula Hill study area within Australia (top left), the focus area (red box, middle left), temporal monitoring stations (black triangles, middle left), and the HDAS measurements (black dots, bottom left). Also shown are ground level photographs of the land surface at the monitoring stations as labelled in the top left corner of each picture.

cover fraction were estimated by the participants and manually recorded in the HDAS. A volumetric soil moisture accuracy of 0.035 m^3/m^3 was determined from an independent calibration check of the universal calibration equation determined by (Merlin et al., 2007) using the thermo-gravimetric technique.

The field measurements of soil moisture were used as the reference for comparing brightness temperature derived soil moisture, in order to validate the rock fraction impact under very dry bare soil conditions. In addition, four monitoring stations were installed throughout the Wirrangula Hill area for the duration of the flight. These included i) Thetaprobes installed vertically at the surface (top 6 cm) and horizontally at 25 cm depth to give temporal variation of soil moisture, ii) thermocouples for measuring soil temperature at depths of 2.5 cm, 5 cm, 15 cm, 25 cm, and 40 cm for estimating effective soil temperature, iii) leaf wetness sensor for indicating the presence of dew, iv) a thermal infrared radiometer for estimating skin temperature, and v) a pluviometer for measuring rainfall. Surface roughness measurements were made for a continuous 2 m long soil profile in north-south and east-west directions at each monitoring station by measuring surface height variations using a pin profiler, together with a ground level photograph.

5.3 Approach

The effects of rock fraction on SMOS brightness temperature observations and soil moisture retrieval accuracy were investigated in three steps as follows:

i) simulate the rock induced error in brightness temperature observations and retrieved soil moisture based on the very dry bare soil assumption and a radio transfer model;

ii) validate the model simulation results using brightness temperature observations and ground soil moisture measurements collected during the SAZE; and

iii) identify the SMOS pixels potentially affected by surface rock globally, using a rock fraction threshold for the SMOS target accuracy of 0.04 m^3/m^3.

Table 5.1: The soil moisture (SM), roughness parameter (H_R), soil temperature (T_S), vegetation optical depth (τ) and vegetation albedo (ω) used for the four synthetic scenarios.

	SM [m^3/m^3]	H_R [-]	T_S [K]	τ [-]	ω [-]
Bare dry soil	0.02	0.5	300	0	0
Bare wet soil	0.2	0.5	300	0	0
Dry soil covered with vegetation	0.02	0.5	300	0.12	0
Wet soil covered with vegetation	0.2	0.5	300	0.12	0

5.4 Synthetic study of rock fraction impact

The effect of surface rock on soil moisture retrieval accuracy was simulated under four soil moisture and vegetation scenarios, including typical dry and wet bare soil and soil covered with medium vegetation. A land surface representation consisting of soil and rock components with a rock cover fraction of f_R was used to assess the soil moisture retrieval error induced solely by rock. Subsequently, the mean soil moisture of the entire medium is defined as the bulk soil moisture

$$SM_B = (1 - f_R) \cdot SM_s, \tag{5.1}$$

where SM_S is the water content of the soil component alone. Similarly, it is assumed that the brightness temperature observation of the bulk medium (TB_B) is the sum of brightness temperatures for soil (TB_S) and rock (TB_R) components, weighted by their cover fractions as

$$TB_B = f_R \cdot TB_R + (1 - f_R) \cdot TB_S . \tag{5.2}$$

In each scenario, the brightness temperature of the soil component was estimated using the τ-ω model based on assigned soil moisture, vegetation water content, roughness parameters, and other parameters required by the τ-ω model, as shown in Table 1. According to a previous study on the dielectric constant of a wide range of rock types at 400 MHz and 35 GHz, the real part of the rock dielectric constant ranges from 2.4 to 9.6 (Ulaby et al., 1986). Subsequently, a dielectric constant of 5.7-j×0.074 was suggested for rock by

Kerr et al. (2010a). Thus, in this study the rock component was assumed to behave like a very dry bare soil with a fixed dielectric constant of 5.7-j×0.074 and roughness parameter *HR* of 0.3 which is the maximum of ground surface height measurements.

Dual-polarised multi-angular brightness temperatures of the entire medium were obtained by estimating brightness temperatures at incidence angles from 0° to 60° with 10° steps. The soil moisture and vegetation water content of the land surface representation were then retrieved simultaneously from the simulated multi-configuration brightness temperatures using the τ-ω model without accounting for the presence of rock. By comparing the retrieved soil moisture with the original "truth" bulk soil moisture, the impacts of rock fraction on soil moisture retrieval accuracy was quantified.

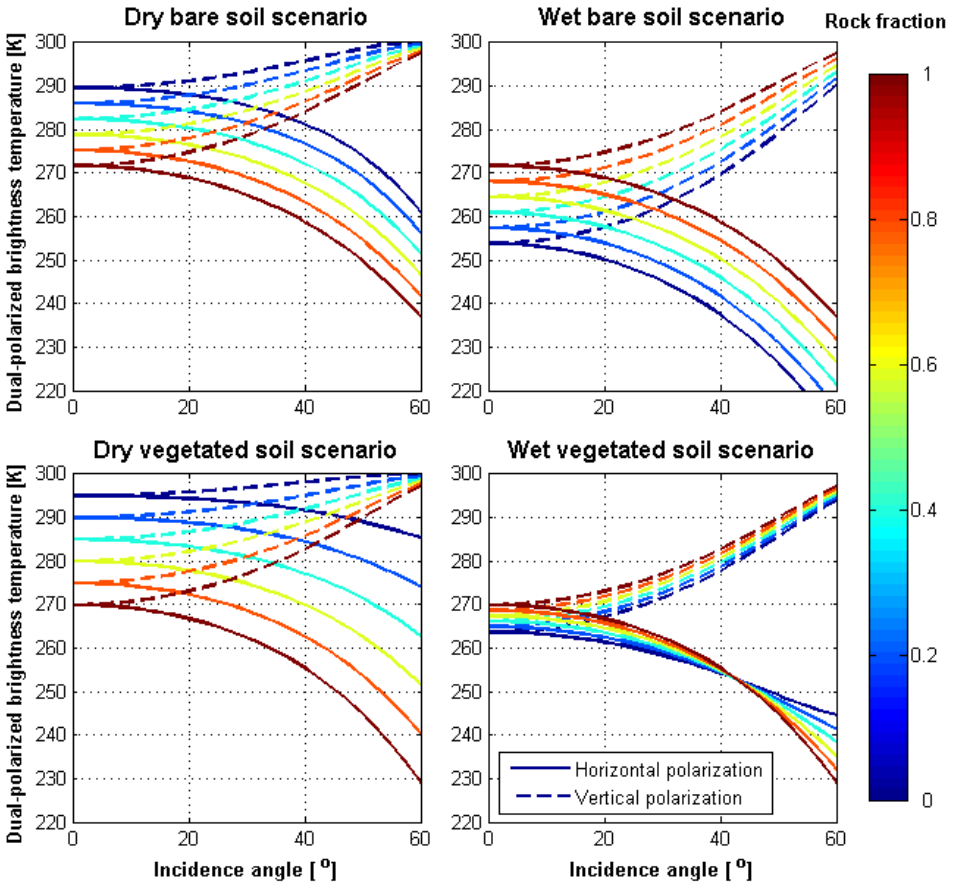

Figure 5.2: Rock fraction impact on the brightness temperature according to incidence angle for four synthetic scenarios, with rock fraction from 0 to 1 with 0.2 steps.

Rock was found to have a considerable impact on the overall brightness temperature response of the land surface (Figure 5.2), with every 0.1 increase in rock fraction introducing up to 2 K difference in brightness temperature. The dielectric constant of rock is relatively consistent compared with that of the surrounding soil, the sign and magnitude of rock impact on brightness temperature ($TB_S - TB_B$) varies with soil moisture and vegetation water content. When rock is mixed with very dry soil, having a lower dielectric constant than rock (dry bare and vegetated soil scenarios), the rock yields an underestimation of the overall brightness temperature. However, it yields an overestimation when mixed with wet soil having high dielectric constant (wet bare and vegetated soil scenarios). Due to the attenuation and emission effects of the vegetation canopy on the overall brightness temperature response,

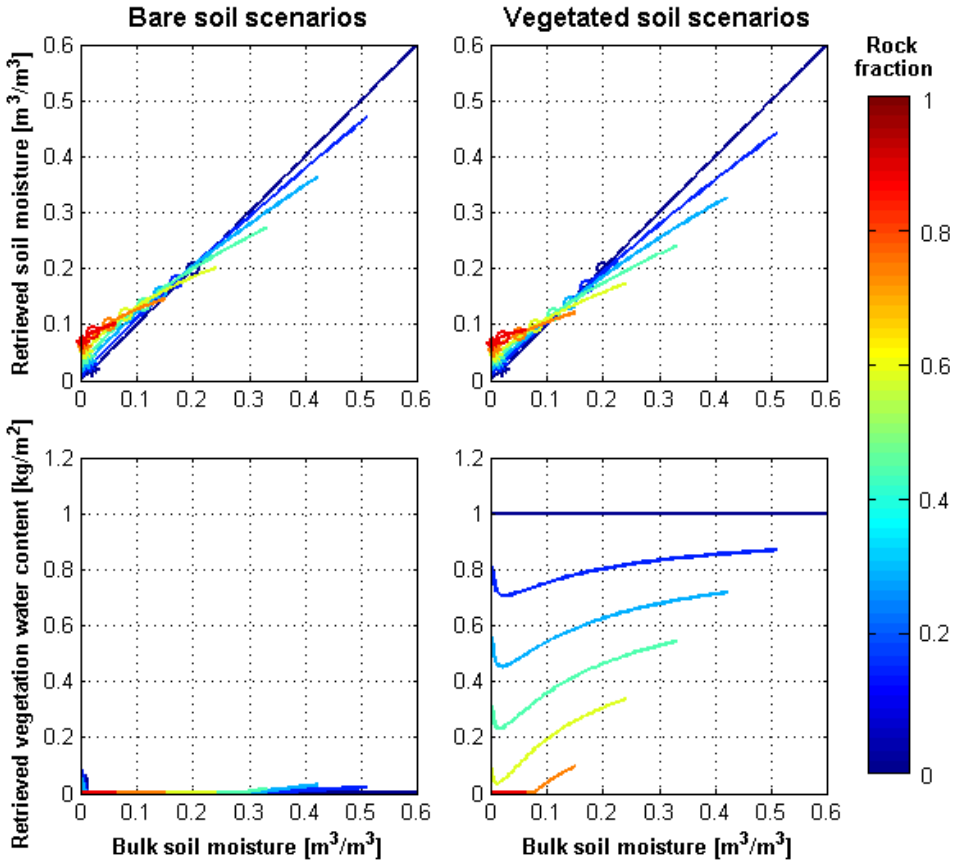

Figure 5.3: Rock fraction impact on the soil moisture retrieval accuracy for bare and vegetated soil scenarios. The curves show bulk soil moisture against retrieved soil moisture for rock cover fraction ranging from 0 to 0.90 with 0.15 steps. The star and circle symbols indicate the 0.02 m^3/m^3 and 0.2 m^3/m^3 water contents of the soil component respectively.

vegetated soil has an increased brightness temperature compared with bare soil. Consequently, the underestimation induced by rock in dry soil and overestimation in wet soil is increased or reduced when the surface is covered with a layer of vegetation, respectively.

The rock induced brightness temperature error is roughly constant with incidence angle, with the exception of the wet vegetated scenario where rock has minimum impact on horizontally polarised brightness temperature at an incidence angle of ~40°. This is a result of the similar angular relationship between rock and wet soil covered with dense vegetation, where rock has a smaller impact across the entire range of incidence angle than in other scenarios. As shown in Figure 5.2, rock has the highest brightness temperature impact in the dry vegetated soil scenario and the lowest impact in the wet vegetated soil scenario. Therefore, the impact of rock fraction on brightness temperature error depends primarily on soil moisture and vegetation water content, and secondarily on incidence angle. During the estimation of rock impacts on SMOS and SMAP later in this chapter, the dependence of rock

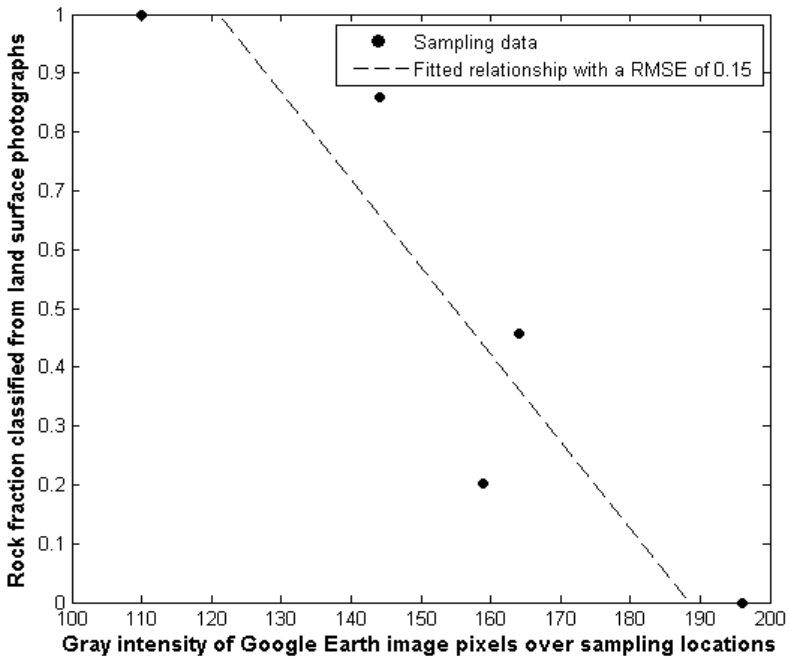

Figure 5.4: The relationship between rock cover fraction classified from land surface photographs and gray scale intensity of corresponding pixels in the Google Earth image where the photographs were taken.

Table 5.2: Land surface parameters used in the soil moisture retrieval algorithm for the Wirrangula Hill study area.

Sand Content [%]	41.8
Clay Content [%]	9.0
Bulk density [g/cm^3]	0.92
Surface soil temperature [K]	289
Deep soil temperature [K]	291
Vegetation water content [kg/m^2]	0
Roughness H_R [-]	0.03
Roughness exponent NR_H [-]	1
Roughness exponent NR_V [-]	0

impact on incidence angle is assumed insignificant and consequently ignored.

Due to the dependence of rock impact on water content of the soil component, multi-angular (0° to 60° with 10° steps) brightness temperature in dual-polarisation was simulated across a wide range of water content of soil component, varying from 0.0 m^3/m^3 to 0.5 m^3/m^3. Soil moisture and

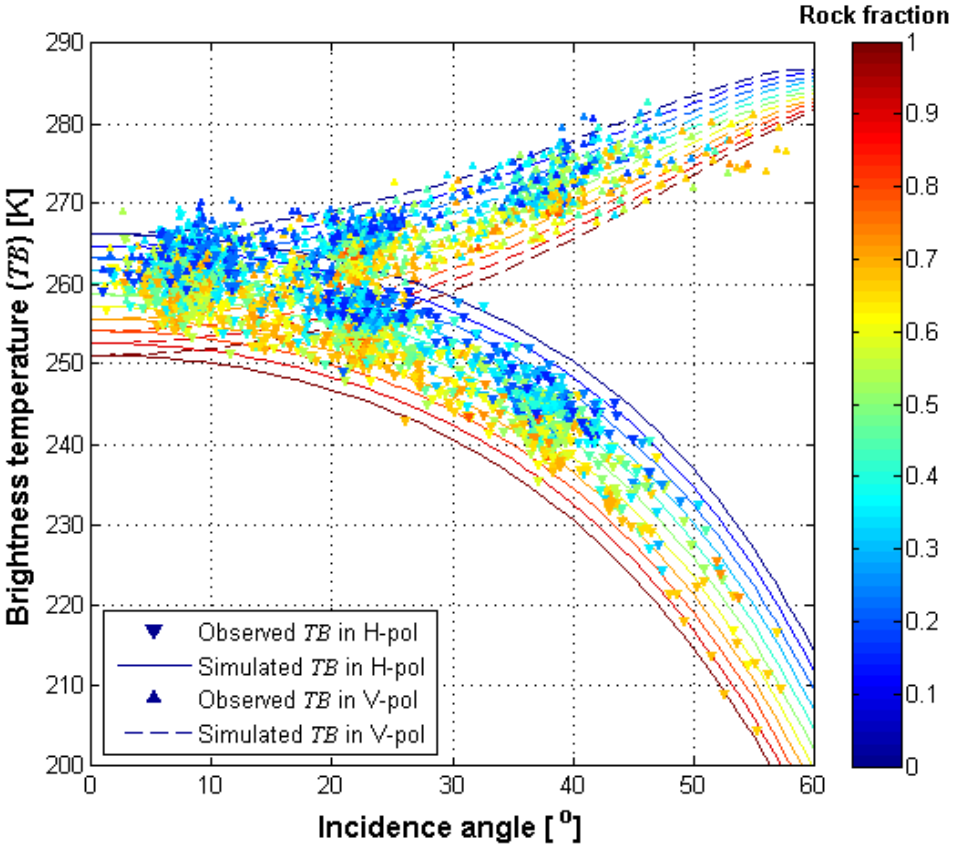

Figure 5.5: The relationship between incidence angle and brightness temperature according to rock fraction.

vegetation water content of the land surface representation were retrieved simultaneously. Figure 5.3 illustrates the curves of retrieved soil moisture and vegetation water content against the truth bulk soil moisture for rock cover fraction ranging from 0 to 0.9 with 0.15 steps. It is clear that without accounting for the presence of rock, the soil moisture retrieval model overestimates the bulk soil moisture under dry soil conditions and underestimates it under wet soil conditions. According to Eqn., the range of bulk soil moisture is limited by the range of water content possible for the soil component and the rock fraction. Under medium-range bulk soil moisture conditions, rock presence typically induces soil moisture retrieval errors below 0.04 m^3/m^3 for most rock cover fractions. However, under extreme dry and wet conditions, soil moisture retrieval could result in an error exceeding the 0.04 m^3/m^3 error budgets of SMOS and SMAP for rock cover fraction larger than 0.4, if the presence of rock is not considered in the soil moisture retrieval.

Compared with bare soil, vegetated soil has a larger rock-induced soil moisture retrieval error, especially under wet soil conditions. The plots in the bottom

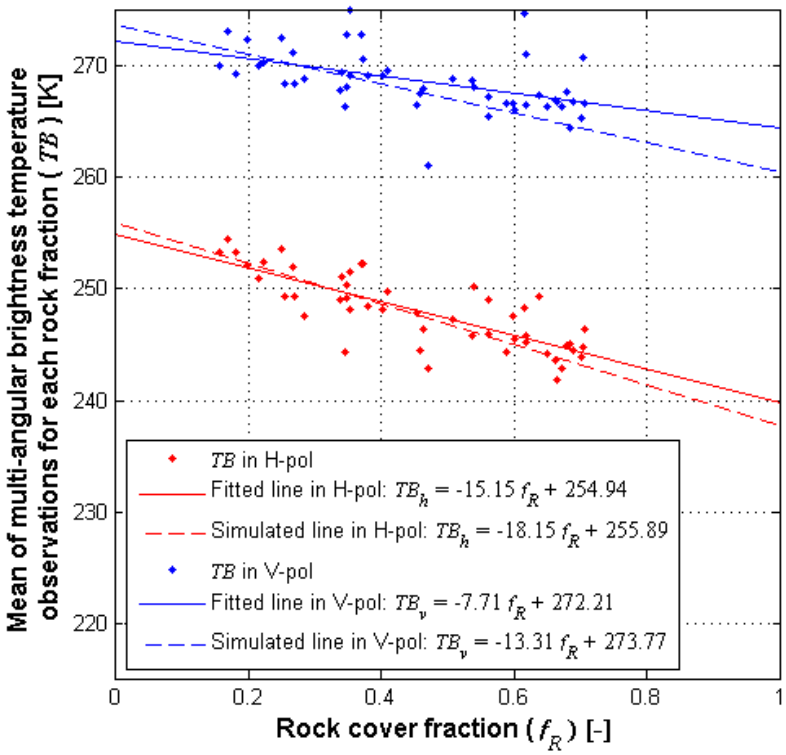

Figure 5.6: The relationship between rock fraction and the mean of brightness temperature observations across incidence angles for each rock fraction.

row of Figure 5.3 illustrate the retrieved vegetation water contents corresponding to retrieved soil moisture shown in the top row. It can be seen that as rock cover fraction is increased, the retrieved vegetation water content is decreased. There are two reasons for this result. First, the rock component in the land surface representation was assumed to behave as bare soil without any vegetation coverage, such that the average vegetation water content of the entire pixel was reduced. Second, the difference between horizontally and vertically polarised brightness temperatures was increased by the presence of rock. Thus, during the soil moisture and vegetation water content retrieval, the retrieved vegetation water content was reduced in the iterative optimization scheme in order to fit both horizontally and vertically polarised brightness temperature inputs with an increased gap, due to the higher sensitivity of vegetation water content to the polarisation difference of brightness temperature than soil moisture.

In the context of the SMOS and the SMAP soil moisture retrieval target accuracy of 0.04 m^3/m^3, soil with medium water content was found to be within the target accuracy while very dry and wet soil only satisfied this accuracy requirement when the rock cover fraction was less than 0.4. Consequently, it is proposed that this threshold can be used to identify the SMOS and SMAP pixels globally where rock-induced soil moisture error may potentially exceed the error budget.

5.5 Validation of rock fraction impact

The rock impact on soil moisture retrieval accuracy determined from the model simulations are validated here under dry bare soil condition using airborne brightness temperature and ground data collected over the Wirrangula Hill study area. Because of the high variation in rock cover fraction at pixel

(100 m) scale across the study area, the first step was to estimate the rock fraction variation across the study area. From the field photographs over the rock soil surface, it was found that the colour of rock was darker than that of soil. Assuming that the darkness of rock and soil is consistent within the study area, the rock fraction was estimated from visible imagery over the entire study

area using a relationship between rock fraction and gray-scale intensity. In this study, a Google Earth image over Wirrangula Hill collected in 2010 was used for the gray-scale intensity. From the ground photographs of rock soil surfaces, the rock fractions were estimated from an un-supervised classification. Using the GPS coordinates of photograph locations, a relationship between rock fraction and the gray-scale intensity of the corresponding pixels in the geo-referenced Google Earth image was established (Figure 5.4). A linear relationship was fitted to the rock fractions and gray intensities with a standard deviation of 0.15. This relationship was then used to estimate the rock fraction within the entire Wirrangula Hill study area, with an uncertainty of ±0.15.

The focus area in the south was divided into a 7 × 30 grid with a resolution of 100 m × 100 m which is the scale of the high resolution brightness

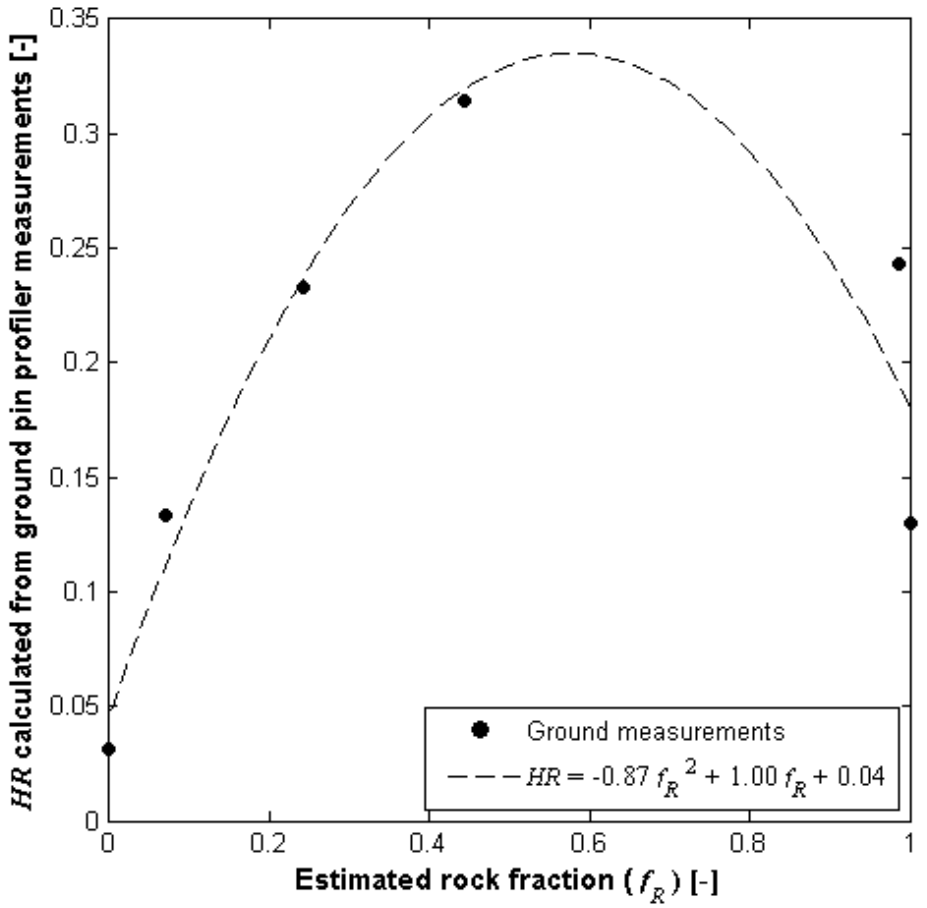

Figure 5.7: The relationship between estimated rock fraction f_R and H_R calculated from ground pin profiler measurements. Ground measurements (dots) were fitted by a second order polynomial function (dashed line).

Table 5.3: Rock impact level.

	1	2	3	4	5	6
Rock fraction [-]	0	0 ~ 0.05	0.05 ~ 0.1	0.1 ~ 0.2	0.2 ~ 0.4	> 0.4
Rock induced TB_h error [K]	0	0 ~ 1	1 ~ 2	2 ~ 4	4 ~ 8	> 8
Rock induced TB_v error [K]	0	0 ~ 0.5	0.5 ~ 1	1 ~ 2	2 ~ 4	> 4
Rock induced SM error [m^3/m^3]	0	0 ~ 0.005	0.005 ~ 0.01	0.01 ~ 0.02	0.02 ~ 0.04	> 0.04

temperature observations. Each pixel was assumed to be homogeneous and its rock fraction estimated from the average gray scale intensity of all Google Earth image pixels within it; rock fraction estimates were also compared against the more subjective field observations recorded by the HDAS. Using the drop-into-bucket approach, the multi-angular brightness temperature observations at the high resolution were grouped for each 100-m pixel without incidence angle normalisation or brightness temperature integration. Since the focus area was sampled by four repeat overpasses of the aircraft at different altitude and attitude, brightness temperature observations were collected at a range of incidence angle from 0 to 60°.

Figure 5.5 illustrates the angular relationship of the observed and simulated brightness temperature data in dual-polarisation, with observations coloured according to the estimated rock fraction of the corresponding pixel. It is clear that there is a good agreement between the observed and simulated brightness temperature data, and that both observed and simulated brightness temperatures decrease with increasing rock fraction. This result not only confirmed the rock cover fraction estimates, but also illustrated the joint impact of rock fraction on brightness temperature. Compared with soil component in the Wirrangula Hill, rock has darker colour, larger particle size and higher dielectric constant where the first two factors result in an increase in brightness temperature via higher physical temperature and surface roughness, and the last factor leads a decrease. According to Figure 5.5, rock fraction has a negative joint impact on brightness temperature, meaning that

the dominated factor of rock impact is higher dielectric constant under very dry bare soil conditions.

To obtain the rock fraction impact on brightness temperature, the brightness temperature data were averaged across all incidence angles in the range of 0° to 60° for each rock fraction, as the rock induced brightness temperature was found to be insensitive to incidence angle. The average brightness temperature is then compared with corresponding rock fraction in Figure 5.6. According to the fitted functions of observed and simulated data, each 0.1 increase of rock fraction causes a decrease of ~2 K and ~1 K in horizontally and vertically

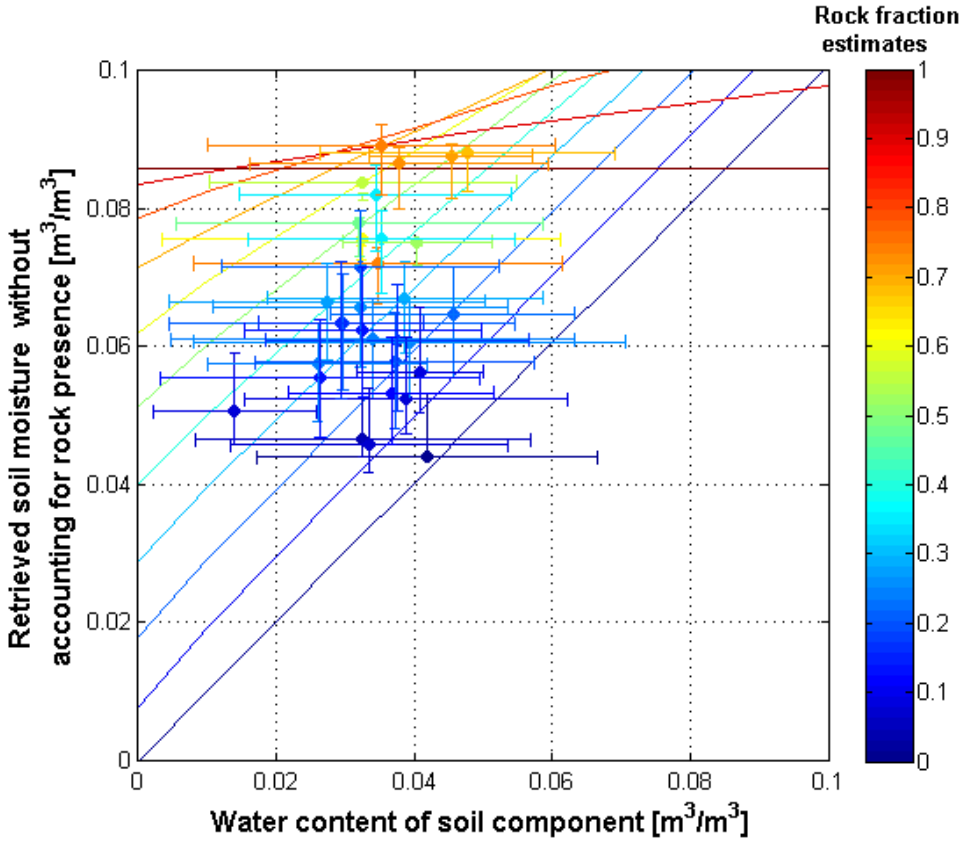

Figure 5.8: Comparison of truth soil moisture and soil moisture retrieved from L-band passive microwave observations in dual-polarisation, without accounting for the presence of rock. The rock cover fraction of data was indicated by colour. The dots show the retrieved soil moisture from the airborne brightness temperature observation against the ground measured soil moisture using the HDAS, and the whiskers show the standard deviation of HDAS measurements within the pixel (horizontal) and the variation of retrieved soil moisture derived from the uncertainty of H_R (vertical). The curves show the model simulated rock effect on soil moisture retrieval accuracy, with rock cover fraction from 0 to 1 with 0.1 steps.

polarised brightness temperatures, respectively. In the context of SMOS 4-K brightness temperature error budgets, a rock fraction of ~0.2 may induce brightness temperature effect in excess of 4 K in horizontal polarisation, while a rock fraction of ~0.4 is required in vertical polarisation to have the same effect.

To validate the impact of rock fraction on soil moisture retrieval accuracy, soil moisture of each 100-m pixel was retrieved from the multi-angular observations over the associated pixel using the τ-ω model. The roughness parameter H_R was determined according to (Kerr et al., 2010a)

$$H_R = (2k\sigma_r)^2, \tag{5.3}$$

where k is the wave number and σ_r is the surface Root-Mean-Squared height calculated from the pin profiler measurements. Figure 5.7 shows the relationship between H_R calculated from surface height measurements and the rock cover fraction estimated from ground photos. According to Zribi et al. (2003), the mean of the squared heights of the surface increases linearly with the cover fraction of rock when rock fraction is less than approximately 0.3 with a moderate mean height of < 25 mm. Similarly, in the Wirrangula Hill study area the measured H_R was found to have a linearly increasing relationship to rock fraction estimate while the rock fraction was less than 0.4. Beyond this the H_R decreased again with full rock cover behaving like a relative flat "pavement". A second order polynomial function was established between rock fraction and H_R roughness parameter, and subsequently used to estimate H_R roughness parameter for brightness temperature simulation and soil moisture retrieval.

To validate the model simulated rock fraction impact on soil moisture retrieval accuracy, the soil moisture of each pixel was retrieved from the airborne observations using the H_R roughness parameter estimated from rock cover fraction, and then compared with the mean of HDAS water content measurements over the soil component of the corresponding pixel. The bulk

soil moisture of each pixel was also retrieved from brightness temperature simulated from truth water content of the soil component and for the rock fraction, without accounting for the presence of rock. Figure 5.8 shows the comparison between observed and simulated soil moisture retrieval results under different rock cover fractions. The whiskers in horizontal and vertical directions indicate the standard deviation of HDAS water content measurements within the pixel and the variation of retrieved soil moisture when accounting for a ±0.15 uncertainty in rock cover fraction. A good agreement between simulated and observed impact of rock fraction on soil moisture retrieval accuracy was found in the comparison of Figure 5.8. Moreover, ignoring even a 0.1 rock fraction in the retrieval model was found to induce error in the retrieved soil moisture of 0.01 m^3/m^3 over bare soil, with a soil moisture content of approximately 0.04 m^3/m^3. In the context of the SMOS and SMAP soil moisture target accuracy of 0.04 m^3/m^3, it was confirmed that approximately 0.4 rock cover fraction can be tolerated under dry bare soil conditions before unacceptable errors occur.

5.6 Rock impact map

In the SMOS Level 2 soil moisture retrieval algorithm, ECOCLIMAP (Masson et al., 2003) is used as the reference land cover dataset, due to its high resolution and fine land surface classification (Kerr et al., 2010a). Due to the

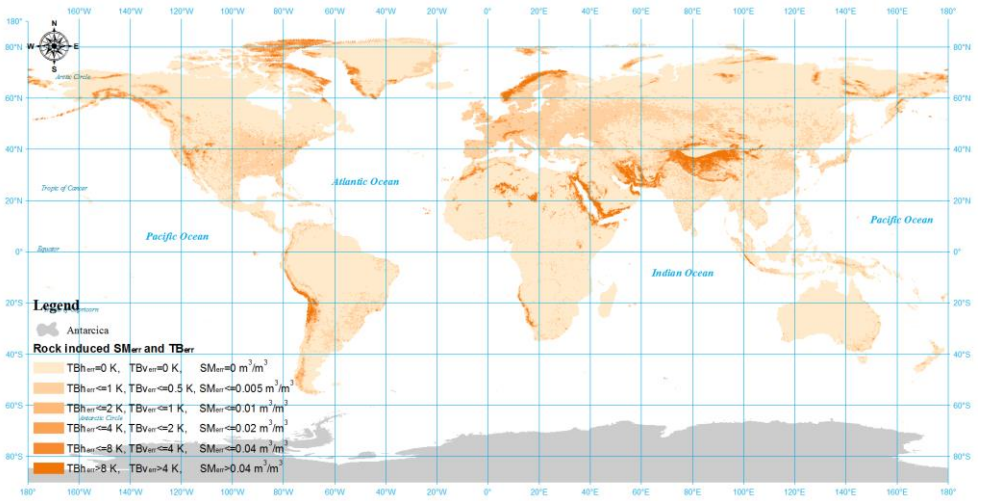

Figure 5.9: Distribution of rock impacted pixels of SMOS over global land mass.

lackage of global rock map, the ECOCLIMAP was developed to initialize the soil-vegetation-atmosphere transfer schemes (SVATs) in meteorological and climate models. Two hundred and fifty ecosystems with homogeneous vegetation were derived from a combination of two global land cover datasets (IGBP/DIS and University of Maryland database; Hansen et al., 2000, Loveland and Belward, 1997, Loveland et al., 2000), the map of the terrestrial climates (Koeppe and De Long, 1958), and the Normalised Difference Vegetation Index (NDVI) data of the Advanced Very High Resolution Radiometer (AVHRR) satellite. The global surface parameter at a resolution ranging from 30 second to 1 degree can be extracted from the ECOCLIMAP by integrating the 30-second data. Consequently, the rock distribution data at the resolution of 30 second were extracted from the ECOCLIMAP 2004, and the cover fraction of barren rock in the SMOS DGG re-sampled 43-km footprints and the SMAP 36-km EASE grid were calculated. All SMOS and SMAP pixels over the global land mass were categorized based on rock fraction impacts on brightness temperature and soil moisture retrieval accuracy, to six levels: i) rock free pixels with no rock-induced brightness temperature impact or subsequent soil moisture retrieval errors; ii) pixels with rock fraction less than 0.05, interpreted as rock induced brightness temperature contribution less than 1 K for horizontal polarisation and 0.5 K for vertical polarisation, and rock induced soil moisture retrieval error less than 0.005 m^3/m^3; iii) pixels with rock fraction less than 0.1, interpreted as rock induced brightness temperature contribution less than 2 K for horizontal polarisation and 1 K for vertical polarisation, and rock induced soil moisture retrieval error less than 0.01 m^3/m^3; iv) pixels with rock fraction less than 0.2, interpreted as rock induced brightness temperature contribution less than 4 K for horizontal polarisation and 2 K for vertical polarisation, and rock induced soil moisture retrieval error less than 0.02 m^3/m^3; v) pixels with rock fraction less than 0.4, interpreted as rock induced brightness temperature contribution less than 8 K for horizontal polarisation and 4 K for vertical polarisation, and rock induced soil moisture retrieval error less than 0.04 m^3/m^3; and vi) pixels with rock fraction greater than 0.4, interpreted as rock induced brightness temperature contribution greater than 8 K for horizontal polarisation and 4 K for vertical

Table 5.4: Statistics of the SMOS and SMAP pixels with rock impact at each level.

	Level	1	2	3	4	5	6
Percentage of the SMOS and (SMAP) pixels [%]	Africa	87.2 (87.5)	7.8 (7.6)	1.3 (1.2)	1.4 (1.3)	1.3 (1.3)	1.0 (1.0)
	Asia	65.0 (67.4)	24.0 (22.3)	2.3 (2.2)	2.5 (2.4)	3.1 (2.7)	3.2 (3.0)
	Europe	24.1 (27.3)	67.1 (64.2)	3.7 (3.6)	2.2 (2.3)	1.5 (1.4)	1.4 (1.2)
	North America	66.0 (66.8)	27.6 (26.6)	2.2 (2.3)	2.3 (2.6)	1.7 (1.6)	0.2 (0.1)
	Oceania	94.5 (94.6)	5.2 (5.1)	0.1 (0.2)	0.1 (0.1)	0.0 (0.0)	0.0 (0.0)
	South America	82.0 (82.5)	13.7 (13.1)	1.2 (1.3)	1.1 (1.3)	0.9 (0.8)	1.0 (1.0)
	Global	71.1 (72.0)	21.7 (21.1)	1.9 (1.9)	1.9 (1.9)	1.8 (1.7)	1.6 (1.4)

polarisation, and rock induced soil moisture retrieval error greater than 0.04 m^3/m^3 (Table 5.3).

Due to the similar pixel size of SMOS and SMAP, this chapter only shows a single plot of rock affected pixels (Figure 5.9). The fraction of rock affected pixels of both the SMOS and SMAP missions were calculated for the main continents and listed in Table 5.4. It can be seen that rock is not homogeneously distributed across the globe. There are more than 1.5% SMOS and SMAP pixels with a rock cover fraction exceeding the 0.4 threshold globally, potentially inducing a soil moisture retrieval error exceeding the target accuracy of 0.04 m^3/m^3 under very dry or wet conditions. In Asia, more than 3% of SMOS and SMAP pixels may be affected by the presence of rock induced soil moisture retrieval errors in excess of the soil moisture error budgets. There are 80 SMOS pixels over Asia, Africa and South America having full rock coverage and the largest expected error of 0.1 m^3/m^3 in retrieved soil moisture. These rock impact maps can be used to mask affected pixels or flag the rock induced uncertainty in the absence of accounting for rock effects in the soil moisture retrieval of SMOS and SMAP.

5.7 Chapter summary

This chapter has examined the assumption that rock behaves like a very dry bare soil with a fixed dielectric constant of 5.7-j×0.074, and investigated the impacts of surface rock using airborne brightness temperature observations and ground soil moisture measurements during the SAZE. The brightness temperature of a mixed rock-soil surface representation was simulated for various rock cover fractions and land surface conditions, using the τ-ω model. The simulated brightness temperature had a good agreement with airborne multi-angular brightness temperature observations, verifying the assumption that rock behaves like very dry bare soil. However, it was also found that the impact of surface rock on soil moisture retrieval accuracy is dependent on the water content of the surrounding soil component, with rock inducing a wet bias of up to ~0.08 m^3/m^3 in retrieved soil moisture under very dry conditions, and dry bias of up to ~0.10 m^3/m^3 under wet conditions, if not accounted for in the soil moisture retrieval models. Based on the SMOS and SMAP target soil moisture retrieval accuracy of 0.04 m^3/m^3, a rock cover fraction threshold of 0.4 was obtained and used to identify SMOS and SMAP pixels likely to have a rock induced soil moisture error above 0.04 m^3/m^3. Approximately 1.5% of SMOS and SMAP pixels globally are expected to have a significant rock induced impact on soil moisture.

6 The effect of urban cover fraction

6.1 Chapter introduction

Apart from anthropogenic emissions, the passive microwave response of urban areas is expected to be a significant contribution to the overall microwave emission from natural surfaces, due to the high proportion of paved surfaces and dwellings made from a range of construction materials. Consequently, this chapter uses the airborne brightness temperature observations collected over eight Australian cities to investigate the effect of urban area on measured brightness temperature and thus soil moisture retrieval accuracy. First, urban extent datasets are assessed for accuracy in estimating the urban cover fraction of corresponding pixels. Applying a moving window technique, the airborne brightness temperature observations at 1-km are integrated to lower spatial resolutions to yield a range of urban cover fractions. Comparing the brightness temperature against the background brightness temperature the urban induced impact is correlated with urban fraction, and an urban cover fraction threshold determined. Finally, this threshold is applied to the global urban extent dataset to estimate the SMOS and SMAP pixels expected to be adversely affected by urban cover world-wide.

6.2 Datasets and study areas

Airborne brightness temperature observations and monitoring station data collected during three Australian airborne field experiments were used to establish the relationship between urban-induced brightness temperature contribution and urban fraction. The NAFE'06 (National Airborne Field Experiment in 2006; Merlin et al., 2008), AACES-1 and AACES-2 (Australian Airborne Cal/val Experiments for SMOS; Peischl et al., 2012b) were conducted in the Murrumbidgee River catchment in south-eastern Australia, during the Australian summers of 2006 (29th Oct. 2006 to 20th Nov. 2010) and 2010 (18th Jan. 2010 to 21st Feb. 2010), and the winter of 2010 (8th Sep. 2010 to

26th Sep. 2010), respectively. Figure 6.1 shows the location of the study areas, monitoring stations, studied cities, the SMAP EASE (Equal-Area Scalable Earth) 36-km grid, and SMOS overlapped footprints which are re-constructed to ~43-km resolution on the SMOS DGG (Discrete Global Grid).

In this study, data collected over 13 sampling days across eight SMOS and SMAP sized areas were analysed (see Table 6.1). The brightness temperature over seven medium-to-large cities across the catchment (listed in Table 6.1) was measured using the Polarimetric L-band Multibeam Radiometer (PLMR) mounted on a scientific aircraft.

The urban area is a combination of manmade structures (e.g. buildings and roads) and natural land surfaces (e.g. parks and gardens), where only manmade structures are expected to have a distinct microwave response from natural soil targets. To qualify the impact of urban areas, the manmade structures in the Murrumbidgee River Catchment were identified using the Land Use New South Wales (LUNSW; New South Wales Department of Environment &

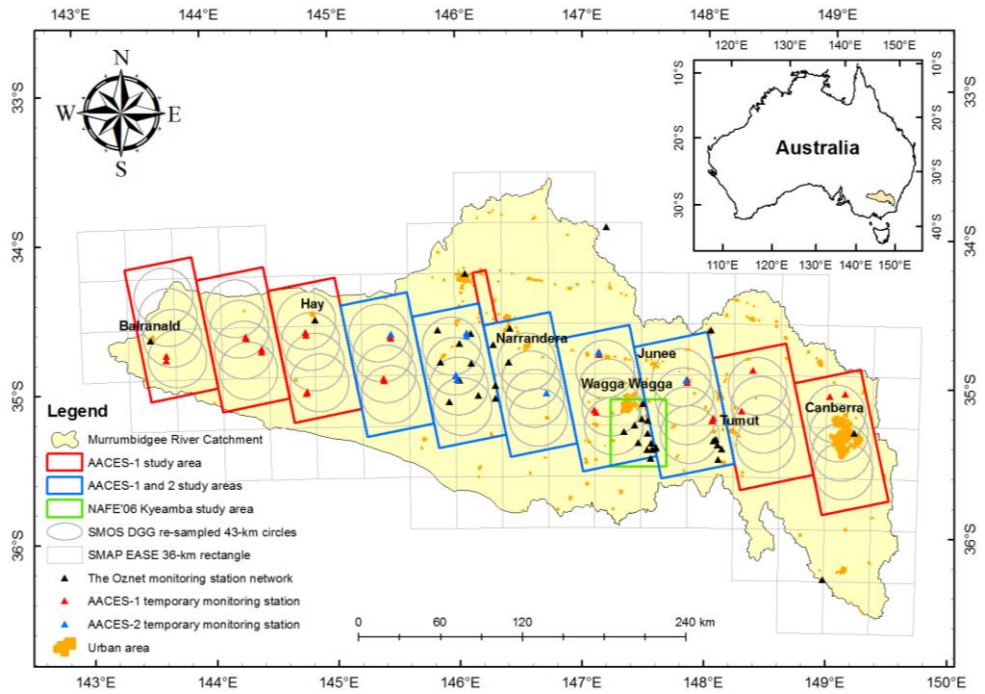

Figure 6.1: Location of the NAFE, AACES-1, and AACES-2 study areas in the Murrumbidgee River catchment in south-eastern Australia (inset). SMOS DGG re-sampled pixels within each AACES flight patch and SMAP EASE pixels over the entire catchment as well as the long-term soil moisture network sites (OzNet) and temporary monitoring stations of AACES campaigns are indicated on the map.

Climate Change, 2007) product due to its high resolution of better than 15 m. The LUNSW is a regional land use dataset mapped in polygon format over the State of New South Wales (NSW), Australia. The land use classification and mapping was undertaken directly from satellite imagery and aerial photography with assistance from existing data sets, local knowledge, and field checking. According to an independent verification conducted by checking the satellite imagery and aerial photographs, the LUNSW has a positional accuracy of 50 m and an attribute accuracy of 0.92~0.99 (New South Wales Department of Environment & Climate Change, 2007). In the LUNSW, urban land use is classified as a combination of 29 subclasses, including industrial/commercial, residential, recreational, landfill, and other urban facilities. The subclasses of urban class in the LUNSW were re-grouped into manmade structures dominated by built-up environment and rural areas dominated by natural land surface. Moreover, the other land surface classes in LUNSW were re-categorized to cropping, grazing, tree or woodland, water surface and mining.

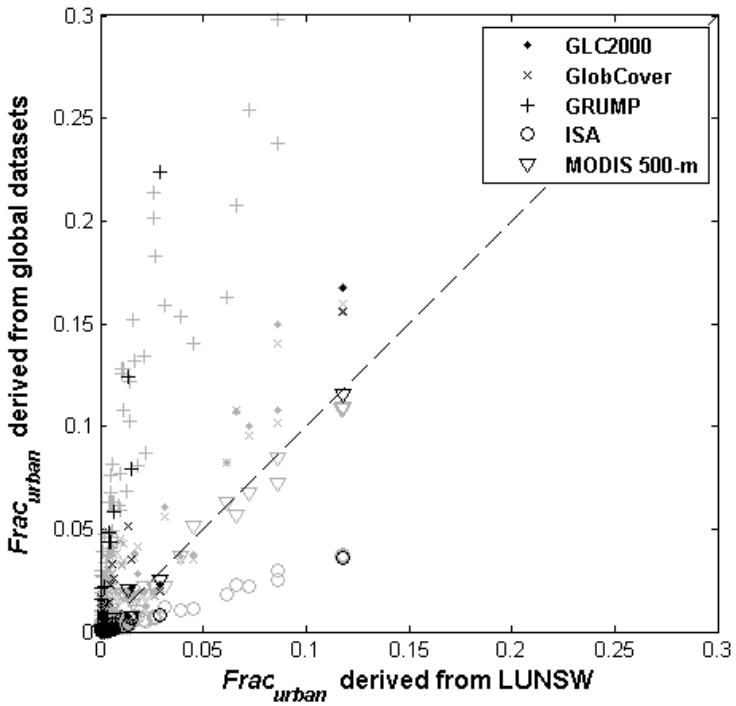

Figure 6.2: Comparison between LUNSW and MODIS 500-m in terms of urban fraction of SMOS DGG re-sampled pixels (gray symbol) and SMAP EASE 36-km pixels (black symbol) over the Murrumbidgee River Catchment.

Table 6.1: The list of flights made over seven cities across the Murrumbidgee River Catchment.

Dataset	Sampling date	Flight patch	Reference time (local)	Studied city	City size derived from the LUNSW (km^2)
NAFE	30th, Oct. 2006	Kyeamba	12.00pm	Wagga Wagga	30.60
	6th, Nov. 2006	Kyeamba	12.00pm	Wagga Wagga	30.60
	20th, Nov. 2006	Kyeamba	12.00pm	Wagga Wagga	30.60
AACES-1	22nd, Jan. 2010	1	6:00 am	Balranald	1.61
	28th, Jan. 2010	3	6:00 am	Hay	2.60
	12th, Feb. 2010	6	6:00 am	Narrandera	4.90
	10th, Feb. 2010	7	6:00 am	Wagga Wagga	30.60
	15th, Feb. 2010	8	6:00 am	Junee	3.48
	18th, Feb. 2010	9	6:00 am	Tumut	4.49
	18th, Feb. 2010	10	6:00 pm	Canberra	170.31
AACES-2	19th, Sep. 2010	6	6:00 am	Narrandera	4.90
	21st, Sep. 2010	7	6:00 am	Wagga Wagga	30.60
	22nd, Sep. 2010	8	6:00 am	Junee	3.48

To identify global SMOS and SMAP pixels with urban induced brightness temperature error in excess of the respective error budgets, a global urban map with appropriate resolution and accuracy is required. There are currently ten different global urban and urban-related land surface maps available, as listed in Table 6.2. Different types of data were used in the classifications, thus they differ in terms of their definition of "urban", spatial resolution and accuracy. For example, the urban maps that are derived from census data and night-time lights relate to population and income level, while the urban maps derived from multispectral data relate more to built-up areas (Potere and Schneider, 2007, Potere et al., 2009). Compared with natural land surfaces, the difference of microwave behaviour of urban areas is due to the distribution of manmade structures not population or other factors. Consequently, only the maps that define urban as built-up or impervious area and have a spatial resolution better than 1 km were considered in this study (i.e. Maps 1 to 6 in Table 6.2).

The accuracies of these maps were assessed in Schneider et al. (2010) by comparing urban maps over 140 randomly sampled cities globally, by manual interpretation using 30-m Landsat data. The assessment result showed that the MODIS (Moderate Resolution Imaging Spectroradiometer) 500-m urban land

cover (MODIS 500-m) dataset had the highest accuracy at pixel level (0.93) and in overall urban size (R^2 = 0.90). The MODIS 500-m is a global urban land use map with a spatial resolution of 500-m, generated using a supervised decision tree algorithm based on MODIS Collection 5 data between 2001 and 2002. In the MODIS 500-m dataset, urban areas are defined as pixels having more than 50% built-up land surface with a minimum size of 1 km^2 (Schneider et al., 2010).

To apply the urban fraction threshold derived from the LUNSW globally, a global urban map was required to calculate the urban fraction of global SMOS and SMAP pixels, which should be classified based on manmade structures and consistent with the LUNSW at the scales of SMOS and SMAP. Consequently, the cover fractions of manmade structures and urban areas in the SMOS DGG pixels with approximately 43-km resolution and SMAP EASE 36-km pixels over the Murrumbidgee River catchment were calculated using the LUNSW and each of the global urban maps respectively. Figure 6.2 shows the urban fractions calculated using each of the global Maps 1 to 5 against the cover fractions of manmade structures using the LUNSW over the corresponding SMOS and SMAP pixels in the Murrumbidgee Catchment.

Due to its lower resolution than its upgraded version (MODIS 500-m dataset), the MODIS 1-km urban land use dataset (Map 6) was discarded in the comparison. It is clear that the GRUMP, GLC2000, and GlobCover datasets overestimate the urban area as compared with manmade structures in the LUNSW, while the ISA dataset provides an underestimate. The mean ratio of pixel urban fraction calculated using each of Maps 1 – 5 to the cover fraction of manmade structure derived from the LUNSW is listed in the last column of Table 6.2, confirming that the MODIS 500-m has the best agreement with manmade structures in the LUNSW, having an urban extent ratio of 0.93. In the context of 0.11 to 0.20 urban fraction threshold obtained from the previous simulation studies (Kerr et al., 2010a, Loew, 2008), the difference between the LUNSW manmade structures and MODIS 500-m is approximately 1% at the SMOS and SMAP scale, which was considered to be negligible. Consequently the MODIS 500-m urban map was selected for

Table 6.2: Key characteristics of ten global urban maps (adapted from Schneider, et al. 2010).

ID	Abbreviation	Map	Factor defining urban or urban-related feature	Resolution	Main source of data	Urban fraction ratio to the LUNSW
1	GLC2000 (Bartholome and Belward, 2005)	Global Land Cover 2000	Artificial surfaces and associated areas	~1 km	SPOT-Vegetation, Nighttime lights data	1.36
2	GlobCover (Arino et al., 2007; ESA, 2008)	GlobCover v2.2	Artificial surfaces and associated areas	~300 m	MERIS	1.37
3	GRUMP (CIESIN, 2004)	Global Rural–Urban Mapping Project	Urban extent	~1 km	VMAP, census data, Nighttime lights maps	3.68
4	ISA (Elvidge et al., 2007)	Global Impervious Surface Area	Impervious surface area	~1 km	Landscan, Nighttime lights data Landset data for training	0.31
5	MODIS 500-m (Schneider et al., 2010)	MODIS Urban Land Cover 500 m	Urban and built-up areas	~500 m	MODIS and Landsat-based map for training and assessment.	0.93
6	MODIS 1-km (Schneider et al., 2003)	MODIS Urban Land Cover 1 km	Urban and built-up areas	~1 km	MODIS, Landsat-based map for training and assessment and LITES	-
7	HYDE (Goldewijk, 2001, 2005)	History Database of the Global Environment v3	Urban and built-up areas	~10 km	Landscan, UN census data, city gazetteers	-
8	VMAP (Danko, 1992)	Vector Map Level Zero	Population	1:1 million	Aeronautical charts, maps	-
9	Lights (Elvidge et al., 2001; Imhoff et al., 1997)	Nighttime Lights v2	Nighttime Lights	~1 km	DMSP-OLS dataset	-
10	LandScan (Bhaduri et al., 2002)	LandScan 2005	Population	~1 km	Geocover maps, VMAP0, MODIS 1-km, Landsat, census data, high-resolution imagery	-

calculating urban fraction of all SMOS and SMAP pixels globally. A key assumption of this step is that the microwave behaviour of the studied cities represents that of urban areas world-wide.

6.3 Approach

The impact of urban fraction on soil moisture retrieval was investigated in four steps, as illustrated in Figure 6.3:

i) the airborne brightness temperature observations at 1 km resolution were used to simulate SMOS and SMAP scenes for a wide range of scene urban fraction (f_U), and the average brightness temperature of urban-free pixels ($TB_{non\text{-}urban}$) and that of all pixels (TB_{all}) calculated for the corresponding scene. To achieve a wide range of scene urban fraction, a 40 km rectangle window was moved within the study area. However, according to the size of the studied cities as listed in Table 6.1, the maximum cover fractions at 40 km are less than the 0.11% to 0.20 urban fraction threshold obtained from the simulation studies of Kerr et al. (2010a) and Loew (2008). To obtain results for a greater range of urban fraction thresholds, the scene was centred on the studied cities and the window size gradually decreased, assuming that the brightness temperature integrated from smaller scales is the same as that at the SMOS and SMAP scales (Panciera et al., 2007). The re-categorized LUNSW dataset was used to determine the urban fraction and identify the urban-free brightness temperature pixels in the 1-km PLMR data;

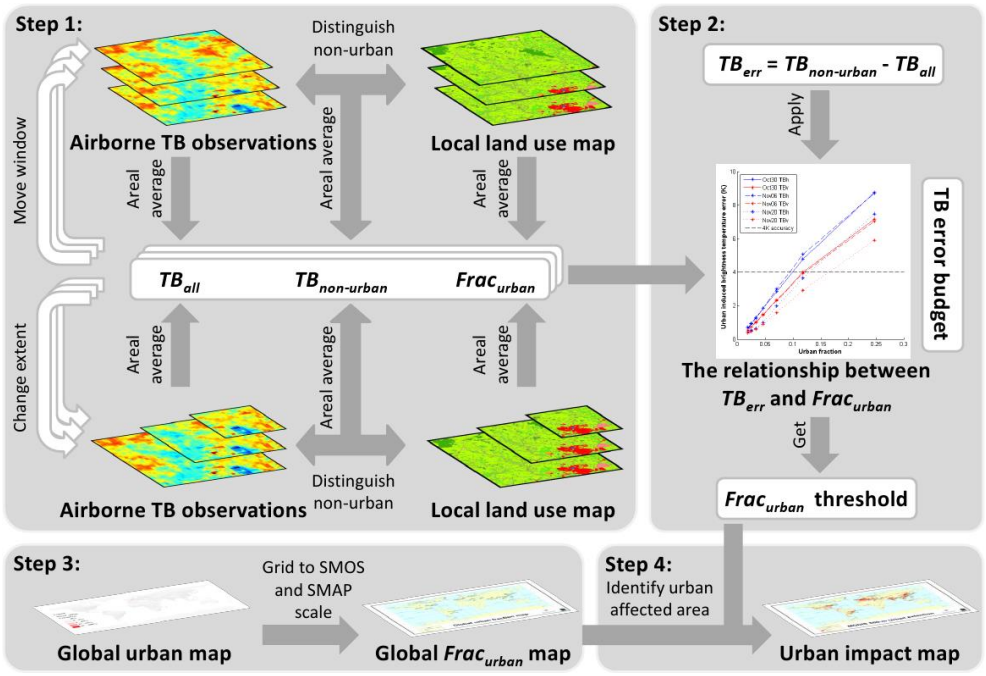

Figure 6.3: Schematic flow chart of methodology.

ii) the SMOS and SMAP radiometric sensitivity of 4 K and 1.3 K (Entekhabi et al., 2010, Kerr et al., 2010b) were used as brightness temperature error budgets to determine the thresholds for urban cover fraction in SMOS and SMAP pixels, below which an urban induced brightness temperature error can be ignored as part of the overall instrument uncertainty. The urban induced brightness temperature error (TB_{err}) is defined hereafter as the difference between $TB_{non\text{-}urban}$ and TB_{all} which represent space-borne brightness temperature observations both with and without correcting for the contribution of urban area respectively. Based on the relationship between f_U and TB_{err}, urban fraction thresholds were derived for the SMOS and SMAP brightness temperature error budgets respectively, ignoring the differences of the pixel shape and size between the SMOS and SMAP;

iii) the MODIS 500-m urban land use map was used to calculate urban fraction of SMOS and SMAP pixels globally. The SMOS mission uses the Icosahedral Snyder Equal Area (ISEA) based Aperture 4 hexagon DGG in Resolution 9, which maps the Earth surface into ~2.6 × 106 hexagon cells with an equal area of ~194 km2 and an equal distance of ~15 km between the centre points of adjacent cells (Sahr et al., 2003). Although the centre points of SMOS L1 and L2 data are fixed on the DGG points, the size and orientation of the pixels vary for the ~1000 km partly overlapped SMOS scenes in the Murrumbidgee River catchment, and the SMOS footprints were simplified to overlapping circles with a diameter of 43 km, being the average SMOS pixel size (Kerr et al., 2010a) centred on the SMOS DGG points. Similarly, the Equal-Area Scalable Earth (EASE) Grid 2.0 (Brodzik et al., 2012), was used for application to SMAP. The EASE grid is defined in three projections: northern and southern hemisphere (Lambert azimuthal equal-area projections) and full global (a cylindrical equal-area projection with standard parallels at ±30°). The global EASE grid at 36-km resolution has been selected for the SMAP radiometer products. Consequently, the urban fractions (f_U) in the SMOS DGG re-sampled 43-km circles and the SMAP 36-km EASE grid were calculated using the MODIS 500-m urban land surface map;

iv) the urban fractions of SMOS and SMAP pixels at global scale were then used together with the thresholds obtained for the SMOS and SMAP radiometric sensitivities obtained in step ii), and then applied to the urban fractions obtained in step iii), to produce global maps of urban effected pixels. A key assumption of this step is that the microwave behavior of the studied cities represents that of urban areas world-wide.

It is important to note that this study does not consider radio-frequency interference contributions from urban areas on the brightness temperatures, but rather the emissions due to changed land surface conditions from impervious surfaces and building materials. Although the use of L-band microwave frequencies is protected, it has been found that SMOS observations were adversely affected by Radio-Frequency-Interference (RFI) in some parts of the world, as shown in Figure 2.8. However, since SMOS was launched in November 2009, a large effort has been made to switch off RFI sources. When all RFI has been removed in the future, urban areas are expected to still impact the brightness temperature observations at SMOS and SMAP scale due to their unique microwave response compared to that of soil, and subsequently confound soil moisture retrieval if their presence is not accounted for. Consequently, this study aims to investigate the impacts of urban areas other than those from RFI.

6.4 Verification using real observations

A range of scenes were simulated for the SMOS and SMAP pixels by moving the window of a scene at SMOS and SMAP scale within the study area, and by reducing the extent of a scene centred on the studied cities. As an example, **Figure 6.4** shows the land use, as well as horizontally and vertically polarised brightness temperature maps of scenes within the Kyeamba study area using airborne observations collected on 6th November 2006 during the NAFE'06 campaign. According to the re-categorized LUNSW classification, this area is dominated by cropping and grazing land, intermixed with manmade structures, rural areas, trees, water bodies and mining area. Compared to brightness temperature maps, the non-soil targets have a distinctive microwave response.

The urban area and open water have ~30 K lower brightness temperature than the surrounding grass and cropping land surfaces, while the brightness temperatures of trees were ~10 K higher. The impact of forest and water bodies was removed by discarding the pixel with more than 0.05 cover fraction of forest and/or water bodies.

Figure 6.4 has a good spatial agreement between the manmade structures and very low brightness temperature pixels, implying a good correlation between re-categorized manmade structures and urban-affected brightness temperature pixels. From Column (a) to (c) in Figure 6.4, a 40 km × 40 km scene was moved from the southernmost part of the study area towards the studied city (Wagga Wagga) in the north, with the urban fraction (f_U) of the scenes varying from 0.001 when the studied city was almost outside of the scene to 0.021 when the studied city was fully in the scene. To obtain a higher range of urban fractions, the scene was positioned over the urban area and the extent of the scene reduced from 40 km to 20 km and then to 10 km (Columns (c) to

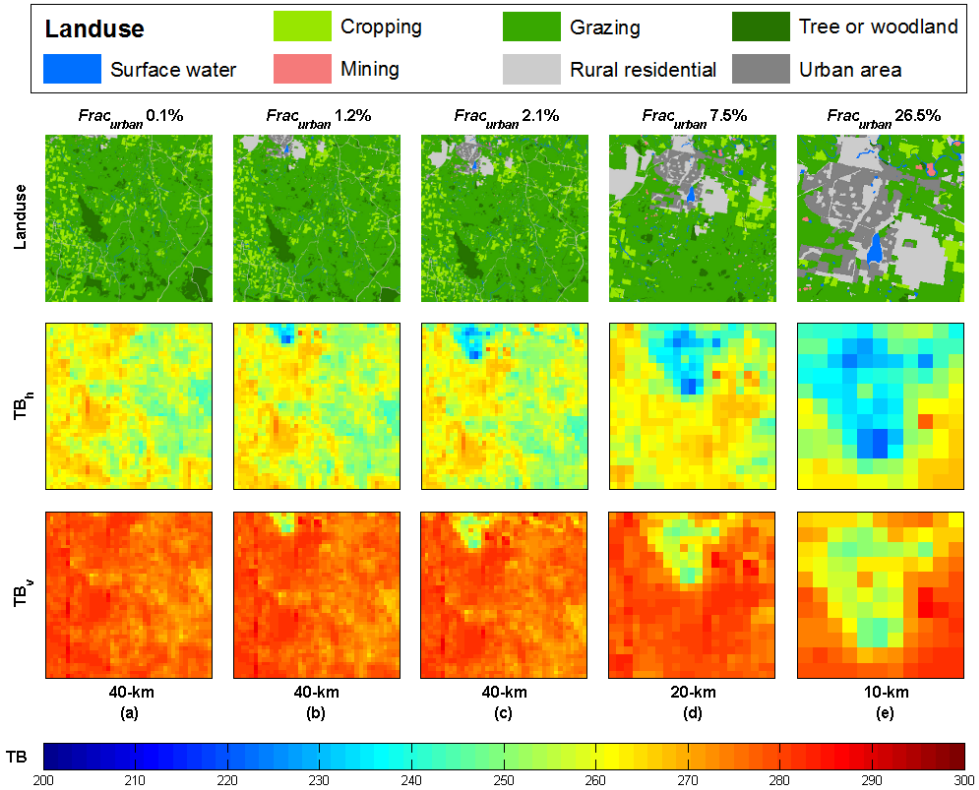

Figure 6.4: LUNSW and dual-polarised brightness temperature (TB_h and TB_v) maps at 38.5° incidence angle in the scenes with different urban fractions over the city of Wagga Wagga on 6 November 2006.

(e)), resulting in urban fractions up to 0.265 in this example.

The brightness temperature observations of all pixels in each scene were then averaged to TB_{all}, and the equivalent urban free brightness temperature estimated as $TB_{non\text{-}urban}$ by discarding all pixels classified as urban. The assumption being that the surrounding brightness temperature response is representative of what would have been observed had the urban area not been there. The corresponding scene urban fraction f_U is also calculated.

This analysis was repeated for a total of 13 flights across the three airborne field experiments. Being opposite to the previous dry bare soil assumption on the microwave behaviour of urban areas, the studied cities were observed to

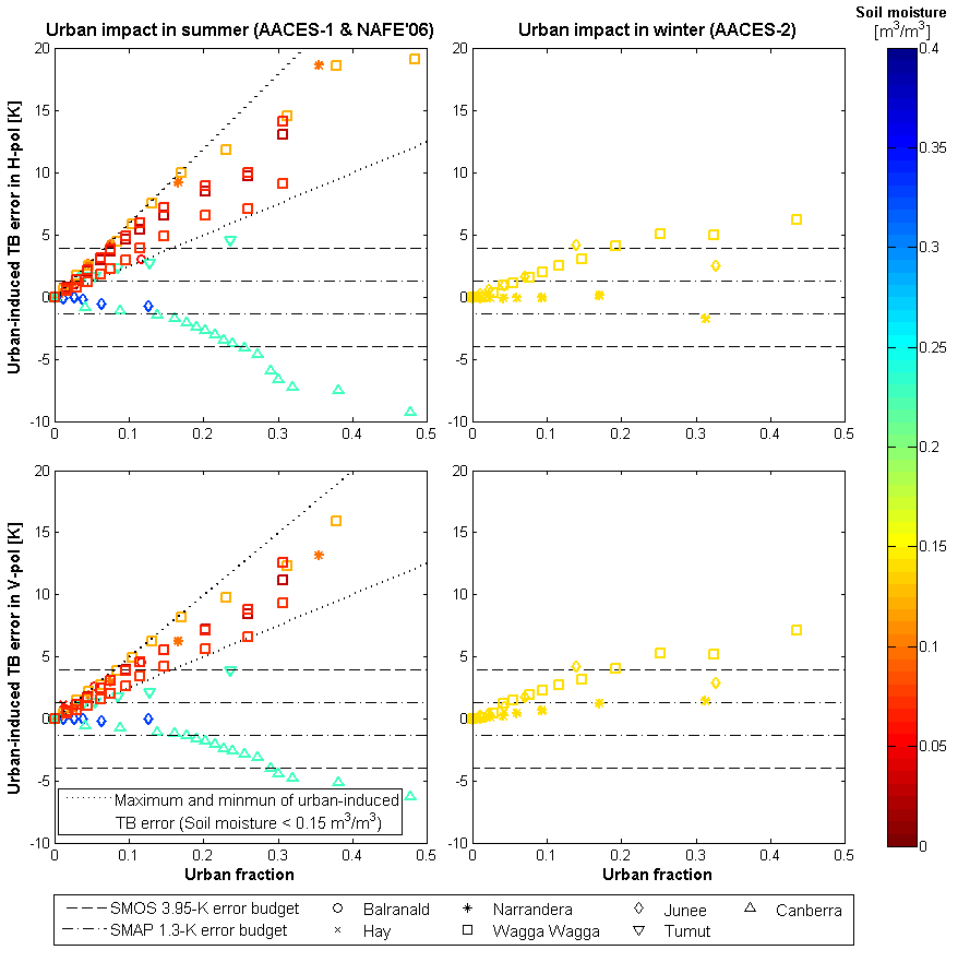

Figure 6.5: The relationship between urban fraction and urban induced brightness temperature error at 38.5° incidence angle for Horizontal (top) and Vertical (bottom) polarisations during summer (left) and winter (right) campaigns. Symbol colour reflects the average soil moisture measurement collected using monitoring stations within the corresponding flight patch.

have a considerable (up to 50 K) lower brightness temperature than surrounding natural grass and cropping lands under most conditions. This phenomenon is also found from the airborne HUT-2D observations collected in December 2006 over the Porvoo area, southern Finland (Rautiainen et al., 2008). A reasonable explanation is that residential buildings usually having tail roofs are expected to behave like dry bare soil, while industrial buildings sometimes having metal roofs have a very low emissivity.

The urban induced brightness temperature TB_{err} calculated from $TB_{non\text{-}urban}$ and TB_{all} is plotted against f_U for summer and winter seasons separately in **Figure 6.5**, with results coded by the average top ~5 cm soil moisture according to monitoring station measurements. As expected, the magnitude of TB_{err} increases as f_U is increased. During the summer campaigns (NAFE'06 and AACES-1), urban areas induced a positive TB_{err}, and the ratio between TB_{err} and f_U was shown to be dependent on the soil moisture condition, with a lower TB_{err} induced by urban area as the soil moisture increased. For soil moisture lower than 0.15 m^3/m^3, the brightness temperature difference between urban

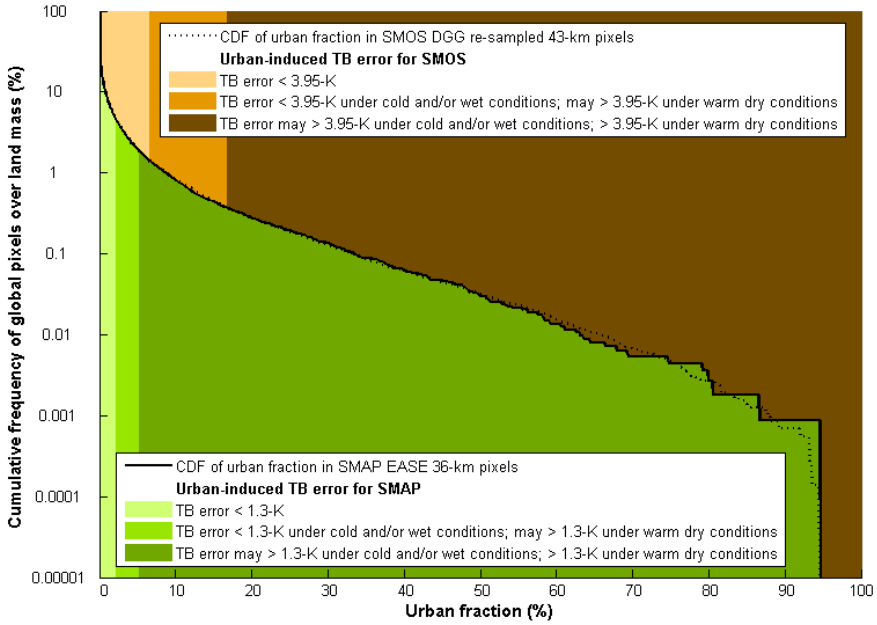

Figure 6.6: Cumulative Distribution Functions (CDF) of urban fraction of SMOS (brown) and SMAP (green) pixels over land mass and the percentage of land pixels that is likely to be adversely affected by urban areas under different conditions.

and urban-free areas was 25 K to 60 K for horizontal polarisation, and 25 K to 50 K for vertical polarisation under warm summer conditions. Similar to urban effects under wet (soil moisture larger than 0.15 m^3/m^3) summer conditions, the impact of urban area was found to be much less in the winter campaign (AACES-2) than that under dry summer conditions. Due to a small soil moisture variation captured during the AACES-2, no clear relationship between TB_{err} and soil moisture was found.

One anomaly to the above results was for the airborne data collected over the city of Canberra on 18 February 2010. In this case a negative relationship between TB_{err} and f_U was obtained, during the flight undertaken around 6pm rather than at 6am. This negative brightness temperature error resulted from two aspects: i) the ratio of industrial buildings drops from ~0.25 for the other studied cities to ~0.1 for the Canberra, while the ratio of residential buildings leaps from ~0.65 to ~0.9 (Table 6.2). Thus the effective emissivity of manmade structures in Canberra is lower than the other studied cities; ii) the physical temperature of urban area should be higher than that of the surrounding natural area in late afternoon due to the solar heating and lower thermal capacity of manmade structures.

To meet the target soil moisture retrieval accuracy of the SMOS and SMAP,

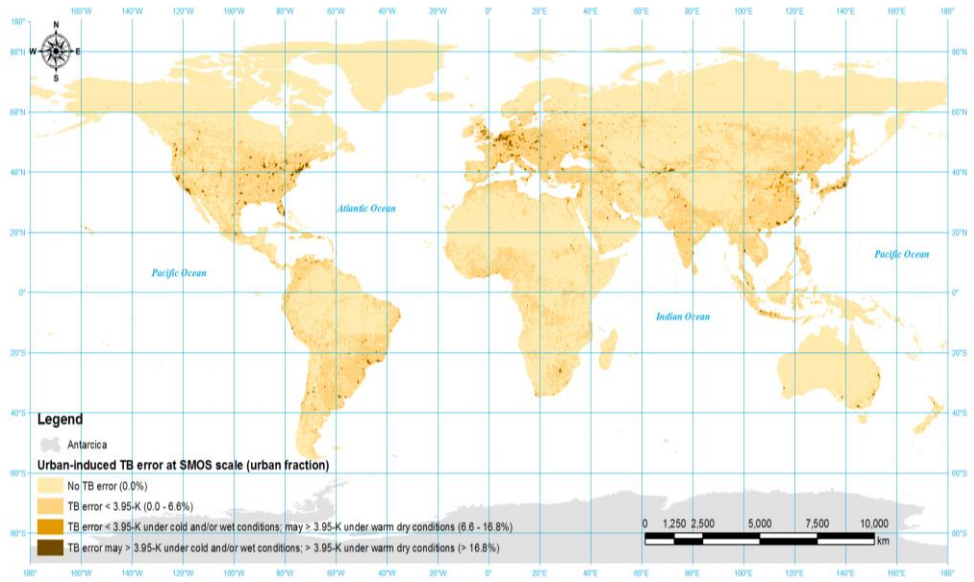

Figure 6.7: Distribution of urban impacted pixels of SMOS over global land mass.

Table 6.3: Statistics of urban impact on the SMOS and SMAP pixels.

Urban impact	Urban fraction threshold for the SMOS (SMAP) [0.01]	Fraction of the SMOS and (SMAP) pixels expected to exceed allowed brightness temperature error [%]						
		Africa	Asia	Europe	North America	Oceania	South America	Global
*	0.0 (0.0)	77.58 (78.83)	63.31 (64.82)	49.22 (52.49)	69.93 (72.43)	94.28 (94.56)	58.55 (60.21)	67.83 (69.51)
**	0.0 – 6.6 (0.0 – 2.2)	22.17 (19.96)	35.12 (29.91)	46.29 (33.47)	28.24 (23.46)	5.35 (4.38)	40.25 (35.5)	30.74 (25.98)
***	6.6 – 16.8 (2.2 – 5.2)	0.20 (0.85)	1.26 (3.18)	3.40 (8.30)	1.12 (2.00)	0.21 (0.52)	0.94 (2.77)	1.06 (2.66)
****	> 16.8 (> 5.2)	0.05 (0.37)	0.32 (2.09)	1.09 (5.75)	0.71 (2.11)	0.16 (0.55)	0.27 (1.53)	0.37 (1.85)

*: no urban-induced brightness temperature error;

**: with urban-induced brightness temperature error less than the error budgets;

***: with urban-induced brightness temperature error less than the error budgets under cold and wet conditions and may larger than the budgets under warm and dry conditions;

****: with urban-induced brightness temperature error may be larger than the error budgets under cold and wet conditions and larger than the budgets under warm and dry conditions.

their brightness temperature error budgets of 4 K for the SMOS and 1.3 K for the SMAP were used as benchmarks for accurate soil moisture retrievals and subsequently urban fraction thresholds for the target soil moisture retrieval accuracy were obtained for the SMOS and SMAP respectively. Thus, urban fraction thresholds of 0.066 for horizontal polarisation and 0.079% for vertical polarisation were obtained for SMOS 4-K error budgets under warm and dry conditions. Similarly, for the lower SMAP 1.3-K error budget, permissible urban fraction thresholds dropped to 0.022 and 0.026 for horizontal and vertical polarisations respectively. Additionally, urban fraction thresholds of 0.168 and 0.052 were obtained for SMOS and SMAP brightness temperature error budgets respectively under cold and/or wet conditions. For the purpose of simplicity, 0.066 and 0.168 were selected as urban fraction thresholds for SMOS brightness temperature at both polarisations, under warm dry conditions and cold and/or wet conditions respectively. These values reduce to 0.022 and 0.052 for SMAP.

6.5 Urban impact map

These urban fraction thresholds have been applied globally, to understand the extent of the urban effect. Consequently the urban fraction at SMOS and SMAP scales over the global land mass were calculated using the MODIS 500-

m dataset. The urban land use raster of the MODIS 500-m dataset were converted to polygon format without any approximation or simplification, and then clipped with the SMOS DGG re-sampled 43-km circles and SMAP EASE 36-km pixels. The areal ratio between clipped area and the corresponding pixel is defined as the urban fraction of the given pixel.

Based on the relationship between the urban-induced error and urban fraction, the maximum brightness temperature error that could be introduced by ignoring the presence of urban is estimated from the calculated urban fraction of SMOS and SMAP pixels. The maximum estimation of urban-induced errors over the global are grouped and showed in Figure 6.6. It is clear that over highly urbanized areas, such as Europe, east China, and U.S, a brightness temperature error of over 4 K may be potentially induced over urban areas where soil moisture retrieval error could exceed the target soil moisture retrieval accuracy.

Figure 6.6 shows the cumulative frequency curves of pixel urban fraction for the SMOS and SMAP missions individually. Due to their similar scales, SMOS and SMAP have similar cumulative distribution curves of urban fraction. Compared with their urban fraction thresholds, there are about 2% of SMOS pixels having urban-induced brightness temperature error in excess of the 4 K

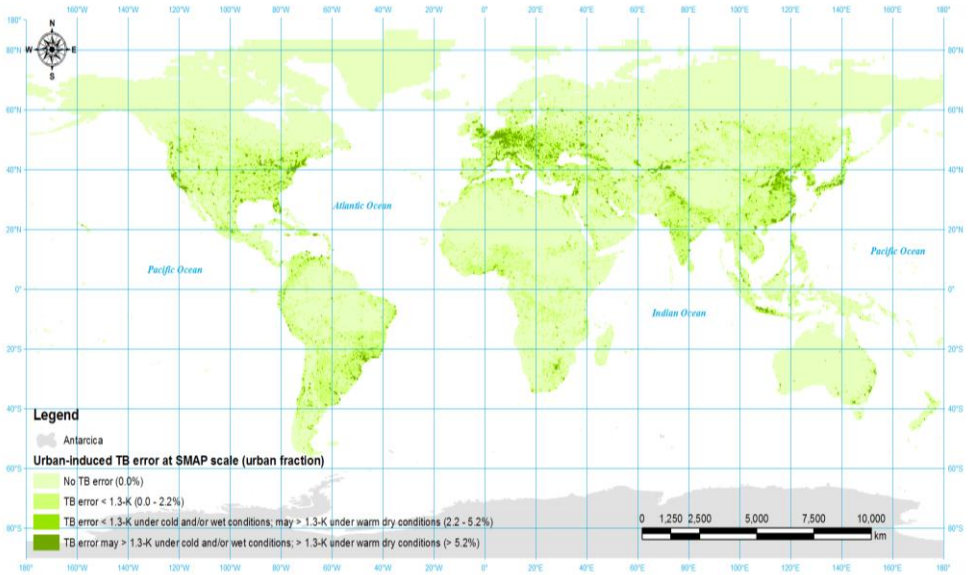

Figure 6.8: Distribution of urban impacted pixels of SMAP over global land mass.

budget under warm dry conditions, reducing to ~0.5% under cold and/or wet conditions, while urban induced brightness temperature potentially exceeds the 1.3 K budget over ~5% SMAP pixels under warm dry conditions, and over ~2% SMAP pixels under cold and/or wet conditions. According to the distribution of urban impacted pixels of SMOS (Figure 6.7) and SMAP (Figure 6.8), the urbanization ratio is not globally uniform and the area with higher density of urban area has more significant urban impact on soil moisture retrieval. The fraction of urban affected pixels were calculated for each individual continent and listed in Table 6.3. For more developed and populated areas, such as Europe, up to 4.5% of SMOS and 14% of SMAP pixels are expected to have urban-induced brightness temperature errors in excess of their radiometric error budgets.

6.6 Chapter summary

This chapter has examined airborne brightness temperature observations over seven cities that have been imaged during three field experiments. Their urban induced brightness temperature impact from the natural background brightness temperature was compared with an urban extent map, showing that urban areas can lead to a brightness temperature of 20 to 50 K lower than the surrounding soil does under dry (with soil moisture less than 0.15 m^3/m^3) and warm conditions, while this brightness temperature difference reduces to less than 20 K under wet or cold conditions. Subsequently, the urban cover fraction thresholds were obtained for the radiometric error budgets of SMOS and SMAP, and these thresholds used to identify the SMOS and SMAP pixels globally that are expected to possibly have non-negligible urban induced brightness temperature impacts under the assumptions of this analysis.

7 The effect of water cover fraction

7.1 Chapter introduction

Since the microwave emission from standing water is significantly different to that of natural land surfaces, standing water within a passive microwave footprint is expected to have a big impact on the observed microwave response. Moreover, standing water has a high temporal variability, due to events such as floods and seasonal variation of lake levels, and in some places there are many small ponds that are not mapped but cover a substantial fraction of the land surface. If the water fraction is known it can be corrected, but how well does this dynamic land surface characteristic need to be known before substantial errors in the derived soil moisture will arise? Consequently, this chapter investigates the water fraction effects on brightness temperature and soil moisture retrieval accuracy, using airborne L-band brightness temperature data collected during three Australian field experiments. The water induced brightness temperature effect and water fraction are compared under different resolutions, sampling days, and land surface conditions, and an water fraction threshold determined. Subsequently, this threshold is applied to a MODIS derived water fraction dataset for Australia over the period 2001 to 2010 to estimate the SMOS pixels expected to be adversely affected by dynamic water fraction deviations from a static water fraction map.

7.2 Data sets and study areas

This study uses airborne passive microwave observations at L-band together with coincident ground sampling data collected during three field experiments. The National Airborne Field Experiment in 2006 (NAFE'06; Merlin et al., 2008) and Australian Airborne Cal/val Experiments for SMOS (AACES-1 and -2; Peischl et al., 2012b) were conducted in the Murrumbidgee River Catchment, southeast of Australia and described in Chapter 3. Figure 7.1

shows the location of the study areas, monitoring stations, flight lines, and calibration lakes of all three experiments, which are relevant to this study. In the calibration lakes of these experiments, Tombullen water storage for NAFE'06 and Lake Wyangan for AACES, a floating monitoring station was installed in the centre of the lake for continuous measurement of surface water temperature and salinity during the whole period of each campaign. The middle panels of Figure 7.2 and Figure 7.3 illustrate the time series of water

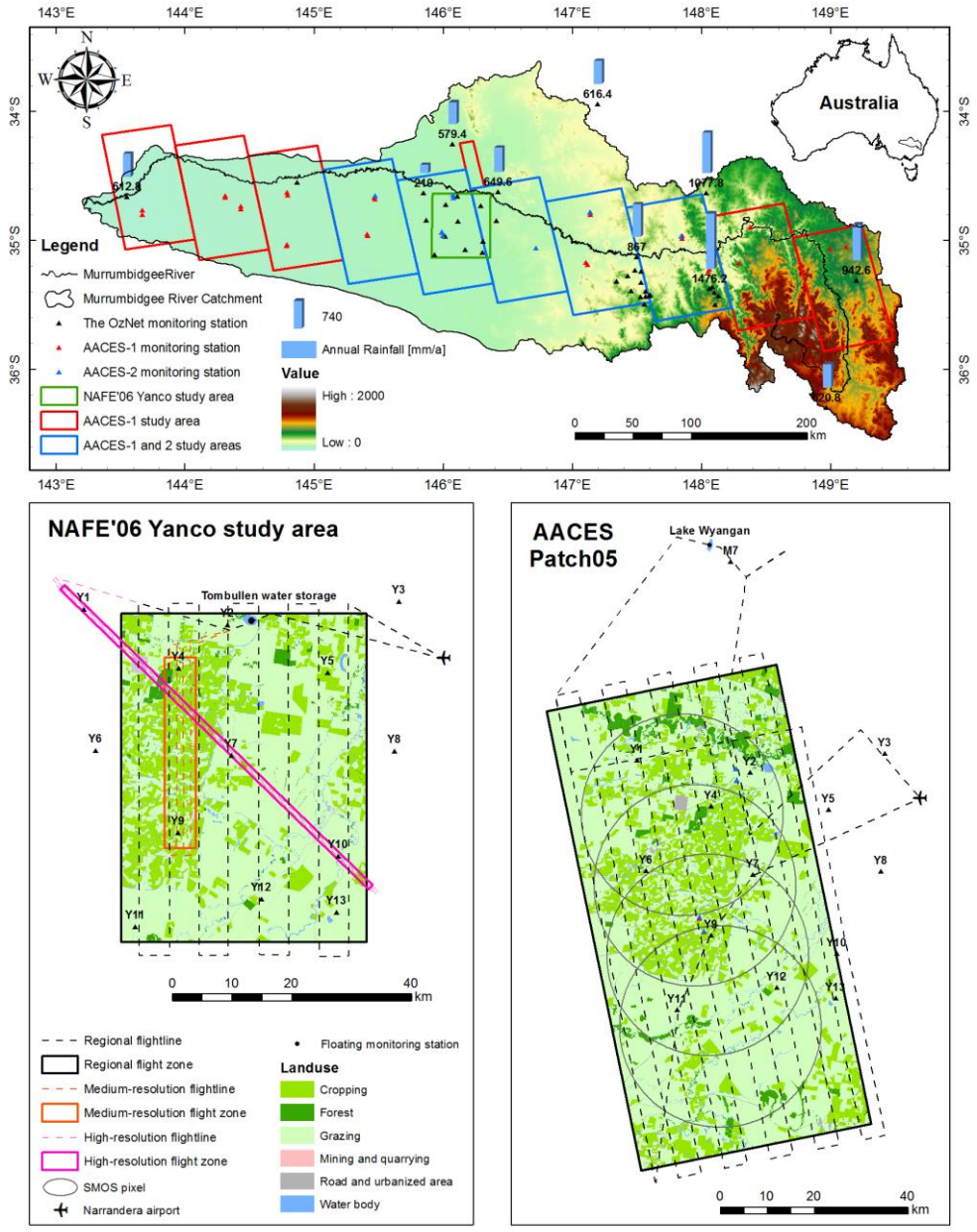

Figure 7.1: Location of the NAFE'06 and AACES study areas in the Murrumbidgee River Catchment, southeast of Australia. Location of calibration lakes is shown in the lower panels.

salinity and temperature. Additionally, the spatial variability of surface water temperature and salinity was examined by making point-based measurement transects from a boat. This transect sampling was conducted once a week during the NAFE'06 and the AACES campaigns. The transect measurements showed small variations of water surface temperature (±2 K) and salinity (±4 ppm) across the calibration lakes, which could induce a brightness temperature uncertainty of less than 3 K on brightness temperature of water bodies. Given the up to 100 K brightness temperature difference between water and soil contributions, this could be ignored for the analysis conducted in this chapter, and so the calibration lakes were assumed as homogeneous water bodies in this study.

To investigate the effects of water fraction, the information about distribution

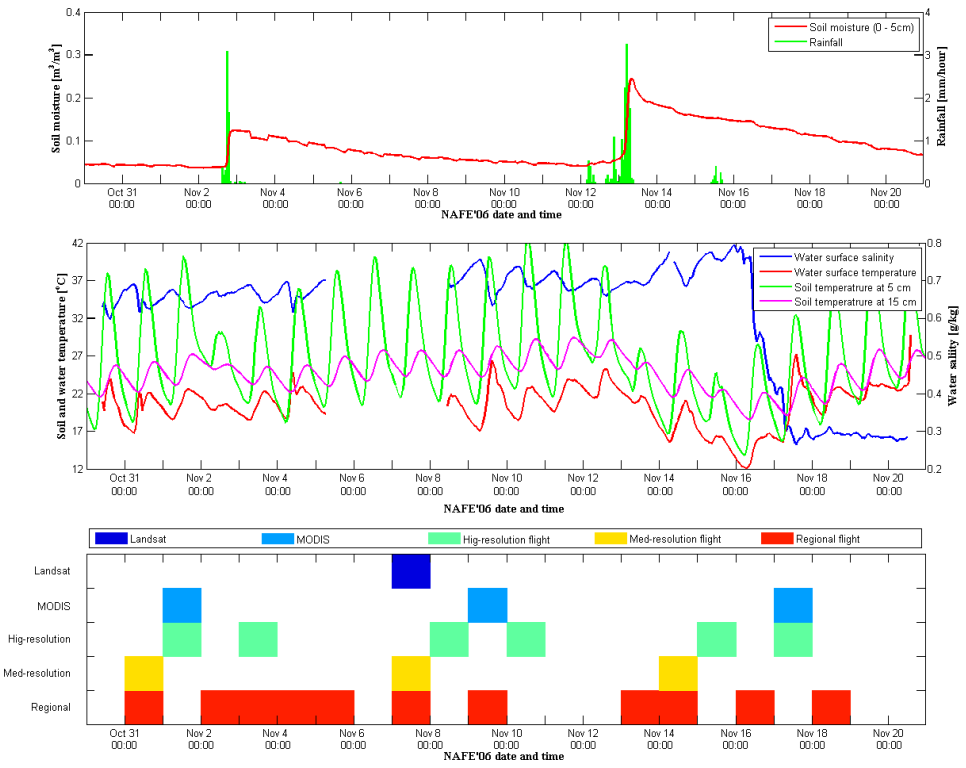

Figure 7.2: The NAFE'06 time series of spatially averaged soil moisture and rainfall measurements across all OzNet monitoring stations within the Yanco study area (upper panel), time series of water surface salinity and water surface temperature of Tombullen water storage, together with soil temperature measurements collected from Y2 site (middle panel), and timetable of Landsat overpass, MODIS overpasses, and PLMR flights at multiple resolutions (lower panel).

of open water bodies is required. Currently, a number of methods have been developed to extract inland water extent using remotely sensed visible/infrared (e.g., Landsat, Moderate-Resolution Imaging Spectro-radiometer (MODIS), and Systeme Probatoire d'Observation de la Terre (SPOT)) and SAR observations (e.g. RADARSAT, JERS-1, and ERS) (Brakenridge et al., 2005, Mertes, 2002, Papa et al., 2006, Prigent et al., 2001, Smith, 1997). Although microwave sensors are able to penetrate clouds and vegetation layer, the application of SAR (active microwave remote sensing) to discriminating water targets is adversely affected by the wind roughening effect (Alsdorf et al., 2007), and space-borne passive microwave sensors suffer from their coarse spatial resolution (Sippel et al., 1994, Smith, 1997). In contrast, mapping open water bodies is more straightforward using visible/infrared observations, and four methods have been developed including: thematic classification method, linear unmixing model, single-band thresholding method, and spectral water index method (Ji et al., 2009).

The spectral water index is one of most widely used water detection methods, which defines an index derived from the ratio, difference, or normalised difference of reflectance observations at two or more visible/infrared bands (Ji et al., 2009). A threshold of the index is then set to distinguish inland water bodies from other land surface targets based on the spectral signature of water. McFeeters (1996) proposed a Normalised Difference Water Index (NDWI) to delineate inland open water, given as

$$\mathrm{NDWI} = \frac{R_{green} - R_{NIR}}{R_{green} + R_{NIR}}, \tag{7.1}$$

where R is reflectance, and the subscripts $green$ and NIR indicate green and near infrared bands. Since the reflectance of water is higher at green band than at near infrared band, which is usually opposite to soil and vegetation, water targets usually have positive NDWI values while those for soil and vegetation targets are negative. However, the NDWI of built-up areas were also found positive, which confuse the separation of water bodies from urbanized areas using the NDWI method (Xu, 2006). Therefore Xu (2006) modified Eqn. (7.1)

by replacing near infrared reflectance R_{NIR} to shortwave infrared reflectance R_{SWIR} as

$$\text{MNDWI} = \frac{R_{green} - R_{SWIR}}{R_{green} + R_{SWIR}}. \tag{7.2}$$

The Modified NDWI (MNDWI; Xu, 2006) was found to have a better performance than the NDWI on delineating water body from built-up areas, soil, and vegetation targets, as the MNDWI of built-up areas is negative and the MNDWI is more distinguishable than the NDWI for water bodies. The MNDWI method also showed a higher classification accuracy and kappa statistics than the NDWI method over lake water, sea water, and river water (Xu, 2006). Generally, the thresholds of spectral water indices, including the NDWI and MNDWI, are location specific depending on the sub-pixel non-

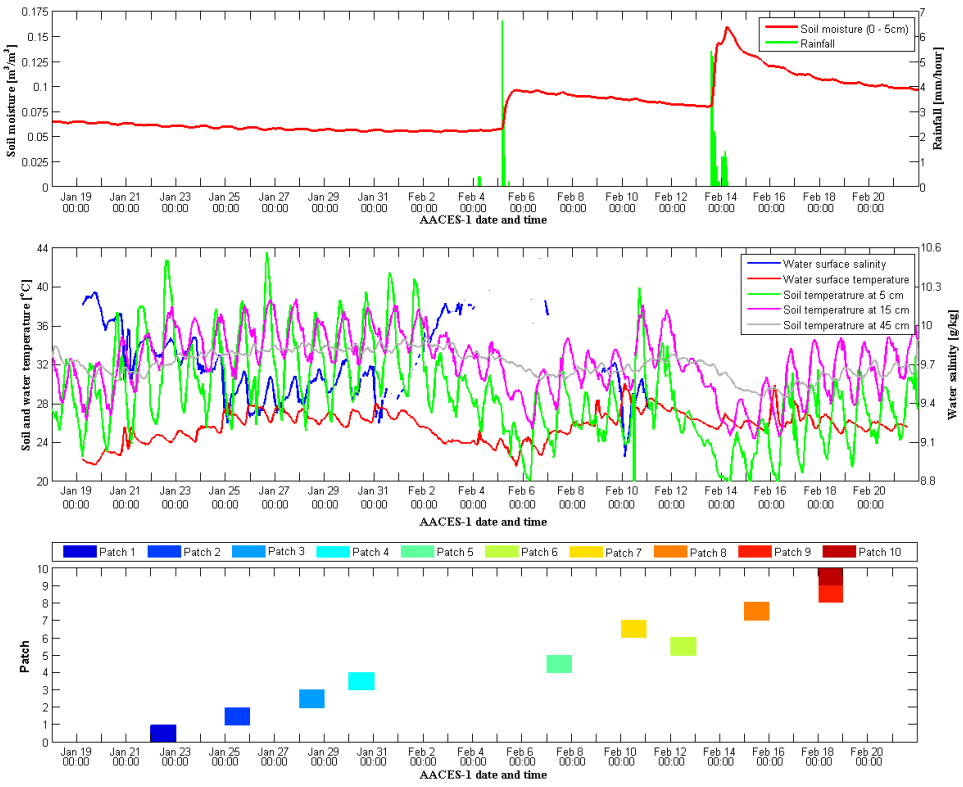

Figure 7.3: The AACES-1 time series of soil moisture and rainfall measurements collected from the monitoring stations in Patch 05 site (upper panel), time series of water surface salinity and water surface temperature of Lake Wyangan, together with soil temperature measurements from M7 site (middle panel), and timetable of the AACES-1 flights (lower panel).

water component, and need to be manually adjusted for each scene. According to a synthetic analysis on the dynamic of water index thresholds (Ji et al., 2009), MNDWI has more stable thresholds than other water indices. Therefore, the MNDWI method was applied in this study to extract water cover information over the Yanco study area from a 30-m Landsat image acquired on November 7th, 2006.

Although the MNDWI data derived from high resolution space-borne visible/infrared observations have high classification accuracy, their applications are limited by their low revisit frequencies (~30 days on average). For the purpose of estimating the effect of the standing water dynamic spatial distribution, an 8-day cloud free water fraction dataset were used (Guerschman et al., 2011). This MODIS water fraction dataset was developed by the Commonwealth Scientific and Industrial Research Organisation (CSIRO) in Australia. The water fraction in a ~500-m grid was estimated from the MODIS visible/infrared data using a classification method which was developed by performing a series of simultaneous classifications using higher resolution Landsat TM data, via on a image segmentation algorithm (Mueller and Lymburner, 2010). The 500-m water fraction data are available over the entire Australia since the launch of the MODIS in 2000, and the data for ten years (2001 to 2010) were used in this study.

7.3 Approach

The effects of water fraction on SMOS and SMAP brightness temperature observations and soil moisture retrieval accuracy were investigated in three steps as follows:

i) assess the accuracy of the MNDWI derived water cover map from a Landsat image along with the MODIS water fraction data, using the High and Regional resolution brightness temperature observations collected from the NAFE'06 and AACES;

ii) examine the effect of water fraction on brightness temperature, using the multi-resolution and multi-temporal observations collected from the NAFE'06,

as well as the AACES observations collected from multiple land surface conditions; and

iii) identify the SMOS pixels potentially affected by standing water over Australia, using a water fraction threshold for the SMOS/SMAP target accuracy of 0.04 m^3/m^3.

7.4 Assessment of water cover and fraction maps

The multi-angular brightness temperature observations over water-free areas and the High resolution brightness temperature observations over Tombullen water storage collected during the entire NAFE'06 were grouped for incidence

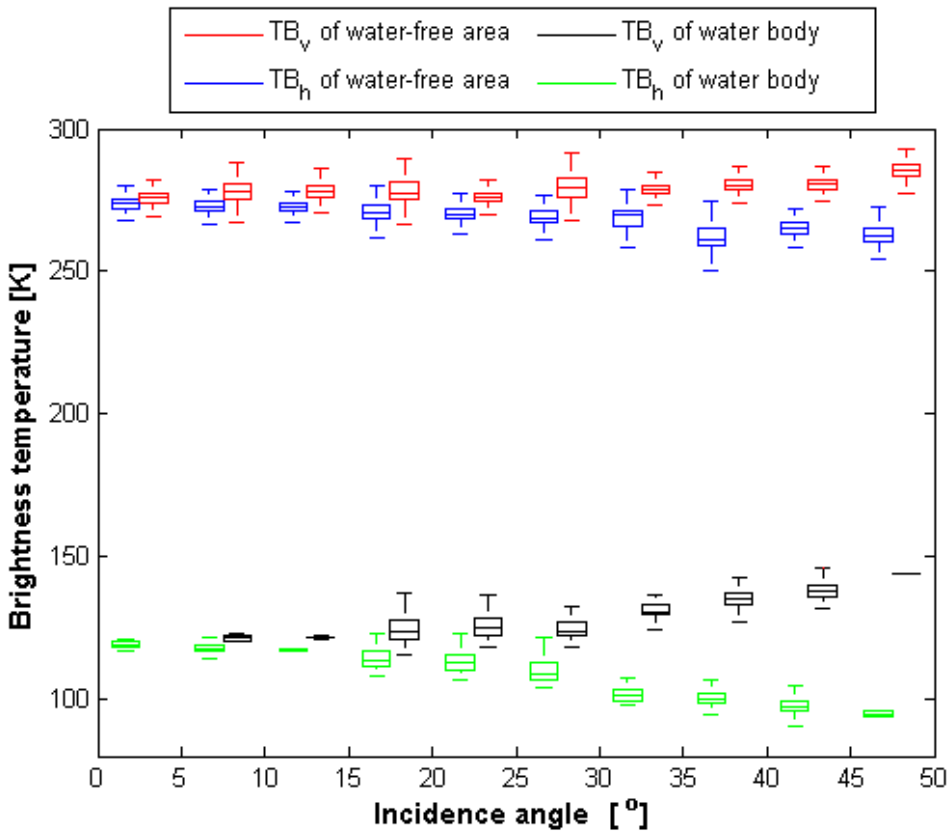

Figure 7.4: The angular relationship of dual-polarised brightness temperature observed over water-free areas during the multi-angular flights and over Tombullen water storage during the Regional flights within the entire period of the NAFE'06. The brightness temperature observations are grouped in 5° steps. The box and whisker illustrate the distribution of brightness temperature observations in each incidence angle step. The central mark and the edges of the box are the median, the 25th and 75th percentiles. The whiskers show the most extreme data points without consideration of outliers.

angles from 0° to 50° in 5°steps and plotted in Figure 7.4. It is clear that a brightness temperature difference of ~150 K exists between water bodies and a nominal land surface. While Figure 7.2 shows the soil moisture, soil temperature, water salinity and water temperature variation during the NAFE'06, the box and whisker plot in Figure 7.4 shows the corresponding brightness temperature impact for the water body and land surface over the Yanco study area during the same period. Consequently, a conservative brightness temperature threshold of 120 K in horizontal polarisation and 150 K in vertical polarisation was determined at the reference incidence angle of 38.5°, to distinguish homogeneous water pixels from those for soil surfaces. Consequently, a binary (0 for water-free pixel or 1 for water fully covered pixel) water cover map was generated from the NAFE'06 High resolution brightness temperature observations, and used as the reference to assess the accuracy of the water cover maps derived from the Landsat data using the MNDWI method.

This threshold method is however unsuitable for the brightness temperature observations at the Medium and Regional resolutions, due to the individual open water bodies in the Yanco study area typically being on order of ~100 m across, meaning that most of the pixels at these scales were either water-free or only partially covered with standing water. Moreover, the limited sampling area covered by the High resolution (50-m) brightness temperature observations meant that its derived water cover map could not be used to assess the accuracy of the 500-m resolution MODIS water fraction map. Thus, the Landsat-derived water cover map acquired on November 7th 2006 using the MNDWI approach was used for validation of the MODIS water cover fraction product. However, the Regional resolution brightness temperature observations collected during the NAFE'06 and AACES were used to verifying the accuracy of the MODIS water fraction indirectly, by assessing the correlation between its water fraction and the water induced brightness temperature offset.

According to the bottom panel of Figure 7.2, there is only one Landsat overpass during the NAFE'06 campaign, being on November 7th, 2010 when

no High resolution brightness temperature observations were collected. However, as the upper panel of Figure 7.2 shows that there was no rainfall event between November 7th and 8th, and that the open water bodies within the Yanco study area were understood to be temporally consistent during such short time periods, it was assumed that a water cover map derived from the Landsat image on November 7th would reflect the conditions on November 8th. Figure 7.5 shows the brightness temperature and Landsat-derived water cover maps. The gray colour indicates the areas where brightness temperatures were observed using the PLMR, and thus compared at pixel level using the two methods. The comparison shows a 98.25% agreement between observed pixels using the brightness temperature threshold and the MNDWI methods. Therefore, the accuracy of the water cover map derived from the Landsat data using the MNDWI method was confirmed and the water cover map on November 7th, 2006 used to identify pixels fully covered with standing water.

The Landsat derived water cover map was integrated to 500-m resolution, and used as the reference to access the accuracy of the MODIS water fraction dataset. The Landsat derived water cover map had a good agreement to the MODIS water fraction dataset at scales from 5 km to 40 km. The Regional

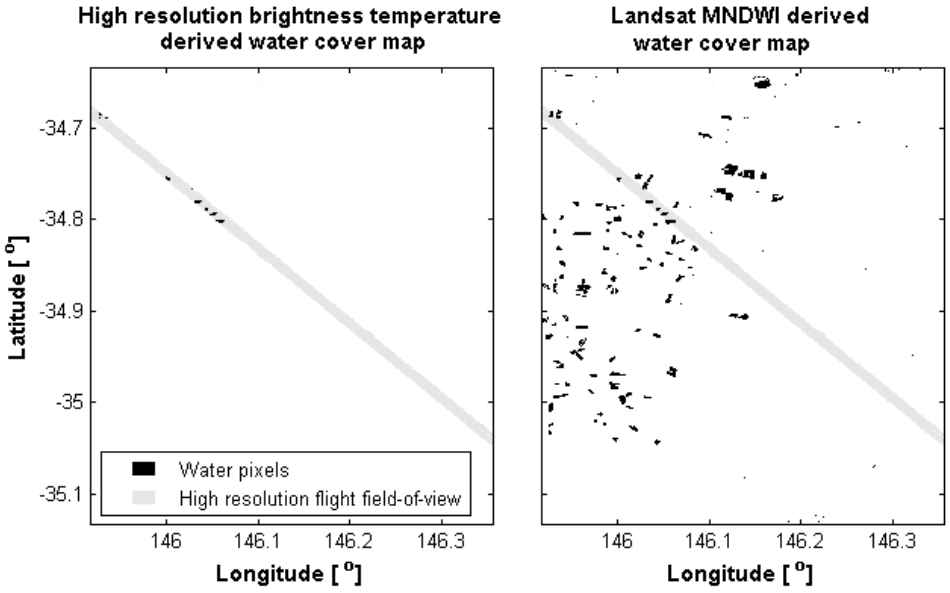

Figure 7.5: The water cover maps derived from the airborne High resolution brightness temperatures using the threshold method and the Landsat visible/infrared data using the MNDWI method over the Yanco study area.

resolution brightness temperature observations made during the NAFE'06 and AACES campaigns were sampled to a 1-km grid that overlays the 500-m grid of the MODIS water fraction dataset. The corresponding MODIS water fraction data were also integrated to the same spatial resolution and compared with the corresponding brightness temperature data. Figure 7.6 shows an example brightness temperature map at horizontal polarisation together with the MODIS water fraction map for November 9th, 2006. It is clear that the two maps have a similar pattern between the pixels with standing water coverage and the pixels with lower brightness temperature values.

7.5 Verification using real observations

The water fraction effects on brightness temperature, and thus the derived soil moisture retrieval accuracy, were studied using brightness temperature observations collected under multiple scales, sampling dates, and land surface conditions during the NAFE'06 and AACES campaigns.

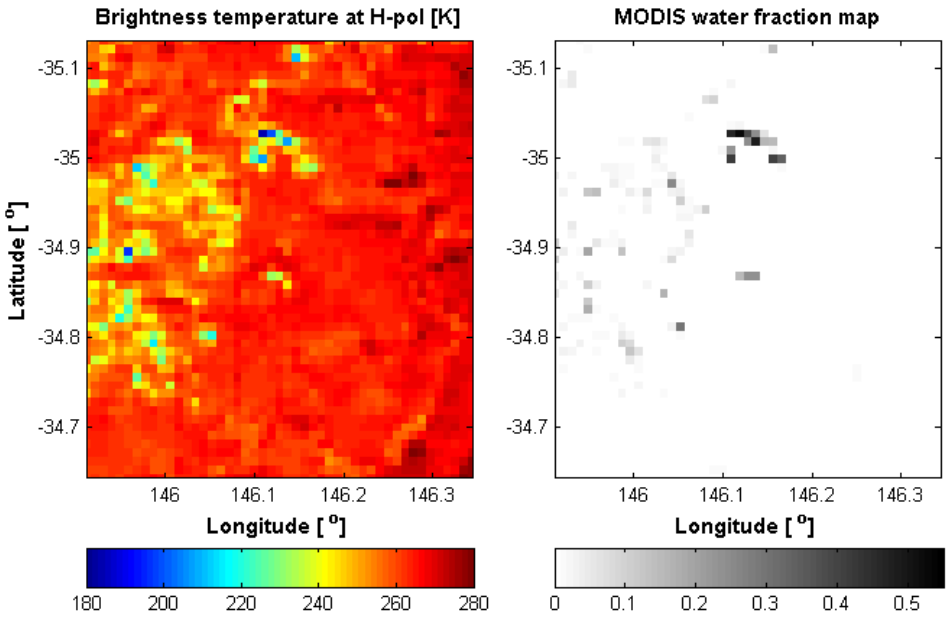

Figure 7.6: Maps of airborne brightness temperature observations at horizontal polarisation and MODIS-derived water fraction data over the Yanco study area on November 9th, 2006.

7.5.1 Water fraction effects at multiple scales

To decouple the impact of scale from those of other factors, multi-resolution brightness temperature observations were used for the same area and sampling day. However, only the Regional and Medium resolution flights were conducted on November 7th, 2006, when the Landsat-derived water cover data were available. However, as explained earlier the distribution of standing water can be assumed similar between November 7th and 8th. Additionally, the time series of top 5cm soil moisture measurements in Figure 7.2 show nearly consistent soil moisture measurements between these two days. The middle panel of Figure 7.2 also shows the similar diurnal variation of soil temperature at the depth of 5 cm and 15cm. Although the water temperature and salinity

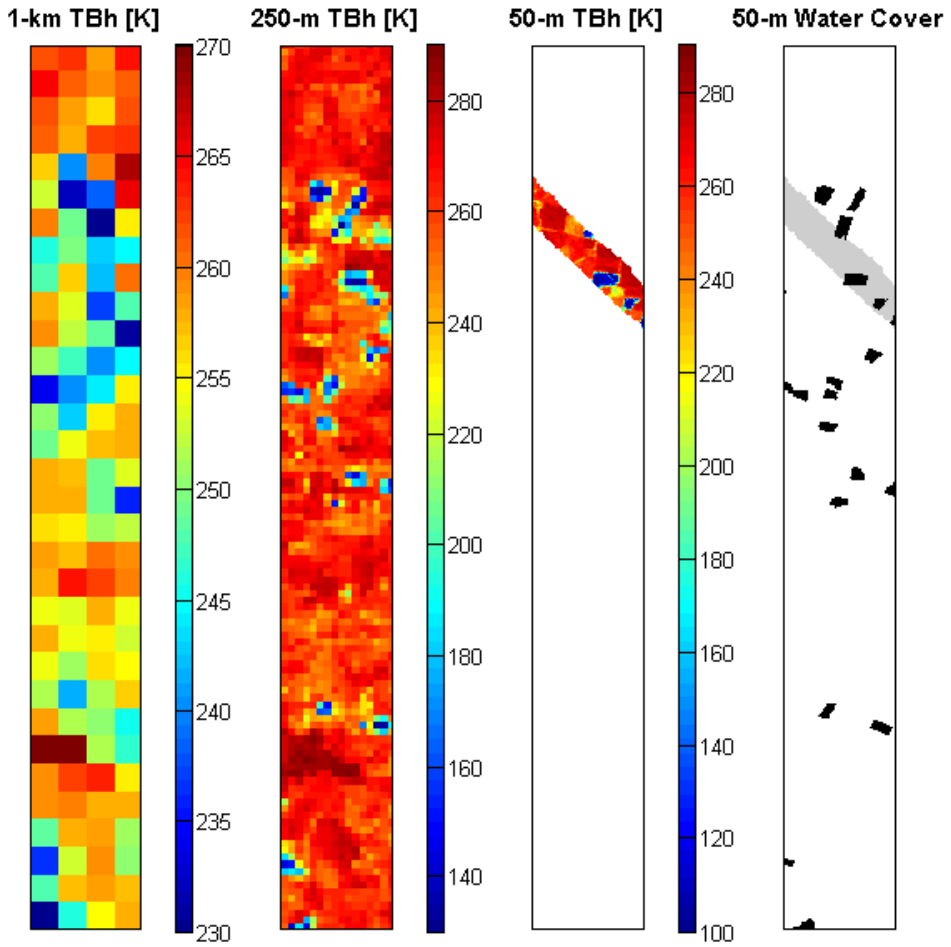

Figure 7.7: Horizontally polarised brightness temperature observations at multiple resolutions, together with the Landsat derived water cover data using the MNDWI classification method. Data are plotted for the Medium resolution flight zone in the Yanco study area.

measurements were missing between November 7th and 8th, the adjacent data suggest that it is reasonable to assume the salinity of the calibration lake was stable before November 17th, and the variation of surface water temperature similar, since its time series pattern was very close to that of 15-cm depth soil temperature. Hence, the High resolution PLMR observations collected on November 7th were assumed the same as what would have been observed on November 8th.

Subsequently, the multi-resolution brightness temperature observations were sampled to the nested grids, by selecting the brightness temperature of the closest observation to the centre point of the given pixel. The water cover fraction map for each scale was generated by sampling the 30-m Landsat-derived water cover map using the MNDWI method with a threshold of zero (Xu, 2006). However, when calculating the water fraction using high resolution Landsat data, it was found that the effect of PLMR footprint and antenna pattern had to be accounted for.

The field-of-view of the PLMR varies with viewing angle such that the field-of-view of inner beams (7°) is about 2 times smaller than that of outer beams (38.5°). Simply averaging the Landsat-derived water fraction within the brightness temperature observation grid generally induced an underestimation of the effective water fraction over the Yanco study area, especially at the Regional resolution and for inner beams. In addition, the antenna sensitivity is reduced from ~20 dB at the centre point of the nominal field-of-view to 3 dB at the edge. Therefore, a weight function was established in this study to account for the observation footprint and the antenna pattern during calculating water fractions of brightness temperature observation pixels. These issues are particularly significant here because of the large brightness temperature difference between water and the land surface.

The weighting method is as follows. For a given brightness temperature pixel with the centre point (x_0 , y_0), a Landsat-derived water fraction pixel (x_{water}, y_{water}) within the footprint should follow the condition that

$$\frac{(x_0 - x_{water})^2}{a_w^{\,2}} + \frac{(y_0 - y_{water})^2}{b_w^{\,2}} \le 1, \tag{7.3}$$

where a_w and b_w are the semi-major and semi-minor radii of the PLMR elliptic field-of-view in x and y directions respectively. According to the PLMR manual (i.e. ProSensing Inc., 2005), the amplitude of the PLMR antenna field-of-view ranges from 3 dB to 20 dB. Therefore, an elliptical weight (W) function was determined as

$$W = 10^{0.3} + (10^2 - 10^{0.3}) \cdot \sqrt{1 - \frac{(x_0 - x)^2}{a^2} - \frac{(y_0 - y)^2}{b^2}}\,. \tag{7.4}$$

The water fraction of each PLMR brightness temperature pixel (f_{PLMR}) can then be calculated from 30-m Landsat-derived binary water cover data within the footprint, as

$$f_{PLMR} = \frac{\sum W(x,y) \cdot f_{Landsat}(x,y)}{\sum W(x,y)}\,. \tag{7.5}$$

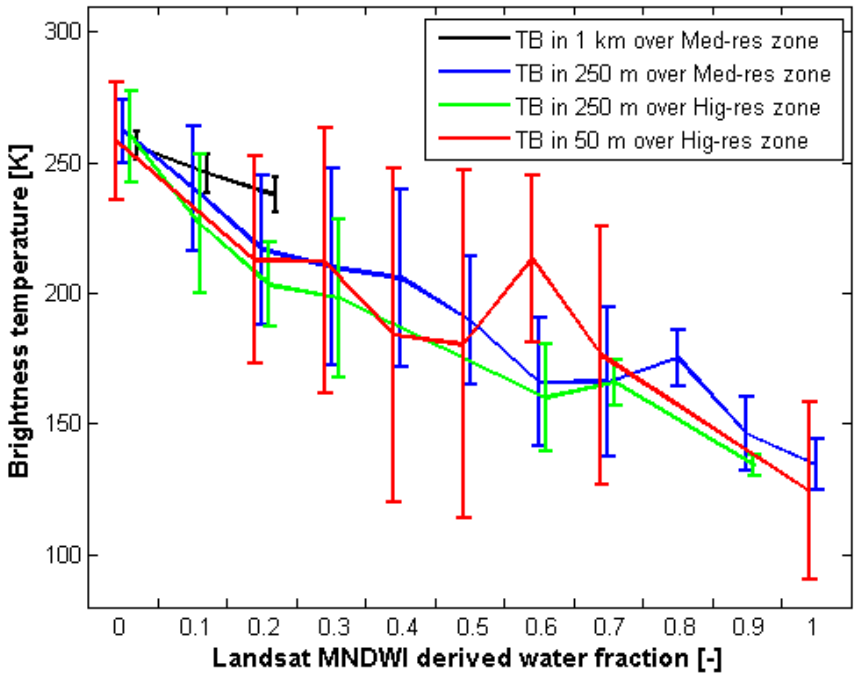

Figure 7.8: Relationship between pixel water fraction and mean brightness temperature for the overlapping areas of the High, Medium, and Regional resolution flights within the Medium and High resolution flight zones. The whiskers show the standard deviation of brightness temperature observations for each water fraction step.

Figure 7.7 shows the Regional, Medium, and High resolution brightness temperature observations at horizontal polarisation, and the water cover map derived from the Landsat data for November 7th, 2006 over the NAFE'06 Medium resolution flight area. A good agreement between the distribution of brightness temperature and that of standing water was found, with the areas identified as water bodies having a very low brightness temperature compared to the surrounding water-free areas. Subsequently, the multi-resolution PLMR brightness temperature observations over the NAFE'06 Medium resolution flight area were compared with corresponding water fraction maps at pixel level. The comparison results are shown in Figure 7.8, with whiskers indicating the standard deviation of brightness temperature observations at each water fraction interval. Since the heterogeneity of brightness temperature increases with spatial resolution, the standard deviation of High resolution brightness temperature is significantly larger than those of Medium and Regional observations.

As expected, all four poly-lines representing the three resolutions within the overlapped areas show a decrease of the brightness temperatures with increasing pixel water fractions. Moreover, the slopes of brightness temperature to water fraction are similar among the Regional, Medium, and High resolution data with only a small bias between them, which might be due

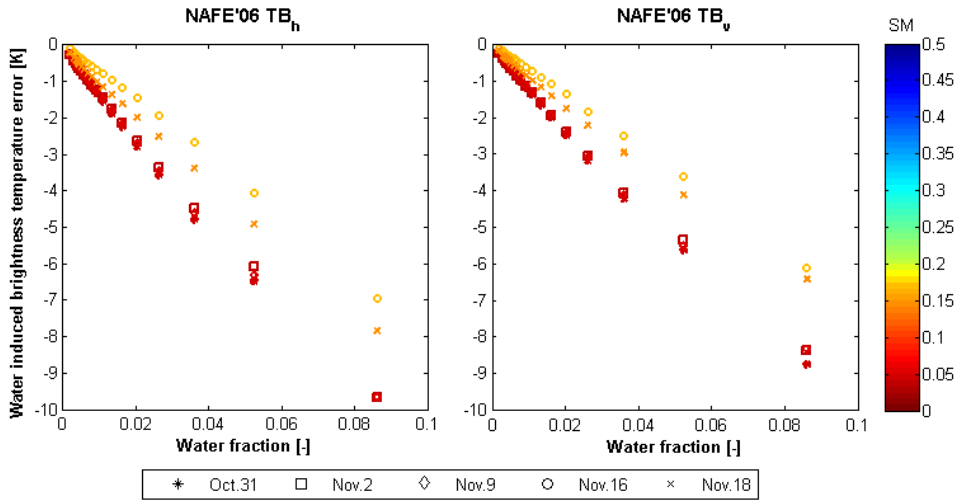

Figure 7.9: The relationship between water fraction and water induced brightness temperature impact, using the NAFE'06 multi-temporal observations in dual-polarisation.

to the change of soil surface temperature between the different resolutions flights. Therefore, the effects of water fraction on brightness temperature, and thus the impact on soil moisture retrieval accuracy were shown to be independent of observation scale. Consequently, the effects of water fraction at the SMOS/SMAP scale can be studied using the Regional resolution brightness temperature observations hereafter.

7.5.2 Water fraction effects at multiple times

During the NAFE'06, a total of 11 Regional resolution flights were conducted over the entire Yanco study area, and used here to investigate the temporal variation of water fraction effects. Given the 500-m spatial resolution and 8 day composite of MODIS-derived water fraction data, the water fraction data were integrated to the 1-km Regional grid and compared with the Regional resolution brightness temperature observations collected on the same day or one day before/after, providing no rainfall event was recorded.

To obtain the relationship between water fraction and its effect on brightness temperature at SMOS/SMAP scale, a moving window technique was applied to simulate the SMOS and SMAP 40-km brightness temperature observations with varying water fractions. The Regional resolution brightness temperature

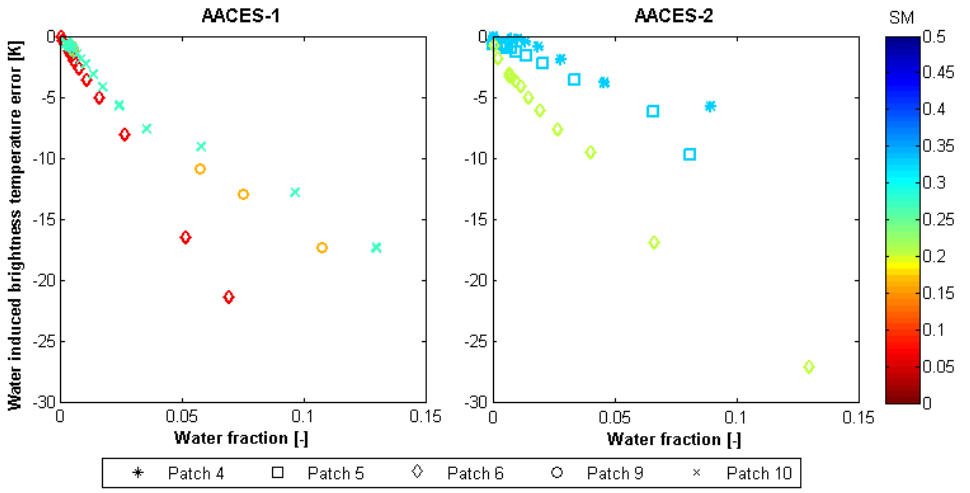

Figure 7.10: The relationship between water fraction and water induced brightness temperature impact, using the AACES multi-spatial observations in horizontal polarisation.

and MODIS water fraction of all 1-km pixels within a 40 km × 40 km window were averaged to simulate the SMOS/SMAP brightness temperature observations TB_{SMOS} and their water fractions f_{water} respectively. Meanwhile, the mean brightness temperature of water-free pixels TB_{free} was assumed as the reference SMOS/SMAP brightness temperature observations without water fraction effects. Hence, a water induced brightness temperature offset (ΔTB_{water}) on the interpretation of brightness temperature observations can be defined as the difference between TB_{SMOS} and TB_{free}. By moving the 40 km × 40 km window within the Yanco study area, a limited range of water fraction (< 0.003) were obtained, which is insufficient to cover the water fraction threshold for the SMOS/SMAP error budget. For a wider range of water fractions, the size of the moving window was reduced gradually to 5 km, assuming that the water fraction effects obtained from a smaller scale are the same as those at the 40-km scale. The reasonableness of this assumption has been confirmed from the multi-resolution study.

The Figure 7.9 presents the relationship between water fraction and water induced brightness temperature offset at horizontal and vertical polarisations using the NAFE'06 Regional resolution brightness temperature observations and MODIS water fraction data. The symbol colour indicates the mean soil moisture measurements across the OzNet monitoring stations within the Yanco study area. As expected, standing water induces a negative brightness temperature offset at both polarisations, whose magnitude varies linearly with increased pixel water fractions. Compared with vertically polarised brightness temperature, brightness temperature at horizontal polarisation is slightly more sensitive to standing water. Since these multi-temporal brightness temperature observations were collected over the same area during about three weeks, soil texture and vegetation water content can be assumed constant, and the variation of slope dependent mainly on soil moisture. The dryer the surrounding soil the larger the water induced brightness temperature offset observed, which is in agreement with the simulation results. According to Figure 7.9, approximately every 0.1 increase in water fraction results in a 10-K

Table 7.1: Statistics of water fraction and induced brightness temperature offset of SMOS sized pixels over Australia according to Figure 7.11.

Water fraction range [0.01]	Estimated water induced brightness temperature impact [K]	Percentage of pixels in range for the minimum water fraction mask [%]	Percentage of pixels in range for the maximum water fraction mask [%]	Percentage of pixels in range for the mean water fraction mask [%]	Percentage of pixels with a water fraction variation in the range [%]
0	0	89.5	0.0	0.0	0
0 – 0.01	0 – 0.005	5.9	0.0	3.0	0
0.01 – 0. 1	0.005 – 0.05	3.6	0.0	55.5	0.04
0. 1 –1	0.05 – 0.5	0.9	20.4	34.7	22.4
1 – 5	0.5 – 2.5	0.0	57.7	5.2	57.3
5 – 10	2.5 - 5	0.0	9.8	0.7	9.1
10 – 20	5 - 10	0.0	6.3	0.5	5.9
20 – 40	10 – 20	0.0	3.7	0.3	3.5
40 – 60	20 - 30	0.0	1.3	0.1	1.1
60 – 100	30 - 50	0.0	0.9	0.0	0.6

brightness temperature offset under dry conditions. For a 4-K brightness temperature error budget, being the target for SMOS, a water fraction of 0.04 can be tolerated in soil moisture retrieval providing all other factors are minimal.

7.5.3 Water fraction effects for multiple land conditions

The effects of water fraction were further investigated under a wider range of soil and vegetation conditions, using the AACES Regional resolution brightness temperature observations. The moving window technique was again used to establish the relationship between MODIS-derived water fraction data and water induced brightness temperature offset for each AACES patch. To minimize the effect of land surface heterogeneity, only the patches with a water body larger than 1.25 km^2, taking a fraction of 0.05 in a 5 km $\times$ 5 km pixel, were considered. The water fraction effect on brightness temperature at horizontal polarisation was plotted in Figure 7.10. The soil moisture in the plot was taken as the mean soil moisture measurement across AACES monitoring stations within each patch. It is again clear that the ratio between water fraction and induced brightness temperature uncertainty decreases with increase in soil moisture. Compared with the NAFE'06, the effect of water fraction was larger under the AACES-1 hot summer conditions, where every 0.1 increase in water

fraction would induce an approximately 20-K brightness temperature offset. During the AACES-2 when water vegetation content was higher and soil temperature was lower than in the AACES-1, the water fraction offset was still mainly dependent on soil moisture. Consequently, every 0.1 increase in water fraction can induce a brightness temperature offset ranging from 30 K under hot dry conditions to only 5 K under wet cold conditions. Accordingly, the water fraction threshold for the 4-K error budget varies from 0.013 to 0.08 for dry soil to wet soil conditions respectively.

7.6 Water impact map

Using the MODIS water fraction data for years 2001 to 2010, the water effects that would have been expected on brightness temperature, and thus derived soil moisture retrieval accuracy, over the entire Australia were estimated at the SMOS/SMAP scale. Due to the similar pixel size of the SMOS 45-km DGG (Discrete Global Grid; Sahr et al., 2003) and SMAP 36-km EASE (Equal-Area Scalable Earth; Brodzik et al., 2012) grid, only the results in the SMOS grid are presented. For the MODIS-derived water fraction data of each sampling day,

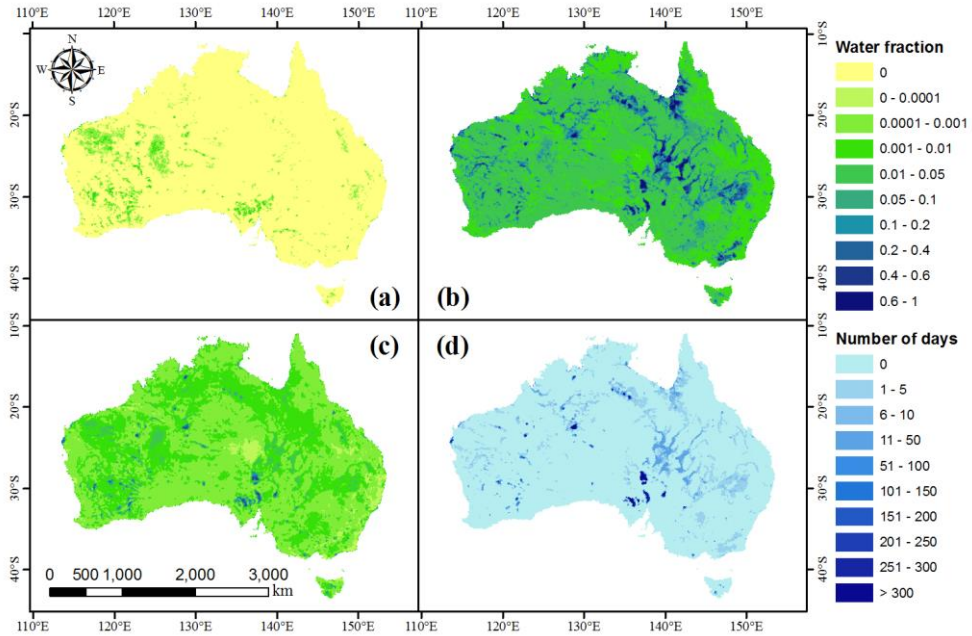

Figure 7.11: Maps of minimum (a), maximum (b), and mean (c) water fractions of 40-km sized pixels over Australia during the years from 2001 to 2010. Panel (d) shows the number of days when water fraction of each pixel exceeded the 0.08 water fraction threshold.

Table 7.2: Statistics of water effected pixels at SMOS scale over Australia for 2001 to 2010.

Number of days	0	1 - 5	6 - 10	11 - 50	51 - 100	101 - 150	151 - 200	201 - 250	251 - 300	> 300
Number of pixels	33514	3426	550	779	96	29	46	21	33	123
Percentage of pixels [%]	86.8	8.9	1.4	2.0	0.3	0.1	0.1	0.1	0.1	0.3

the 500-m water fraction grid were re-sampled to the SMOS grid, assuming that the pixel was a circle centered on a DGG node with a diameter of 45 km. Due to the overlapping nature of the SMOS grid, the water fraction offset is plotted on a Voronoi polygon grid generated from the SMOS DGG points.

The panels (a), (b), and (c) of Figure 7.11 show the minimum, maximum, and mean water fraction respectively of each SMOS pixel during the period 2001 to 2010. It is clear that most of Australia had a maximum water fraction less than 0.05, while some areas experienced heavy rain events leading to over 0.4 of the land surface being flooded. If a static inland water fraction map was used in the soil moisture retrieval model, to correct or flag the effect of standing water, a large uncertainty on brightness temperature and thus retrieved soil moisture could be induced by ignoring the dynamic standing water contribution. Assuming the mean water fraction as the static inland water fraction map, the largest water fraction estimation error likely to be made was approximated by the maximum water fraction shown in Figure 7.11(b), as the mean water fraction was generally close to zero.

Table 7.1 provides a statistics summary of the minimum, maximum, and mean water fraction of SMOS pixels over Australia during the ten year period 2001 to 2010. In addition, the maximum variation from the mean water fraction was also counted for each water fraction interval, and the corresponding water induced brightness temperature offset estimated. Accordingly, a water fraction of 0.08 can be taken as a conservative threshold for the 4-K brightness temperature error budget of SMOS for general soil moisture and vegetation conditions. In the worst case of maximum water fraction there were 13.5% (5227 out of a total 38617) pixels expected to have a soil moisture retrieval

error that exceeds the target accuracy of 0.04 m^3/m^3, if the mean water fraction was used as the static water fraction map. Additionally, the number of days when water fraction exceeded the 0.08 water fraction threshold is shown in Figure 7.11(d) for each pixel. According to the summary of water affected pixels in Table 7.2, although 86.8% of pixels were not affected by the presence of standing water, the standing water induced error exceeded the target accuracy more than 10 times per year on average for 0.6% (252 out of a total 38617) of pixels.

7.7 Chapter summary

This chapter has examined the impacts of standing water on brightness temperature using airborne observations and monitoring stations data collected during three field campaigns. Using NAFE'06 multi-resolution brightness temperature observations, the relationship between water fraction and brightness temperature was found to be consistent across sampling scales, confirming that the impacts of non-soil targets derived from airborne observations with a high resolution can be applied to the scale of SMOS and SMAP. Moreover, the relationship between water fraction and brightness temperature was found be related primarily to the water content of sub-pixel soil component. Under dry warm conditions, an underestimation of water fraction of 0.1 was found to induce a brightness temperature error of up to 30 K. This was verified under a range of land surface conditions using the AACES-1 and AACES-2 dataset; it was also found that the impact of water fraction is reduced under wet cold conditions, with a water fraction underestimation of 0.1 introducing a brightness temperature error of only 5 K. Subsequently, the water fraction thresholds were obtained and used to identify water affected SMOS and SMAP pixels across Australia using MODIS derived water fraction data for the period 2001 to 2010. The number of days when water fraction exceeded the threshold was also counted, showing the occurrence frequency of non-negligible standing water problems, if only a static water map was used. It should be noted that SMAP radar observations are expected to provide a capability identify water pixels and detect pixel water fraction with a tolerance level of 5% error when 10% of a 36km pixel is

occupied by water bodies. This capacity potentially limits the impact of water on SMAP brightness temperature within 2.5 K, based on analysis using a 5% water fraction uncertainty

8 Conclusions and future work

Passive microwave observations are widely accepted as the most promising approach to measure the near surface soil moisture at regional and global scales, due to its all-weather capability, direct relationship with soil moisture through soil permittivity, and reduced sensitivity to vegetation canopy and surface roughness. Therefore, the European Space Agency's (ESA) Soil Moisture and Ocean Salinity (SMOS) mission, launched in November 2009, and the National Aeronautics and Space Administration's (NASA) Soil Moisture Active and Passive (SMAP) mission, scheduled to be launched in 2014, both employ a L-band (1.41 GHz) radiometer to measure microwave emission from the land surface globally every 2 - 3 days, to retrieve the top ~5 cm soil moisture through a radiometric transfer model with a target accuracy of 0.04 m3/m3. However this technique suffers from its coarse spatial resolution, which is on the order of 40 km, due to technological limitations on current antenna technology. Moreover, the land surface is heterogeneous at such scales in most places in the world, with non-soil targets, such as urban area, standing water, and surface rock within the field-of-view. The concern is that such targets will confound the brightness temperature observations and potentially result in soil moisture retrieval error in excess of the SMOS and SMAP target accuracy if unaccounted for in retrieval algorithms.

This thesis has explored the effects of surface rock, urban area, and standing water on the accuracy of soil moisture retrieved from L-band brightness temperature observations at the scale of the SMOS and SMAP radiometers. Analysis was undertaken using airborne brightness temperature observations over SMOS and SMAP sized study areas during five field experiments across the last eight years. For each mixed-pixel, the spatially averaged brightness temperature of the soil component is defined as the reference value. Subsequently, the difference in brightness temperature between the entire pixel and the reference value is considered as the non-soil contribution, and thus the

brightness temperature contribute that is expected to adversely impact on the retrieved soil moisture.

Taking the SMOS and SMAP radiometric sensitivity of 4 K and 1.3 K respectively, and soil moisture retrieval target accuracy of 0.04 m^3/m^3 as the allowed error budgets, a cover fraction threshold was obtained for each non-soil target of interest. Finally, the SMOS and SMAP radiometer pixels with non-soil induced soil moisture retrieval error that is likely to exceed 0.04 m^3/m^3 were identified, demonstrating the possible extent of non-soil target impacts on soil moisture retrieval accuracy from space-borne L-band passive microwave observations if not appropriately accounted for in the soil moisture retrieval algorithms.

8.1 The CDF-based normalisation method

Before integrating airborne data to the scale of SMOS and SMAP pixels, the multi-angular brightness temperature observations collected in push-broom mode needed to be normalised to a fixed reference angle due to the strong dependency of microwave emission on incidence angle. However, the existing methods were found to suffer from a striping problem when applied over heterogeneous land surfaces due to their linear approximation assumptions. Consequently, a nonlinear normalisation method was developed and verified in this study using L-band airborne radiometer and radar observations collected during two Australian field experiments. The CDF-based method normalises multi-angle observations by matching the CDF of data viewed at non-reference angles. This method is based on the assumption that the observation sequence between incidence angles is consistent.

According to a synthetic study on microwave radiometer observations, the RMSE of the normalisation methods is limited to between 2 and 13 K depending on polarisation and land surface condition. The CDF-based normalisation method had the lowest RMSE of the three methods, with an accuracy which is close to the theoretical minimum. When verified on real microwave radiometer observations from two airborne field experiments (SAZE and AACES-1), the CDF-based method had the least stripping and the

highest accuracy with a RMSE improvement of up to ~5 K over the existing linear normalisation methods, when compared with independent reference data collected in transit flights. In the context of the SMOS brightness temperature error budget of 4 K, this improvement is significant when simulating space-borne observations over heterogeneous land surface with appropriate accuracy. Therefore, the CDF-based method was used to normalise all airborne brightness temperature observations used in this thesis.

8.2 The effect of rock cover fraction

The effects of surface rock on brightness temperature observations and soil moisture retrieval accuracy were examined using both synthetic data and observations collected during the SAZE field experiment. It was also confirmed that rock can be assumed as very dry bare soil with a fixed dielectric constant of 5.7-j*0.074.

Using this assumption, the microwave emission from the land surface covered with a wide range of rock fraction was simulated for various soil moisture and vegetation content conditions using the τ-ω model. The simulation results showed that the effects of rock fraction on brightness temperature and soil moisture retrieval accuracy are dependent mainly on water content of the surrounding soil. Under dry soil conditions, rock decreases the brightness temperature resulting in an overestimation of soil moisture, while under wet soil conditions it causes an increase in brightness temperature and an underestimation on soil moisture, if the presence of rock is not accounted for in soil moisture retrieval models. Moreover, for the SMOS and SMAP target accuracy of 0.04 m^3/m^3, a rock cover fraction threshold of 0.4 was obtained.

The rock effect simulations were validated using airborne passive microwave observations and ground in-situ soil moisture measurements collected from the Wirrangula Hill study area. The L-band (1.413 GHz) brightness temperature at ~100 m and top ~5 cm soil moisture point measurements within a 700 m × 3,000 m focus area was characterized as bare soil covered with sparse bush, and rock fractions of up to 1. Using a Google Earth image and ground level photographs over the study area, a relationship between gray intensity and rock

fraction was established and used to estimate the cover fraction within the focus area. Subsequently, the rock cover fraction impacts on brightness temperature and soil moisture retrieval accuracy were compared with results from the synthetic rock simulation. The comparison results showed a good agreement between observed and simulated rock effects, verifying the very dry bare soil assumption on rock and rock cover fraction threshold of 0.40 for the 0.04 m^3/m^3 error budget.

To identify the global SMOS and SMAP pixels with expected urban-induced soil moisture error in excess of the 0.04 m^3/m^3, the obtained rock fraction threshold was applied to the global rock distribution map extracted from the ECOCLIMAP dataset, which is the land surface map for the SMOS L2 retrieval algorithm. Over the land mass, approximately 1.5% of all SMOS and SMAP pixels may have significant rock induced soil moisture errors during the retrieval. Moreover, these results might be conservative as it has been assumed that the entire soil moisture error budget can be attributed to rock induced effects alone.

8.3 The effect of urban cover fraction

This study demonstrated the effect of urban area on the SMOS and SMAP brightness temperature observations using data acquired from three airborne field experiments (NAFE'06, AACES-1, and AACES-2) conducted in the Murrumbidgee River Catchment, in south-eastern Australia. The airborne brightness temperature observations at 1 km resolution over seven medium-to-large cities were used together with the Land Use: New South Wales dataset on urban areas to establish the relationship between urban-induced brightness temperature error and urban fraction.

As expected, urban induced brightness temperature error increased with urban fraction and was a function of soil moisture and temperature conditions. Moreover, a threshold of urban fraction was identified for SMOS and SMAP based on their radiometric error budgets of 4 K and 1.3 K. Under warm dry (top ~5cm soil moisture < 0.15 m^3/m^3) conditions, SMOS pixels with more than 0.066 urban fraction and SMAP pixels with more than 0.022 urban

fraction are expected to have brightness temperature impacts in excess of their error budgets. However, under cold and/or wet conditions the tolerance increased to 16.8% for SMOS and 5.2% for SMAP respectively. Notably, these tolerances are much tighter than the 0.11 ~ 0.20 tolerance suggested by earlier studies based on model simulation.

Using these thresholds, global SMOS and SMAP pixels expected to exhibit non-negligible urban-induced brightness temperature contributions in excess of the tolerated amount were identified, assuming similar microwave behaviours between the studied cities and urban areas in the other parts of the world. Using the MODIS 500-m global urban extent map, the urban fraction of SMOS and SMAP pixels were calculated globally, and the thresholds applied. Over land, approximately 2% of all SMOS pixels may have significant urban induced brightness temperature impacts, reducing to about 0.5% of pixels under cold and/or wet conditions. Similarly, SMAP is expected to have up to 5% of pixels with significant urban-induced brightness temperature impacts, reducing to about 2% under cold or wet conditions.

The study also found that for more populated continents such as Europe, there may be as many as 14% of pixels that have significant urban induced impacts, leading to soil moisture errors greater than 0.04 m^3/m^3 if urban is not accounted for in the retrieval algorithm. However, results have been extrapolated globally based on the microwave behaviour of only seven medium to large sized Australian cities, which may not be representative of the microwave response from urban areas elsewhere. Consequently, further studies of this nature should be conducted over different types of cities in other places of the world in order to validate the applicability of these results globally. Conversely, these results might be conservative as it has been assumed that the entire radiometric error budget can be attributed to urban induced effects alone.

8.4 The effect of water cover fraction

This study investigated the effect of water fraction on space-borne L-band passive microwave observations using data acquired from three airborne field

experiments (NAFE'06, AACES-1 and AACES-2), conducted over the Murrumbigee River Catchment in southeast of Australia. The airborne brightness temperature observations were used together with water fraction estimates from a Landsat-derived water mask using the MNDWI method and a MODIS-derived water fraction.

The multi-resolution brightness temperature observations in the NAFE'06 dataset were used to examine the effects of water fraction at different scales, showing an independent relationship between water induced brightness temperature uncertainties and the scale of observations. Consequently, it could be assumed that the effects of water fraction at the SMOS and SMAP scale are the same as those at smaller scales. The effect of water fraction on brightness temperature was studied at the SMOS and SMAP scale using the NAFE'06 multi-temporal brightness temperature observations. Over the same study area under consistent vegetation conditions, an obvious relationship between the water content of the soil component and the effect of water fraction on brightness temperature was obtained.

To further validate water fraction effects under a wider range of soil moisture and vegetation water content conditions, the multi-spatial brightness temperature observations collected during the AACES experiments were used. The relationships of water induced brightness temperature uncertainties and pixel water fraction obtained from both AACES summer and winter campaigns showed a high dependence of water fraction effects on soil moisture. The thresholds of water fraction obtained from field experiment data under the conditions from dry bare soil to wet vegetated soil ranged from 0.01 to 0.08.

The dynamics of water fraction effects were also investigated using MODIS-derived water fraction data for a ten year period from 2001 to 2010. The water fraction of each SMOS pixel over Australia was calculated using MODIS water fraction data. The map of mean water fraction for SMOS pixels across the ten years was used to evaluate the effects of standing water dynamic. Taking 0.08 as a conservative threshold of water fraction to achieve the SMOS and SMAP 0.04 m^3/m^3 target accuracy under general land surface conditions, there were

13.5 % pixels that may be significantly affected by water bodies in the assumed worst case when all pixels reached their maximum water fraction simultaneously. However, 86.8% of pixels were not affected by the presence of standing water, while only 0.6% of pixels had a water induced brightness temperature uncertainty that would have exceeded the threshold more than 100 times during the 2001 and 2010 period.

8.5 Recommendations for future work

The potential impact of non-soil targets on soil moisture retrieval has been demonstrated in this thesis through analysis of Australian field campaign data and modelling. The following section discusses some future work that will augment that presented in this thesis.

8.5.1 Verification in other parts of world

Since non-soil targets have different microwave responses from soil, their presence within a sensors' field-of-view might confound the brightness temperature observations, and thus degrade the soil moisture retrieval if not carefully accounted for. The impacts of surface rock, urban area, and standing water on the brightness temperature and soil moisture retrieval accuracy were demonstrated using airborne brightness temperature at L-band collected during several Australian field experiments. It was founded that the magnitude of brightness temperature and soil moisture uncertainties induced by non-soil targets are related to the land surface characteristics of the surrounding area, and are highly dependent on the temperature and water content of the soil component. However, the relationship between non-soil target cover fraction and induced brightness temperature was developed under typical Australian conditions, which might not correctly represent other parts of the world, particularly in terms of urban areas. As these thresholds have been used to extrapolate the potentially impacted SMOS and SMAP pixels globally, under the assumption that the microwave responses of non-soil targets are similar across the world, it is important that more field experiments be undertaken

and/or analysed globally to validate this result under a wider range of land surface conditions.

8.5.2 Study on joint impacts of non-soil targets

The impacts of each non-soil target were obtained individually in this thesis, and consequently the maps of SMOS and SMAP pixels where such impacts are expected to exceed tolerable limits identified individually using the cover fraction map of the given non-soil target accordingly. However, in reality more than one type of the studied non-soil targets may co-exist within the same pixel. The impacts of different non-soil targets may accumulate and induce increased uncertainties of brightness temperature and soil moisture, or counteract to reduce the induced uncertainties. For example, the presence of surface rock could result in underestimation under wet conditions, while standing water induces overestimation, meaning that the combination of surface rock and standing water impacts may cancel each other out. Therefore, the joint impacts of non-soil targets need to be examined based on the results presented in this thesis.

8.5.3 Modeling the microwave responses of non-soil targets

For better understanding the impacts of non-soil targets, the microwave characteristic of each non-soil target needs to be carefully studied, and models established to simulate their brightness temperatures. For non-soil targets with a consistent distribution and characteristics, such as rock, their microwave response could be modelled from land surface classification maps and understanding their dielectric constant and surface roughness. For non-soil targets with a varying distribution and relatively consistent characteristics, such as standing water, the modelling of their microwave contribution is fairly straightforward and depends primarily on accurate knowledge of the cover fraction. In this case the real-time distribution information can be obtained either from another high resolution sensor on the same platform, or from other high resolution satellites. However, to estimate the microwave contribution of other non-soil targets with varying distribution and

characteristics, such as urban areas, more ground-based and airborne field experiments are required to understand their microwave response such that it can be modelled. Moreover, there is a need to develop better techniques to estimate the distribution of the individual component contributors.

8.5.4 Extension of soil moisture retrieval algorithm

This thesis has shown that the presence of surface rock, urban areas, and standing water could confound the soil moisture interpretation of SMOS and SMAP pixels, and introduce additional error in soil moisture if not accounted for in the retrieval models. The SMOS and SMAP pixels identified as having a potential soil moisture retrieval error greater than 0.04 m^3/m^3 can be easily masked. However, the soil moisture over those pixels could technically be retrieved by simulating the microwave contribution of non-soil targets, and then removing it from the SMOS and SMAP brightness temperature observations. Though, such an approach has not been applied or tested.

References

ADEGOKE, J. O. & CARLETON, A. M. 2002. Relations between soil moisture and satellite vegetation indices in the US Corn Belt. *Journal of hydrometeorology,* 3**,** 395-405.

ALBERGEL, C., CALVET, J. C., MAHFOUF, J. F., RÜDIGER, C., BARBU, A., LAFONT, S., ROUJEAN, J. L., WALKER, J., CRAPEAU, M. & WIGNERON, J. P. 2010. Monitoring of water and carbon fluxes using a land data assimilation system: a case study for southwestern France. *Hydrology and Earth System Sciences Discussions,* 7**,** 1705-1744.

ALBERGEL, C., RÜDIGER, C., PELLARIN, T., CALVET, J. C., FRITZ, N., FROISSARD, F., SUQUIA, D., PETITPA, A., PIGUET, B. & MARTIN, E. 2008. From near-surface to root-zone soil moisture using an exponential filter: an assessment of the method based on in-situ observations and model simulations. *Hydrology and Earth System Sciences,* 12**,** 1323-1337.

ALSDORF, D. E., RODRÍGUEZ, E. & LETTENMAIER, D. P. 2007. Measuring surface water from space. *Reviews of Geophysics,* 45.

ALTESE, E., BOLOGNANI, O., MANCINI, M. & TROCH, P. A. 1996. Retrieving soil moisture over bare soil from ERS 1 synthetic aperture radar data: Sensitivity analysis based on a theoretical surface scattering model and field data. *Water Resources Research,* 32**,** 653-661.

ANAGNOSTOU, E. N., NEGRI, A. J. & ADLER, R. F. 1999. Statistical adjustment of satellite microwave monthly rainfall estimates over Amazonia. *Journal of Applied Meteorology,* 38**,** 1590-1598.

ÅNGSTRÖM, A. 1925. The albedo of various surfaces of ground. *Geografiska Annaler,* 7**,** 323-342.

ARNOLD, J. E. 1999. *Soil moisture* [Online]. http://www.ghcc.msfc.nasa.gov/landprocess/lp_home.html. [Accessed 5 Aug. 2012].

ASNER, G. P. 1998. Biophysical and biochemical sources of variability in canopy reflectance. *Remote Sensing of Environment,* 64**,** 234-253.

ASNER, G. P. & LOBELL, D. B. 2002. Moisture effects on soil reflectance. *Soil Science Society of America Journal,* 66**,** 722-727.

ATLAS, D., ROSENFELD, D. & WOLFF, D. 1990. Climatologically tuned reflectivity-rain rate relations and links to area- time integrals. *Journal of Applied Meteorology,* 29**,** 1120-1135.

AUBERT, D., LOUMAGNE, C. & OUDIN, L. 2003. Sequential assimilation of soil moisture and streamflow data in a conceptual rainfall–runoff model. *Journal of Hydrology,* 280**,** 145-161.

AUSTRALIAN BUREAU OF RURAL SCIENCE. 2001. *Mean Monthly and Mean Annual Rainfall and Temperature Data* [Online]. Melbourne, Australia: Bureau of Meteorology, Australia. Available: http://www.bom.gov.au/climate/how/newproducts/IDCraintempgrids.shtml [Accessed 13 Auguest 2013].

BAKER, J., SPAANS, E., NADLER, A. & LAPID, I. 1993. COMMENTS ON: TIME DOMAIN REFLECTOMETRY MEASUREMENTS OF WATER CONTENT ANDELECTRICAL CONDUCTIVITY OF LAYERED SOIL COLUMNS. REPLY. *Soil Science Society of America journal,* 57**,** 1395-1396.

BARRETT, B. W., DWYER, E. & WHELAN, P. 2009. Soil moisture retrieval from active spaceborne microwave observations: An evaluation of current techniques. *Remote Sensing,* 1**,** 210-242.

BASTIAANSSEN, W. G. M., MOLDEN, D. J. & MAKIN, I. W. 2000. Remote sensing for irrigated agriculture: examples from research and possible applications. *Agricultural water management,* 46**,** 137-155.

BECKMANN, P. & SPIZZICHINO, A. 1963. *The Scattering of Electromagnetic Waves from Rough Surfaces*, New York, Paris.

BELCHER, D. J. 1952. The measurement of soil moisture and density by neutron and gamma-ray scattering. *Highway Research Board Special Report.*

BELJAARS, A. C. M., VITERBO, P., MILLER, M. J. & BETTS, A. K. 1996. The anomalous rainfall over the United States during July 1993: Sensitivity to land surface parameterization and soil moisture anomalies. *Monthly Weather Review,* 124**,** 362-383.

BEN-DOR, E., IRONS, J. & EPEMA, G. 1999. Soil Reflectance. *Manual of Remote Sensing, Remote Sensing for the Earth Sciences,* 3**,** 111.

BERG, A. A. & MULROY, K. M. 2006. Streamflow predictability in the Saskatchewan/Nelson River basin given macroscale estimates of the initial soil moisture status. *Hydrological sciences journal,* 51**,** 642-654.

BETTS, A. K., BALL, J. H., BELJAARS, A. C. M., MILLER, M. J. & VITERBO, P. Coupling between land-surface boundary-layer parameterizations and rainfall on local and regional scales: Lessons from the wet summer of 1993. 1994. 174-181.

BETTS, A. K., BALL, J. H., BELJAARS, A. C. M., MILLER, M. J. & VITERBO, P. A. 1996. The land surface–atmosphere interaction: A review based on observational and global modeling perspectives. *Journal of Geophysical Research,* 101**,** 7209-7225.

BILSKIE, J. 1997. Using dielectric properties to measure soil water content. *Sensors-the Journal of Applied Sensing Technology,* 14**,** 26-33.

BINDLISH, R. & BARROS, A. P. Sub-pixel variability of remotely sensed soil moisture: an inter-comparison study of SAR and ESTAR. 1999. IEEE, 1917-1920 vol. 4.

BINDLISH, R. & BARROS, A. P. 2000. Multifrequency soil moisture inversion from SAR measurements with the use of IEM. *Remote Sensing of Environment,* 71**,** 67-88.

BINDLISH, R., CROW, W. T. & JACKSON, T. J. 2009. Role of passive microwave remote sensing in improving flood forecasts. *IEEE Geoscience and Remote Sensing Letters,* 6**,** 112-116.

BOLTEN, J. D., CROW, W. T., ZHAN, X., JACKSON, T. J. & REYNOLDS, C. A. 2010. Evaluating the utility of remotely sensed soil moisture retrievals for operational agricultural drought monitoring. *Selected Topics in Applied Earth Observations and Remote Sensing, IEEE Journal of,* 3**,** 57-66.

BRAKENRIDGE, G. R., NGHIEM, S. V., ANDERSON, E. & CHIEN, S. 2005. Space - based measurement of river runoff. *Transactions on American Geophysical Union,* 86**,** 185-188.

BROCCA, L., HASENAUER, S., LACAVA, T., MELONE, F., MORAMARCO, T., WAGNER, W., DORIGO, W., MATGEN, P., MARTÍNEZ-FERNÁNDEZ, J. & LLORENS, P. 2011. Soil moisture estimation through ASCAT and AMSR-E sensors: an intercomparison and validation study across Europe. *Remote Sensing of Environment*.

BRODZIK, M. J., BILLINGSLEY, B., HARAN, T., RAUP, B. & SAVOIE, M. H. 2012. EASE-Grid 2.0: Incremental but Significant Improvements for Earth-Gridded Data Sets. *ISPRS International Journal of Geo-Information,* 1**,** 32-45.

BURKE, E. J., SHUTTLEWORTH, W. J. & FRENCH, A. N. 2001. Using vegetation indices for soil-moisture retrievals from passive microwave radiometry. *Hydrology and Earth System Sciences,* 5**,** 671-678.

CAI, W., COWAN, T., BRIGGS, P. & RAUPACH, M. 2009. Rising temperature depletes soil moisture and exacerbates severe drought conditions across southeast Australia. *Geophysical Research Letters,* 36**,** L21709.

CALVET, J., NOILHAN, J. & BESSEMOULIN, P. 1998. Retrieving the root-zone soil moisture from surface soil moisture or temperature estimates: A feasibility study based on field measurements. *Journal of Applied Meteorology,* 37**,** 371-386.

CALVET, J. C., FRITZ, N., FROISSARD, F., SUQUIA, D., PETITPA, A. & PIGUET, B. In situ soil moisture observations for the CAL/VAL of SMOS: the SMOSMANIA network. 2007. IEEE, 1196-1199.

CAMPBELL, G. S. & ANDERSON, R. Y. 1998. Evaluation of simple transmission line oscillators for soil moisture measurement. *Computers and electronics in agriculture,* 20**,** 31-44.

CAMPBELL SCIENTIFIC 1998. CS615 water content reflectometer user guide. *Campbell Scientific, Inc.* Logan, UT.

CAMPS, A., VALL-LLOSSERA, M., DUFFO, N., TORRES, F. & CORBELLA, I. 2005. Performance of sea surface salinity and soil moisture retrieval algorithms with different auxiliary datasets in 2-D L-band aperture synthesis interferometric radiometers. *IEEE Transactions on Geoscience and Remote Sensing,* 43**,** 1189-1200.

CARLSON, T. N., GILLIES, R. R. & PERRY, E. M. 1994. A method to make use of thermal infrared temperature and NDVI measurements to infer surface soil water content and fractional vegetation cover. *Remote Sensing Reviews,* 9**,** 161-173.

CASTILLO, V. M., GOMEZ-PLAZA, A. & MARTıNEZ-MENA, M. 2003. The role of antecedent soil water content in the runoff response of semiarid catchments: a simulation approach. *Journal of Hydrology,* 284**,** 114-130.

CHANG, D. & ISLAM, S. 2003. Effects of topography, soil properties and mean soil moisture on the spatial distribution of soil moisture: A stochastic analysis. *Scaling methods in soil physics***,** 193-225.

CHANZY, A., SCHMUGGE, T. J., CALVET, J.-C., KERR, Y., VAN OEVELEN, P. J., GROSJEAN, O. & WANG, J. R. 1997. Airborne

microwave radiometry on a semi-arid area during HAPEX-Sahel. *Journal of Hydrology,* 188**,** 285-309.

CHARPENTIER, M. A. & GROFFMAN, P. M. 1992. Soil moisture variability within remote sensing pixels. *Journal of Geophysical Research,* 97**,** 18987-18,995.

CHAUHAN, N., MILLER, S. & ARDANUY, P. 2003. Spaceborne soil moisture estimation at high resolution: a microwave-optical/IR synergistic approach. *International Journal of Remote Sensing,* 24**,** 4599-4622.

CHEN, D., HUANG, J. & JACKSON, T. J. 2005. Vegetation water content estimation for corn and soybeans using spectral indices derived from MODIS near-and short-wave infrared bands. *Remote Sensing of Environment,* 98**,** 225-236.

CHEN, K. S., YEN, S. K. & HUANG, W. P. 1995. A simple model for retrieving bare soil moisture from radar-scattering coefficients. *Remote sensing of environment,* 54**,** 121-126.

CHEN, Y. & OR, D. 2006. Geometrical factors and interfacial processes affecting complex dielectric permittivity of partially saturated porous media. *Water Resour. Res,* 42**,** W06423.

CHOUDHURY, B., SCHMUGGE, T. & MO, T. 1982. A parameterization of effective soil temperature for microwave emission. *Journal of Geophysical Research,* 87**,** 1301-1304.

CHOUDHURY, B., SCHMUGGE, T. J., CHANG, A. & NEWTON, R. 1979. Effect of surface roughness on the microwave emission from soils. *Journal of Geophysical Research,* 84**,** 5699-5706.

CHUNG, D. M., TRONG, B. D. & ANH, V. T. L. Passive microwave remote sensing for estimation of rice water content in Vietnam. 2003. IEEE, 905-907.

CLAPS, P. & LAGUARDIA, G. Assessing spatial variability of soil water content through thermal inertia and NDVI. 2003. 378-387.

CONIL, S., DOUVILLE, H. & TYTECA, S. 2007. The relative influence of soil moisture and SST in climate predictability explored within ensembles of AMIP type experiments. *Climate dynamics,* 28**,** 125-145.

COSH, M. H., JACKSON, T. J., BINDLISH, R. & PRUEGER, J. H. 2004. Watershed scale temporal and spatial stability of soil moisture and its role in validating satellite estimates. *Remote sensing of Environment,* 92**,** 427-435.

CROW, W., BINDLISH, R. & JACKSON, T. 2005. The added value of spaceborne passive microwave soil moisture retrievals for forecasting rainfall-runoff partitioning. *Geophys. Res. Lett,* 32**,** L18.

CROW, W. T., BERG, A. A., COSH, M. H., LOEW, A., MOHANTY, B. P., PANCIERA, R., DE ROSNAY, P., RYU, D. & WALKER, J. P. 2012. Upscaling sparse ground-based soil moisture observations for the validation of coarse-resolution satellite soil moisture products. *Reviews of Geophysics,* 50**,** RG2002.

CZAJKOWSKI, K. P., GOWARD, S. N., STADLER, S. J. & WALZ, A. 2000. Thermal remote sensing of near surface environmental variables: application over the Oklahoma Mesonet. *The Professional Geographer,* 52**,** 345-357.

D'URSO, G. & MINACAPILLI, M. 2006. A semi-empirical approach for surface soil water content estimation from radar data without a-priori information on surface roughness. *Journal of Hydrology,* 321**,** 297-310.

DAI, A., TRENBERTH, K. E. & QIAN, T. 2004. A global dataset of Palmer Drought Severity Index for 1870-2002: Relationship with soil moisture and effects of surface warming. *Journal of Hydrometeorology,* 5**,** 1117-1130.

DALAL, R. & HENRY, R. 1986. Simultaneous determination of moisture, organic carbon, and total nitrogen by near infrared reflectance spectrophotometry. *Soil Science Society of America Journal,* 50**,** 120-123.

DALTON, F., DASBERG, S., RHOADES, J. & NADLER, A. 1990. Time domain reflectometry: simultaneous in-situ measurement of soil water content and salinity BARD final report. *Project no. US-868084. Bet Dagan, Israel.*

DALTON, F., HERKELRATH, W., RAWLINS, D. & RHOADES, J. 1984. Time-domain reflectometry: Simultaneous measurement of soil water content and electrical conductivity with a single probe. *Science,* 224**,** 989.

DASBERG, S. & HOPMANS, J. 1992. Time domain reflectometry calibration for uniformly and nonuniformly wetted sandy and clayey loam soils. *Soil Science Society of America Journal,* 56**,** 1341-1345.

DAVENPORT, I. J., SANDELLS, M. J. & GURNEY, R. J. 2008. The effects of scene heterogeneity on soil moisture retrieval from passive microwave data. *Advances in Water Resources,* 31**,** 1494-1502.

DAVIDSON, J., BIGGAR, J. & NIELSEN, D. l963. Gamma radiation attenuation for measuring bulk density and transient water flow in porous media. *J. Geophys. Res,* 68**,** 4777-4783.

DAVIS, J. & CHUDOBIAK, W. 1975. In situ meter for measuring relative permittivity of soils. *Geol. Surv. Can. Pap,* 75**,** 75-79.

DE ROSNAY, P., GRUHIER, C., TIMOUK, F., BAUP, F., MOUGIN, E., HIERNAUX, P., KERGOAT, L. & LEDANTEC, V. 2009. Multi-scale soil moisture measurements at the Gourma meso-scale site in Mali. *Journal of Hydrology,* 375**,** 241-252.

DE ROSNAY, P., WIGNERON, J.-P., HOLMES, T. & CALVET, J.-C. 2006. Parameterizations of the effective temperature for L-band radiometry. Inter-comparison and long term validation with SMOSREX field experiment. *In:* MÄTZLER, C., ROSENKRANZ, P. W., BATTAGLIA, A. & WIGNERON, J.-P. (eds.) *Thermal Microwave Radiation- Applications for Remote Sensing.* London, UK: IEE Electromagnetic Waves Series.

DE WIT, A. J. W. & VAN DIEPEN, C. 2007. Crop model data assimilation with the Ensemble Kalman filter for improving regional crop yield forecasts. *Agricultural and Forest Meteorology,* 146**,** 38-56.

DOBSON, M. C., ULABY, F. T., HALLIKAINEN, M. T. & EL-RAYES, M. A. 1985. Microwave dielectric behavior of wet soil-Part II: Dielectric mixing models. *Geoscience and Remote Sensing, IEEE Transactions on***,** 35-46.

DOUGLASS, J. E. 1966. Volumetric calibration of neutron moisture probes. *Soil Science Society of America Journal,* 30**,** 541-544.

DRUSCH, M. 2007. Initializing numerical weather prediction models with satellite-derived surface soil moisture: Data assimilation experiments

with ECMWF's integrated forecast system and the TMI soil moisture data set. *Journal of geophysical research,* 112**,** D03102.

DRUSCH, M., WOOD, E. F. & SIMMER, C. 1999. Up-scaling effects in passive microwave remote sensing: ESTAR 1.4 GHz measurements during SGP'97. *Geophysical Research Letters,* 26**,** 879-882.

DUBOIS, P. C. & VAN ZYL, J. An empirical soil moisture estimation algorithm using imaging radar. 1994. IEEE, 1573-1575 vol. 3.

DUBOIS, P. C., VAN ZYL, J. & ENGMAN, T. 1995. Measuring soil moisture with imaging radars. *Geoscience and Remote Sensing, IEEE Transactions on,* 33**,** 915-926.

DUPIGNY-GIROUX, L. A. & LEWIS, J. E. 1999. A moisture index for surface characterization over a semiarid area. *Photogrammetric Engineering & Remote Sensing,* 65**,** 937-945.

ENGMAN, E. T. 1990. Progress in microwave remote sensing of soil moisture. *Canadian Journal of Remote Sensing,* 16**,** 6-14.

ENGMAN, E. T. 1991. Applications of microwave remote sensing of soil moisture for water resources and agriculture. *Remote Sensing of Environment,* 35**,** 213-226.

ENGMAN, E. T. Soil moisture needs in earth sciences. Proceedings of International Geoscience and Remote Sensing Symposium, 1992. 477-479.

ENGMAN, E. T. & CHAUHAN, N. 1995. Status of microwave soil moisture measurements with remote sensing. *Remote Sensing of Environment,* 51**,** 189-198.

ENTEKHABI, D. 1995. Recent advances in land-atmosphere interaction research. *Reviews of Geophysics,* 33**,** 995-1003.

ENTEKHABI, D., ASRAR, G. R., BETTS, A. K., BEVEN, K. J., BRAS, R. L., DUFFY, C. J., DUNNE, T., KOSTER, R. D., LETTENMAIER, D. P. & MCLAUGHLIN, D. B. 1999. An agenda for land surface hydrology research and a call for the second international hydrological decade. *Bulletin of the American Meteorological Society,* 80**,** 2043-2058.

ENTEKHABI, D., NJOKU, E. G., O'NEILL, P. E., KELLOGG, K. H., CROW, W. T., EDELSTEIN, W. N., ENTIN, J. K., GOODMAN, S. D., JACKSON, T. J. & JOHNSON, J. 2010. The soil moisture active passive (SMAP) mission. *Proceedings of the IEEE,* 98**,** 704-716.

ENTEKHABI, D., RODRIGUEZ-ITURBE, I. & CASTELLI, F. 1996. Mutual interaction of soil moisture state and atmospheric processes. *Journal of Hydrology,* 184**,** 3-17.

ESCORIHUELA, M. J., KERR, Y. H., DE ROSNAY, P., WIGNERON, J.-P., CALVET, J. C. & LEMAÎTRE, F. 2007. A simple model of the bare soil microwave emission at L-band. *IEEE Transactions on Geoscience and Remote Sensing,* 45**,** 1978-1987.

FALLOON, P., JONES, C. D., ADES, M. & PAUL, K. 2011. Direct soil moisture controls of future global soil carbon changes: An important source of uncertainty. *Global Biogeochemical Cycles,* 25**,** GB3010.

FAMIGLIETTI, J. S., DEVEREAUX, J. A., LAYMON, C. A., TSEGAYE, T., HOUSER, P. R., JACKSON, T. J., GRAHAM, S. T., RODELL, M. & VAN OEVELEN, P. J. 1999. Ground-based investigation of soil moisture variability within remote sensing footprints during the

Southern Great Plains 1997(SGP 97) Hydrology Experiment. *Water Resources Research,* 35**,** 1839-1851.

FELLNER-FELDEGG, H. 1969. Measurement of dielectrics in the time domain. *The Journal of Physical Chemistry,* 73**,** 616-623.

FERGUSON, H. & GARDNER, W. H. 1962. Water content measurement in soil columns by gamma ray absorption. *Soil Science Society of America Journal,* 26**,** 11-14.

FRIEDL, M. A. & DAVIS, F. W. 1994. Sources of variation in radiometric surface temperature over a tallgrass prairie. *Remote Sensing of Environment,* 48**,** 1-17.

FUNG, A. K. 1994. Microwave Scattering, Emission Model and Its Application. Artech House, Norwood, MA.

FUNG, A. K., LI, Z. & CHEN, K. S. 1992. Backscattering from a randomly rough dielectric surface. *IEEE Transactions on Geoscience and Remote Sensing,* 30**,** 356-369.

GABARRÓ, C., FONT, J., CAMPS, A. & VALL-LLOSSERA, M. Retrieved sea surface salinity and wind speed from L-band measurements for WISE and EUROSTARRS campaigns. EuroSTARRS, WISE, LOSAC Campaigns. Proceedings of the First Results Workshop, 2003. 163-171.

GALANTOWICZ, J. F., ENTEKHABI, D. & NJOKU, E. G. 2000. Estimation of soil-type heterogeneity effects in the retrieval of soil moisture from radiobrightness. *IEEE Transactions on Geoscience and Remote Sensing,* 38**,** 312-315.

GAO, B. C. 1996. NDWI—a normalized difference water index for remote sensing of vegetation liquid water from space. *Remote Sensing of Environment,* 58**,** 257-266.

GARDNER, W. & KIRKHAM, D. 1952. Determination of soil moisture by neutron scattering. *Soil Science,* 73**,** 391.

GILLIES, R. R. & CARLSON, T. N. 1995. Thermal remote sensing of surface soil water content with partial vegetation cover for incorporation into climate models. *Journal of Applied Meteorology,* 34.

GILLIES, R. R., KUSTAS, W. P. & HUMES, K. S. 1997. A verification of the'triangle'method for obtaining surface soil water content and energy fluxes from remote measurements of the Normalized Difference Vegetation Index (NDVI) and surface e. *International Journal of Remote Sensing,* 18**,** 3145-3166.

GITHEKO, A. K., LINDSAY, S. W., CONFALONIERI, U. E. & PATZ, J. A. 2000. Climate change and vector-borne diseases: a regional analysis. *Bulletin of the World Health Organization,* 78**,** 1136-1147.

GOUWELEEUW, B. T., VAN DIJK, A. I. J. M., GUERSCHMAN, J. P., DYCE, P. & OWE, M. 2012. Space-based passive microwave soil moisture retrievals and the correction for a dynamic open water fraction. *Hydrology and Earth System Sciences,* 16**,** 1635-1645.

GRIMALDI, C., GRIMALDI, M. & VAUCLIN, M. 1994. The effect of the chemical composition of a ferrallitic soil on neutron probe calibration. *Soil Technology,* 7**,** 233-247.

GRISMER, M. E., BALI, K. M. & ROBINSON, F. E. 1995. Field-scale neutron probe calibration and variance analysis for clay soil. *Journal of Irrigation and Drainage Engineering,* 121**,** 354.

GROTE, K., ANGER, C., KELLY, B., HUBBARD, S. & RUBIN, Y. 2010. Characterization of soil water content variability and soil texture using GPR groundwave techniques. *Journal of Environmental & Engineering Geophysics,* 15**,** 93-110.

GUERSCHMAN, J. P., WARREN, G., BYRNE, G., LYMBURNER, L., MUELLER, N. & VAN DIJK, A. I. J. M. 2011. *MODIS-based standing water detection for flood and large reservoir mapping: algorithm development and applications for the Australian continent*, CSIRO.

GURR, C. G. 1962. Use of gamma rays in measuring water content and permeability in unsaturated columns of soil. *Soil Science,* 94**,** 224.

HALLIKAINEN, M. T., ULABY, F. T., DOBSON, M. C., EL-RAYES, M. A. & WU, L. K. 1985. Microwave dielectric behavior of wet soil-part 1: empirical models and experimental observations. *IEEE Transactions on Geoscience and Remote Sensing***,** 25-34.

HANSEN, M. C., DEFRIES, R. S., TOWNSHEND, J. R. G. & SOHLBERG, R. 2000. Global land cover classification at 1 km spatial resolution using a classification tree approach. *International Journal of Remote Sensing,* 21**,** 1331-1364.

HAWLEY, M. E., JACKSON, T. J. & MCCUEN, R. H. 1983. Surface soil moisture variation on small agricultural watersheds. *Journal of Hydrology,* 62**,** 179-200.

HILLEL, D. 1998. *Environmental Soil Physics,* San Diego, Academic Press.

HOKETT, S. L., CHAPMAN, J. B. & CLOUD, S. D. 1992. Time domain reflectometry response to lateral soil water content heterogeneities. *Soil Science Society of America Journal,* 56**,** 313-316.

HORNBUCKLE, B. K. & ENGLAND, A. W. 2005. Diurnal variation of vertical temperature gradients within a field of maize: Implications for satellite microwave radiometry. *IEEE Geoscience and Remote Sensing Letters,* 2**,** 74-77.

HORNBUCKLE, B. K., ENGLAND, A. W., DE ROO, R. D., FISCHMAN, M. A. & BOPRIE, D. L. 2003. Vegetation canopy anisotropy at 1.4 GHz. *IEEE Transactions on Geoscience and Remote Sensing,* 41**,** 2211-2223.

HUPET, F., TROUGHT, M. C. T., GREVEN, M., GREEN, S. R. & CLOTHIER, B. E. 2005. Data requirements for identifying macroscopic water stress parameters: A study on grapevines. *Water Resources Research,* 41**,** W06008.

IDSO, S. B., JACKSON, R. D., REGINATO, R. J., KIMBALL, B. A. & NAKAYAMA, F. S. 1975. The dependence of bare soil albedo on soil water content. *Journal of Applied Meteorology,* 14**,** 109-113.

JACKSON, R. D., IDSO, S. B. & REGINATO, R. J. 1976. Calculation of evaporation rates during the transition from energy-limiting to soil-limiting phases using albedo data. *Water Resources Research,* 12**,** 23-26.

JACKSON, T. J. 2001. Multiple resolution analysis of L-band brightness temperature for soil moisture. *IEEE Transactions on Geoscience and Remote Sensing,* 39**,** 151-164.

JACKSON, T. J., CHEN, D., COSH, M., LI, F., ANDERSON, M., WALTHALL, C., DORIASWAMY, P. & HUNT, E. 2004a. Vegetation water content mapping using Landsat data derived

normalized difference water index for corn and soybeans. *Remote Sensing of Environment,* 92**,** 475-482.

JACKSON, T. J., GASIEWSKI, A. J., OLDAK, A., KLEIN, M., NJOKU, E. G., YEVGRAFOV, A., CHRISTIANI, S. & BINDLISH, R. 2002. Soil moisture retrieval using the C-band polarimetric scanning radiometer during the Southern Great Plains 1999 Experiment. *IEEE Transactions on Geoscience and Remote Sensing,* 40**,** 2151-2161.

JACKSON, T. J., HAWLEY, M. E. & O'NEILL, P. E. 1987. Preplanting soil-moisture using passive microwave sensors. *Journal of the American Water Resources Association,* 23**,** 11-19.

JACKSON, T. J., HSU, A. Y., VAN DE GRIEND, A. & EAGLEMAN, J. R. 2004b. Skylab L-band microwave radiometer observations of soil moisture revisited. *International Journal of Remote Sensing,* 25**,** 2585-2606.

JACKSON, T. J., KOSTOV, K. G. & SAATCHI, S. S. 1992. Rock fraction effects on the interpretation of microwave emission from soils. *IEEE Transactions on Geoscience and Remote Sensing,* 30**,** 610-616.

JACKSON, T. J. & LE VINE, D. E. 1996. Mapping surface soil moisture using an aircraft-based passive microwave instrument: algorithm and example. *Journal of Hydrology,* 184**,** 85-99.

JACKSON, T. J. & O'NEILL, P. E. 1987. Salinity effects on the microwave emission of soils. *IEEE Transactions on Geoscience and Remote Sensing***,** 214-220.

JACKSON, T. J. & SCHMUGGE, T. J. 1989. Passive microwave remote sensing system for soil moisture: Some supporting research. *IEEE Transactions on Geoscience and Remote Sensing,* 27**,** 225-235.

JACKSON, T. J. & SCHMUGGE, T. J. 1991. Vegetation effects on the microwave emission of soils. *Remote Sensing of Environment,* 36**,** 203-212.

JACKSON, T. J., SCHMUGGE, T. J. & ENGMAN, E. T. 1996. Remote sensing applications to hydrology: soil moisture. *Hydrological Sciences Journal,* 41**,** 517-530.

JACKSON, T. J., SCHMUGGE, T. J., NICKS, A. D., COLEMAN, G. A. & ENGMAN, E. T. 1981. Soil moisture updating and microwave remote sensing for hydrological simulation. *Hydrological Sciences Journal,* 26**,** 305-319.

JACKSON, T. J., SCHMUGGE, T. J. & WANG, J. R. 1982. Passive microwave sensing of soil moisture under vegetation canopies. *Water Resources Research,* 18**,** 1137-1142.

JACOBS, J. M., MOHANTY, B. P., HSU, E. C. & MILLER, D. 2004. SMEX02: Field scale variability, time stability and similarity of soil moisture. *Remote Sensing of Environment,* 92**,** 436-446.

JACOBSEN, O. H. & SCHJOENNING, P. Comparison of TDR calibration functions for soil water determination. 1995. SP.

JI, L., ZHANG, L. & WYLIE, B. 2009. Analysis of dynamic thresholds for the normalized difference water index. *Photogrammetric Engineering and Remote Sensing,* 75**,** 1307-1317.

JOSHI, C. & MOHANTY, B. P. 2010. Physical controls of near - surface soil moisture across varying spatial scales in an agricultural landscape during SMEX02. *Water Resources Research,* 46**,** W12503.

JUNG, M., REICHSTEIN, M., CIAIS, P., SENEVIRATNE, S. I., SHEFFIELD, J., GOULDEN, M. L., BONAN, G., CESCATTI, A., CHEN, J. & DE JEU, R. 2010. Recent decline in the global land evapotranspiration trend due to limited moisture supply. *Nature,* 467**,** 951-954.

KABELA, E. D., HORNBUCKLE, B. K., COSH, M. H., ANDERSON, M. C. & GLEASON, M. L. 2009. Dew frequency, duration, amount, and distribution in corn and soybean during SMEX05. *Agricultural and forest meteorology,* 149**,** 11-24.

KAUFMAN, Y. J. & TANRE, D. 1992. Atmospherically resistant vegetation index (ARVI) for EOS-MODIS. *IEEE Transactions on Geoscience and Remote Sensing,* 30**,** 261-270.

KAUFMANN, R. K., D'ARRIGO, R. D., LASKOWSKI, C., MYNENI, R. B., ZHOU, L. & DAVI, N. K. 2004. The effect of growing season and summer greenness on northern forests. *Geophysical Research Letters,* 31.

KERR, Y. H. & NJOKU, E. G. 1990. A semiempirical model for interpreting microwave emission from semiarid land surfaces as seen from space. *IEEE Transactions on Geoscience and Remote Sensing,* 28**,** 384-393.

KERR, Y. H., SECHERRE, F., LASTENET, J. & WIGNERON, J.-P. SMOS: Analysis of perturbing effects over land surfaces. 2003. IEEE, 908-910 vol. 2.

KERR, Y. H., WALDTEUFEL, P. & BERGER, M. 2001. Mission objectives and scientific requirements of the Soil Moisture and Ocean Salinity (SMOS) Mission. *MRD, ESA: ESTEC, Noordwijk (NL),* 44.

KERR, Y. H., WALDTEUFEL, P., RICHAUME, P., DAVENPORT, I., FERRAZZOLI, P. & WIGNERON, J.-P. 2010a. SMOS level 2 processor soil moisture algorithm theoretical basis document (ATBD). *SM-ESL (CBSA), CESBIO, Toulouse, SO-TN-ARR-L2PP-0037, Issue 3.4*.

KERR, Y. H., WALDTEUFEL, P., WIGNERON, J.-P., DELWART, S., CABOT, F., BOUTIN, J., ESCORIHUELA, M. J., FONT, J., REUL, N. & GRUHIER, C. 2010b. The SMOS Mission: New Tool for Monitoring Key Elements ofthe Global Water Cycle. *Proceedings of the IEEE,* 98**,** 666-687.

KIM, C. P. & STRICKER, J. N. M. 1996. Influence of spatially variable soil hydraulic properties and rainfall intensity on the water budget. *Water Resources Research,* 32**,** 1699-1712.

KIM, C. P., STRICKER, J. N. M. & FEDDES, R. A. 1997. Impact of soil heterogeneity on the water budget of the unsaturated zone. *Water Resources Research,* 33**,** 991-999.

KIM, G. & BARROS, A. P. 2002. Space–time characterization of soil moisture from passive microwave remotely sensed imagery and ancillary data. *Remote Sensing of Environment,* 81**,** 393-403.

KIM, G., CHUNG, J. H. & KIM, J. S. 2002. Spatial characterization of soil moisture estimates from the Southern Great Plain (SGP 97) hydrology experiment. *KSCE Journal of Civil Engineering,* 6**,** 177-184.

KIRDIASHEV, K. P., CHUKHLANTSEV, A. A. & SHUTKO, A. M. 1979. Microwave radiation of the earth's surface in the presence of vegetation cover. *Radiotekhnika i Elektronika,* 24**,** 256-264.

KITE, G. W. & PIETRONIRO, A. 1996. Remote sensing applications in hydrological modelling. *Hydrological Sciences Journal,* 41**,** 563-591.

KOEPPE, C. E. & DE LONG, G. 1958. *Weather and climate*.

KOSTER, R. D., DIRMEYER, P. A., GUO, Z., BONAN, G., CHAN, E., COX, P., GORDON, C. T., KANAE, S., KOWALCZYK, E. & LAWRENCE, D. 2004. Regions of strong coupling between soil moisture and precipitation. *Science,* 305**,** 1138-1140.

KOSTER, R. D., GUO, Z., YANG, R., DIRMEYER, P. A., MITCHELL, K. & PUMA, M. J. 2009. On the nature of soil moisture in land surface models. *Journal of Climate,* 22**,** 4322-4335.

KOSTER, R. D., MAHANAMA, S. P. P., LIVNEH, B., LETTENMAIER, D. P. & REICHLE, R. H. 2010. Skill in streamflow forecasts derived from large-scale estimates of soil moisture and snow. *Nature Geoscience,* 3**,** 613-616.

KOSTER, R. D., SUAREZ, M. J., HIGGINS, R. W. & VAN DEN DOOL, H. M. 2003. Observational evidence that soil moisture variations affect precipitation. *Geophysical Research Letters,* 30**,** 1241.

KRAJEWSKI, W. F., ANDERSON, M. C., EICHINGER, W. E., ENTEKHABI, D., HORNBUCKLE, B. K., HOUSER, P. R., KATUL, G. G., KUSTAS, W. P., NORMAN, J. M. & PETERS-LIDARD, C. 2006. A remote sensing observatory for hydrologic sciences: A genesis for scaling to continental hydrology. *Water Resources Research,* 42**,** W07301.

LAMBIN, E. F. & EHRLICH, D. 1996. The surface temperature-vegetation index space for land cover and land-cover change analysis. *International Journal of Remote Sensing,* 17**,** 463-487.

LAURENT, B., MARTICORENA, B., BERGAMETTI, G., LÉON, J. F. & MAHOWALD, N. M. 2008. Modeling mineral dust emissions from the Sahara desert using new surface properties and soil database. *Journal of Geophysical Research,* 113**,** D14218.

LAWLESS, G. P., MACGILLIVRAY, N. A. & NIXON, P. R. 1963. Soil moisture interface effects upon readings of neutron moisture probes. *Soil Science Society of America Journal,* 27**,** 502-507.

LE VINE, D. M., KAO, M., TANNER, A. B., SWIFT, C. T. & GRIFFIS, A. 1990. Initial results in the development of a synthetic aperture microwave radiometer. *IEEE Transactions on Geoscience and Remote Sensing,* 28**,** 614-619.

LEESE, J., JACKSON, T., PITMAN, A. & DIRMEYER, P. 2001. Meeting summary: GEWEX/BAHC International Workshop on Soil Moisture Monitoring, Analysis, and Prediction for Hydrometeorological and Hydroclimatological Applications. *Bulletin of the American Meteorological Society,* 82**,** 1423-1430.

LEONE, A. P. & SOMMER, S. 2000. Multivariate analysis of laboratory spectra for the assessment of soil development and soil degradation in the southern Apennines (Italy). *Remote Sensing of Environment,* 72**,** 346-359.

LILLESAETER, O. 1982. Spectral reflectance of partly transmitting leaves: laboratory measurements and mathematical modeling. *Remote Sensing of Environment,* 12**,** 247-254.

LILLESAND, T. M., KIEFER, R. W. & CHIPMAN, J. W. 2004. *Remote sensing and image interpretation*, John Wiley & Sons Ltd.

LIU, W., BARET, F., GU, X., TONG, Q., ZHENG, L. & ZHENG, B. 2002. Relating soil surface moisture to reflectance. *Remote Sensing of Environment,* 81**,** 238-246.

LIU, Y. Y., VAN DIJK, A. I. J. M., DE JEU, R. A. M. & HOLMES, T. R. H. 2009. An analysis of spatiotemporal variations of soil and vegetation moisture from a 29 - year satellite - derived data set over mainland Australia. *Water Resources Research,* 45.

LOEW, A. 2008. Impact of surface heterogeneity on surface soil moisture retrievals from passive microwave data at the regional scale: The Upper Danube case. *Remote Sensing of Environment,* 112**,** 231-248.

LOEW, A., DALL'AMICO, J., SCHLENZ, F. & MAUSER, W. The Upper Danube soil moisture validation site: measurements and activities. Earth Observation and Water Cycle conference, 18–20 November 2009 2009 Frascati, Rome. 2924.

LOVELAND, T. R. & BELWARD, A. S. 1997. The IGBP-DIS global 1km land cover data set, DISCover: first results. *International Journal of Remote Sensing,* 18**,** 3289-3295.

LOVELAND, T. R., REED, B. C., BROWN, J. F., OHLEN, D. O., ZHU, Z., YANG, L. & MERCHANT, J. W. 2000. Development of a global land cover characteristics database and IGBP DISCover from 1 km AVHRR data. *International Journal of Remote Sensing,* 21**,** 1303-1330.

MALICKI, M. A., PLAGGE, R. & ROTH, C. H. 1996. Improving the calibration of dielectric TDR soil moisture determination taking into account the solid soil. *European Journal of Soil Science,* 47**,** 357-366.

MARTÍN-NEIRA, M., RIBÓ, S. & MARTÍN-POLEGRE, A. J. 2002. Polarimetric mode of MIRAS. *IEEE Transactions on Geoscience and Remote Sensing,* 40**,** 1755-1768.

MARTÍNEZ-FERNÁNDEZ, J. & CEBALLOS, A. 2005. Mean soil moisture estimation using temporal stability analysis. *Journal of Hydrology,* 312**,** 28-38.

MARTINEZ-VAZQUEZ, A., CAMPS, A., LOPEZ-SANCHEZ, J. M., VALL-LLOSSERA, M. & MONERRIS, A. 2009. Numerical simulation of the full-polarimetric emissivity of vines and comparison with experimental data. *Remote Sensing,* 1**,** 300-317.

MASSON, V., CHAMPEAUX, J. L., CHAUVIN, F., MERIGUET, C. & LACAZE, R. 2003. A global database of land surface parameters at 1-km resolution in meteorological and climate models. *Journal of Climate,* 16**,** 1261-1282.

MATTIKALLI, N. M., ENGMAN, E. T., JACKSON, T. J. & AHUJA, L. R. 1998. Microwave remote sensing of temporal variations of brightness temperature and near-surface soil water content during a watershed-scale field experiment, and its application to the estimation of soil physical properties. *Water Resources Research,* 34**,** 2289-2299.

MÄTZLER, C., ROSENKRANZ, P. W., BATTAGLIA, A. & WIGNERON, J.-P. 2006. *Thermal microwave radiation: applications for remote sensing,* London, UK, IET Electromagnetic Waves Series.

MCCAULEY, G. N. & STONE, J. F. 1972. Source-detector geometry effect on neutron probe calibration. *Soil Science Society of America Journal,* 36**,** 246-250.

MCFEETERS, S. K. 1996. The use of the Normalized Difference Water Index (NDWI) in the delineation of open water features. *International Journal of Remote Sensing,* 17**,** 1425-1432.

MCMULLAN, K. D., BROWN, M. A., MARTÍN-NEIRA, M., RITS, W., EKHOLM, S., MARTI, J. & LEMANCZYK, J. 2008. SMOS: The payload. *IEEE Transactions on Geoscience and Remote Sensing,* 46**,** 594-605.

MEESTERS, A. G. C. A., DE JEU, R. A. M. & OWE, M. 2005. Analytical derivation of the vegetation optical depth from the microwave polarisation difference index. *IEEE Geoscience and Remote Sensing Letters,* 2**,** 121-123.

MERLIN, O., WALKER, J. P., KALMA, J. D., KIM, E. J., HACKER, J., PANCIERA, R., YOUNG, R., SUMMERELL, G., HORNBUCKLE, J. & HAFEEZ, M. 2008. The NAFE'06 data set: Towards soil moisture retrieval at intermediate resolution. *Advances in Water Resources,* 31**,** 1444-1455.

MERLIN, O., WALKER, J. P., PANCIERA, R., YOUNG, R. K., J. D. & KIM, E. J. 2007. Calibration of a Soil Moisture Sensor in Heterogeneous Terrain with the National Airborne Field Experiment (NAFE) Data. *In:* OXLEY, L. & KULASIRI, D. (eds.) *MODSIM 2007 International Congress on Modelling and Simulation.* Modelling and Simulation Society of Australia and New Zealand.

MERTES, L. A. K. 2002. Remote sensing of riverine landscapes. *Freshwater Biology,* 47**,** 799-816.

MIRONOV, V. L., DOBSON, M. C., KAUPP, V. H., KOMAROV, S. A. & KLESHCHENKO, V. N. 2004. Generalized refractive mixing dielectric model for moist soils. *IEEE Transactions on Geoscience and Remote Sensing,* 42**,** 773-785.

MLADENOVA, I. E., JACKSON, T. J., BINDLISH, R. & HENSLEY, S. 2013. Incidence Angle Normalization of Radar Backscatter Data. *IEEE Transactions on Geoscience and Remote Sensing.*

MO, T., CHOUDHURY, B. J., SCHMUGGE, T. J., WANG, J. R. & JACKSON, T. J. 1982. A model for microwave emission from vegetation-covered fields. *Journal of Geophysical Research,* 87**,** 11229-11,237.

MO, T. & SCHMUGGE, T. J. 1987. A parameterization of the effect of surface roughness on microwave emission. *IEEE Transactions on Geoscience and Remote Sensing***,** 481-486.

MOHANTY, B. P., FAMIGLIETTI, J. S. & SKAGGS, T. H. 2000a. Evolution of soil moisture spatial structure in a mixed vegetation pixel during the Southern Great Plains 1997 (SGP97) Hydrology Experiment. *Water Resources Research,* 36**,** 3675-3686.

MOHANTY, B. P. & SKAGGS, T. H. 2001. Spatio-temporal evolution and time-stable characteristics of soil moisture within remote sensing footprints with varying soil, slope, and vegetation. *Advances in Water Resources,* 24**,** 1051-1067.

MOHANTY, B. P., SKAGGS, T. H. & FAMIGLIETTI, J. S. 2000b. Analysis and mapping of field-scale soil moisture variability using high-resolution, ground-based data during the Southern Great Plains 1997(SGP 97) Hydrology Experiment. *Water Resources Research,* 36**,** 1023-1031.

MONERRIS, A., VALL-LLOSSERA, M., CAMPS, A. & PILES, M. Rock Fraction Effects on the Surface Soil Moisture Estimates From L-Band Radiometric Measurements. 2008. IEEE, II-711-II-714.

MOORE, I. D., BURCH, G. J. & MACKENZIE, D. H. 1988. Topographic effects on the distribution of surface soil water and the location of ephemeral gullies. *Transactions of the American Society of Agricultural Engineers,* 31**,** 1098-1107.

MORAN, M. S., CLARKE, T. R., INOUE, Y. & VIDAL, A. 1994. Estimating crop water deficit using the relation between surface-air temperature and spectral vegetation index. *Remote Sensing of Environment,* 49**,** 246-263.

MORAN, M. S., PETERS-LIDARD, C. D., WATTS, J. M. & MCELROY, S. 2004. Estimating soil moisture at the watershed scale with satellite-based radar and land surface models. *Canadian Journal of Remote Sensing,* 30**,** 805-826.

MUELLER, N. & LYMBURNER, L. 2010. Extracting landscape features in emergency response situations: combining fuzzy logic and Gaussian statistics in object-oriented analysis. *15th Australasian Remote Sensing & Photogrammetry Conference (ARSPC).* Alice Springs.

NADLER, A., LAPID, I. & DASBERG, S. 1991. Time domain reflectometry measurements of water content and electrical conductivity of layered soil columns. *Soil Science Society of America Journal,* 55**,** 938-943.

NADLER, A. & LAPID, Y. 1996. An improved capacitance sensor for in situ monitoring of soil moisture. *Soil Research,* 34**,** 361-368.

NATIONAL RESEARCH COUNCIL 2007. *Earth science and applications from space: national imperatives for the next decade and beyond*, National Academies Press.

NEMANI, R., PIERCE, L., RUNNING, S. & GOWARD, S. 1993. Developing satellite-derived estimates of surface moisture status. *Journal of Applied Meteorology,* 32**,** 548-557.

NEW SOUTH WALES DEPARTMENT OF ENVIRONMENT & CLIMATE CHANGE. 2007. *Metadata statement: Land Use mapping - New South Wales, Metadata statement* [Online]. Available: http://www.canri.nsw.gov.au/download/NSW_Land_Use_Mapping_metadata.pdf [Accessed July 17 2011].

NEWTON, R. & ROUSE JR, J. 1980. Microwave radiometer measurements of soil moisture content. *IEEE Transactions on Antennas and Propagation,* 28**,** 680-686.

NJOKU, E. G. & ENTEKHABI, D. 1996. Passive microwave remote sensing of soil moisture. *Journal of Hydrology,* 184**,** 101-129.

NJOKU, E. G., HOOK, S. J. & CHEHBOUNI, A. Effects of surface heterogeneity on thermal remote sensing of land parameters. Workshop on Saling Up Hydrological Variables using Remote Sensing, June 10-12 1996 Institute of Hydrology, Wallingford, UK.

NJOKU, E. G., JACKSON, T. J., LAKSHMI, V., CHAN, T. K. & NGHIEM, S. V. 2003. Soil moisture retrieval from AMSR-E. *IEEE Transactions on Geoscience and Remote Sensing,* 41**,** 215-229.

NJOKU, E. G. & LI, L. 1999. Retrieval of land surface parameters using passive microwave measurements at 6-18 GHz. *IEEE Transactions on Geoscience and Remote Sensing,* 37**,** 79-93.

NJOKU, E. G., WILSON, W. J., YUEH, S. H., DINARDO, S. J., LI, F. K., JACKSON, T. J., LAKSHMI, V. & BOLTEN, J. 2002. Observations of soil moisture using a passive and active low-frequency microwave airborne sensor during SGP99. *IEEE Transactions on Geoscience and Remote Sensing,* 40**,** 2659-2673.

NOBORIO, K. 2001. Measurement of soil water content and electrical conductivity by time domain reflectometry: a review. *Computers and Electronics in Agriculture,* 31**,** 213-237.

NORBIATO, D., BORGA, M., E.S., D., GAUME, E. & ANQUETIN, S. 2008. Flash flood warning based on rainfall thresholds and soil moisture conditions: An assessment for gauged and ungauged basins. *Journal of Hydrology,* 362**,** 274-290.

OH, Y., SARABANDI, K. & ULABY, F. T. 1992. An empirical model and an inversion technique for radar scattering from bare soil surfaces. *IEEE Transactions on Geoscience and Remote Sensing,* 30**,** 370-381.

OLIOSO, A., CHAUKI, H., COURAULT, D. & WIGNERON, J. P. 1999. Estimation of evapotranspiration and photosynthesis by assimilation of remote sensing data into SVAT models. *Remote Sensing of Environment,* 68**,** 341-356.

OLIVA, R., DAGANZO, E., KERR, Y. H., MECKLENBURG, S., NIETO, S., RICHAUME, P. & GRUHIER, C. 2012. SMOS radio frequency interference scenario: Status and actions taken to improve the RFI environment in the 1400–1427-MHz passive band. *IEEE Transactions on Geoscience and Remote Sensing,* 50**,** 1427-1439.

OWE, M., DE JEU, R. & WALKER, J. P. 2001. A methodology for surface soil moisture and vegetation optical depth retrieval using the microwave polarisation difference index. *IEEE Transactions on Geoscience and Remote Sensing,* 39**,** 1643-1654.

PAMPALONI, P. & PALOSCIA, S. 1986. Microwave emission and plant water content: A comparison between field measurements and theory. *IEEE Transactions on Geoscience and Remote Sensing***,** 900-905.

PANCIERA, R. 2009. *Effect of land surface heterogeneity on satellite near-surface soil moisture observations.* PhD thesis, University of Melbourne.

PANCIERA, R., MERLIN, O., YOUNG, R. & WALKER, J. P. 2006. The Hydraprobe Data Acquisition System (HDAS): User Guide. University of Melbourne, Melbourne, Australia.

PANCIERA, R., WALKER, J. P., JACKSON, T. J., RYU, D., GRAY, D., MONERRIS, A., YARDLEY, H., TANASE, M. A., RÜDIGER, C., WU, X., GAO, Y. & J., H. 2012. The Soil Moisture Active Passive Experiments (SMAPEx): Towards Soil Moisture Retrieval from the SMAP Mission. *IEEE Transactions on Geoscience and Remote Sensing.*

PANCIERA, R., WALKER, J. P., KALMA, J. D., KIM, E. J., HACKER, J. M., MERLIN, O., BERGER, M. & SKOU, N. 2008. The

NAFE'05/CoSMOS data set: Toward SMOS soil moisture retrieval, downscaling, and assimilation. *IEEE Transactions on Geoscience and Remote Sensing,* 46**,** 736-745.

PANCIERA, R., WALKER, J. P., KIM, E., KALMA, J. & MERLIN, O. 2007. Multiresolution soil moisture retrieval from passive microwave sensors: A preliminary study. *MODSIM 2007 International Congress on Modelling and Simulation.*

PAPA, F., PRIGENT, C., DURAND, F. & ROSSOW, W. B. 2006. Wetland dynamics using a suite of satellite observations: A case study of application and evaluation for the Indian Subcontinent. *Geophysical Research Letters,* 33.

PEISCHL, S., WALKER, J. P., RÜDIGER, C., YE, N., KERR, Y. H., KIM, E., BANDARA, R. & ALLAHMORADI, M. 2012a. The AACES field experiments: SMOS calibration and validation across the Murrumbidgee River catchment. *Hydrology and Earth System Sciences,* 9**,** 2763-2795.

PEISCHL, S., WALKER, J. P., RÜDIGER, C., YE, N., KERR, Y. H., KIM, E., BANDARA, R. & ALLAHMORADI, M. 2012b. The AACES field experiments: SMOS calibration and validation across the Murrumbidgee River catchment. *Hydrology and Earth System Sciences,* 9**,** 2763-2795.

PELLETIER, J. D., MALAMUD, B. D., BLODGETT, T. & TURCOTTE, D. L. 1997. Scale-invariance of soil moisture variability and its implications for the frequency-size distribution of landslides. *Engineering Geology,* 48**,** 255-268.

PETTORELLI, N., VIK, J. O., MYSTERUD, A., GAILLARD, J. M., TUCKER, C. J. & STENSETH, N. C. 2005. Using the satellite-derived NDVI to assess ecological responses to environmental change. *Trends in Ecology & Evolution,* 20**,** 503-510.

POTERE, D. & SCHNEIDER, A. 2007. A critical look at representations of urban areas in global maps. *GeoJournal,* 69**,** 55-80.

POTERE, D., SCHNEIDER, A., ANGEL, S. & CIVCO, D. L. 2009. Mapping urban areas on a global scale: which of the eight maps now available is more accurate? *International Journal of Remote Sensing,* 30**,** 6531-6558.

PRICE, J. C. 1977. Thermal inertia mapping: a new view of the earth. *Journal of Geophysical Research,* 82**,** 2582-2590.

PRIGENT, C., MATTHEWS, E., AIRES, F. & ROSSOW, W. B. 2001. Remote sensing of global wetland dynamics with multiple satellite data sets. *Geophysical Research Letters,* 28**,** 4631-4634.

PRIHODKO, L. & GOWARD, S. N. 1997. Estimation of air temperature from remotely sensed surface observations. *Remote Sensing of Environment,* 60**,** 335-346.

PROSENSING INC. 2005. Polarimetric L-band Multi-beam Radiometer (PLMR) Technical Report. Amherst, Massachusetts USA.

RAUTIAINEN, K., KAINULAINEN, J., AUER, T., PIHLFLYCKT, J., KETTUNEN, J. & HALLIKAINEN, M. T. 2008. Helsinki University of Technology L-band airborne synthetic aperture radiometer. *IEEE Transactions on Geoscience and Remote Sensing,* 46**,** 717-726.

REDELSPERGER, J. L., THORNCROFT, C., DIEDHIOU, A., LEBEL, T., PARKER, D. & POLCHER, J. 2006. African Monsoon Multidisciplinary Analysis (AMMA): An international research project and field campaign. *Bulletin of the American Meteorological Society,* 87**,** 1739-1746.

REGINATO, R. J. & VAN BAVEL, C. H. M. 1964. Soil water measurement with gamma attenuation. *Soil Science Society of America Proceedings,* 28**,** 721-724.

REICHLE, R. H. & KOSTER, R. D. 2004. Bias reduction in short records of satellite soil moisture. *Geophysical Research Letters,* 31.

RICE, S. O. 1951. Reflection of electromagnetic waves from slightly rough surfaces. *Communications on pure and applied mathematics,* 4**,** 351-378.

ROTH, K., SCHULIN, R., FLÜHLER, H. & ATTINGER, W. 1990. Calibration of time domain reflectometry for water content measurement using a composite dielectric approach. *Water Resources Research,* 26**,** 2267-2273.

RÜDIGER, C., WALKER, J. P., KERR, Y. H., KIM, E. J., HACKER, J. M., GURNEY, R., BARRETT, D. & LE MARSHALL, J. 2013. Towards Vicarious Calibration of Microwave Remote Sensing Satellites in Arid Environments. *IEEE Transactions on Geoscience and Remote Sensing.*

RÜDIGER, C., WESTERN, A. W., WALKER, J. P., SMITH, A. B., KALMA, J. D. & WILLGOOSE, G. R. 2010. Towards a general equation for frequency domain reflectometers. *Journal of Hydrology,* 383**,** 319-329.

RYU, D. & FAMIGLIETTI, J. S. 2005. Characterization of footprint-scale surface soil moisture variability using Gaussian and beta distribution functions during the Southern Great Plains 1997 (SGP97) hydrology experiment. *Water Resources Research,* 41**,** W12433.

SADEGHI, A. M., HANCOCK, G. D., WAITE, W. P., SCOTT, H. D. & RAND, J. A. 1984. Microwave measurements of moisture distributions in the upper soil profile. *Water Resources Research,* 20**,** 927-934.

SAHA, S. K. 1995. Assessment of regional soil moisture conditions by coupling satellite sensor data with a soil-plant system heat and moisture balance model. *Remote Sensing,* 16**,** 973-980.

SAHR, K., WHITE, D. & KIMERLING, A. J. 2003. Geodesic discrete global grid systems. *Cartography and Geographic Information Science,* 30**,** 121-134.

SALVUCCI, G. D. 2001. Estimating the moisture dependence of root zone water loss using conditionally averaged precipitation. *Water Resources Research,* 37**,** 1357-1365.

SANDHOLT, I., RASMUSSEN, K. & ANDERSEN, J. 2002. A simple interpretation of the surface temperature/vegetation index space for assessment of surface moisture status. *Remote Sensing of Environment,* 79**,** 213-224.

SATALINO, G., MATTIA, F., DAVIDSON, M. W. J., LE TOAN, T., PASQUARIELLO, G. & BORGEAUD, M. 2002. On current limits of soil moisture retrieval from ERS-SAR data. *IEEE Transactions on Geoscience and Remote Sensing,* 40**,** 2438-2447.

SCHAEFER, G. L. & PAETZOLD, R. F. SNOTEL (SNOwpack TELemetry) and SCAN (Soil Climate Analysis Network). Automated Weather Station (AWS) workshop, March 6-10 2001 Lincoln, NE.

SCHLESINGER, W. H., RAIKES, J. A., HARTLEY, A. E. & CROSS, A. F. 1996. On the spatial pattern of soil nutrients in desert ecosystems. *Ecology,* 77**,** 364-374.

SCHMUGGE, T. 1978. Remote sensing of surface soil moisture. *Journal of Applied Meteorology,* 17**,** 1549-1557.

SCHMUGGE, T., O'NEILL, P. E. & WANG, J. R. 1986. Passive microwave soil moisture research. *IEEE Transactions on Geoscience and Remote Sensing***,** 12-22.

SCHMUGGE, T. J. & JACKSON, T. J. 1994. Mapping surface soil moisture with microwave radiometers. *Meteorology and Atmospheric Physics,* 54**,** 213-223.

SCHMUGGE, T. J., JACKSON, T. J. & MCKIM, H. L. 1980. Survey of methods for soil moisture determination. *Water Resources Research,* 16**,** 961-979.

SCHNEIDER, A., FRIEDL, M. A. & POTERE, D. 2010. Mapping global urban areas using MODIS 500-m data: New methods and datasets based on 'urban ecoregions'. *Remote Sensing of Environment,* 114**,** 1733-1746.

SCHNÜRER, J., CLARHOLM, M., BOSTRÖM, S. & ROSSWALL, T. 1986. Effects of moisture on soil microorganisms and nematodes: a field experiment. *Microbial Ecology,* 12**,** 217-230.

SENEVIRATNE, S. I., CORTI, T., DAVIN, E. L., HIRSCHI, M., JAEGER, E. B., LEHNER, I., ORLOWSKY, B. & TEULING, A. J. 2010. Investigating soil moisture–climate interactions in a changing climate: A review. *Earth-Science Reviews,* 99**,** 125-161.

SHAMAN, J. & DAY, J. F. 2005. Achieving operational hydrologic monitoring of mosquitoborne disease.

SHI, J., CHEN, K. S., LI, Q., JACKSON, T. J., O'NEILL, P. E. & TSANG, L. 2002. A parameterized surface reflectivity model and estimation of bare-surface soil moisture with L-band radiometer. *IEEE Transactions on Geoscience and Remote Sensing,* 40**,** 2674-2686.

SHI, J., JIANG, L., ZHANG, L., CHEN, K. S., WIGNERON, J.-P. & CHANZY, A. 2005. A parameterized multifrequency-polarisation surface emission model. *IEEE Transactions on Geoscience and Remote Sensing,* 43**,** 2831-2841.

SHI, J., WANG, J., HSU, A., O'NEILI, P. & ENGMAN, E. T. Estimation of soil moisture and surface roughness parameters using L-band SAR measurements. Proceeding of IEEE Transaction on Geosicence and Remote Sensing, 1995. 507-509 vol. 1.

SHI, J., WANG, J., HSU, A. Y., O'NEILL, P. E. & ENGMAN, E. T. 1997. Estimation of bare surface soil moisture and surface roughness parameter using L-band SAR image data. *IEEE Transactions on Geoscience and Remote Sensing,* 35**,** 1254-1266.

SHOSHANY, M., SVORAY, T., CURRAN, P. J., FOODY, G. M. & PEREVOLOTSKY, A. 2000. The relationship between ERS-2 SAR backscatter and soil moisture: generalization from a humid to semi-arid transect. *International Journal of Remote Sensing,* 21**,** 2337-2343.

SHUTKO, A. M. & REUTOV, E. M. 1982. Mixture formulas applied in estimation of dielectric and radiative characteristics of soils and

grounds at microwave frequencies. *IEEE Transactions on Geoscience and Remote Sensing*, 29-32.

SIPPEL, S. J., HAMILTON, S. K., MELACK, J. M. & CHOUDHURY, B. J. 1994. Determination of inundation area in the Amazon River floodplain using the SMMR 37 GHz polarisation difference. *Remote Sensing of Environment,* 48, 70-76.

SIVAPALAN, M., BEVEN, K. & WOOD, E. F. 1987. On Hydrologic Similarity. *Water Resources Research,* 23, 2266-2278.

SMITH, A. B., WALKER, J. P., WESTERN, A. W., YOUNG, R. I., ELLETT, K. M., PIPUNIC, R. C., GRAYSON, R. B., SIRIWARDENA, L., CHIEW, F. H. S. & RICHTER, H. 2012. The Murrumbidgee soil moisture monitoring network data set. *Water Resources Research,* 48, W07701.

SMITH, L. C. 1997. Satellite remote sensing of river inundation area, stage, and discharge: A review. *Hydrological processes,* 11, 1427-1439.

SMITH, R. C. G. & CHOUDHURY, B. J. 1991. Analysis of normalized difference and surface temperature observations over southeastern Australia. *Remote Sensing,* 12, 2021-2044.

SMITH, S. J. & BOWERS, S. A. 1972. Spectrophotometric determination of soil water content. *Soil Science Society of America Journal,* 36, 978-980.

SOMMER, S., HILL, J. & MEGIER, J. 1998. The potential of remote sensing for monitoring rural land use changes and their effects on soil conditions. *Agriculture, Ecosystems & Environment,* 67, 197-209.

SPERRY, J. S., HACKE, U. G., OREN, R. & COMSTOCK, J. P. 2002. Water deficits and hydraulic limits to leaf water supply. *Plant, Cell & Environment,* 25, 251-263.

SRIDHAR, V., HUBBARD, K. G., YOU, J. & HUNT, E. D. 2008. Development of the soil moisture index to quantify agricultural drought and its "user friendliness" in severity-area-duration assessment. *Journal of Hydrometeorology,* 9, 660-676.

TOPP, G. C., DAVIS, J. L. & ANNAN, A. P. 1980. Electromagnetic determination of soil water content: Measurements in coaxial transmission lines. *Water Resources Research,* 16, 574-582.

TOPP, G. C., DAVIS, J. L. & ANNAN, A. P. 1982a. Electromagnetic determination of soil water content using TDR: I. Applications to wetting fronts and steep gradients. *Soil Science Society of America Journal,* 46, 672-678.

TOPP, G. C., DAVIS, J. L. & ANNAN, A. P. 1982b. Electromagnetic determination of soil water content using TDR: II. Evaluation of installation and configuration of parallel transmission lines. *Soil Science Society of America Journal,* 46, 678-684.

TRAMUTOLI, V., CLAPS, P., MARELLA, M., PERGOLA, N. & SILEO, C. Feasibility of hydrological application of thermal inertia from remote sensing. 2000. 16-18.

TROCH, P. A., VANDERSTEENE, F., SU, Z., HOEBEN, R. & WUETHRICH, M. Estimating microwave observation depth in bare soil through multi-frequency scatterometry. 1997. 1996.

TSANG, L. & NEWTON, R. W. 1982. Microwave emissions from soils with rough surfaces. *Journal of Geophysical Research,* 87, 9017-9024.

TSANG, L., NJOKU, E. & KONG, J. A. 1975. Microwave thermal emission from a stratified medium with nonuniform temperature distribution. *Journal of Applied Physics,* 46**,** 5127-5133.

TURNER, W., SPECTOR, S., GARDINER, N., FLADELAND, M., STERLING, E. & STEININGER, M. 2003. Remote sensing for biodiversity science and conservation. *Trends in Ecology & Evolution,* 18**,** 306-314.

ULABY, F. T., DUBOIS, P. C. & VAN ZYL, J. 1996. Radar mapping of surface soil moisture. *Journal of Hydrology,* 184**,** 57-84.

ULABY, F. T., MOORE, R. K. & FUNG, A. K. 1981. *Microwave remote sensing: Active and passive. Volume I-Microwave remote sensing fundamentals and radiometry.*

ULABY, F. T., MOORE, R. K. & FUNG, A. K. 1982. *Microwave remote sensing: Active and passive. Volume II-Radar remote sensing and surface scattering and emission theory.*

ULABY, F. T., MOORE, R. K. & FUNG, A. K. 1986. *Microwave remote sensing: Active and Passive. Volume III-Volume Scattering and Emission Theory, Advanced Systems and Applications.*

ULABY, F. T., RAZANI, M. & DOBSON, M. C. 1983. Effects of vegetation cover on the microwave radiometric sensitivity to soil moisture. *IEEE Transactions on Geoscience and Remote Sensing***,** 51-61.

ULABY, F. T. & WILSON, E. A. 1985. Microwave attenuation properties of vegetation canopies. *IEEE Transactions on Geoscience and Remote Sensing***,** 746-753.

VAN BAVEL, C. H. M., NIELSEN, D. R. & DAVIDSON, J. M. 1961. Calibration and characteristics of two neutron moisture probes.

VAN DE GRIEND, A. A. & ENGMAN, E. T. 1985. Partial area hydrology and remote sensing. *Journal of Hydrology,* 81**,** 211-251.

VAN DE GRIEND, A. A. & WIGNERON, J.-P. 2004. The b-factor as a function of frequency and canopy type at H-polarisation. *IEEE Transactions on Geoscience and Remote Sensing,* 42**,** 786-794.

VAN ZYL, J. J., CHAPMAN, B. D., DUBOIS, P. & SHI, J. 1993. The effect of topography on SAR calibration. *IEEE Transactions on Geoscience and Remote Sensing,* 31**,** 1036-1043.

VELDKAMP, E. & O'BRIEN, J. J. 2000. Calibration of a frequency domain reflectometry sensor for humid tropical soils of volcanic origin. *Soil Science Society of America Journal,* 64**,** 1549-1553.

VERSTRAETEN, W. W., VEROUSTRAETE, F., VAN DER SANDE, C. J., GROOTAERS, I. & FEYEN, J. 2006. Soil moisture retrieval using thermal inertia, determined with visible and thermal spaceborne data, validated for European forests. *Remote Sensing of Environment,* 101**,** 299-314.

VINNIKOV, K. Y., ROBOCK, A., SPERANSKAYA, N. A. & SCHLOSSER, C. A. 1996. Scales of temporal and spatial variability of midlatitude soil moisture. *Journal of Geophysical Research,* 101**,** 7163-7174.

VOLANTE, J. N., ALCARAZ-SEGURA, D., MOSCIARO, M. J., VIGLIZZO, E. F. & PARUELO, J. M. 2011. Ecosystem functional changes associated with land clearing in NW Argentina. *Agriculture, Ecosystems & Environment.*

WAGNER, W., NAEIMI, V., SCIPAL, K., DE JEU, R. & MARTÍNEZ-FERNÁNDEZ, J. 2007. Soil moisture from operational meteorological satellites. *Hydrogeology Journal,* 15**,** 121-131.

WALKER, J. P. & HOUSER, P. R. 2004. Requirements of a global near-surface soil moisture satellite mission: accuracy, repeat time, and spatial resolution. *Advances in Water Resources,* 27**,** 785-801.

WALKER, J. P., HOUSER, P. R. & WILLGOOSE, G. R. 2004. Active microwave remote sensing for soil moisture measurement: a field evaluation using ERS - 2. *Hydrological Processes,* 18**,** 1975-1997.

WALKER, J. P., RUDIGER, C., PEISCHL, S., YE, N., ALLAHMORADI, M., RYU, D., KERR, Y., KIM, E., GURNEY, R., BARRETT, D. & LE MARSHALL, J. 2009. Australian Airborne Cal/val Experiments for SMOS (AACES): Experiment Plan. Department of Civil and Environmental Engineering, The University of Melbourne.

WANG, J. R. 1983. Passive microwave sensing of soil moisture content: The effects of soil bulk density and surface roughness. *Remote Sensing of Environment,* 13**,** 329-344.

WANG, J. R. & CHOUDHURY, B. J. 1981. Remote Sensing of Soil Moisture Content, Over Bare Field at 1.4 GHz Frequency. *Journal of Geophysical Research,* 86**,** 5277-5282.

WANG, J. R., O'NEILL, P. E., JACKSON, T. J. & ENGMAN, E. T. 1983. Multifrequency measurements of the effects of soil moisture, soil texture, and surface roughness. *IEEE Transactions on Geoscience and Remote Sensing***,** 44-51.

WANG, J. R. & SCHMUGGE, T. J. 1980. An empirical model for the complex dielectric permittivity of soils as a function of water content. *IEEE Transactions on Geoscience and Remote Sensing***,** 288-295.

WANG, J. R., SHIUE, J. C., SCHMUGGE, T. J. & ENGMAN, E. T. 1990. The< e1> L</e1>-band PBMR measurements of surface soil moisture in FIFE. *IEEE Transactions on Geoscience and Remote Sensing,* 28**,** 906-914.

WANG, L. & QU, J. J. 2007. NMDI: A normalized multi-band drought index for monitoring soil and vegetation moisture with satellite remote sensing. *Geophysical Research Letters,* 34**,** L20405.

WANG, L. & QU, J. J. 2009. Satellite remote sensing applications for surface soil moisture monitoring: A review. *Frontiers of Earth Science in China,* 3**,** 237-247.

WANG, L., QU, J. J., ZHANG, S., HAO, X. & DASGUPTA, S. 2007a. Soil moisture estimation using MODIS and ground measurements in eastern China. *International Journal of Remote Sensing,* 28**,** 1413-1418.

WANG, X., XIE, H., GUAN, H. & ZHOU, X. 2007b. Different responses of MODIS-derived NDVI to root-zone soil moisture in semi-arid and humid regions. *Journal of hydrology,* 340**,** 12-24.

WANG, X. & ZHANG, Z. A Review: Theories, Methods and Development of Soil Moisture Monitoring by Remote Sensing. 2005. 4505-4507.

WEAVER, C. P. & AVISSAR, R. 2001. Atmospheric disturbances caused by human modification of the landscape. *BULLETIN-AMERICAN METEOROLOGICAL SOCIETY,* 82**,** 269-282.

WEGMULLER, U. & MATZLER, C. 1999. Rough bare soil reflectivity model. *Geoscience and Remote Sensing, IEEE Transactions on,* 37**,** 1391-1395.

WEITZ, A., GRAUEL, W., KELLER, M. & VELDKAMP, E. 1997. Calibration of time domain reflectometry technique using undisturbed soil samples from humid tropical soils of volcanic origin. *Water Resources Research,* 33**,** 1241-1249.

WESTERN, A. W., GRAYSON, R. B., BLÖSCHL, G., WILLGOOSE, G. R. & MCMAHON, T. A. 1999. Observed spatial organization of soil moisture and its relation to terrain indices. *Water Resources Research,* 35**,** 797-810.

WIGNERON, J.-P., CHANZY, A., CALVET, J. C. & BRUGUIER, N. 1995. A simple algorithm to retrieve soil moisture and vegetation biomass using passive microwave measurements over crop fields. *Remote Sensing of Environment,* 51**,** 331-341.

WIGNERON, J.-P., KERR, Y. H., WALDTEUFEL, P., SALEH, K., ESCORIHUELA, M. J., RICHAUME, P., FERRAZZOLI, P., DE ROSNAY, P., GURNEY, R. & CALVET, J. C. 2007. L-band Microwave Emission of the Biosphere (L-MEB) Model: Description and calibration against experimental data sets over crop fields. *Remote Sensing of Environment,* 107**,** 639-655.

WIGNERON, J.-P., LAGUERRE, L. & KERR, Y. H. 2001. A simple parameterization of the L-band microwave emission from rough agricultural soils. *IEEE Transactions on Geoscience and Remote Sensing,* 39**,** 1697-1707.

WIGNERON, J.-P., PARDÉ, M., WALDTEUFEL, P., CHANZY, A., KERR, Y., SCHMIDL, S. & SKOU, N. 2004. Characterizing the dependence of vegetation model parameters on crop structure, incidence angle, and polarisation at L-band. *IEEE Transactions on Geoscience and Remote Sensing,* 42**,** 416-425.

WILHEIT, T. T. 1978. Radiative transfer in a plane stratified dielectric. *IEEE Transactions on Geoscience Electronics,* 16**,** 138-143.

WILSON, R. G. 1971. Methods of measuring soil moisture. *Technical Manual Series.* Ottawa, Canada: Canadian National Commission for the International Hydrological Decade.

WOOD, E. F., LETTENMAIER, D. P. & ZARTARIAN, V. G. 1992. A land-surface hydrology parameterization with subgrid variability for general circulation models. *Journal of Geophysical Research,* 97**,** 2717-2728.

XU, H. 2006. Modification of normalised difference water index (NDWI) to enhance open water features in remotely sensed imagery. *International Journal of Remote Sensing,* 27**,** 3025-3033.

XUE, H. & NI, S. 2006. Progress in the study on monitoring of soil moisture with thermal infrared remote sensing [J]. *Agricultural Research in the Arid Areas,* 6.

YOUNG, R., WALKER, J., YEOH, N., SMITH, A., ELLETT, K., MERLIN, O. & WESTERN, A. 2008. Soil moisture and meteorological observations from the Murrumbidgee catchment. *Department of Civil and Environmental Engineering, The University of Melbourne.*

ZRIBI, M., GARCLA, J. C., AQID, N., ADAR, E. & CIARLETTI, V. 2003. Modelling of ERS-2 radar backscattering over rocky arid regions. *International Journal of Remote Sensing,* 24**,** 5229-5242.

ZRIBI, M., PARDÉ, M., BOUTIN, J., FANISE, P., HAUSER, D., DECHAMBRE, M., KERR, Y., LEDUC-LEBALLEUR, M., REVERDIN, G. & SKOU, N. 2011. CAROLS: A new airborne L-band radiometer for ocean surface and land observations. *Sensors,* 11**,** 719-742.